NASA Technical Paper 3114

November 1991

Wind Tunnel Investigation of the Interaction and Breakdown Characteristics of Slender-Wing Vortices at Subsonic, Transonic, and Supersonic Speeds

Gary E. Erickson

NASA

**NASA
Technical
Paper
3114**

1991

Wind Tunnel Investigation of the Interaction and Breakdown Characteristics of Slender-Wing Vortices at Subsonic, Transonic, and Supersonic Speeds

Gary E. Erickson
*Langley Research Center
Hampton, Virginia*

National Aeronautics and
Space Administration

Office of Management

Scientific and Technical
Information Program

Summary

A wind tunnel investigation was conducted in the NASA Ames 6- by 6-Foot Transonic/Supersonic Wind Tunnel of slender-wing vortex flows at subsonic, transonic, and supersonic speeds. A sharp-leading-edge, 65° cropped delta wing was tested with and without a leading-edge extension (LEX) at free-stream Mach numbers from 0.40 to 1.60, Reynolds numbers based on the wing centerline chord from approximately 2.48×10^6 to 5.43×10^6, and angles of attack from $-2°$ to 24°. Emphasis was placed on improving the understanding of vortex development, interactions, and breakdown, shock wave development, and vortex-shock interactions. The test data included off-body and surface flow visualizations, wing upper surface static pressure distributions, and six-component forces and moments. The present results show the transition from the low-speed, "classical" vortex regime to the transonic regime, beginning at a free-stream Mach number of 0.60, where vortices coexist with shock waves. The direct interaction of the wing primary vortex with a normal, or terminating, shock wave near the trailing edge and the development of shock-induced secondary boundary-layer flow separation on the wing upper surface are confirmed. The onset and progression of core breakdown with the angle of attack were sensitive to the Mach number. The shock effects at transonic speeds were reduced, and in some cases eliminated, by the interaction of the wing and LEX vortices. The vortex surface pressure signatures and the direct interaction of the wing and LEX vortex cores (the cores wrapping around each other) diminished at transonic and supersonic speeds. The interacting wing and LEX vortices were bounded by a complex system of shock waves at supersonic speeds. However, footprints of the shock waves were not manifested in the surface pressure distributions.

Introduction

The exploitation of vortex flows to enhance the maneuverability of fighter airplanes spans two decades, beginning with the early designs that led to the YF-16 and YF-17 lightweight fighter prototypes. Despite the many years of vortex research, however, the ability to understand, predict, and control these complex fluid flows on high-performance airplanes has not fully matured. Details of the vortex behavior about fighter airplanes in the present U.S. inventory are still emerging (refs. 1 and 2). The incomplete understanding of the vortex development and breakdown and of the vortex-vortex, vortex-shock, and vortex-tail interactions has limited the effective control of these powerful rotating flows. As a consequence, the full impact of the vortices on the high-angle-of-attack characteristics, including the departure/spin susceptibility and the fatigue life of airframe components, is frequently not recognized until well after an airplane has gone into production. These flow phenomena will continue to be of importance to derivative and new-generation airplanes. For this reason, fundamental-flow modeling experiments are required to augment the understanding of vortex flows over wide ranges of test conditions and configuration variables to help verify advanced computational fluid dynamics (CFD) methods and to develop vortex control mechanisms for enhanced maneuverability at high angles of attack.

The purpose of this study was to improve the understanding of the vortex flow characteristics on both the wing-alone configuration and the wing with a leading-edge extension (LEX). Testing was conducted in the NASA Ames 6- by 6-Foot Transonic/Supersonic Wind Tunnel at subsonic through supersonic speeds using a generic model of a 65° cropped delta wing. This model was used previously in reference 3. The LEX was built for the model in order to study interacting, or coupled, vortex flows. The experimental results included off-body flow visualizations using a laser vapor screen technique, surface flow visualizations using a fluorescent oil method, wing upper surface static pressure distributions, and model six-component forces and moments.

Symbols and Abbreviations

B.L.	buttline
C_D	drag coefficient, Drag/$q_\infty S_{\text{wing}}$
CFD	computational fluid dynamics
C_L	lift coefficient, Lift/$q_\infty S_{\text{wing}}$
C_m	pitching-moment coefficient referenced to $0.57c$, Pitching moment/$q_\infty S_{\text{wing}}\bar{c}$
$C_{p,u}$	wing upper surface static pressure coefficient, $(p_{l,u} - p_\infty)/q_\infty$
$C_{p,v}$	vacuum pressure coefficient, $-2/\gamma M_\infty^2$
C_p^*	pressure coefficient corresponding to local speed of sound, $\frac{2}{\gamma M_\infty^2}\left\{\left[\frac{(\gamma-1)M_\infty^2+2}{\gamma+1}\right]^{3.5}-1\right\}$
c	wing centerline chord, 23.62 in.
$\bar{c}$	wing mean aerodynamic chord, 16.06 in.
LEX	wing leading-edge extension

M_N	component of Mach number normal to leading edge, $M_\infty \cos\Lambda_{\text{LE}}(1 + \sin^2\alpha \tan^2\Lambda_{\text{LE}})^{1/2}$
M_∞	free-stream Mach number
M.S.	model station
$p_{l,u}$	local upper surface static pressure, lb/ft^2
p_0	tunnel stagnation pressure, lb/ft^2
p_∞	free-stream static pressure, lb/ft^2
q_∞	free-stream dynamic pressure, lb/ft^2
R_c	Reynolds number based on wing centerline chord c
S_{wing}	reference wing area, 254.51 in^2
s	local semispan distance, in.
T_0	tunnel stagnation temperature, °F
V_∞	free-stream velocity
W.L.	waterline
x	distance along wing centerline chord measured from apex, in.
y	distance along wing local semispan measured from model centerline, in.
α	angle of attack, deg
α_N	angle of attack normal to leading edge, $\tan^{-1}(\tan\alpha/\cos\Lambda_{\text{LE}})$, deg
γ	ratio of specific heat constants
Λ_{LE}	wing leading-edge sweep angle, 65°

Experimental Investigation

Model Description and Test Apparatus

Tests were conducted on an untwisted and uncambered model of a 65° cropped delta wing with sharp leading edges. Geometric details of the model are summarized in table I. The model is shown in the photographs in figure 1. The wing had an NACA 64A005 airfoil section from the 40-percent chord station to the trailing edge. A sharp leading edge was obtained by fairing a biconvex circular-arc section into the NACA profile from the 40-percent chord station to the wing leading edge. The wing was mounted in a high position on a fuselage that served as a housing for balance and pressure instrumentation. (See fig. 1.) The fuselage tapered down to a small radius along approximately the forward 35-percent portion of its length, and it terminated 0.50 in. (model scale) from the apex of the wing. This portion of the fuselage could be replaced with an alternate forward fuselage section having an integral strut, or "gooseneck," to allow the installation of a wing leading-edge extension (LEX) having a 65°/90° planform. The wing LEX assembly is illustrated in figure 1(b). The LEX area (left and right sides) was 15 percent of the reference wing area. Sketches of the model planform and of cross sections at selected model stations are shown in figure 2. The LEX was bolted to the gooseneck and was a flat plate, 0.25-in. thick, and had symmetrically beveled leading and side edges (fig. 2). For additional support, the trailing edge of the LEX was grooved to allow an overlap with the wing leading edge as sketched in figure 2. The juncture of the wing and the LEX was then faired to provide a smooth transition. The right wing was instrumented with three spanwise rows of upper surface static pressure orifices. The pressure rows were located at $x/c = 0.30$, 0.60, and 0.80, where x is the distance along the wing centerline chord c measured from the apex. The total number of orifices was 64. The pressure measurement stations are illustrated in figure 3. The pressures were measured using two 48-port, electronically scanned pressure modules. One module was located inside the model fuselage. The second module was located in an instrumentation housing mounted to the sting body by the support system strut as shown in figure 4. The wing pressure lines were routed through the fuselage and then out along the model sting to the housing.

Table I. Geometric Details of Model

Wing aspect ratio	1.38
Reference wing span, in.	18.74
Wing centerline chord, in.	23.62
Wingtip chord, in.	3.54
Wing mean aerodynamic chord, in.	16.06
Model length (LEX off), in.	24.60
Model length (LEX on), in.	32.28
Reference wing area, in^2	254.51
LEX area, in^2	38.11
Wing leading-edge sweep angle, deg	65
Wing trailing-edge sweep angle, deg	0
Wing taper ratio	0.15

The model forces and moments were measured using a six-component, internally mounted, strain gauge balance. The balance measurements were obtained in separate runs with the wing pressure lines removed. The force and moment coefficients for the wing-alone and wing-LEX configurations were based on the reference wing area S_{wing}.

An angle-of-attack measurement device (tilt sensor) was installed in the model support system. The measurements were corrected for balance and sting deflection under load.

The nominal angle-of-attack range of the sting body in the Ames 6- by 6-foot facility is from 12° to $-12°$. Running the model inverted, in combination with a 10° sting socket, allowed a maximum positive angle of attack of 24° (including sting and balance deflection due to the aerodynamic load). The model surface pressure and balance measurements were obtained in this fashion. Sketches of the model in the inverted and upright positions are shown in figure 4.

Flow Visualization Techniques

The off-body flow visualization was conducted using a laser vapor screen technique (ref. 4). Water was injected into the diffuser section from a single orifice located in the tunnel ceiling to increase the relative humidity level in the test section. At the subsonic speeds, the water vapor in the free stream condensed within the vortical flows about the model. Illumination of the cross flow using a sheet of laser light revealed bright vortices with a darker background. The water vapor condensed in the free stream at the transonic and supersonic speeds, and the vortices appeared as dark regions surrounded by a light background. The model was painted flat black to reduce the reflection of laser light and to provide an adequate contrast with the cross-flow patterns. An 18-W argon-ion laser was used in the present experiment, although the power output was typically maintained in the 8- to 10-W range. The laser head and optical components were located on the port side of the test section. The light sheet was directed to the model through a 46-in-diameter schlieren window. (See fig. 4). The axial position of the light sheet was varied remotely to provide coverage of the model cross flow from the LEX to the near wake of the model. A light-sheet orientation normal to the wing plane was maintained at all angles of attack by manually rotating the light-sheet optics. The light-sheet orientation with respect to the model is shown in figure 5. The cross-flow visualizations were documented with the model inverted using video and 70-mm still cameras mounted in separate housings on the model sting support system just upstream of the strut. The upstream view provided by these cameras remained fixed with respect to the model at all angles of attack. Video and 70-mm still cameras were also mounted outside the test section in a one-quarter front position with respect to the model. The cameras were directed through the schlieren window in the starboard side of the test section opposite the laser light-sheet source.

Alignment of the light sheet along the length of the vortices was possible by rotating and vertically translating the light-sheet generator optics. The light sheet intersected the model apex and sliced lengthwise through the vortical flows as sketched in figure 5. A single plane of illumination was frequently inadequate in flow situations where the vortex core paths were highly curved in vertical planes. This was most pronounced on the wing–LEX configuration. The lengthwise light-sheet cuts were obtained with the model upright. This allowed viewing the flow field from the window in the test section ceiling. The video and still cameras were relocated to the ceiling window above the model. Figure 6 sketches the three camera-viewing orientations that were used during the laser vapor screen flow visualization. All the vapor screen results were obtained independently of the model pressure and balance measurements.

A fluorescent oil technique was used to obtain the wing upper surface flow patterns. The model was run in the upright position for this phase of the experiment. Prior to an oil flow run, the model was coated with a mixture of oil and fluorescent pigment. Once the test conditions were achieved, sufficient time was allowed for the flow to become fully established. Photographs were then taken during the run with a 70-mm camera synchronized to a series of strobe lights with fluorescent filters positioned in the tunnel ceiling. The oil flow visualization was also conducted independently of the pressure, force, and vapor screen runs.

Wind Tunnel Facility and Test Conditions

The model surface static pressures, forces and moments, and off-body and surface flow visualizations were obtained in the NASA Ames 6- by 6-Foot Transonic/Supersonic Wind Tunnel. The wing-alone and wing–LEX models are shown sting mounted in the wind tunnel test section in figure 7. The 6- by 6-foot facility is a closed-circuit, single-return tunnel equipped with an asymmetric sliding-block nozzle and a test section with a slotted floor and ceiling. The Mach number is continuously variable from 0.25 to 2.20. The tunnel stagnation pressure can be varied from 0.3 to 1.0 atm and the Reynolds number range is from 1×10^6 per foot to 5×10^6 per foot. A more detailed description of the Ames facility is provided in reference 5.

The test results were obtained at free-stream Mach numbers of 0.40, 0.60, 0.80, 0.85, 0.90, 0.95, 1.20, and 1.60. The six-component forces and moments were obtained at angles of attack from -2° to 24°. The wing surface static pressure and vapor screen flow visualizations were obtained at $\alpha = 8^\circ$ to 24°. Surface oil flow visualization was conducted at $\alpha = 12^\circ$ to 20°. The maximum free-stream dynamic pressure was 250 lb/ft^2 (psf) because of a limitation in the model sting normal force. The tunnel stagnation pressure varied with the Mach number. The Reynolds number based on the wing centerline chord (R_c) varied from approximately 2.48×10^6 to 5.43×10^6. The range of test conditions is listed in table II.

Table II. Wind Tunnel Test Conditions

M_∞	p_0, lb/ft^2	T_0, °F	R_c
0.40	2235	65	5.43×10^6
.60	1242	67	4.21
.80	851	68	3.39
.85	792	68	3.23
.90	750	68	3.09
.95	711	68	3.01
1.20	603	70	2.68
1.60	597	72	2.48

Base pressures and balance cavity pressures were measured and used to adjust the drag data to the condition of free-stream static pressure acting over the fuselage cavity and base areas. Tunnel wall corrections were not applied since the test section ceiling and floor of the 6- by 6-foot facility are slotted. The wing, LEX, and fuselage were tested with free transition.

Discussion of Results

Representative results obtained in the NASA Ames 6- by 6-Foot Transonic/Supersonic Wind Tunnel are presented in two major sections corresponding to the 65° cropped delta wing-alone and the wing LEX configurations, respectively. Test results obtained at subsonic, transonic, and supersonic Mach numbers are discussed. At each Mach number, the wing surface static pressure distributions are analyzed with the assistance of off-body and surface flow visualizations, where available. The original vapor screen video tapes were used in the analysis of the off-surface flow visualization in cases where still photographs were not available. The surface pressure and flow visualization results are then correlated with the model force and moment data trends. All force and moment coefficients are based on the reference wing area S_{wing}.

The upper surface static pressure coefficient $C_{p,u}$ on the right wing at $x/c = 0.30$, 0.60, and 0.80 is plotted against the local semispan distance y measured from the model centerline, normalized by the local semispan s. Consequently, y/s values of 0 and 1 correspond to the model centerline and the wing leading edge, respectively. The pressure data at all three measurement stations are superimposed on a semispan representation of the wind tunnel model to provide a "three-dimensional" perspective of the $C_{p,u}$ distributions. (See fig. 8.) Surface static pressure data were available at $\alpha = 8^\circ$ to 24° in 2° increments. For clarity, however, the surface pressure distributions at $\alpha \approx 12^\circ$, 16°, 20°, and 24° are typically plotted. To isolate the onset of vortex breakdown on the wing-alone configuration, the surface pressures at $\alpha \approx 20^\circ$, 22°, and 24° are also plotted.

The majority of the laser vapor screen results correspond to cross-flow visualizations obtained from two viewing angles: a view looking upstream from the model support system and a view from a one-quarter front position. Lengthwise "cuts" of the laser light sheet through the vortices are shown on a limited basis, where the flow was observed from the tunnel ceiling. The viewing angles were sketched previously in figure 6.

65° Cropped Delta Wing Alone

$M_\infty = 0.40$. Figure 8 presents the wing surface static pressure distributions at $M_\infty = 0.40$ and $\alpha \approx 12^\circ$, 16°, 20°, and 24°. The wing leading-edge vortex induces pronounced suction pressure peaks at $x/c = 0.30$ and 0.60 that increase in magnitude and move inboard as the angle of attack increases from 12° to 24°. A similar trend occurs at $x/c = 0.80$ up to $\alpha \approx 20^\circ$.

The vortical flow pressure signature on the wing-alone configuration is nonconical. This is due to the upstream influence of the trailing-edge pressure recovery that causes the vortex-induced suction pressure peak to diminish from the forward to aft measurement stations at a given angle of attack. The spanwise location of the suction peak also moves inboard slightly. The pressure distribution at $\alpha \approx 20^\circ$ is isolated in figure 9 to illustrate these points. In contrast, the off-body flow is conical in character as shown in figure 10, which presents a lengthwise cut of the laser light sheet along the vortex core. The vortex core curves inboard slightly along the rear portion of the wing because of the wingtip cropping.

The footprint of the leading-edge vortex is apparent in the upper surface oil flow pattern in figure 11 corresponding to $\alpha \approx 20^\circ$. The lines of primary flow reattachment and secondary boundary-layer separation, the region of spanwise flow induced by the primary vortex, and the secondary vortex region are denoted in the photograph. The important features of the vortex-dominated flow are also sketched in figure 11 to assist in the interpretation of the oil flow pattern. The secondary vortex, which rotates in a sense opposite to the primary leading-edge vortex, induces the minor suction peak indicated in the pressure distributions in figure 9.

At $\alpha \approx 24^\circ$, the diminished suction peak and the slight broadening of the pressure distribution under the vortical flow at $x/c = 0.80$ are indicators of vortex breakdown at, or near, this measurement station. The pressure distributions at $\alpha \approx 20^\circ$, 22°, and 24° are shown in figure 12 to examine in greater detail the onset of vortex breakdown effects over the wing. The diminished suction peak magnitude is first manifested as the angle of attack is increased from 22° to 24°. Vortex breakdown effects will be discussed in more detail at $M_\infty = 0.60$ in the next subsection.

The advent of vortex breakdown upstream of the wing trailing edge is manifested as a break in the lift curve at $\alpha \approx 22^\circ$, a corresponding discontinuity in the drag polar, and a mild, unstable break in the pitching-moment curve. These effects are illustrated in figure 13.

M_∞ ***= 0.60.*** The wing surface pressure distributions at $M_\infty = 0.60$ are shown in figure 14 at $\alpha \approx 12^\circ$, 16°, 20°, and 24°. Locally supercritical flow exists underneath the leading-edge vortex at $x/c = 0.30$ and 0.60 beginning at $\alpha \approx 12^\circ$. This is apparent by comparing the local surface pressures to C_p^*, the critical pressure coefficient ($C_p^* = -1.294$ at $M_\infty = 0.60$). Supersonic "pockets" are evident at all three pressure rows at $\alpha = 16^\circ$, and the vortex-induced supercritical flow regions expand as the angle of attack increases to 20°.

The wing surface pressures at $\alpha = 20^\circ$ are shown separately in figure 15 for comparison with the off-body and surface flow visualization results presented in figures 16–18. The lengthwise cut through the vortex using the laser light sheet (fig. 16) reveals a stable core, and the vortex trajectory is consistent with the suction pressure peak locations in figure 15. The vapor screen result clearly shows the development of feeding sheet discontinuities along the length of the wing leading edge. This flow phenomenon is associated with an instability of the three-dimensional shear flow. A diagram of the flow (from ref. 6) is presented in figure 16. At low angles of attack, the shear layer instability is characterized by numerous, noninteracting streamwise vortices. At higher angles of attack, the vortices follow a spiral path about the central, dominant vortical flow as sketched in figure 16. This flow structure has been observed in references 1, 2, and 6–9 encompassing low subsonic through supersonic speeds and Reynolds numbers corresponding to laminar, transitional, and turbulent flows. The feeding sheet discontinuities cannot be detected in the surface oil flow patterns in figures 17 and 18. Instead, the footprint of a single, large primary vortex is apparent in the surface flow. The superposition of the pressure distribution at $x/c = 0.60$ on the oil flow photograph in figure 18 shows the relationship between the key features of the surface pressures and corresponding surface flow pattern. Tertiary separation is apparent in the surface flow as a bright line situated outboard of the secondary separation. However, the surface streamlines between secondary and tertiary separation lines do not show any indication of a reattachment induced by a tertiary vortex, which may be too weak to scrub the oil in this region.

The outward bending of the secondary separation line in figure 17 at about 45 percent of the distance along the wing centerline chord is indicative of a transitional surface flow. The Reynolds number based on the chord distance to transition is approximately 1.89×10^6, which is similar to the flow conditions in reference 10 where transition was observed on a 75° delta wing at low speed. Closer examination of the surface flow just downstream of the kink in the secondary separation line reveals the trace of a shock wave. The footprint of a shock wave can be detected in surface flow patterns by a sudden change in the direction of the surface streamlines, as sketched in figure 19. The surface flow in the region of the shock wave is shown in more detail in the expanded view in figure 18, and schematic representations of the cross flow and surface flow are shown in figure 19. The shock is situated between the leading-edge vortex and the wing surface and may extend from approximately the apex region to 70 percent of the distance along the model centerline chord. Along the forward portion of the wing, the laminar boundary layer separates at the shock wave. Farther aft, the transition to turbulent flow enables the boundary layer to negotiate the shock-induced adverse pressure gradient. Secondary separation then occurs outboard of the shock position as sketched in figure 19. This result is consistent with the hypothesis of reference 11 that embedded shock waves first appear in the vortex-dominated flow about slender wings at free-stream Mach numbers of approximately 0.60. The shock wave development is also consistent with the supersonic pockets indicated in the pressure distributions in figure 15, and it marks the onset of transonic flow mechanisms about the model of a 65° cropped delta wing.

The pressure data shown previously in figure 14 reveal a decrease in the vortex-induced suction pressure level and a broadening of the pressure distribution at $x/c = 0.80$ and $\alpha \approx 24°$. The surface pressures are entirely subcritical at this station. The $C_{p,u}$ distributions in figure 20 suggest that vortex breakdown becomes fully established at $x/c = 0.80$ as the angle of attack increases from approximately 22° to 24°. The diminished magnitude of the vortex suction peak at $x/c = 0.60$ is due to the upward movement of the vortex away from the wing surface. The appearance of vortex breakdown over the wing is confirmed in the laser vapor screen photographs corresponding to planes normal to the wing at $x/c = 0.40$, 0.60, 0.80, and 1.00 and $\alpha = 24°$ in figure 21. A stable vortex has a donut-shaped cross flow in laser vapor screen patterns at subsonic speeds. The core region is characterized by a low level of water vapor condensate, whereas the outer region of the vortex features a high condensate level. Upon breakdown, condensate migrates to the core region, and the expanded vortex cross flow has a more uniform distribution of condensed water vapor. The vortex breakdown phenomenon is asymmetric. The vortical flow over the right wing bursts sooner than the left-wing vortex. This was also observed at $M_\infty = 0.40$.

Vortex breakdown asymmetries have been observed in references 12 and 13 on 65° and 63.4° delta wings, respectively, at free-stream Mach numbers of 0.60 and 0.80. Reference 12 has suggested that model imperfections, model support system effects, and asymmetric free-stream flow conditions are likely sources of the asymmetric flow development about the 65° swept wing. The wing is not slender enough to promote the contact of the primary vortex pair and ensuing hydrodynamic instability phenomenon leading to asymmetric vortex paths and breakdown positions that have been discussed in reference 14. The model surface definition was determined using a three-dimensional validator, and no imperfections were revealed from these measurements. A possible source of the asymmetric bursting in the present test is the downstream blockage caused by the instrumentation housing mounted to the side of the sting body (fig. 4). The housing is biased toward the starboard wing (model inverted) which exhibited the earlier vortex bursting. The occurrence of vortex breakdown, albeit asymmetric, promotes the lift-curve slope decrease at $\alpha = 24°$ in figure 22.

M_∞ ***= 0.80.*** The wing upper surface pressure distributions at $\alpha \approx 12°$, 16°, 20°, and 24° are presented in figure 23 corresponding to a free-stream Mach number of 0.80. The character of the pressure distributions at $M_\infty = 0.80$ changes in comparison to the results at the lower Mach numbers. The primary vortex-induced suction peak magnitudes diminish. The pressure rise outboard of the suction peaks is more gradual, and the difference between the primary and secondary vortex suction pressure levels is less pronounced. A comparison of the pressure data to the critical pressure coefficient ($C_p^* = -0.435$ at $M_\infty = 0.80$) reveals large regions of supersonic flow along the wing upper surface.

For clarity, the pressure distributions at $\alpha = 20°$ are isolated in figure 24. The corresponding surface flow pattern is illustrated in figure 25. The pressure signatures of the primary and secondary vortices have comparable magnitudes at $x/c = 0.30$ and 0.60. The primary suction peak is located just inboard of the secondary separation line, whereas the secondary suction peak is positioned just outboard of the tertiary separation line. This is illustrated in figure 25 where the pressure distribution at $x/c = 0.30$ is superimposed on the surface flow pattern. The secondary separation line is farther inboard at $M_\infty = 0.80$ in comparison with the results at the lower Mach numbers. For example, the spanwise position of the secondary separation determined from the oil flow pattern at $M_\infty = 0.80$ and $x/c = 0.30$ is at $y/s \approx 0.56$. The corresponding secondary separation position at $M_\infty = 0.60$ (fig. 17) is at $y/s \approx 0.63$. In addition, there is no evidence of the transitional pattern or changes in the surface streamline direction through a shock wave that were apparent at $M_\infty = 0.60$ (fig. 17). The inboard movement of the secondary separation with the Mach number, the sharp angle at which the surface streamlines approach the secondary separation line as sketched in figure 26, and the pronounced pressure signature of the secondary vortex at $M_\infty = 0.80$ are indicators of shock-induced boundary-layer separation. References 8, 13, and 15 have presented data on 55° cropped delta, 63.4° delta, and 65° cropped delta wings, respectively, where the secondary separation was sensitive to the Mach number, becoming shock induced at $M_\infty \geq 0.80$. Supersonic cross-flow Mach number components normal to the local isobar surfaces under the vortex were estimated in reference 16 for a 65° cropped delta wing with rounded leading edge corresponding to $M_\infty = 0.85$ and $\alpha = 20°$. A shock wave was considered likely because of the flow deceleration in the spanwise direction.

The occurrence of shock-induced secondary separation also helps to clarify the results obtained on the 63.4° delta wing in reference 13. In this study, it was found that the intensity and position of the suction peaks underneath the primary vortex were basically unchanged over the test Reynolds number range from 3.5×10^6 to 10.0×10^6 at $M_\infty = 0.80$. This is in contrast to results obtained at lower Mach numbers where the pressure signature of the primary vortex was sensitive to the Reynolds number (ref. 10). At the subsonic speeds, increasing the Reynolds number moves the secondary separation outboard, weakens the secondary vortex, and causes a downward displacement of the primary vortex toward the wing surface with a concurrent increase in the primary suction pressure peak. At the higher Mach numbers, however, a strong shock wave situated between the primary vortex and wing surface "fixes" the location of secondary boundary-layer separation, thus rendering the secondary vortex and its impact on the primary vortical flow insensitive to the Reynolds number.

The data in figure 23 show a flattening of the pressure distribution and diminished suction pressure level underneath the vortex at $x/c = 0.80$ and $\alpha \approx 24°$. Laser vapor screen flow visualizations were not obtained on the wing-alone model at this Mach number. However, the character of the pressure distributions is consistent with the onset of vortex breakdown at this measurement station. The pressure data in figure 27 indicate that the influence of vortex bursting is not manifested in the surface pressures until the angle of attack is increased from 22° to 24°. This is similar to the effect observed at $M_\infty = 0.60$ in figure 20.

The pressure distribution at $x/c = 0.60$ and $\alpha \approx 24°$ in figure 27 displays a similar, although less pronounced, effect that may be due to the advance of vortex breakdown toward this station and the lift-off of the vortical flow from the wing surface. Despite the appearance of fully established core bursting at $x/c = 0.80$, the surface flow underneath the expanded rotating flow remains supersonic. At $x/c = 0.60$, however, there is a local pocket of subsonic flow along the inboard 20 percent of the local semispan.

Vortex burst effects are reflected in the lift, drag, and pitching-moment characteristics in figure 28. The lift curve exhibits a drop-off at $\alpha > 22°$, the drag polar displays a corresponding discontinuity, and a slight unstable break in the pitching-moment curve is apparent.

$M_\infty = 0.85$. The wing surface pressures at $\alpha \approx 12°$, 16°, 20°, and 24° corresponding to a free-stream Mach number of 0.85 are presented in figure 29. The character of the pressure distributions is similar to the result obtained at $M_\infty = 0.80$ (fig. 23). At $\alpha = 20°$ and $x/c = 0.80$, however, there is a more pronounced increase in the spanwise distribution of the vortex-induced suction pressures and broadening of the pressure distribution at the higher Mach number. These effects are coincident with the development of a normal shock wave situated at $x/c \approx 0.85$. This flow situation is analogous to the shock that terminates the supersonic region on a two-dimensional airfoil in order for the flow to recover to subsonic conditions at the trailing edge. This shock wave is often referred to as a terminating or rear shock. Reference 16 presented schlieren flow visualization results obtained at $M_\infty = 0.85$ and $\alpha = 21°$ on the model used in the present experiment, but with a rounded leading edge. The schlieren results showed the development of a shock wave over the rear wing region. At a higher angle of attack (25°), the shock exhibited a rapid upstream movement. Figures 30, 31, and 32 present the wing surface pressure, surface oil flow, and laser vapor screen results obtained at $\alpha = 20°$. The surface pressures are supercritical at all pressure measurement stations ($C_p^* = -0.302$). The surface flow pattern shows the trace of the terminating shock situated downstream of the last pressure row. The shock extends laterally through the wing vortex and can be detected by the sudden change in the surface flow direction along the inboard portion of the wing as sketched in figure 31. The shock also promotes the discontinuities in the lines of secondary and tertiary separation.

The laser vapor screen results in figure 32 do not reveal any significant change in the vortex cross flow in the region of the vortex rear-shock interaction. The present results indicate that the passage of the vortex through the rear shock wave does not cause vortex breakdown at $\alpha = 20°$.

The pressure distributions at $x/c = 0.80$ in figure 33 show a slight decrease in the suction pressure level across the span, except directly underneath the primary vortex, as the angle of attack increases from 20° to 22°. This coincides with the advancement of vortex breakdown toward the aft pressure row on the right wing. The vapor screen results corresponding to $\alpha = 22°$ in figure 34 show the burst vortex over the wing. The breakdown phenomenon is asymmetric at $M_\infty = 0.85$. The leading-edge vortex on the left side of the model is stable into the model wake. The surface flow visualizations obtained in references 12 and 17 on 65° delta and cropped delta wings also revealed asymmetries in the vortical flows at $M_\infty = 0.85$. At $\alpha = 24^\circ$, the vortex breakdown was symmetric, as shown in the vapor screen photographs in figure 35. The symmetry of the burst positions may be imposed by the strong terminating shock wave at this angle of attack. The burst position advanced forward to $x/c \approx 0.7$, which promotes the decline in the suction pressure level and the nearly uniform pressure distribution at $\alpha = 24^\circ$ and $x/c = 0.80$ in figures 33 and 36. The lift-off of the vortex causes the reduction in the vortex-induced suction pressure level at $x/c = 0.60$ (fig. 33).

The lift coefficient exhibits an abrupt decrease as the angle of attack increases from 21° to 22° as shown in figure 37, which correlates with the onset of vortex breakdown over the wing. The lift-curve break occurs at a slightly lower angle of attack at $M_\infty = 0.85$ relative to the results at the lower Mach numbers, which may be due to the vortex-shock interaction.

M_∞ = ***0.90.*** The wing surface pressure distributions at $M_\infty = 0.90$ and $\alpha \approx 12^\circ$, 16°, 20°, and 24° are shown in figure 38. Laser vapor screen flow visualizations were not obtained at this Mach number. The pressure distributions up to $\alpha \approx 20^\circ$ are indicative of a stable leading-edge vortical flow. The primary and secondary vortex-induced suction pressure maxima at each pressure row increase gradually with the angle of attack.

The results at $\alpha \approx 20^\circ$ are examined in more detail in figures 39 and 40, which present the wing surface pressures and the corresponding upper surface oil flow pattern, respectively. The secondary and tertiary boundary-layer separation lines are well defined in the oil flow photograph in figure 40. A determination of the flow behavior between the separation lines is not possible, however, because of insufficient details in the surface pattern. The surface flow at the three pressure measurement stations is supersonic ($C_p^* = -0.188$). The surface flow visualization reveals the development of a terminating, or normal, shock wave situated at $x/c \approx 0.95$. Comparing this result with the corresponding surface flow pattern at $M_\infty = 0.85$ and $\alpha = 20^\circ$ in figure 31 reveals an aft displacement of the shock at the higher Mach number amounting to 10 percent of the wing centerline chord. Along the outer portion of the wing, two spiral nodes are apparent. The separated flows emanating from these nodes rotate in the opposite sense to each other. This was determined from real-time observation of the developing surface flow pattern.

The flattening of the pressure distribution and the diminished suction pressure level at $\alpha = 24^\circ$ and $x/c = 0.80$ in figure 38 are indicators of leading-edge vortex core breakdown. The pressure distributions in figure 41, which correspond to angles of attack of 20°, 22°, and 24°, suggest that vortex bursting advances to the aft pressure row as the angle of attack increases from 20° to 22°. This accounts for the discontinuities in the lift, drag, and pitching-moment curves in figure 42. The forward advancement of the vortex breakdown position is more rapid at $M_\infty = 0.90$ in comparison with the result at $M_\infty = 0.85$ (fig. 33), and it may be caused by the interaction of the vortex with a stronger shock at the higher Mach number. However, this trend does not persist at higher angles of attack. At $\alpha = 24^\circ$, for example, the pronounced decrease in the vortex suction level that was apparent at $M_\infty = 0.85$ and $x/c = 0.60$ (fig. 33) does not occur at the higher Mach number.

M_∞ = ***0.95.*** The wing surface static pressure distributions corresponding to a free-stream Mach number of 0.95 are shown in figure 43. There is no indication of vortex breakdown at these measurement stations up to the maximum angle of attack of 24°. The vortex-induced suction pressure levels and the suction pressure maxima increase gradually with the angle of attack.

The surface pressure signature of the leading-edge vortex is more conical at this higher Mach number. At $\alpha = 20^\circ$ (fig. 44), for example, the footprint of the wing leading-edge vortex is at approximately the same span location and of comparable magnitude at the three pressure measurement stations. The corresponding vapor screen and surface oil flow visualizations are illustrated in figures 45 and 46, respectively. The off-body flow visualizations reveal stable, symmetric vortical flows to the trailing edge of the wing. The surface flow pattern provides no indication of the terminating shock wave that was apparent at $M_\infty = 0.85$ and $M_\infty = 0.90$.

The pressure data in figure 47 at $\alpha \approx 20^\circ$, 22°, and 24° show no evidence of the onset of vortex core breakdown over the wing. However, the vapor screen flow visualizations in figure 48 reveal a bursting of the right-wing vortex at $x/c \approx 0.90$ and $\alpha = 24^\circ$.

The delay of vortex breakdown onset to a higher angle of attack at $M_\infty = 0.95$ is due to the diminished upstream influence of the wing trailing edge and the corresponding less severe, adverse longitudinal pressure gradient. This eliminates the discontinuities in the lift, drag, and pitching-moment curves (fig. 49) that were apparent at the lower Mach numbers.

$M_\infty = 1.20$. The wing surface pressure distributions at $M_\infty = 1.20$ and $\alpha \approx 12^\circ$, 16°, 20°, and 24° are presented in figure 50. Laser vapor screen flow visualization was not conducted at this Mach number. The pressure data reveal an expansion from the primary reattachment position to a maximum suction pressure plateau at each measurement station. The suction pressure levels induced by the wing vortex flow increase up to $\alpha = 20^\circ$. The surface pressures appear to reach a limiting value, however, at the higher angles of attack. At $\alpha = 24^\circ$, the vortex-induced suction pressure level at $x/c = 0.30$ is virtually unchanged relative to $\alpha = 20^\circ$, whereas the suction pressures underneath the vortex diminish at $x/c = 0.60$ and 0.80. The maximum suction pressure obtained at $M_\infty = 1.20$ is approximately 87 percent of the vacuum limit ($C_{p,v} = -0.992$). It is plausible that the experimental data have reached a maximum attainable suction pressure level at this Mach number, which would account for the "roof-top" pressure distributions.

The suction pressure plateaus that are apparent in the wing surface pressures at $\alpha = 20^\circ$ in figure 51 extend from a location just inboard of the shock-induced secondary separation line to a location immediately outboard of the tertiary separation line. This is illustrated in figure 52 where the wing surface pressures at $x/c = 0.60$ are superimposed on the oil flow pattern at $\alpha = 20^\circ$. The character of the surface flow is similar to the result obtained at $M_\infty = 0.95$ in figure 46.

The drop-off in the vortex suction pressure levels along the rear portion of the wing at the higher angles of attack causes the plateau in the lift curve and the slight unstable break in the pitching-moment curve in figure 53.

$M_\infty = 1.60$. The wing surface static pressures obtained at $M_\infty = 1.60$ are presented in figure 54 for angles of attack of approximately 12°, 16°, 20°, and 24°. Vapor screen and oil flow visualizations were not obtained at this Mach number.

The Mach number component normal to the wing leading edge is subsonic through the range of angle of attack in the present test, and therefore primary flow separation occurs at the sharp leading edge. The data in figure 54 are characterized by "roof-top" pressure distributions. The suction pressures underneath the wing vortex approach a limiting value at all three measurement stations as the angle of attack increases beyond 20°. The maximum suction pressure obtained at this Mach number is approximately 92 percent of the vacuum limit ($C_{p,v} = -0.558$).

At this higher supersonic free-stream Mach number, it is likely that a cross-flow shock wave develops above the primary vortical flow. For example, at $\alpha = 20^\circ$ the angle of attack and Mach number component normal to the wing leading edge are $\alpha_N = 40.7^\circ$ and $M_N = 0.838$, respectively. These conditions fall within the vortex with the shock region in the α_N-M_N space shown in figure 55 (taken from ref. 18). The effect of the shock appears limited to the flow region above the wing, since no shock effects are indicated in the surface pressure distributions. The development of this shock will be discussed in more detail in a following section on the wing LEX configuration.

The lift, drag, and pitching-moment characteristics are presented in figure 56. Nonlinear effects associated with vortex development are nominal at $M_\infty = 1.60$ in comparison with the results at the lower Mach numbers.

Mach number effects. The effect of the Mach number on the wing upper surface static pressure distributions at $\alpha = 20^\circ$ and 24° is shown in figures 57 and 58, respectively. These angles of attack correspond to conditions prior to, and after, the onset of vortex core breakdown over the wing at the subsonic and transonic speeds.

The broadening of the vortex-induced pressure distribution and the inboard displacement of the maximum vortex-induced suction pressure at a given chord station suggest that the vortex is flatter and is situated farther inboard as the Mach number increases. These trends have been observed in vapor screen experiments conducted in reference 6. The vacuum pressure limit will also affect the character of the pressure distributions, particularly at the higher Mach numbers. The value of $C_{p,v}$ at various Mach numbers is denoted in figures 57 and 58. At the supersonic free-stream conditions, the experimental surface pressures may approach a limiting value of about 90 percent of vacuum pressure. Similar maximum suction pressure levels were obtained on delta wings at supersonic speeds in reference 18.

The secondary vortex suction peak moves inboard with Mach number. This effect is most prominent at Mach numbers from 0.40 to 0.85. At $M_\infty \geq 0.85$, the secondary separation is shock induced and is less sensitive to further increases in the Mach number.

Along the inboard portion of the wing, the suction pressures associated with the primary vortex-induced reattached flow typically increase with the Mach number up to $M_\infty = 0.95$. The increase in the attached-flow surface pressures offsets the reduced pressure signature of the leading-edge vortex up to $M_\infty = 0.95$. Although pressure data were not obtained on the lower surface, the expected effect is an increase in the positive pressures on the compression side of the wing as the Mach number increases. (See ref. 11.)

The Mach number effect is similar at $\alpha = 24°$ and $x/c = 0.30$ (fig. 58). Farther aft, however, the data trends are different because of the influence of vortex core breakdown. At $M_\infty = 0.40$, 0.60, and 0.85, vortex bursting is situated between the second and third pressure rows. Within this range of the Mach number, the surface pressures at $x/c = 0.60$ and 0.80 display the same sensitivity to the Mach number that was observed at $\alpha = 20°$. Increasing the Mach number to 0.95, however, promotes an increase in the suction pressure levels at these stations. This is due to the aft displacement of core breakdown to a position downstream of $x/c = 0.80$. Within the Mach number range from 0.95 to 1.60, vortex breakdown effects are not manifested in the wing pressure distributions. As a consequence, the effect of increasing Mach number is to broaden the pressure distributions and reduce the vortex-induced suction pressure levels. These trends are identical to those obtained at $\alpha = 20°$.

Increasing the Mach number increases the lift-curve slope at zero incidence (fig. 59). At angles of attack prior to vortex breakdown ($\alpha < 21°$), the lift increases with the Mach number from $M_\infty = 0.40$ to 0.95. A concurrent effect is an improvement in the drag polar shape. The lift curves at $M_\infty = 0.40$ to 0.85 collapse on each other at $\alpha > 21°$ because of the onset of vortex breakdown. This is not the case at $M_\infty = 0.95$ where the lift continues to increase up to the maximum angle of attack of 24°. The lift increment due to the Mach number diminishes at $M_\infty = 1.20$ and the corresponding lift curve eventually converges on the subsonic data ($M_\infty = 0.40$ and 0.60) at the higher angles of attack. This is due to the slow rate of increase of the vortex-induced suction pressures with the angle of attack imposed by the vacuum pressure limit. There is a marked reduction in the nonlinear lift at $M_\infty = 1.60$ relative to the lower Mach numbers, which is consistent with the reduced vortex pressure signatures. Wave drag and the diminished nonlinear lift effect result in the drag increase at $M_\infty = 1.20$ and 1.60.

The pitching-moment curves exhibit a stable shift at low lift levels as the Mach number increases. At $M_\infty = 0.40$ to 0.85, the wing-alone configuration exhibits longitudinal instability. The aft shift in the center of pressure at the higher Mach numbers results in neutral, or slightly positive, longitudinal stability.

65° Cropped Delta Wing With LEX on

$M_\infty = 0.40$. Figure 60 presents the wing upper surface static pressure distributions with the leading-edge extension (LEX) on at M_∞=0.40 and $\alpha \approx 12°$, 16°, 20°, and 24°. The pressure distributions at each angle of attack are also isolated in figures 61–64 to facilitate the comparisons to the off-body and surface flow visualizations. The flow visualization results are shown in figures 65–69. The laser vapor screen cross-flow visualizations at $x/c = 0.60$ and 0.80 and angles of attack from 12° to 24° are presented in figures 65 and 66, respectively. Vapor screen results at $\alpha = 20°$ and several cross-plane stations along the wing are shown in figure 67. A lengthwise cut through the vortical flows using the laser light sheet, viewed from the tunnel ceiling, and the corresponding surface oil flow pattern at $\alpha = 20°$ are contained in figures 68 and 69, respectively.

The footprints of the LEX and wing vortices at $\alpha = 12°$ are apparent in the pressure distributions in figures 60 and 61. The suction peak induced by the wing vortex is positioned near the leading edge at $x/c = 0.30$ (peak at $y/s \approx 0.94$), and then it moves inboard ($y/s \approx 0.78$) at $x/c = 0.60$ and 0.80. Concurrent with the inboard movement of the wing vortex is the development of a secondary vortex suction peak situated between the primary peak and the wing leading edge. The suction pressure maxima induced by the LEX vortex as it passes over the wing are located at $y/s \approx 0.70$ at $x/c = 0.30$ and $y/s \approx 0.40$ at $x/c = 0.60$ and 0.80. The LEX vortex is closer to the wing leading edge as it first enters the wing flow field. The LEX vortex position along the local semispan is farther inboard at the mid and aft pressure rows because of the nearly streamwise trajectory of the vortex along the wing. The LEX vortex-induced suction peaks are significantly less than the corresponding suction peaks associated with the wing vortex. The lateral spacing of the LEX and wing vortex footprints indicates there is no direct core interaction at this angle of attack, that is, the vortex cores do not coil around each other. This is confirmed in the laser vapor screen photographs in figures 65(a) and 66(a) which show the vortex cross-flow patterns at $\alpha = 12°$ and $x/c = 0.60$ and 0.80, respectively. The LEX and wing vortices appear as stable, donut-shaped flows that are widely spaced. The secondary vortex region is also revealed in the photograph at $x/c = 0.80$ in figure 66(a).

The vortex-induced suction pressure levels increase at $\alpha = 16°$ (figs. 60 and 62). The wing vortex exhibits a more pronounced inboard migration, particularly at $x/c = 0.80$. The suction peak induced by the wing leading-edge vortex at $x/c = 0.80$ is less in comparison with the result obtained at $\alpha = 12°$. This is not due to vortex breakdown but, instead, to an upward movement of the vortex core away from the wing surface. In contrast, the LEX vortex suction pressure maxima increase in magnitude and their positions are unchanged relative to $\alpha = 12°$. The reduced lateral spacing of the LEX and wing vortices and the migration of the wing vortex are illustrated in the vapor screen photographs in figures 65(c) and 66(c) at $x/c = 0.60$ and 0.80, respectively.

The character of the surface pressures at $x/c = 0.30$ and $\alpha = 20°$ (figs. 60 and 63) is unchanged relative to the results at lower angles of attack. This is not the case, however, at $x/c = 0.60$ and 0.80. The pressure signatures of the wing and LEX vortices are less distinguishable at $x/c = 0.60$ and would be difficult to identify without the vapor screen flow visualizations. This is due to the inboard and upward movement of the wing vortex as shown in figure 65(e). At $x/c = 0.80$, the pressure distribution is marked by a single, pronounced suction peak. The flow visualization photograph in figure 66(e) at $\alpha = 20°$ and $x/c = 0.80$ reveals a strong interaction of the wing and LEX vortex cores. The wing vortex moves inboard and upward over the LEX vortex. As a consequence, its footprint in the surface pressures is lost. The LEX vortex moves downward and outboard as a result of its interaction with the wing vortical flow. The location of the LEX vortex core coincides with the single suction peak at the aft pressure row. The large increase in the suction peak magnitude at this higher angle of attack results from the combined effect of the increased LEX vortex strength and its proximity to the wing surface.

A more detailed description of the wing and LEX vortex core interaction at $\alpha = 20°$ is provided in figures 67, 68, and 69. The vapor screen results in figure 67 show the cross-flow patterns at several stations ranging from $x/c = 0.50$ to 1.00. The intertwining of the wing and LEX vortex cores from $x/c = 0.80$ to 1.00 is apparent. The wing vortex core moves inboard and upward to a position directly above the LEX vortex. After having reached the top of its helical trajectory, the wing vortex continues to move inboard but rotates downward as it approaches the trailing edge. The LEX vortex also follows a helical path and displays an outboard and downward movement during the initial stages of its interaction with the wing vortex, followed by an outboard and upward displacement near the trailing edge. From $x/c = 0.50$ to 1.00, the vortices complete a rotation of approximately 130° about each other. The lengthwise cut of the laser light sheet through the vortical flows in figure 68 clearly illustrates the strong flow-field interaction at $\alpha = 20°$. The corresponding surface oil flow pattern is shown in figure 69. The surface streamlines reflect the combined influence of the interacting vortices, and the individual signatures of the vortical flows cannot be distinguished. The migration of the wing vortex away from the leading edge along the rear portion of the wing promotes the corresponding inboard movement of the secondary separation line and a region of separated and reverse flow near the wingtip.

The wing–LEX vortex interaction increases at $\alpha = 24°$ (figs. 65(g) and 66(g)). The vortices are stable and of increased strength at this higher angle of attack, and the suction pressure levels display a corresponding increase at all three measurement stations (figs. 60 and 64). This is in contrast to the result obtained on the wing-alone configuration (fig. 8) where the effect of vortex breakdown was manifested at the aft pressure row. The broad, single-peak pressure distribution at $x/c = 0.60$ is induced by the adjoining LEX and wing vortices depicted in the vapor screen photograph in figure 65(g). The more pronounced suction peak at $x/c = 0.80$ is promoted by the LEX vortex, which is shown in the flow visualization photograph in figure 66(g). At this station, the wing vortex is positioned above and slightly inboard of the LEX vortical flow. The coiling of the wing and LEX vortices is more pronounced at this higher angle of attack, which can be seen by comparing the vapor screen results at $\alpha = 20°$ and 24° in figures 66(e) and 66(g), respectively. The increased interaction displaces the LEX vortex farther outboard, which is consistent with the outward movement of the suction pressure peak at $x/c = 0.80$ as the angle of attack increases from 20° to 24°.

M_∞ = 0.60. The wing surface pressure distributions at $M_\infty = 0.60$ and $\alpha \approx 12°$, 16°, 20°, and 24° are presented in figure 70. The laser vapor screen cross-flow visualizations at $x/c = 0.60$, 0.80, and 1.00 for the same angle-of-attack range are shown in figures 71, 72, and 73, respectively. The pressure data trends at $M_\infty = 0.60$ are similar to those obtained at $M_\infty = 0.40$ (fig. 60). Increasing the angle of attack promotes an increase in the suction pressure levels underneath the vortical flows up to the maximum angle of attack of 24°. The double-peak pressure distributions at $x/c = 0.60$ and 0.80 at $\alpha = 12°$ and 16° change to broader single-peak distributions at the higher angles of attack. This is the result of the increased mutual proximity and direct interaction (coiling) of the wing and LEX vortex cores. Comparing the wing surface pressures to the critical pressure coefficient ($C_p^* = -1.294$) reveals only a small supersonic pocket underneath the wing vortex at $x/c = 0.60$ and $\alpha = 12°$ and $16°$. The supercritical region at this station expands at $\alpha = 20°$, whereas a small pocket of supersonic flow appears under the wing vortex at $x/c = 0.30$. At $\alpha = 24°$, supersonic regions exist at all three pressure rows, and they are most extensive at $x/c = 0.60$ and 0.80 where the wing and LEX vortices are coupled. The growth and movement of the vortical flows as the angle of attack increases are clearly illustrated in the vapor screen photographs in figures 71–73. At $x/c = 0.60$ (fig. 71), the upward and inboard movement of the wing leading-edge vortex toward the LEX vortex is a prominent feature of the cross flow. The vortices are situated side by side at $\alpha = 24°$ and induce the broad single-peak pressure distribution shown previously in figure 70. The vortex interaction is more pronounced at $x/c = 0.80$ (fig. 72), and at $\alpha = 20°$ the wing and LEX vortex cores begin to rotate about each other. This coincides with the loss of the twin suction peaks in the wing surface pressures (fig. 70). The secondary separation is defined by a dark region in figure 72. This separation zone broadens at $\alpha = 24°$ as the wing vortex migrates inboard and upward. The wing LEX vortex cores begin to wrap around each other at $\alpha = 16°$ and $x/c = 1.00$ (fig. 73). By $\alpha = 24°$ (fig. 73(d)), the vortices have completed a 180° rotation about each other relative to the core positions at $\alpha = 12°$.

Increasing the Mach number from 0.40 to 0.60 reduces the interaction of the wing and LEX vortices at a given angle of attack and model station. This is due to the decreased vortex strengths at the higher Mach number and, as a consequence, the reduced velocities that the vortices induce on each other. The analytical solutions presented in reference 19 indicate that increasing the Mach number promotes a significant reduction in the circumferential and axial velocity components within an inviscid, conical vortex core. Flow-field measurements about a 63.4° delta wing obtained in reference 11 confirm a reduction in vortex circulation because of increasing Mach number. At $\alpha = 20°$ and $x/c = 0.80$, the rotation of the vortices about each other at $M_\infty = 0.40$ (fig. 66(e)) is about 35° greater relative to the cross-flow pattern at $M_\infty = 0.60$ (fig. 72(c)). This effect is more pronounced at $\alpha = 24°$ where the core rotation at $M_\infty = 0.40$ (fig. 66(g)) is approximately 45° greater in comparison with the result at $M_\infty = 0.60$ (fig. 72(d)).

Additional correlations of the wing surface pressures with the off-body and surface flow visualizations are provided in figures 74–87 for $M_\infty = 0.60$. The wing pressure distributions at $\alpha = 12°$ are presented in figure 74 for comparison with the vapor screen cross-flow patterns (fig. 75), lengthwise laser light-sheet section (fig. 76), and surface oil flow pattern (fig. 77). The footprints of the wing and LEX primary vortices and the wing secondary vortex are discernible in the surface pressures at $x/c = 0.60$ and 0.80 (fig. 74). The lateral spacing of the primary vortex suction peaks indicates that there is no direct interaction of the vortex cores. The vapor screen cross-flow visualizations at $x/c = 0.60$, 0.80, and 1.00 (fig. 75) illustrate this flow situation. The secondary vortex can also be discerned at $x/c = 0.80$ at a location that is consistent with the pressure measurements. The paths of the wing and LEX vortices are clearly defined in the lengthwise "slice" of the laser light sheet through the vortical flows as shown in figure 76. There is no intertwining of the vortices at any point over the wing or into the model wake. The ability of the light sheet to illuminate most of the core lengths is an indicator of the lack of curvature (in the vertical direction) of the vortex paths. The signatures of two, distinct vortices are manifested in the surface flow pattern in figure 77.

The lateral spacing of the wing and LEX primary vortex suction peaks diminishes slightly at $x/c = 0.60$ and 0.80 and $\alpha = 16°$ relative to $\alpha = 12°$ as shown in figure 78. This is consistent with the vapor screen cross-flow visualizations in figure 79. Interaction of the wing and LEX vortex cores first occurs over the wing at this angle of attack. The intertwining of the vortex cores near the wing trailing edge is apparent in the cross-flow pattern in figure 79, the lengthwise light-sheet cut in figure 80, and the surface streamlines in figure 81. In the lengthwise section of the light sheet, the definition of the LEX vortex is lost near the trailing edge as it moves downward and out of the plane of the light sheet. The upward movement of the wing leading-edge vortex along the rear portion of the wing renders the wing vortex-induced surface flow less distinguishable in figure 81.

The increased interaction of the wing and LEX vortices is apparent in the surface pressures at $\alpha = 20°$ in figure 82. The footprints of the wing and LEX vortices at $x/c = 0.60$ are less distinguishable. However, examination of the corresponding cross-flow pattern in figure 83(a) shows the adjoining vortices, and their locations along the local semispan are identified in the pressure distribution. The maximum suction pressure plateau at $x/c = 0.80$ is consistent with the vortex structure illustrated in the vapor screen photograph in figure 83(b). Here, the wing and LEX vortices begin to intertwine, and the vortices combine to induce the "roof-top" pressure distribution. At the trailing edge ($x/c = 1.00$ in figure 83(c)), the vortices have rotated 125° about each other relative to their orientation at $x/c = 0.60$. The lengthwise laser light-sheet section through the vortical flows in figure 84 illustrates the stronger interaction of the primary vortex cores. The LEX vortices dip below the plane of the light sheet at $x/c \approx 0.80$. The increased interaction between the wing and LEX vortices at $\alpha = 20^\circ$ smears the individual footprints of the wing and LEX vortices in the surface flow pattern in figure 85.

The migration of the wing vortex away from the leading edge promotes the region of separated and reverse flow near the wingtip. It has been observed in reference 9 that the strong interaction of two corotating vortices will promote a more extensive region of flow separation along the outer portion of the wing. The separated flow region near the wingtip is identified in the vapor screen photograph in figure 83(c).

It is interesting to note that the lateral spacing between the wing primary vortex suction peak (where discernible in the pressure distributions) and the secondary separation line in the oil flow pattern is greater in comparison with the results obtained on the wing-alone configuration at the same Mach number and angle of attack. (See figs. 14 and 16.) Typically, the primary vortex suction peak on the wing alone is located immediately inboard of the secondary separation. This is an indicator of a severe adverse pressure gradient in the spanwise direction. The flow induced on the main wing by the LEX vortex and the upward and inboard movement of the wing vortex "softens" this pressure gradient, thereby delaying boundary-layer separation. This also reduces/eliminates the region of tertiary separation that was such a prevalent feature of the wing-alone surface flow.

The wing surface pressures and off-body flow visualizations at $\alpha = 24^\circ$ are presented in figures 86 and 87. The wing and LEX vortices are situated side by side at $x/c = 0.60$ (fig. 87(a)) and induce a broad region of high suction pressures. At $x/c = 0.80$ (fig. 87(b)), the wing vortex moves to a position above and outboard of the LEX vortex, whereas the LEX vortex shifts downward and outboard. The single suction pressure peak at this station is situated between the wing and LEX vortex core spanwise positions. The photograph at $x/c = 1.00$ (fig. 87(c)) reveals a symmetric flow situation consisting of two stable, coupled primary vortical flows on the left and right sides of the model. In contrast, the wing alone exhibited vortex breakdown asymmetry (fig. 21).

$M_\infty = 0.80$. The wing upper surface static pressures at $\alpha = 12^\circ$, 16°, 20°, and 24° are presented in figure 88 corresponding to $M_\infty = 0.80$. On the basis of the results obtained at $M_\infty = 0.40$ and 0.60, the locations and interactive behavior of the wing and LEX vortices can be partially inferred from the vortex signatures in the pressure distributions. For example, the reduced lateral spacing of the wing and LEX vortex suction peaks at the higher angles of attack is an indicator of the impending direct interaction of the vortex cores. The surface pressures at $x/c = 0.80$ transition from a double-peak to a single-peak distribution as the angle of attack increases from 20° to 24°. This result indicates that the closely coupled nature of the wing and LEX vortical flows is maintained at the low transonic Mach numbers.

At $\alpha = 12^\circ$, the surface flow underneath the wing vortex is supercritical at all three measurement stations ($C_p^* = -0.435$), whereas the LEX vortex induces supersonic flow at $x/c = 0.60$ only. The supercritical regions increase in size as the angle of attack increases. At $\alpha = 24^\circ$, the flow at all pressure measurement locations is supersonic.

The wing surface pressures at $\alpha = 16^\circ$ in figure 89 can be compared with the laser vapor screen flow visualization results at $x/c = 0.60$, 0.80, 1.00, and 1.20, presented in figures 90 and 91. The cross-flow visualizations were not well defined at $x/c = 0.30$ and are not presented. An examination of the original photographs at this station indicated that the wing and LEX vortices were situated at $y/s \approx 0.70$ and 0.92, respectively. These positions did not vary significantly with the angle of attack. The positions of the wing and LEX vortices at $x/c = 0.60$ and 0.80 correlate with the locations of the double suction peaks in the pressure distributions. The wing vortex is flatter at these stations in comparison with the cross-flow structure observed at lower Mach numbers. (See figs. 65(c) and 66(c) at $M_\infty = 0.40$ and figs. 79(a) and 79(b) at $M_\infty = 0.60$.) At the wing trailing edge ($x/c = 1.00$) and in the model wake ($x/c = 1.20$), the wing vortex begins to migrate inboard and upward. The wake roll-up downstream of the trailing edge is also apparent. The interaction of the wing and LEX vortices is weaker at $M_\infty = 0.80$ relative to the results obtained at $M_\infty = 0.40$ and 0.60. This is typical of the behavior of interacting, corotating vortices as the Mach number increases. (See ref. 9.)

The wing surface pressures, off-body flow visualizations, and surface oil flow pattern at $\alpha = 20^\circ$ are shown in figures 92 95. At $x/c = 0.60$, the wing and

LEX vortices are adjacent to each other, as indicated in figures 93(a) and 94(a). Of the two vortices, the wing vortex is closer to the surface at this station. The effect of the adjoining vortices is to induce the continuously increasing suction pressures in figure 92 from the centerline to a maximum level at $y/s \approx 0.75$. This coincides with the spanwise position of the wing primary vortex. The surface streamlines in figure 95 exhibit a gentle curvature underneath the wing vortex and approach the line of secondary separation at a glancing angle. The character of the surface streamlines indicates that the secondary separation is pressure gradient induced. In contrast, shock-induced boundary-layer separation occurred on the wing alone at the same Mach number and angle of attack (fig. 25). On the wing alone, secondary separation occurred farther inboard, and the surface streamlines intersected the line of secondary separation at a steep angle. (See fig. 26.)

At $x/c = 0.80$, the wing vortex moves inboard and upward, whereas the LEX vortex moves downward slightly as indicated in the vapor screen photographs in figures 93(b) and 94(b). The maximum suction pressures induced by the vortical flows are comparable and situated closer together at this station (fig. 92). The surface pressures are nearly uniform along the outer 35 percent of the local semispan. The oil flow pattern in figure 95 reveals a large region of separated and reverse flow along the outer wing and the development of two spiral nodes of flow separation. When the wing LEX vortex flow interaction becomes pronounced, the wing vortex shears away from the leading edge. As a result, the outer wing region is no longer scrubbed by the leading-edge vortical flow. The inboard migration of the wing vortex promotes a discontinuity in the leading-edge "feeding sheet," as shown in the cross-flow patterns in figures 93(b) and 94(b). Another vortex, rotating in the same sense as the wing primary vortex, forms from the leading edge near the tip. This vortex appears as a small, dark region having a circular cross section that rolls up along with the LEX and wing vortices. Cross-flow visualizations at the wing trailing edge ($x/c = 1.00$) (figs. 93(c) and 94(c)) and in the near wake ($x/c = 1.10$) (figs. 93(d) and 94(d)) illustrate the coupled nature of the three vortices. The region of separated flow along the outer wing is also indicated in the cross-flow patterns.

Based on visual observations and the wing surface pressure distributions in figure 88, the wing and LEX vortices are stable over the wing at $\alpha = 24°$. This is in contrast to the results obtained on the wing alone where the effect of vortex breakdown was apparent up to $x/c = 0.60$ (fig. 27).

$M_\infty = 0.85$. The wing surface pressure distributions at $M_\infty = 0.85$ and $\alpha = 12°$, $16°$, $20°$, and $24°$ are presented in figure 96. The wing and LEX vortex footprints are distinguishable at $\alpha = 12°$ and $16°$. Their increased mutual proximity and, ultimately, direct interaction at higher angles of attack smears the double-peak character of the pressure distributions at $x/c = 0.60$ and 0.80. The surface flow is mostly supersonic at $\alpha = 12°$ ($C_p^* = -0.302$) and is entirely supercritical at the three measurement stations at the higher angles of attack.

The test results at $\alpha = 12°$ are isolated in figures 97, 98, and 99 which include the wing surface pressures, laser vapor screen cross-flow patterns, and the surface oil flow pattern, respectively. The vapor screen and oil flow visualizations reveal the wing and LEX vortices along the length of the wing. The lateral spacing of the vortical flows is sufficient to preclude the intertwining of the cores at any point over the wing. The wing vortex at $x/c = 0.30$ appears as a small, dark region of approximately circular cross section situated very close to the leading edge. The LEX vortex is manifested as a much larger, circular region positioned inboard of the wing vortical flow and farther from the surface. The qualitative results are consistent with the suction peak locations in the surface pressure data. At $x/c = 0.60$ and 0.80, the wing vortex cross sections in figures 94(b) and 94(c) become elliptical.

The density of the water vapor condensate remains low in the region bounded by the feeding sheet. In contrast, the LEX vortex, which starts as a dark region, remains circular and a bright band of condensation appears outside the core region. At $x/c = 0.80$ (fig. 98(c)), secondary separation is visible outboard the wing primary vortex. The primary and secondary vortex signatures are discernible in the corresponding pressure distributions at these stations. The wing vortex cross section becomes nearly circular at the trailing edge ($x/c = 1.00$, fig. 98(d)) since it is no longer fed by vorticity from the leading edge. The LEX vortex core moves toward the surface along the rear portion of the wing and is at approximately the same vertical location as the wing leading-edge vortex at this station. Close examination of the surface flow underneath the wing vortex in figure 99 indicates that the surface streamlines approach the line of secondary separation at a steep angle. The character of the surface flow is similar to that observed on the wing alone, which suggests the development of a shock wave between the vortex and wing surface that is of sufficient strength to separate the boundary layer.

The surface pressure and off-body flow trends at $\alpha = 16^\circ$ in figures 100 and 101 are similar to those at $\alpha = 12^\circ$. There is a more pronounced upward and inboard migration of the wing leading-edge vortex at the higher angle of attack. In addition, the wing and LEX vortices and their associated suction pressure maxima are in closer proximity. For this reason, it is more difficult to distinguish their respective footprints in the surface oil flow pattern in figure 102. The wing vortex can be distinguished by the greater spanwise flow component that it induces on the surface. There is a large change in the surface flow direction inboard of the secondary separation line. This is the footprint of a cross-flow shock between the vortex and wing surface. In contrast to the result obtained at $\alpha = 12^\circ$, the shock below the wing vortex is not strong enough to promote boundary-layer separation. The surface streamlines approach the shock at a more glancing angle because of the upward movement of the wing vortex as it interacts with the LEX vortical flow. The Mach number component normal to the shock diminishes even though the total velocity increases. This is similar to the results obtained in reference 20 on the F-4 wing at transonic speeds. As a consequence, the flow traverses the shock and then separates farther outboard because of the adverse pressure gradient in the spanwise direction.

The interpretation of the pressure distributions at $\alpha = 20^\circ$ in figure 103 is aided by the cross-flow visualizations presented in figure 104. The wing and LEX vortices are clearly seen in the off-body flow, but their individual footprints become smeared along the aft portion of the wing as they interact more strongly. The vortex spanwise locations at $x/c = 0.30$ and 0.60 are indicated in the wing pressure distributions. At $x/c = 0.80$, the wing vortex migrates upward and inboard, which causes the feeding sheet discontinuity and the roll-up of another vortex from the leading edge. The combined effect of the interacting wing and LEX vortices is to induce a suction peak approximately midway between the adjoining vortical flows. At the trailing edge ($x/c = 1.00$), the multiple vortices begin to rotate about each other (fig. 104(d)). By comparison, the vortices rotated another 135° at this station at $M_\infty = 0.40$ (fig. 67) such that the LEX vortex was situated outboard of the wing vortical flow. Several flow details can be discerned in the photograph in figure 104(d), including the interacting primary vortices, the developing wingtip vortex, and the zone of separation along the outer region of the wing. The latter is clearly seen in the surface oil flow photograph in figure 105, and it is a direct result of the migration of the wing vortex away from the leading edge. The surface pressures across this region are uniform (fig. 103). There is no indication of shock wave development over the wing. In contrast, the surface flow pattern on the wing alone at $M_\infty = 0.85$ and $\alpha = 20^\circ$ (fig. 31) revealed shock-induced secondary flow separation and a terminating, or normal, shock wave situated at $x/c \approx 0.85$. However, the separated flow near the wingtip was less extensive on the wing-alone configuration.

The pressure distributions and vapor screen flow visualizations at $\alpha = 24^\circ$ are presented in figures 106–108. The pressure distributions are deceivingly simple and do not reflect the complexity of the off-body flow. The suction pressure peak near the leading edge at $x/c = 0.30$ is induced by the wing vortex that appears as a small, dark hole in the vapor screen cross-flow pattern in figure 107(a). The footprint of the much larger LEX vortex is barely discernible in the pressure distribution because of its distance above the wing surface. The wing vortex exhibits a rapid inboard and upward movement and is flattened at $x/c = 0.60$ (figs. 107(b) and 108(a)). Concurrently, the LEX vortex moves downward and is also compressed as a result of its proximity to the wing vortex. A continously increasing suction pressure level is induced underneath the dual vortex system. At $x/c = 0.80$, the wing vortex "shears away" from the leading edge and moves to a position above, but still outboard of, the LEX vortex (figs. 107(c) and 108(b)). The latter continues to move downward toward the wing surface. The suction peak at $y/s \approx 0.40$ in figure 106 is close to the span location where the wing and LEX vortices intersect. A large region of separated and reverse flow exists along the outer 50 percent of the local wing semispan and is contained in the dark band near the surface indicated in figures 107(c) and 108(b). The surface pressures through this region are uniform. The wing vortex rotates to a position nearly directly above the LEX vortex at the trailing edge ($x/c = 1.00$). The two vortices are visible in the vapor screen photographs in figures 107(d) and 108(c) as a dark, elongated region. The cross section of the separated flow from the outer wing panel is larger at this station and is identified in the vapor screen photographs. The formation of another vortex from the leading edge due to the migration of the wing vortical flow is seen in the photographs in figures 107 and 108 at $x/c = 0.80$ and 1.00. This vortex is coupled to the wing and LEX vortices.

$M_\infty = 0.90$. The wing surface pressure distributions at $M_\infty = 0.90$ and $\alpha \approx 12^\circ$, 16°, 20°, and 24° are presented in figure 109. The pressure data trends are similar to those obtained at $M_\infty = 0.85$ (fig. 96). There is some evidence that the wing and LEX vortex flow interaction diminishes at $M_\infty = 0.90$ since the vortex surface pressure signatures remain distinct to higher angles of attack relative to $M_\infty = 0.85$. The surface flow is supercritical at all pressure measurement locations and angles of attack ($C_p^* = -0.188$).

The wing surface pressures, off-body flow visualizations, and surface flow pattern at $\alpha = 16°$ are shown in figures 110–113. The wing and LEX vortices are clearly visible in the vapor screen photographs. Their locations at $x/c = 0.60$ and 0.80 are in qualitative agreement with the distinct footprints in the pressure distributions. Visual observations revealed discontinuities in the leading-edge feeding sheet just downstream of $x/c = 0.80$ that were due to the migration of the wing primary vortex away from the leading edge. These disturbances are manifested as small vortices in the vapor screen photographs near the trailing edge ($x/c = 1.00$) (figs. 111 and 112(c)). The developing tip vortex is also visible. The surface flow pattern (fig. 113) reveals a number of shock waves coexisting with the vortical flows. Shock-induced secondary separation occurs on the LEX, and a terminating (normal) shock wave is apparent just downstream of the LEX planform break. On the main wing, the surface streamlines bend abruptly as they pass through a shock situated between the wing leading-edge vortex and surface. However, the shock strength is not sufficient to promote boundary-layer separation. A line of secondary separation is apparent outboard of the shock position. A normal shock is manifested in the surface flow at $x/c \approx 0.90$, which extends through the wing and LEX vortices. The vortices remain stable downstream of the shock, as illustrated in the off-body flow visualizations in figures 111 and 112(c).

The individual signatures of the wing and LEX vortices are still apparent in the pressure distributions at $\alpha = 20°$ as shown in figure 114. The manner in which the vortices interact with each other near the trailing edge ($x/c = 1.00$) is illustrated in the vapor screen photographs in figure 115. A triple, corotating vortex system is apparent, consisting of the LEX vortex and two vortices shed from the wing leading edge. The shock waves that were evident in the surface flow pattern on the wing at $\alpha = 16°$ are not present at $\alpha = 20°$ (fig. 116). Although the wing and LEX vortex strengths increase at the higher angle of attack, the surface flow underneath the wing vortex has a reduced spanwise component. This is due to the upward movement of the wing vortex from the surface. The more oblique angle of the surface flow under the vortex (relative to the shock position at $\alpha = 16°$) precludes the development of the shock even though the total velocity at the surface increases. Along the aft portion of the wing, the downward movement of the LEX vortex toward the surface results in a larger spanwise flow component. The surface flow is at a more glancing angle relative to the normal shock position than was observed at the lower angle of attack. The "three-dimensional relief" effect associated with the LEX vortex eliminates the terminating shock wave. A large pool of oil accumulates along the outer portion of the wing. This stagnant flow region is promoted by the migration of the wing primary vortex. The trace of the stalled region near the wingtip is also identified in the vapor screen patterns in figure 115.

$M_\infty = 0.95$. The wing upper surface static pressure distributions at $M_\infty = 0.95$ are presented in figure 117 corresponding to $\alpha \approx 12°$, 16°, 20°, and 24°. The wing surface pressures at $\alpha = 16°$, 20°, and 24° are also highlighted in figures 118, 119, and 120, respectively, for comparison with the flow visualization results. The wing and LEX vortex footprints can be identified in the pressure distributions at $\alpha = 16°$ (fig. 118). At $\alpha = 20°$ (fig. 119) and $\alpha = 24°$ (fig. 120), the vortex footprints are less discernible because of the closer proximity and eventual interaction of the wing and LEX vortices. This is illustrated in the vapor screen images at $x/c = 0.80$ and $\alpha = 16°$, 20°, and 24° in figure 121. The lateral spacing of the vortices at $\alpha = 16°$ (fig. 121(a)) is sufficient to preclude direct interaction, and the vortex positions are consistent with the footprints in the wing pressure distributions in figure 118. The upward and inboard movement of the wing vortex as the angle of attack increases to 20° is apparent in the photograph in figure 121(b). The wing and LEX vortices are situated side by side at approximately the same distance above the surface. The mutual proximity of the vortices smears their individual signatures in the surface pressures (fig. 119). The broadening of the pressure distribution at this station is even more apparent at $\alpha = 24°$ (fig. 120). The off-body flow that promotes this pressure distribution is shown in figure 121(c). The vortices begin to rotate about each other at this pressure row and angle of attack. The wing vortex is positioned above and outboard of the LEX vortex. The migration of the wing vortex away from the leading edge promotes the uniform pressure distribution along the outer region of the wing.

The vortex flows at $\alpha = 20°$ and 24° are examined in more detail in figures 122–124. The cross-flow patterns at $\alpha = 20°$ and $x/c = 0.80$, 0.90, 1.00, and

1.10 are shown in figure 122. The vortices rotate approximately 45° about each other along this distance. There is some indication in the vapor screen photographs at $x/c = 1.00$ and 1.10 (figs. 122(c) and 122(d), respectively) that multiple vortices are shed from the wing leading edge. A zone of flow separation along the outer wing region is shown in the surface oil flow pattern in figure 123. However, in comparison with the result obtained at $M_\infty = 0.80$ to 0.90 (figs. 95, 105, and 116), the extent of the outer panel flow separation decreases. Aside from the separated flow near the tip, the surface flow on the main wing is "well-behaved." Despite the high free-stream Mach number, shock waves are not manifested in the wing surface streamlines. However, this is not the case on the LEX. The surface flow on the LEX exhibits shock-induced secondary separation, tertiary separation, and a normal shock wave downstream of the break in the leading-edge sweep. The surface flow patterns downstream of the shock location, along with the vapor screen observations over the wing, indicate that the LEX vortex does not break down upon passing through this shock wave.

The wing–LEX vortex interaction is more pronounced at $\alpha = 24°$ as shown in figure 124 at $x/c = 0.60$, 0.80, and 1.00. The vortices are in close proximity at $x/c = 0.60$. The vortex cross-sectional shapes are distorted as a result of the flow that each vortex induces on the other. At the trailing edge ($x/c = 1.00$), it is difficult to isolate the individual vortices within the large, dark region above the wing. One can deduce from the flow patterns at the three model stations that the wing vortex migrates to a position almost directly above the LEX vortex at $x/c = 1.00$. This represents a rotation of the vortices about each other of approximately 90° from $x/c = 0.60$ to 1.00.

M_∞ = 1.20. The wing surface pressures at $M_\infty = 1.20$ and $\alpha \approx 12°$, 16°, 20°, and 24° are presented in figure 125. Laser vapor screen flow visualization was conducted at this Mach number, but the photographs were not of sufficient clarity to be presented in this report. However, reference will be made to the off-surface flow-field observations to aid the interpretation of the pressure distributions. The suction pressure levels induced by the vortices diminish at this higher Mach number. The maximum attainable suction pressure on the wing upper surface is limited by the vacuum pressure. The wing and LEX vortex effects continue to be manifested in the pressure distributions at the supersonic free-stream conditions. The laser vapor screen observations revealed an interaction of the wing and LEX vortices that was similar to the results shown previously at $M_\infty = 0.95$ in figures 121, 122, and 124.

The wing surface pressures and surface oil flow pattern at $\alpha = 12°$ are shown in figures 126 and 127, respectively. The character of the pressure distributions at the three measurement stations is consistent with the signatures of the wing and LEX vortices in the surface streamline pattern. The lateral spacing of the vortices that is implicit in the surface flow indicates that there is no direct interaction of the vortex cores. The secondary flow separation is shock induced at this angle of attack.

The surface pressures and oil flow pattern at $\alpha = 16°$ in figures 128 and 129 reflect the growth and increased mutual proximity of the wing and LEX vortices, particularly over the rear portion of the wing. However, direct vortex core interaction is not indicated. A cross-flow shock is manifested in the surface streamlines underneath the wing vortex. The shock is not strong enough, however, to cause boundary-layer separation. Instead, the line of secondary separation occurs outboard of the shock.

The pressure distribution at $x/c = 0.30$ and $\alpha = 20°$ in figure 130 shows two distinct suction peaks induced by the wing and LEX vortices. The corresponding surface flow pattern is presented in figure 131. The surface flow along the LEX reveals shock-induced secondary separation and, farther outboard, a line of tertiary separation. Downstream of the wing LEX junction, the oil accumulates along a line that defines the boundary between the wing and LEX vortices. The vapor screen flow-field observations in this region revealed a pronounced upward movement and stretching of the wing vortex from the wing LEX junction to $x/c = 0.30$. The location and structure of the wing vortex was conducive to a downward movement of the LEX vortical flow toward the surface.

The wing and LEX vortices are in closer proximity to each other at $x/c = 0.60$. The induced effects associated with both vortical flows are barely distinguishable in the pressure distribution in figure 130. The vortices begin to rotate about each other at $x/c = 0.80$, which masks their individual footprints. The surface streamlines along the outer wing region exhibit a sudden change in direction as they pass through a cross-flow shock underneath the wing vortex. Similar to the result obtained at $\alpha = 16°$, the shock is not strong enough to cause boundary-layer separation, which occurs much farther outboard.

The vapor screen observations showed a pronounced stretching and upward and inboard movement of the wing vortex at $\alpha = 24°$ as a result of its interaction with the LEX vortex. At $x/c = 0.60$, the vortices were adjoining and were visible in the cross flow as a large, flattened region having a low level of water vapor condensate. At $x/c = 0.80$, a rotation of the vortices about each other was apparent. Their combined effect is to promote a broad single-peak pressure distribution as shown in figure 132. The vapor screen results presented in the next subsection corresponding to $M_\infty = 1.60$ provide further insight into the flow at $M_\infty = 1.20$. The vortex cross-flow behavior was similar in many respects at both Mach numbers.

M_∞ = ***1.60.*** The wing surface pressure distributions at $M_\infty = 1.60$ and $\alpha \approx 12°$, $16°$, $20°$, and $24°$ are presented in figure 133. The pressure distributions are relatively flat, and the suction pressure levels increase slowly as the angle of attack increases. However, the complexity of the off-surface flow is not manifested in the wing pressure distributions.

The direct interaction of the wing and LEX vortices persists at this higher supersonic Mach number. In addition, numerous shock waves appear in the cross flow that interact with the vortical flows. The laser vapor screen flow visualizations obtained at several cross-flow stations and $\alpha = 24°$ are shown in figure 134. At $x/c = 0.30$ (fig. 134(a)), the wing vortex is small and is situated close to the leading edge, whereas the larger LEX vortex is located inboard and farther above the surface. A cross-flow shock is perceptible above the LEX vortex and is identified in figure 134. The flattened cross section of the wing vortex, which is typical of the flow structure at supersonic speeds, is apparent at $x/c = 0.40$ (fig. 134(b)). The wing and LEX vortex cross sections are also distorted as a result of their mutual proximity and the flow velocities that they induce on each other. At this station, shocks are now visible above the wing and LEX vortices and beneath the LEX vortical flows. Farther aft at $x/c = 0.50$ (fig. 134(c)), a cross-flow, or centerline, shock is manifested between the LEX vortices. This interactive system of four primary vortices and seven shock waves (above the complete model) persists at the remaining cross-flow stations from $x/c = 0.55$ to 0.80 (figs. 134(d)–134(h)). The direct interaction of the wing and LEX vortices and their changing cross-sectional shapes are apparent at these model locations. At $x/c = 0.70$ and 0.80 (figs. 134(g) and 134(h)), the wing vortex moves to a position above, but still outboard of, the LEX vortex.

Mach number effects. The effect of Mach number on the wing surface pressures is shown in figures 135 and 136 at $\alpha = 20°$ and $24°$, respectively. There is a consistent decrease in the vortex-induced peak suction pressure levels at all three measurement stations as the Mach number increases. Since vortex breakdown did not occur on the wing–LEX model at any angle of attack or Mach number in the present test, the principal effects of compressibility will be manifested in the magnitudes of the vortex pressure signatures and their locations. Examination of the data at $\alpha = 24°$ (fig. 136) and $x/c = 0.80$ shows an inboard movement and diminished magnitude of the single suction pressure peak as the Mach number increases from 0.40 to 0.85. Because of their diminished strengths, the vortex cores "unwind," and their signatures are less pronounced at the higher Mach numbers. For example, at $M_\infty = 0.40$ (fig. 66(g)), the wing vortex is situated on top of the LEX vortex that is in close proximity to the surface. At $M_\infty = 0.85$ (fig. 107(c)), the coiling of the vortex cores is less severe, and the LEX vortex is positioned farther inboard and away from the surface in comparison to the lower Mach number. The direct interaction of the vortical flows continues to decrease at $M_\infty = 0.95$ with a consequent broadening of the pressure distribution and the loss of a distinct suction peak. At higher Mach numbers ($M_\infty = 1.20$ and 1.60), the character of the observed wing and LEX vortex interaction is similar to that at $M_\infty = 0.95$. The wing surface pressure signatures are limited at the supersonic speeds by the vacuum pressure, as denoted in figures 135 and 136.

The lift, drag, and pitching-moment characteristics are presented in figure 137. The lift-curve slope at zero angle of attack increases with the Mach number at $M_\infty = 0.40$ to 0.95. The lift at a given angle of attack is highest at $M_\infty = 0.95$. At the higher angles of attack, however, the lift increment due to compressibility diminishes and the lift curves collapse on each other. Increasing the Mach number to 1.20 promotes a reduction in the lift-curve slope at $\alpha = 0°$ relative to $M_\infty = 0.95$. The diminished vortex-induced lift effect at higher angles of attack is also apparent. At $M_\infty = 1.60$, the lift-curve slope at $\alpha = 0°$ and the vortex lift are significantly reduced. The compressibility effects on the drag are small until the free-stream Mach number becomes supersonic. Increasing the Mach number promotes an aft shift in the aerodynamic center with a consequent stable shift in the pitching-moment curves.

Comparisons of Wing-Alone and Wing–LEX Configurations

Representative comparisons of the pressure distributions obtained on the wing-alone and wing–LEX configurations are presented in figures 138 and 139 at $M_\infty = 0.60$ and 0.85, respectively. Test data obtained at $\alpha = 16^\circ$, 20°, and 24° are shown.

At $M_\infty = 0.60$ and $\alpha = 16^\circ$ (fig. 138(a)), the wing leading-edge vortex signature is reduced and shifted outboard with the LEX on. Along the inboard portion of the wing, however, the LEX vortex promotes higher suction pressure levels at $x/c = 0.30$, 0.60, and 0.80. This trend continues at $\alpha = 20^\circ$ (fig. 138(b)). At the aft pressure row, however, the wing vortex is situated farther inboard with the LEX on because of its interaction with the LEX vortical flow. The wing–LEX flow interaction also reduces the magnitude and spanwise extent of the secondary vortex-induced surface pressures. Vortex core breakdown occurs on the wing-alone configuration at $\alpha = 24^\circ$, and its effect is manifested in the pressure distributions at $x/c = 0.60$ and 0.80 in figure 138(c). The interacting wing and LEX vortices are stable at this angle of attack, and the overall suction pressure levels are higher.

The data trends are similar at $M_\infty = 0.85$ (fig. 139). It is interesting to note that the secondary vortex arising from the shock-induced boundary-layer separation on the wing alone occasionally induces a suction peak comparable to, or greater than, the wing primary vortex with the LEX on. At $\alpha = 24^\circ$ and $x/c = 0.80$ (fig. 139(c)), the wing-alone pressure distribution is induced by the burst leading-edge vortex, whereas the corresponding surface pressures with the LEX on are associated with the stable interacting wing and LEX vortices. Despite the difference in the off-body flows, however, the surface pressures are comparable. The impact of the wing–LEX vortex system is localized and is manifested as a single suction peak at $y/s \approx 0.40$.

The lift, drag, and pitching-moment characteristics of the wing-alone and wing–LEX configurations are illustrated in figures 140–146, corresponding to $M_\infty = 0.40$ to 1.60. All coefficients are based on the reference wing area S_{wing}. At $M_\infty = 0.40$ and 0.60 (figs. 140 and 141), the LEX promotes a more nonlinear lift curve and eliminates the breaks in the lift, drag, and pitching-moment curves associated with vortex bursting on the wing alone. However, the increased area ahead of the moment reference center causes a large unstable shift in the pitching-moment curves. The trends are similar at $M_\infty = 0.80$ and 0.90 (figs. 142 and 143, respectively) except that the vortex lift increments are absent at angles of attack below those for vortex bursting on the wing alone. The principal effect of the LEX at $M_\infty = 0.95$ to 1.60 (figs. 144–146) is the unstable shift in the pitching-moment curve.

Concluding Remarks

A wind tunnel investigation was conducted of the interaction and breakdown characteristics of slender-wing vortices at subsonic, transonic, and supersonic speeds. A model of a 65° cropped delta wing having sharp leading edges was tested with and without a leading-edge extension (LEX) at free-stream Mach numbers M_∞ from 0.40 to 1.60, Reynolds numbers based on the wing centerline chord from approximately 2.48×10^6 to 5.43×10^6, and angles of attack α from -2° to 24°. The testing was performed in the NASA Ames 6- by 6-Foot Transonic/Supersonic Wind Tunnel. Emphasis was placed on improving the understanding of vortex development, interactions, and breakdown; shock wave development; and vortex-shock interactions. The test data included off-body flow visualizations using a laser vapor screen technique; wing upper surface flow patterns using a fluorescent oil method; wing upper surface static pressure distributions; and model six-component forces and moments.

Transonic flow mechanisms were first apparent on the wing-alone configuration (LEX off) at a free-stream Mach number of 0.60. Locally supersonic flow existed on the wing surface underneath the leading-edge vortex. The flow along the wing upper surface was transitional. The surface flow patterns also revealed a cross-flow shock wave situated between the vortex and wing surface. Along the forward portion of the wing where the surface boundary layer was laminar, the secondary separation was shock induced. The boundary layer was turbulent farther aft, however, and was able to penetrate the shock wave without separating.

At $M_\infty \geq 0.80$, the cross-flow shock strength increased sufficiently to promote an inboard movement of the secondary separation line and the development of a large region of tertiary flow separation. The shock-induced separation resulted in stronger secondary vortex signatures that were comparable with those induced by the wing primary vortex. The secondary vortex location and strength were insensitive to the Reynolds number at the higher transonic speeds since the shock "fixed" the boundary-layer separation location.

The leading-edge vortex interacted with a normal, or terminating, shock wave along the rear portion of the wing at $M_\infty = 0.85$ and 0.90. The pressure distributions and total lift, drag, and pitching-moment characteristics suggested that the vortex–shock interaction caused the leading-edge vortex to burst over the wing at a slightly lower angle of attack.

The character of the lift, drag, and pitching-moment curves was similar over the range of M_∞ from 0.40 to 0.90. In all cases, the drop-off in the lift and the unstable pitching-moment break at the higher angles of attack coincided with the onset of vortex bursting over the wing.

Vortex breakdown onset was delayed to a higher angle of attack at $M_\infty = 0.95$ because of the diminished trailing-edge pressure recovery effect and the corresponding reduction in the adverse longitudinal pressure gradient. The drop-off in the lift and the unstable pitching-moment break that were observed at lower Mach numbers did not occur at $M_\infty = 0.95$ up to $\alpha = 24^\circ$.

Increasing the Mach number reduced the leading-edge vortex strength and the corresponding footprints in the wing pressure distributions. However, the lift at a given angle of attack increased with the Mach number up to $M_\infty = 0.95$. At higher Mach numbers, the lift decreased.

Adding the LEX promoted a vortex-dominated flow field characterized by a strong interaction of the wing and LEX vortices at the subsonic speeds. Direct interaction of the vortices occurred, featuring a coiling of the vortex cores about each other.

The flow velocities that the wing and LEX vortices induced on each other diminished at the higher Mach numbers because of the reduced vortex strengths. As a consequence, the coiling of the vortex cores was less pronounced.

The velocity components normal to the shock positions observed on the wing alone were reduced as a result of the wing LEX vortex interaction. The strengths of the cross-flow shock under the wing vortex and the terminating shock along the rear portion of the wing were reduced. In some cases, the shocks were eliminated altogether.

The wing vortex exhibited an inboard and upward migration because of its interaction with the LEX vortical flow. This caused a more extensive region of separated and reverse flow near the tip in comparison with the results obtained with the LEX off.

The interacting wing and LEX vortices were stable up to the maximum angle of attack of 24°. In addition, the asymmetric vortex breakdown that was observed on the wing alone did not occur on the wing LEX configuration. The stabilization of the wing vortex in the presence of the LEX vortical flow eliminated the discontinuities in the lift, drag, and pitching-moment curves that occurred on the wing alone.

A complex interaction of shock waves and vortices occurred on the wing LEX configuration at the supersonic speeds. Multiple shock waves were observed above, below, and between the interacting wing and LEX vortices. The complexity of the off-body flows was not manifested in the wing surface pressures, which were nearly uniform across the span.

NASA Langley Research Center
Hampton, VA 23665-5225
September 9, 1991

References

1. Campbell, James F.; Chambers, Joseph R.; and Rumsey, Christopher L.: Observation of Airplane Flow Fields by Natural Condensation Effects. AIAA-88-0191, Jan. 1988.
2. Erickson, Gary E.; Hall, Robert M.; Banks, Daniel W.; Del Frate, John H.; Schreiner, John A.; Hanley, Robert J.; and Pulley, Craig T.: Experimental Investigation of the F/A-18 Vortex Flows at Subsonic Through Transonic Speeds (Invited Paper). *A Collection of Technical Papers—AIAA 7th Applied Aerodynamics Conference*, July–Aug. 1989, pp. 519–594. (Available as AIAA-89-2222.)
3. Elsenaar, A.: How It All Started: The International Vortex Flow Experiment on Euler Code Validation in Retrospect. *Symposium on International Vortex Flow Experiment on Euler Code Validation—Proceedings*, A. Elsenaar and G. Eriksson, eds., FFA, Flygtekniska Försöksanstalten (Sweden), Oct. 1986, pp. 17–19.
4. McGregor, I.: The Vapour-Screen Method of Flow Visualization. *J. Fluid Mech.*, vol. 11, pt. 4, Dec. 1961, pp. 481–511.
5. *Ames Research Facilities Summary—1974*. NASA/Ames Research Center.
6. Squire, L. C.; Jones, J. G.; and Stanbrook, A.: *An Experimental Investigation of the Characteristics of Some Plane and Cambered 65° Delta Wings at Mach Numbers From 0.7 to 2.0.* R. & M. No. 3305, British Aeronautical Research Council, 1963.
7. Payne, F. M.; Ng, T. T.; Nelson, R. C.; and Schiff, L. B.: Visualization and Flow Surveys of the Leading Edge Vortex Structure on Delta Wing Planforms. AIAA-86-0330, Jan. 1986.
8. Erickson, Gary E.; Rogers, Lawrence W.; Schreiner, John A.; and Lee, David G.: Subsonic and Transonic Vortex Aerodynamics of a Generic Forebody Strake-Cropped Delta Wing Fighter. AIAA-88-2596, June 1988.
9. Erickson, Gary E.; Rogers, Lawrence W.; Schreiner, John A.; and Lee, David G.: Further Studies of the Subsonic and Transonic Vortex Flow Aerodynamics of a Close-Coupled Forebody-Slender Wing Fighter. AIAA-88-4369, Aug. 1988.

10. Carcaillet, R.; Manie, F.; Pagan, D.; and Solignac, J. L.: *Leading Edge Vortex Flow Over a 75 Degree-Swept Delta Wing Experimental and Computational Results.* ONERA T.P. No. 1986–122, Sept. 1986.
11. Vorropoulos, G.; and Wendt, J. F.: Laser Velocimetry Study of Compressibility Effects on the Flow Field of a Delta Wing. *Aerodynamics of Vortical Type Flows in Three Dimensions*, AGARD-CP-342, July 1983, pp. 9-1–9-13.
12. Bannink, W. J.: Some Recent Results on Vortex Bursting on a Delta Wing at High Subsonic Speeds. *Validation of Computational Fluid Dynamics, Volume 1—Symposium Papers and Round Table Discussion*, AGARD-CP-437, Vol. 1, Dec. 1988, pp. 9-21–9-23.
13. Schrader, Karl F.; Reynolds, Gregory A.; and Novak, Charles J.: Effects of Mach Number and Reynolds Number on Leading-Edge Vortices at High Angle-of-Attack. AIAA-88-0122, Jan. 1988.
14. Keener, Earl R.; and Chapman, Gary T.: Similarity in Vortex Asymmetries Over Slender Bodies and Wings. *AIAA J.*, vol. 15, no. 9, Sept. 1977, pp. 1370–1373.
15. Hartmann, K.: Force and Pressure Measurements Including Surface Flow Visualizations on a Cropped Delta Wing. *Symposium on International Vortex Flow Experiment on Euler Code Validation Proceedings*, A. Elsenaar and G. Eriksson, eds., FFA, Flygtekniska Försöksanstalten (Sweden), Oct. 1986, pp. 63–87.
16. Boersen, S. J.; and Elsenaar, A.: Tests on the AFWAL 65° Delta Wing at NLR: A Study of Vortex Flow Development Between Mach = .4 and 4. *Symposium on International Vortex Flow Experiment on Euler Code Validation Proceedings*, A. Elsenaar and G. Eriksson, eds., FAA, Flygtekniska Försöksanstalten (Sweden), Oct. 1986, pp. 23–36.
17. Bannink, W. J.; and Houtman, E. M.: Experiments on the Transonic Flow Over a Delta Wing at High Angles of Attack. *Symposium on International Vortex Flow Experiment on Euler Code Validation Proceedings*, A. Elsenaar and G. Eriksson, eds., FFA, Flygtekniska Försöksanstalten (Sweden), Oct. 1986, pp. 37–46.
18. Miller, David S.; and Wood, Richard M.: *Lee-Side Flow Over Delta Wings at Supersonic Speeds.* NASA TP-2430, 1985.
19. Küchemann, D.: *The Aerodynamic Design of Aircraft.* Pergamon Press, Inc., c.1978.
20. Grose, G. G.; Brady, C. C.; and Bristow, D. R.: *Investigation of Scaling Effects in Transonic Wind Tunnel Testing.* AFFDL-TR-72-60, U.S. Air Force, June 1972.

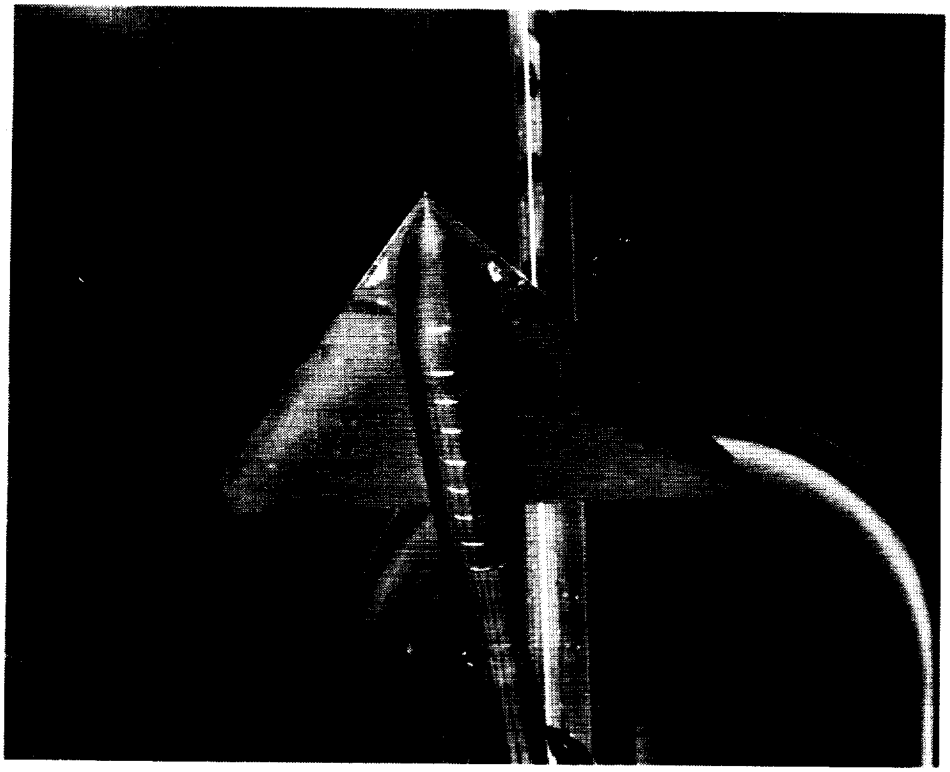

(a) Wing alone.

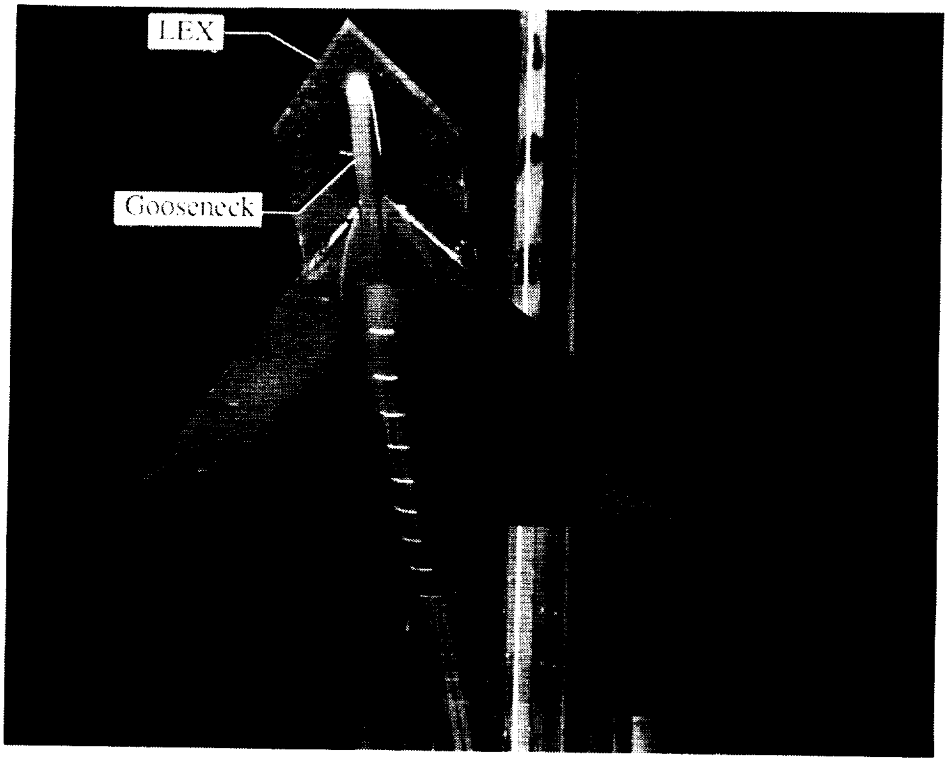

(b) Wing-LEX assembly.

Figure 1. Models of 65° cropped delta wing with and without LEX.

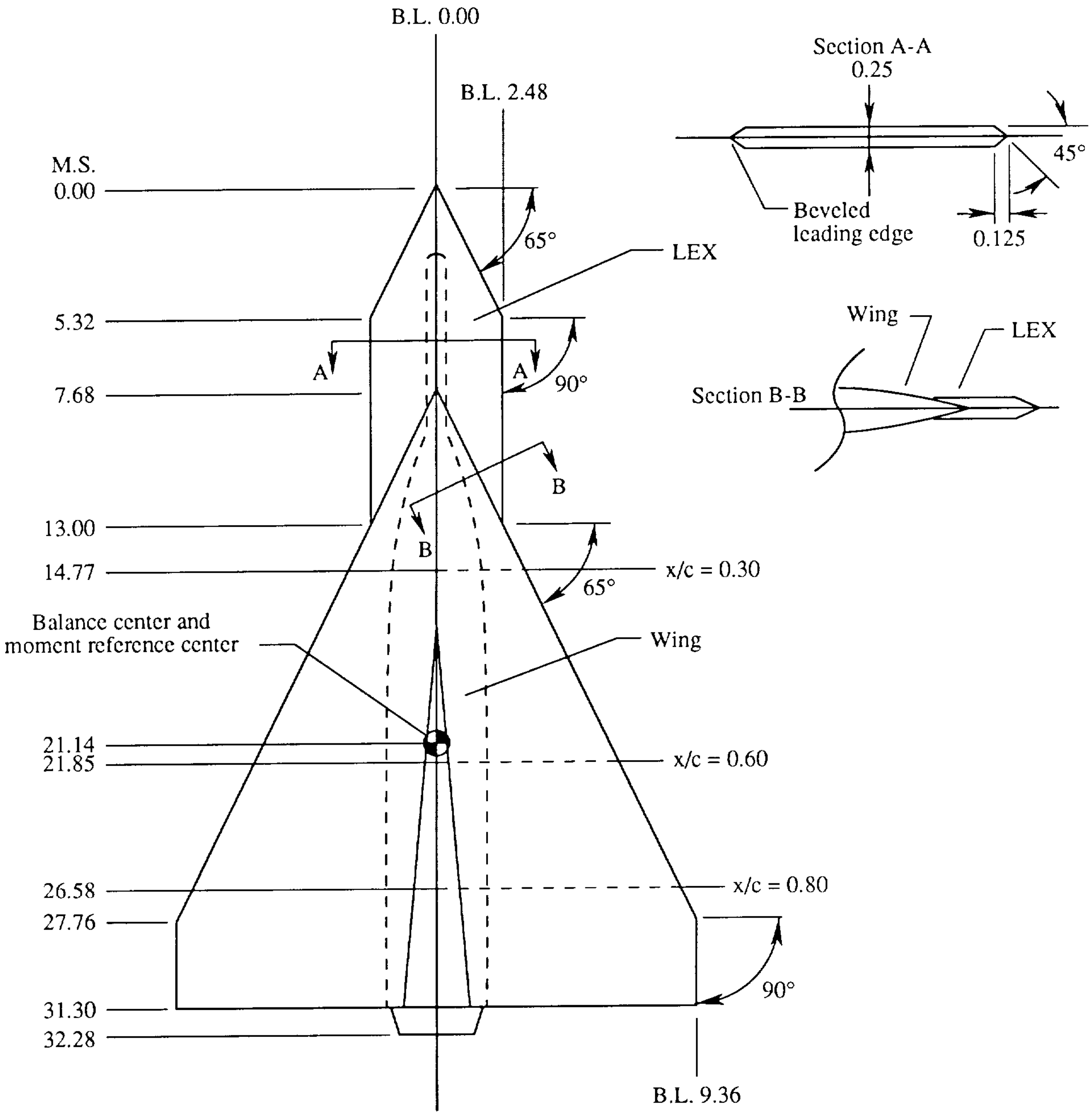

(a) Model planform.

Figure 2. Geometry details of model of 65° cropped delta wing. All dimensions are given in inches.

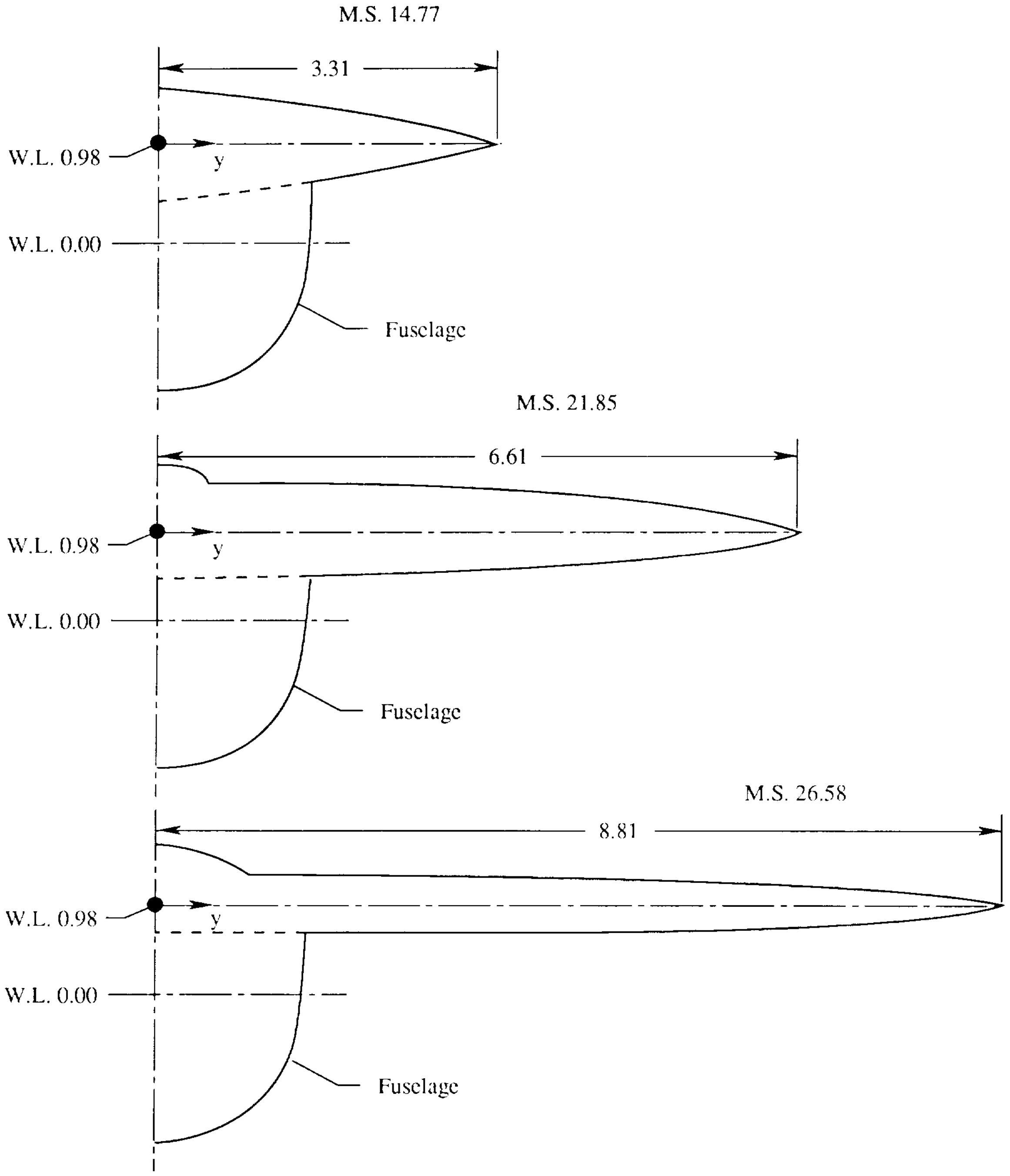

(b) Model cross sections.

Figure 2. Concluded.

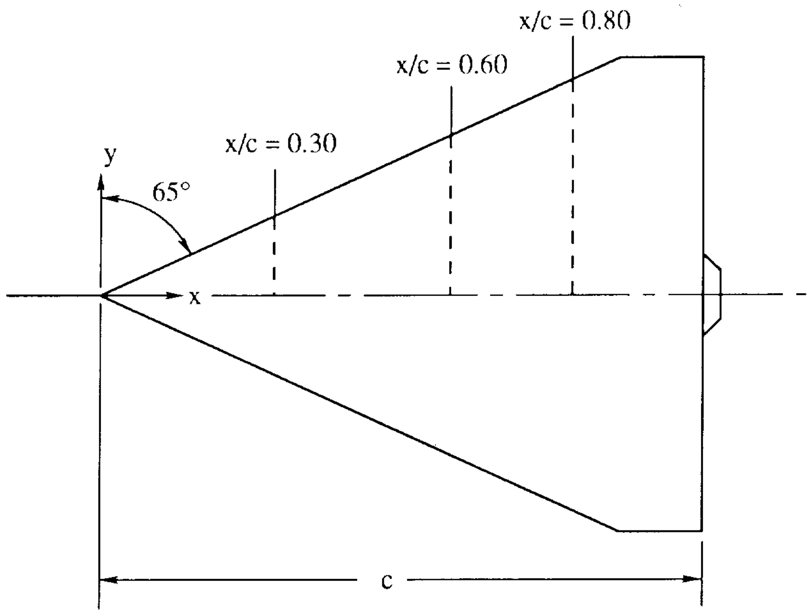

(a) Wing alone.

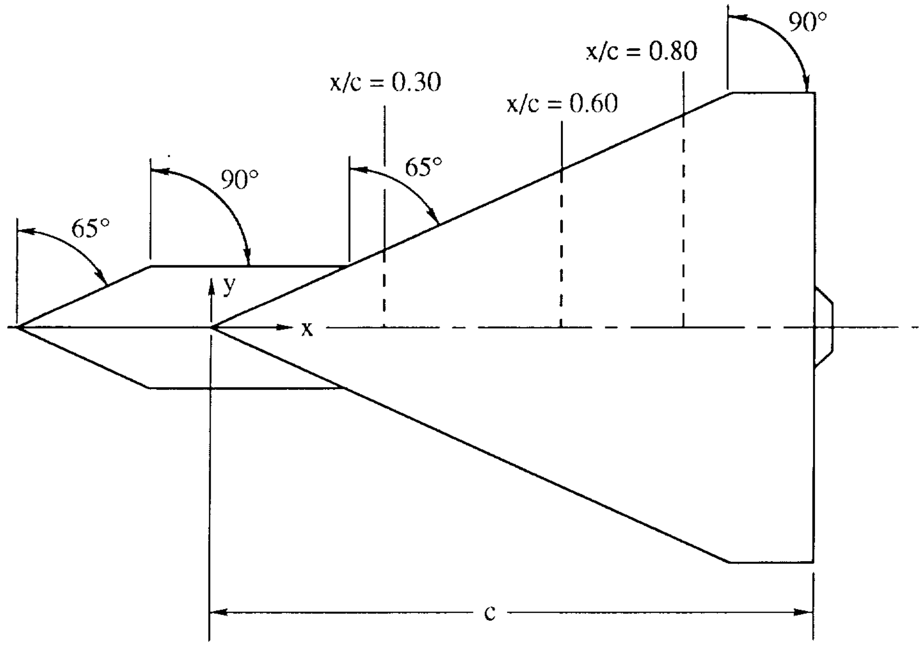

(b) Wing–LEX assembly.

Figure 3. Measurement stations for wing upper surface static pressure.

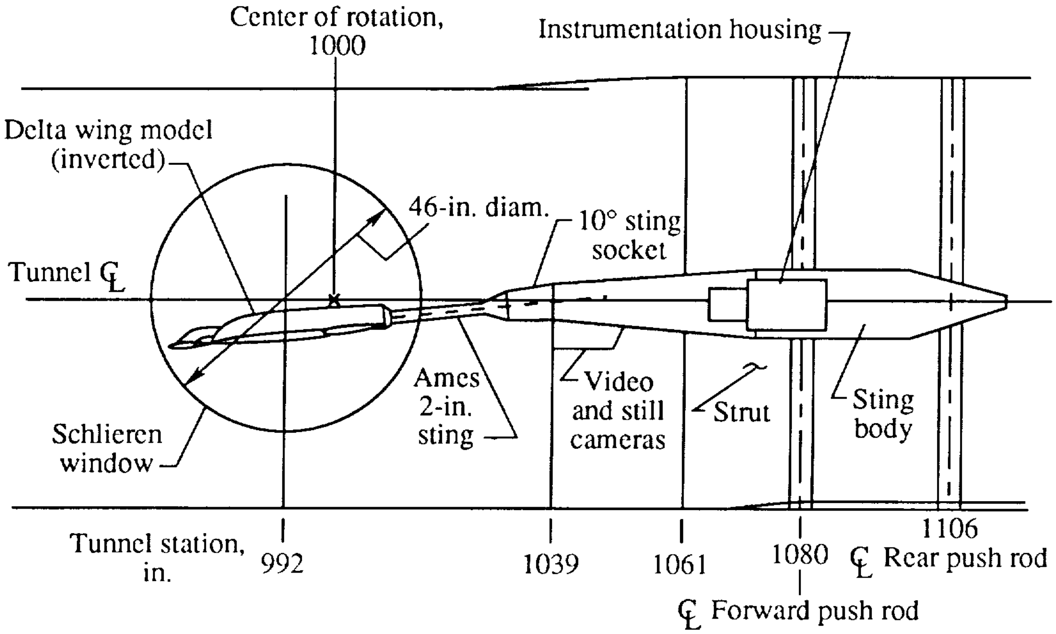

(a) Inverted position.

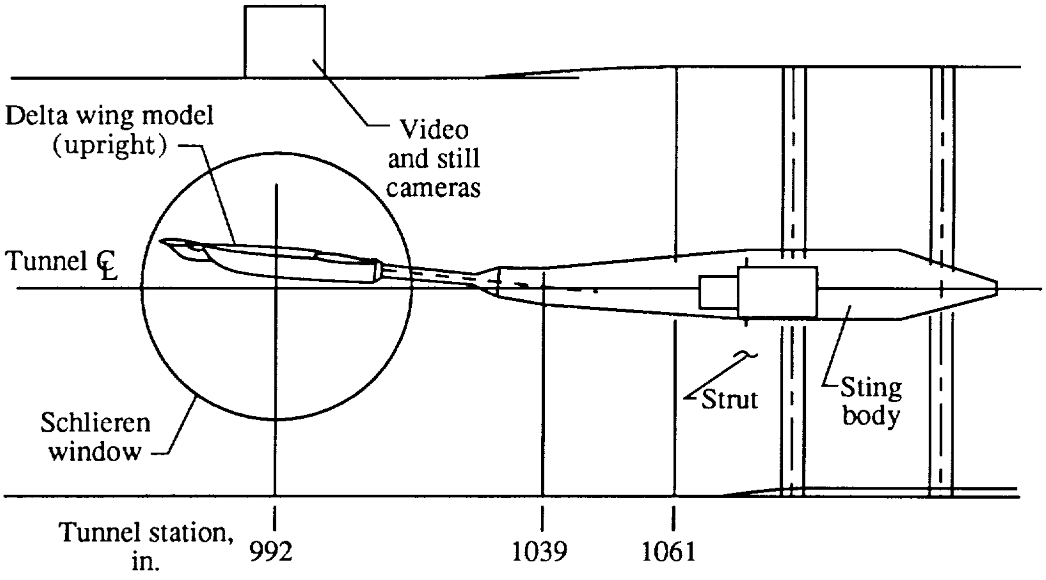

(b) Upright position.

Figure 4. Sketches of model installed in wind tunnel in inverted and upright positions.

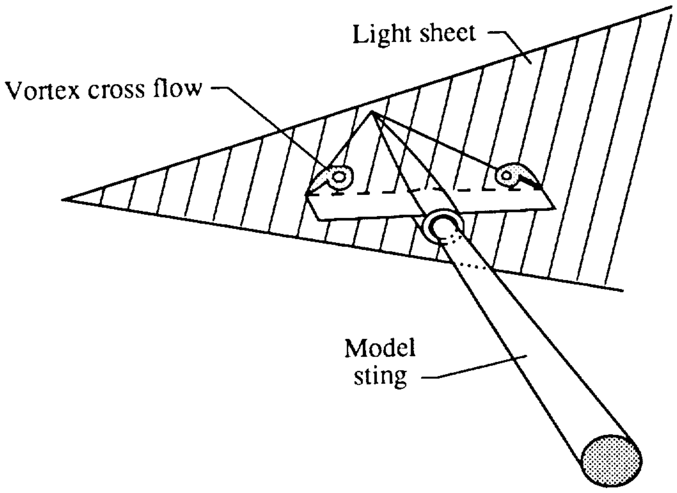

(a) Light sheet normal to wing plane.

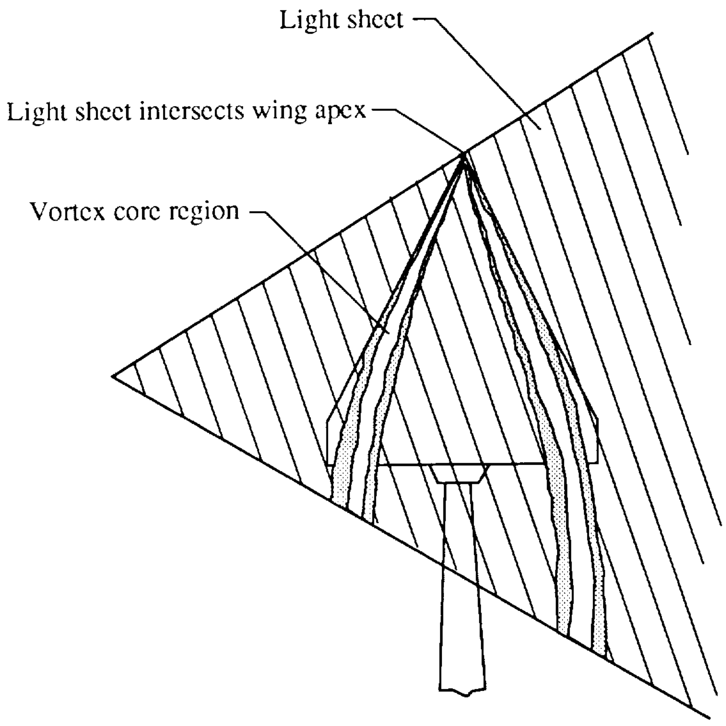

(b) Light sheet along vortex core path.

Figure 5. Laser light-sheet orientation with respect to model.

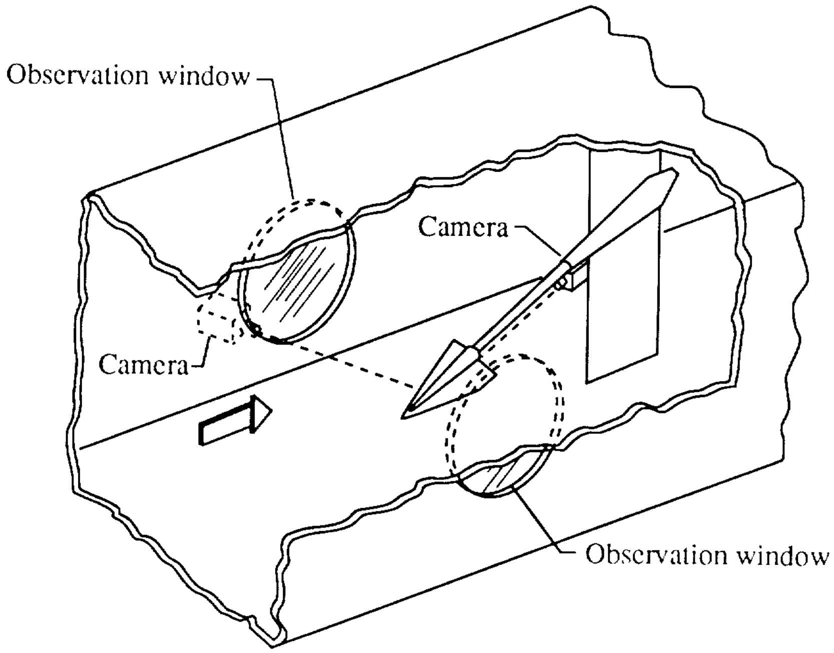

(a) Model inverted.

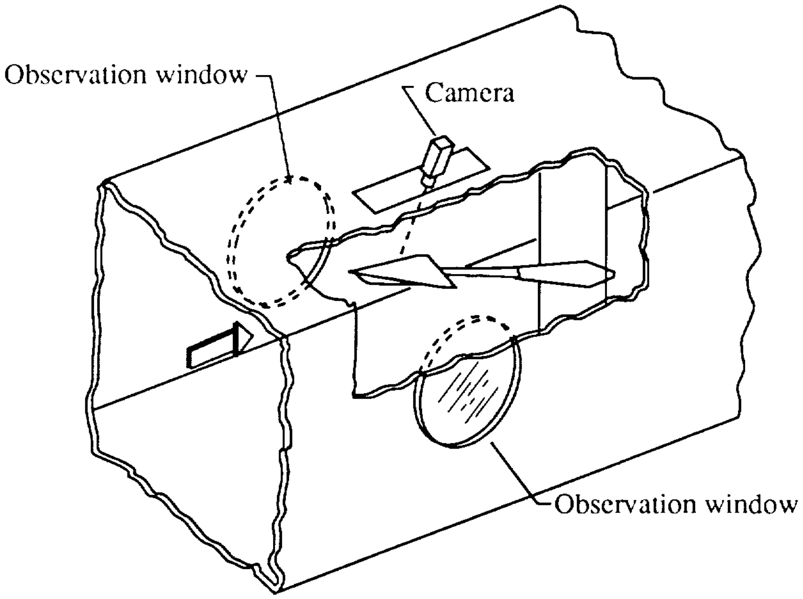

(b) Model upright.

Figure 6. Camera locations and viewing angles for flow visualization.

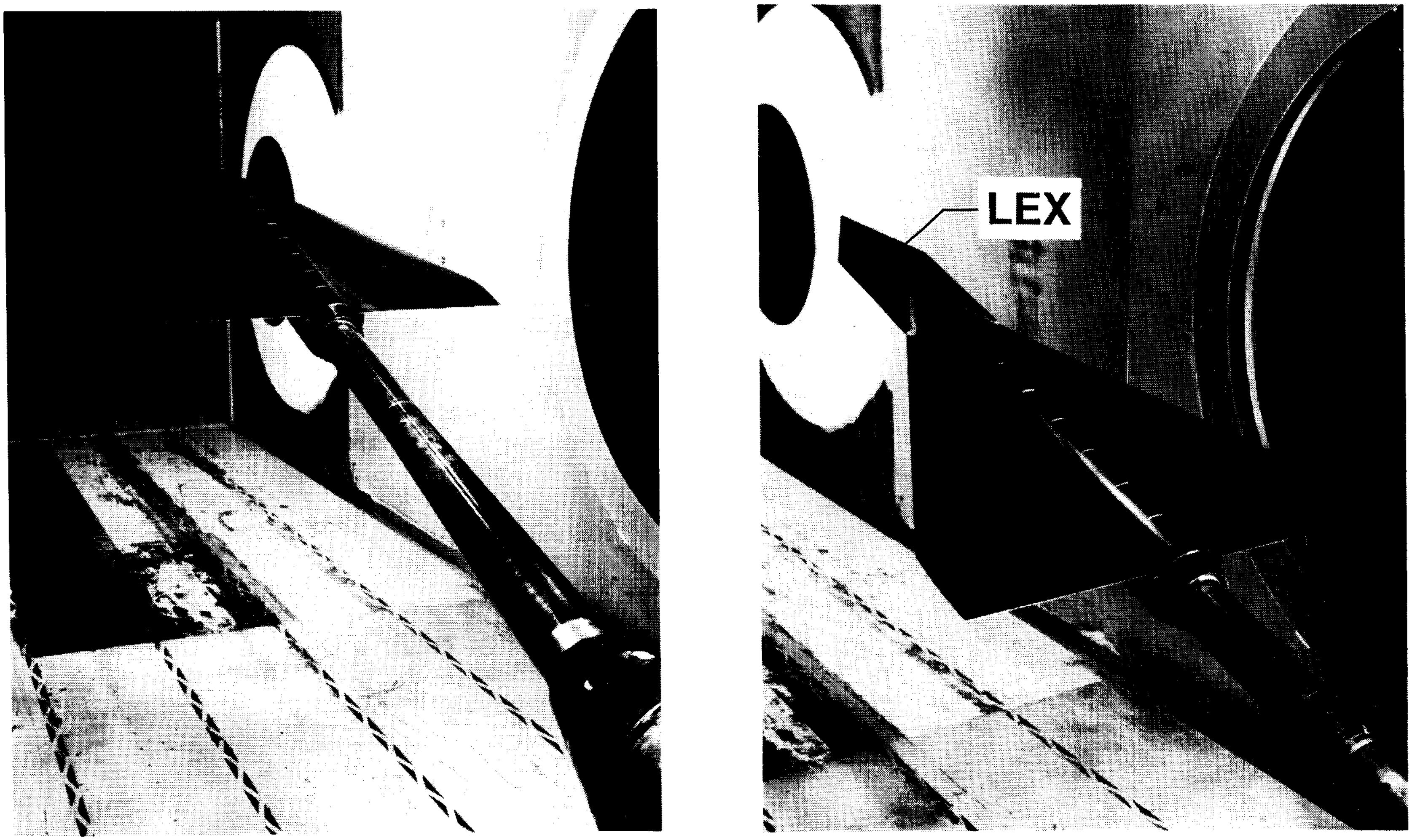

(a) Wing alone.

(b) Wing–LEX assembly.

Figure 7. Photographs of model of 65° cropped delta wing installed in the NASA Ames 6- by 6-Foot Transonic/Supersonic Wind Tunnel.

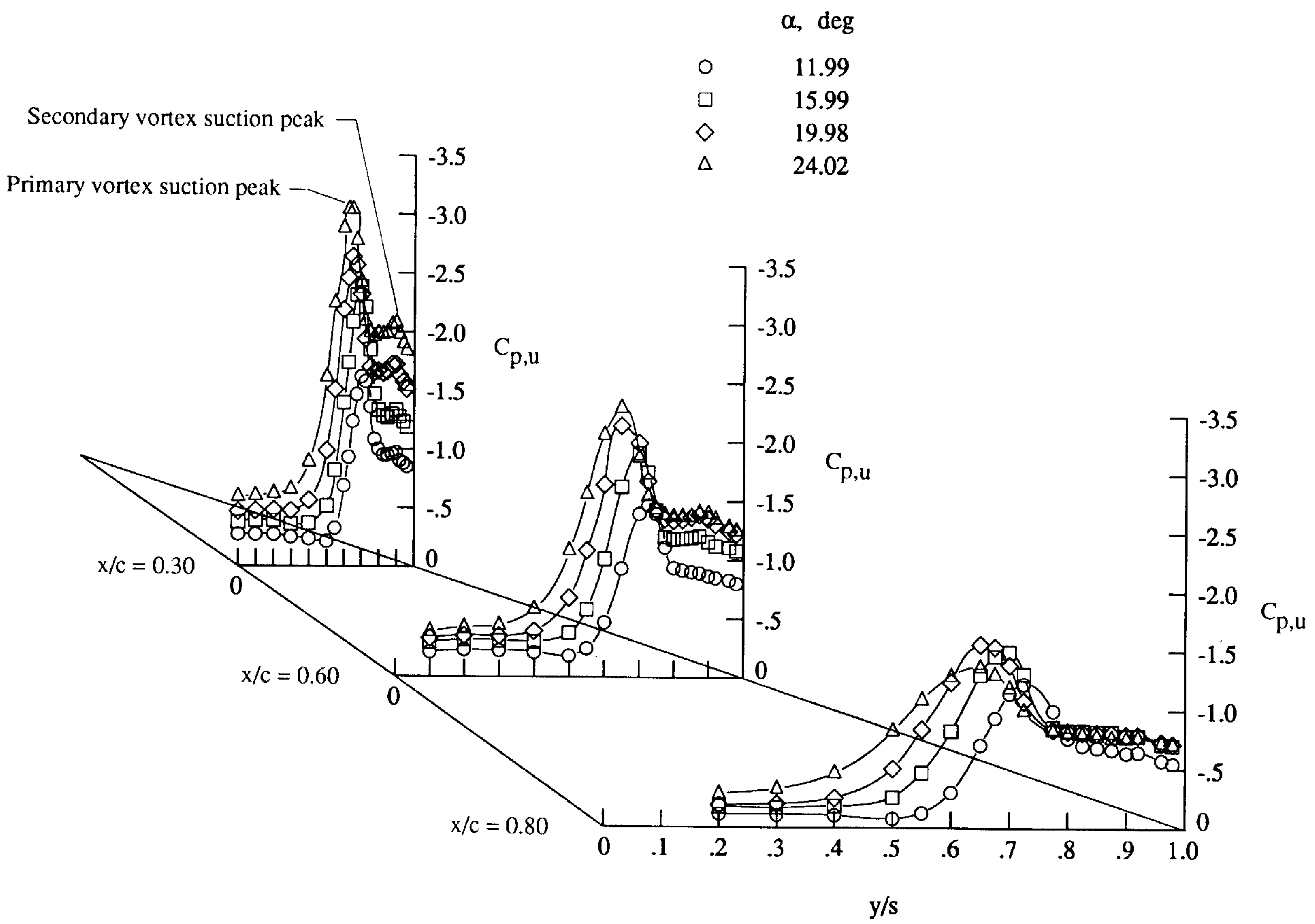

Figure 8. Wing upper surface static pressure distributions at $M_\infty = 0.40$ with LEX off.

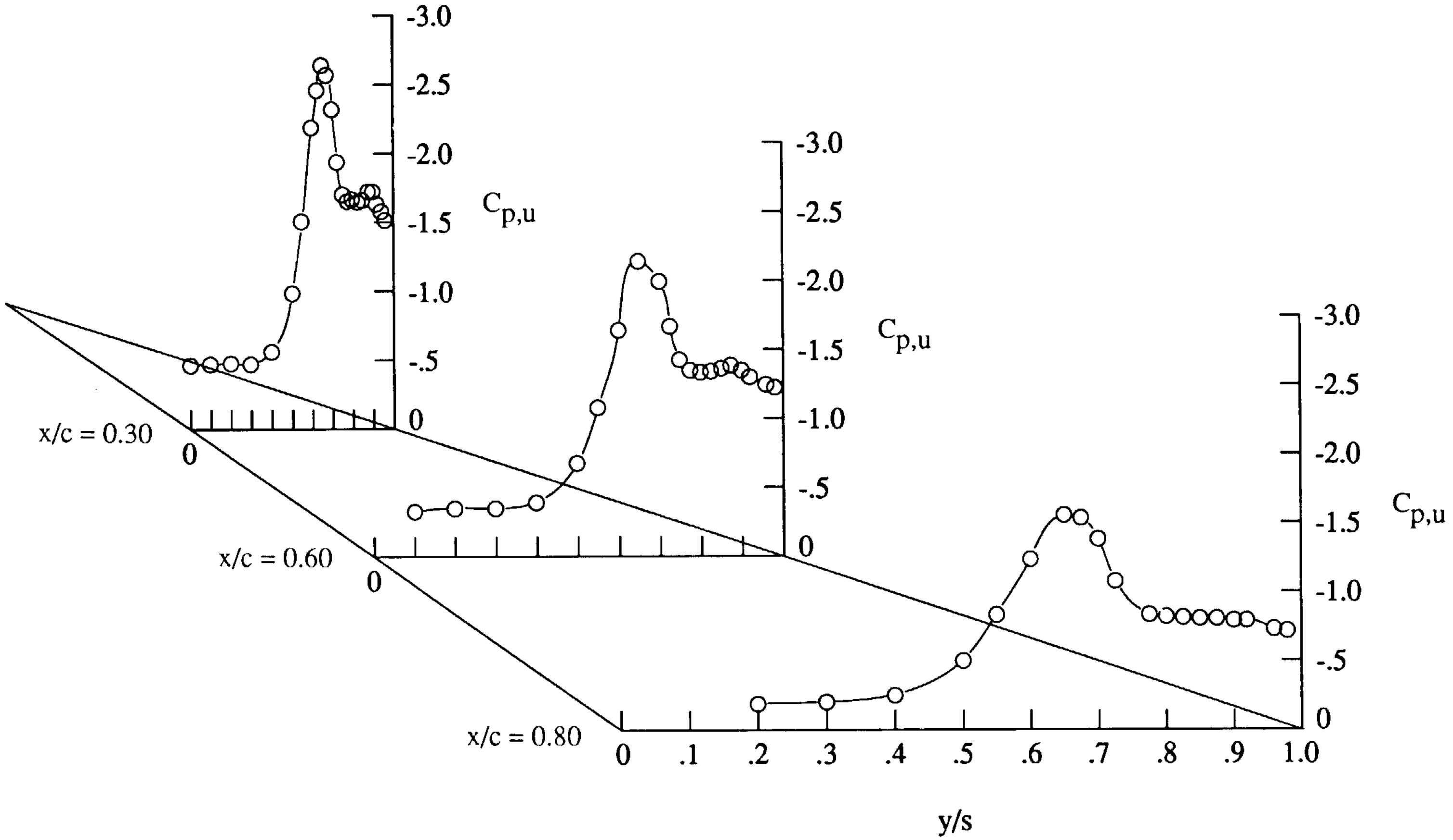

Figure 9. Wing upper surface static pressure distributions at $\alpha = 20°$ and $M_\infty = 0.40$ with LEX off.

ORIGINAL PAGE
BLACK AND WHITE PHOTOGRAPH

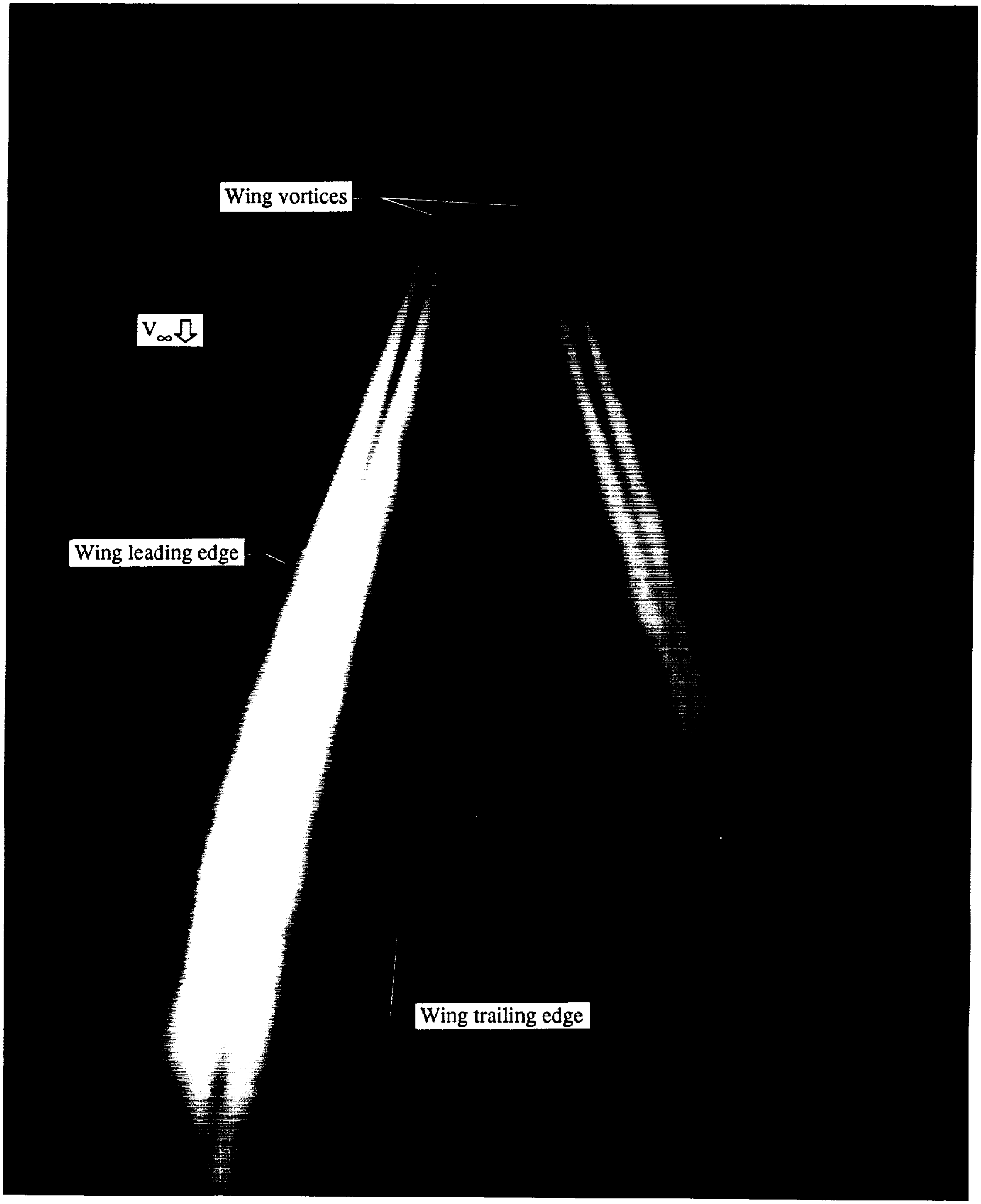

Figure 10. Laser vapor screen flow visualization at $\alpha = 20^\circ$ and $M_\infty = 0.40$ with LEX off.

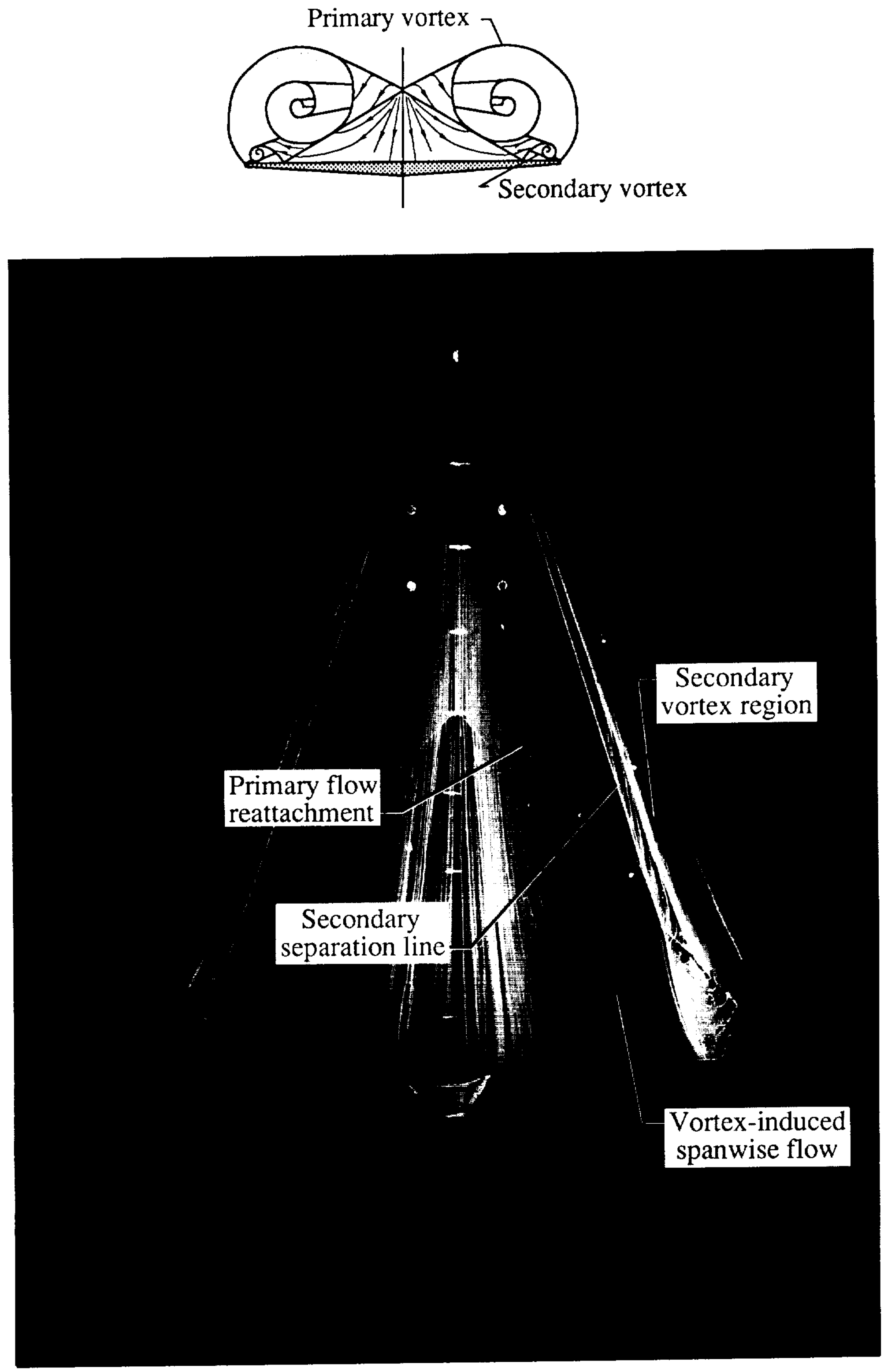

Figure 11. Wing upper surface oil flow pattern at $\alpha = 20^\circ$ and $M_\infty = 0.40$ with LEX off.

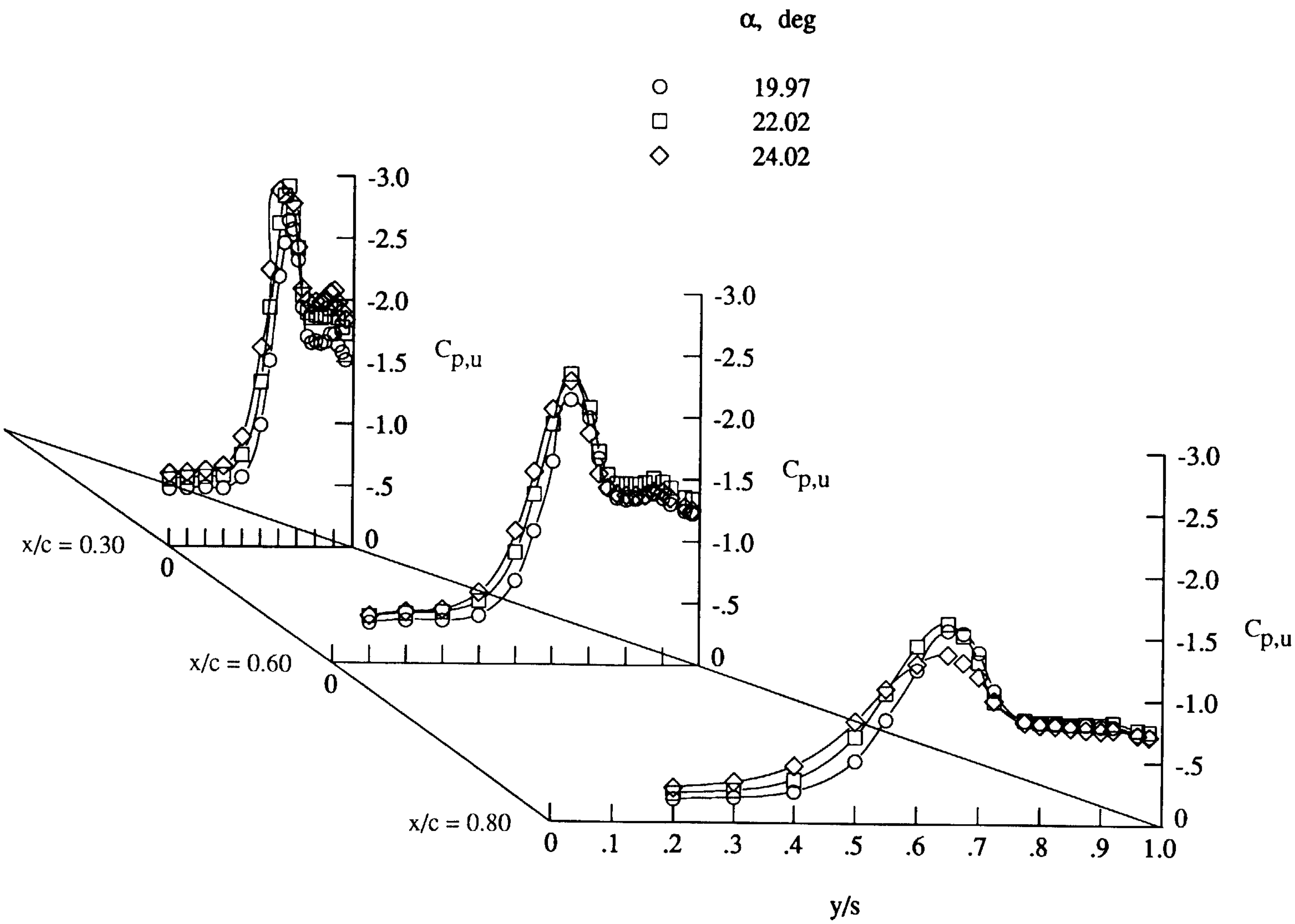

Figure 12. Wing upper surface static pressure distributions at $M_\infty = 0.40$ with LEX off.

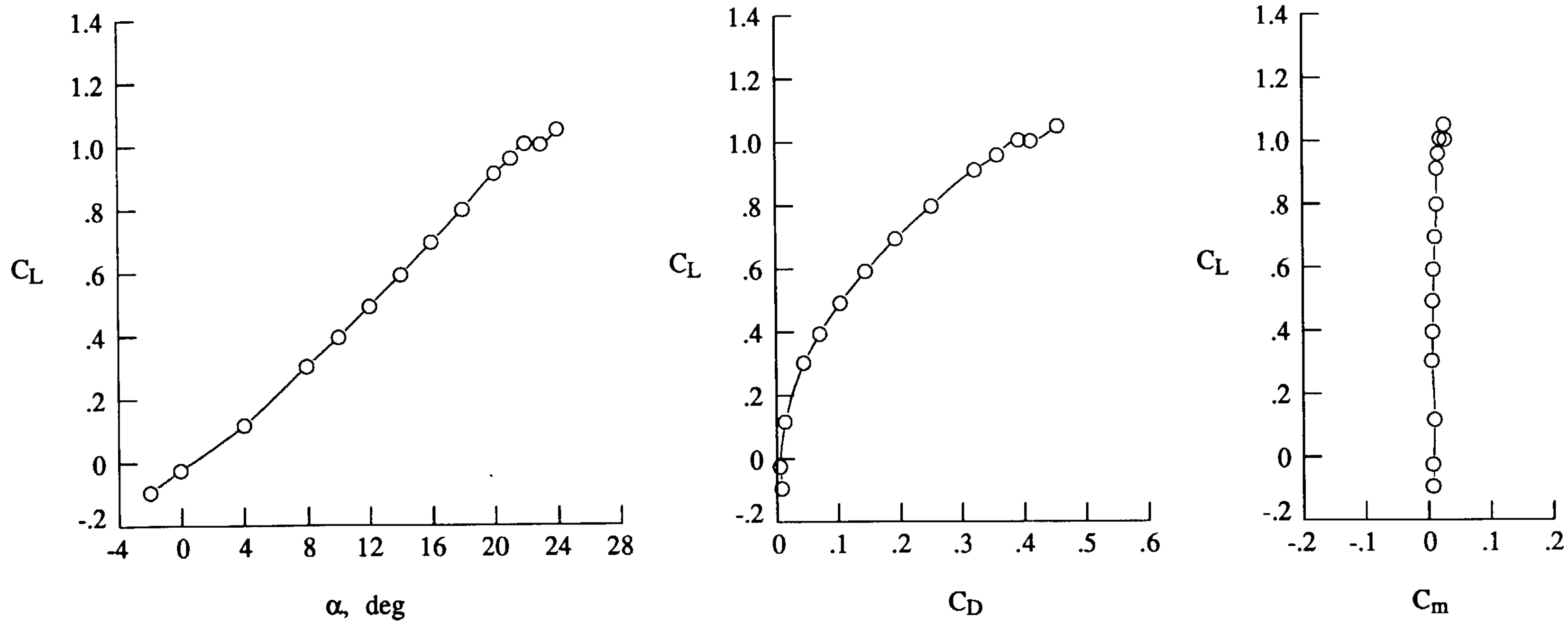

Figure 13. Lift, drag, and pitching-moment characteristics at $M_\infty = 0.40$ with LEX off.

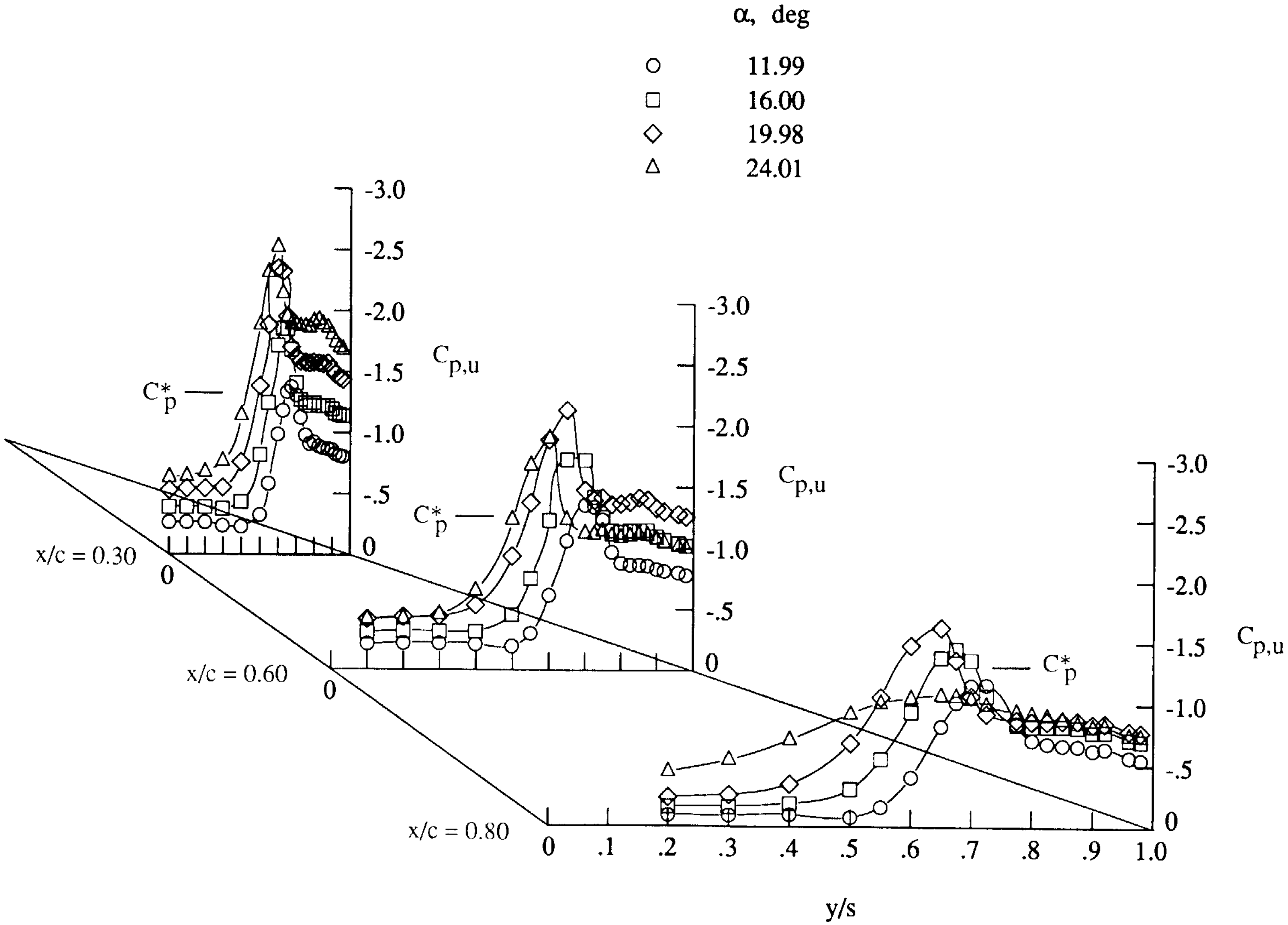

Figure 14. Wing upper surface static pressure distributions at $M_\infty = 0.60$ with LEX off.

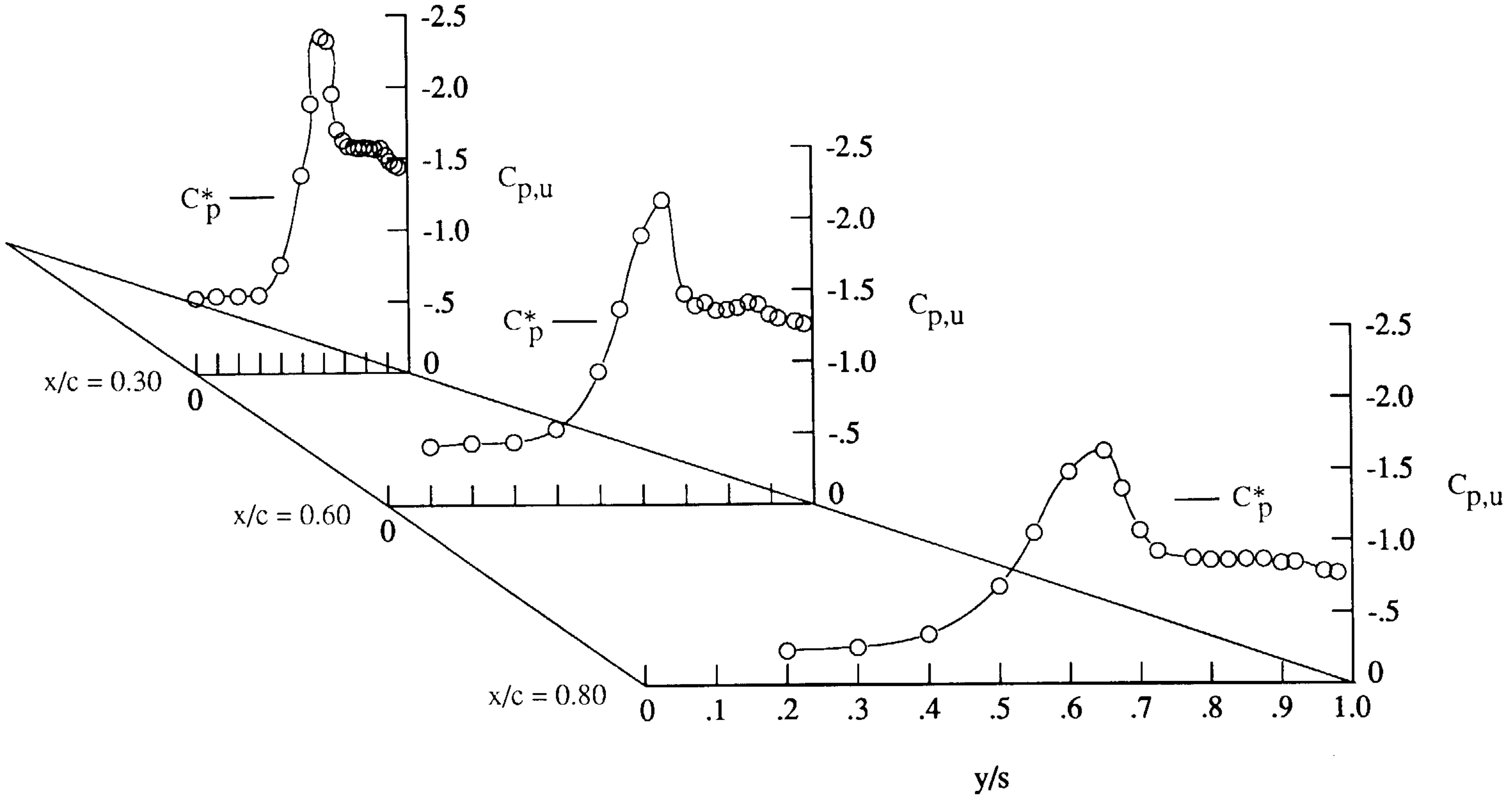

Figure 15. Wing upper surface static pressure distributions at $\alpha = 20°$ and $M_\infty = 0.60$ with LEX off.

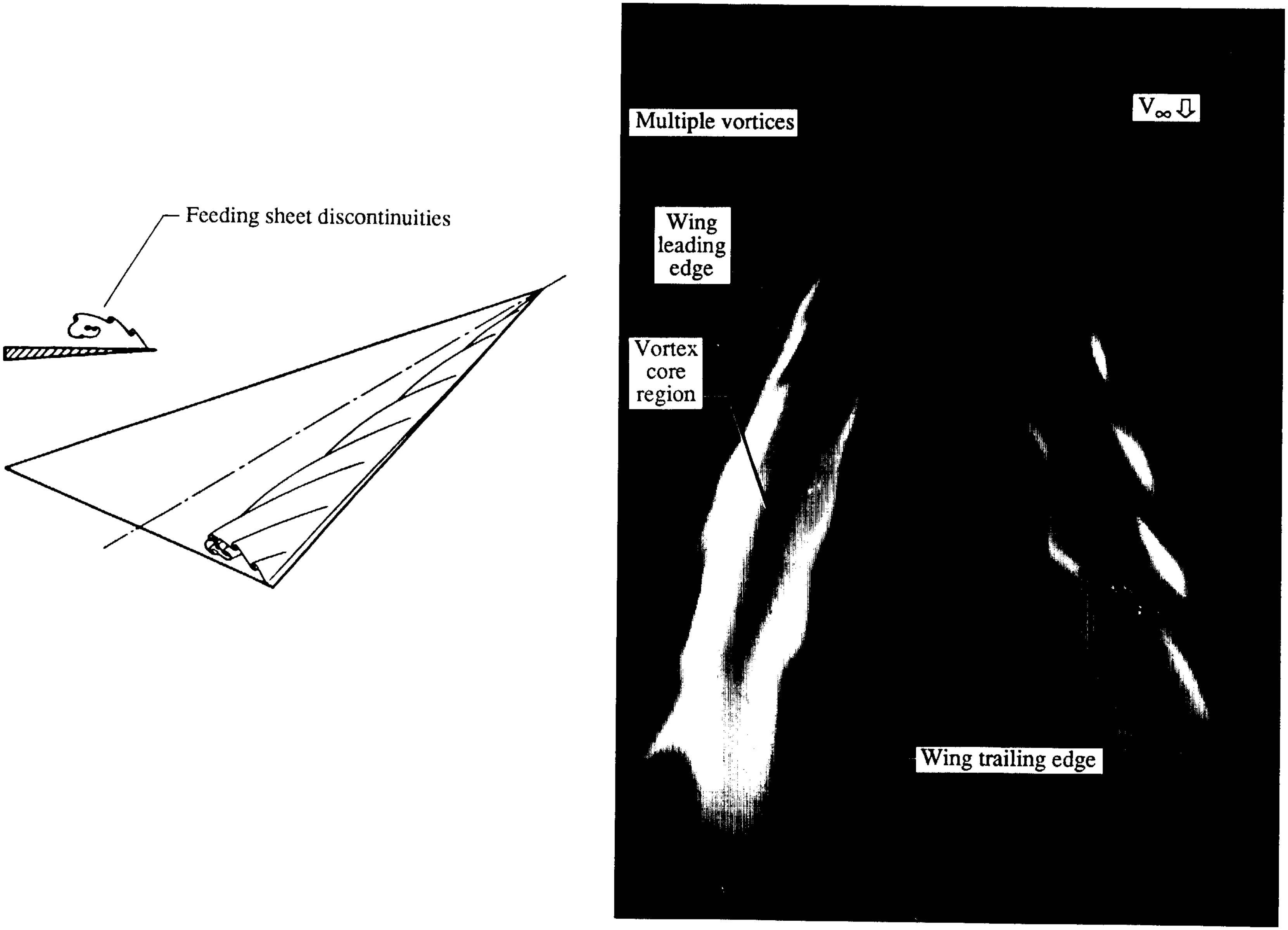

Figure 16. Laser vapor screen flow visualization at $\alpha = 20°$ and $M_\infty = 0.60$ with LEX off. Sketch taken from reference 6.

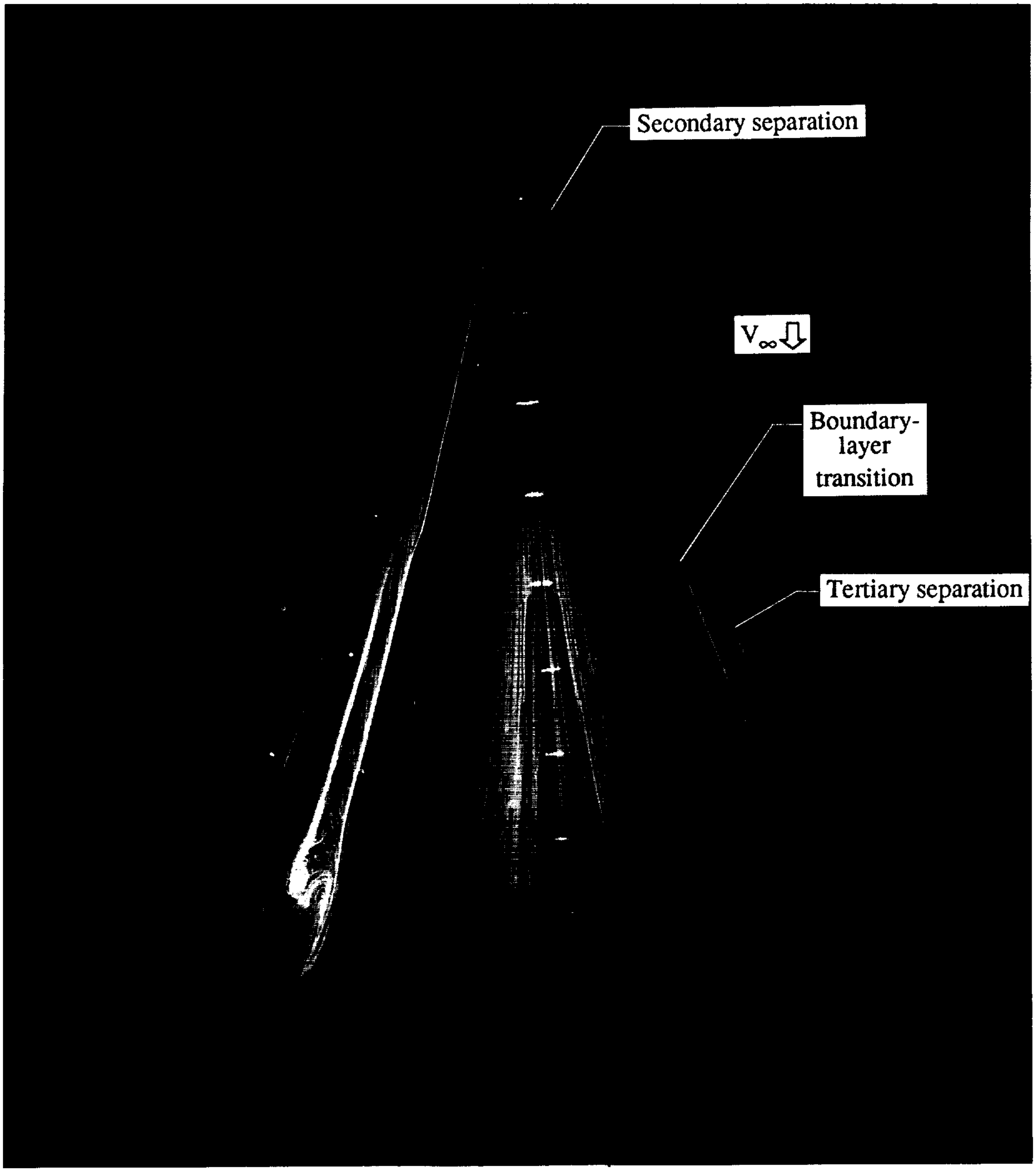

Figure 17. Wing upper surface oil flow pattern at $\alpha = 20^\circ$ and $M_\infty = 0.60$ with LEX off.

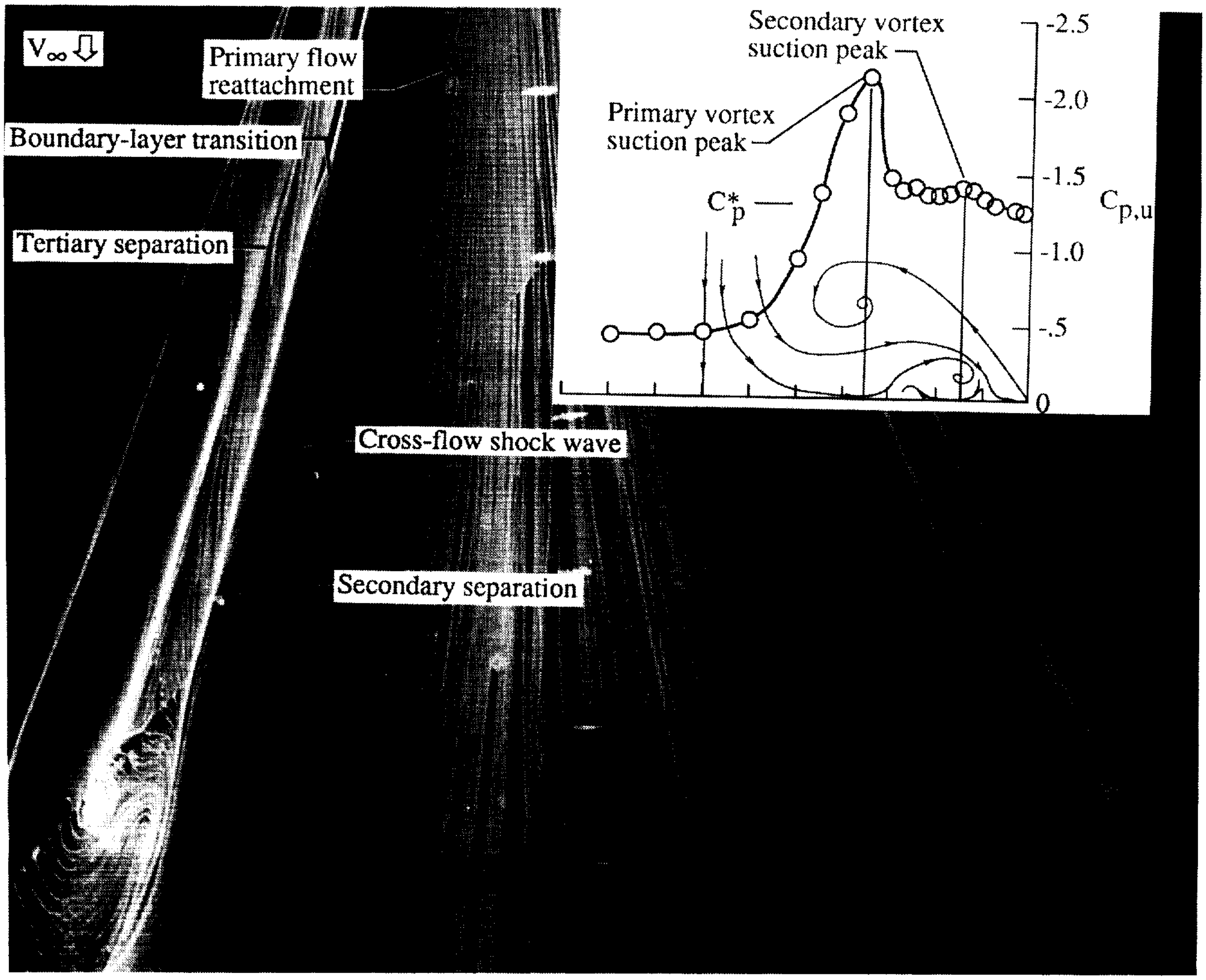

Figure 18. Enlarged view of wing surface flow at $\alpha = 20°$ and $M_\infty = 0.60$ with LEX off.

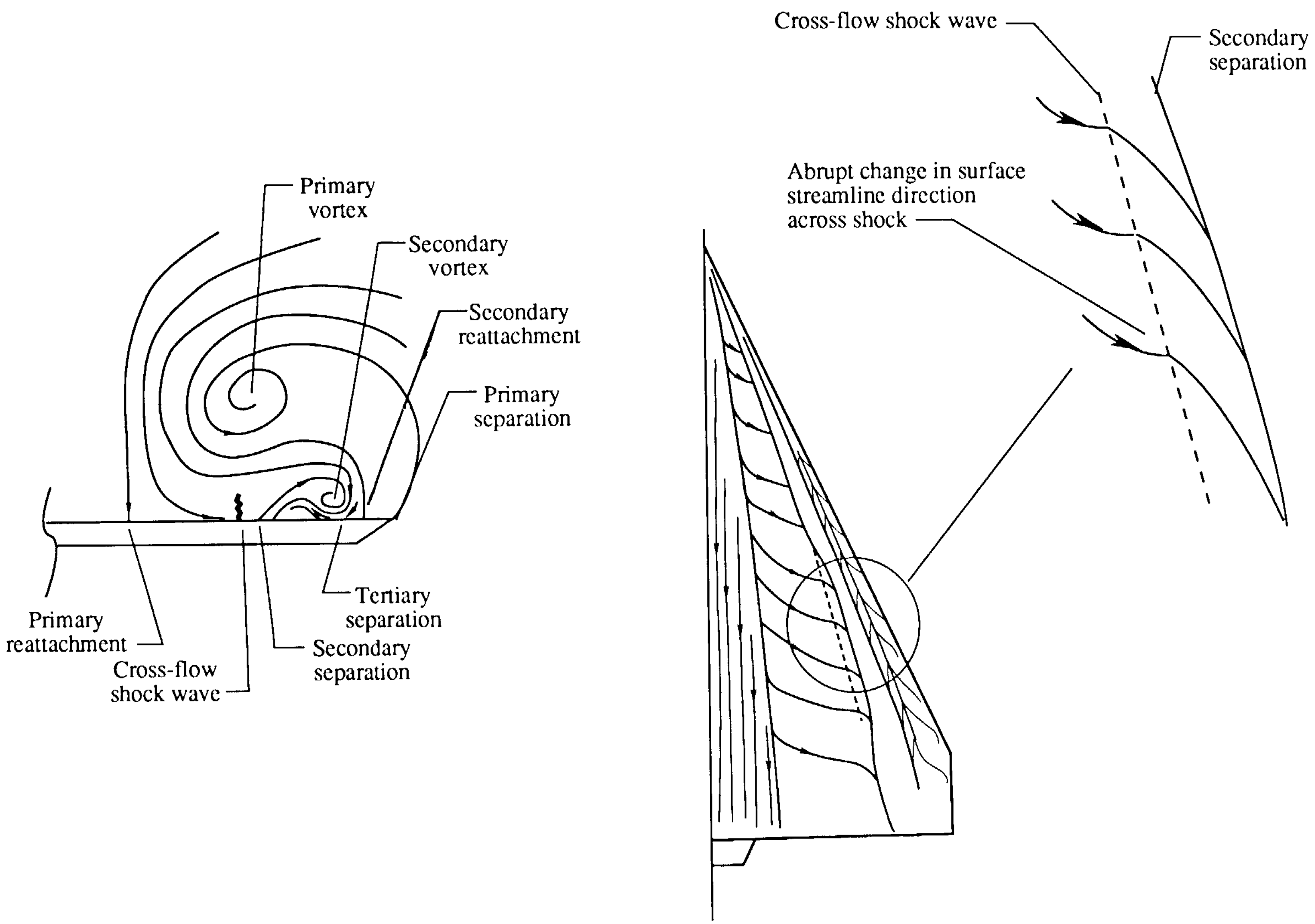

Figure 19. Schematic representations of model cross flow and surface flow.

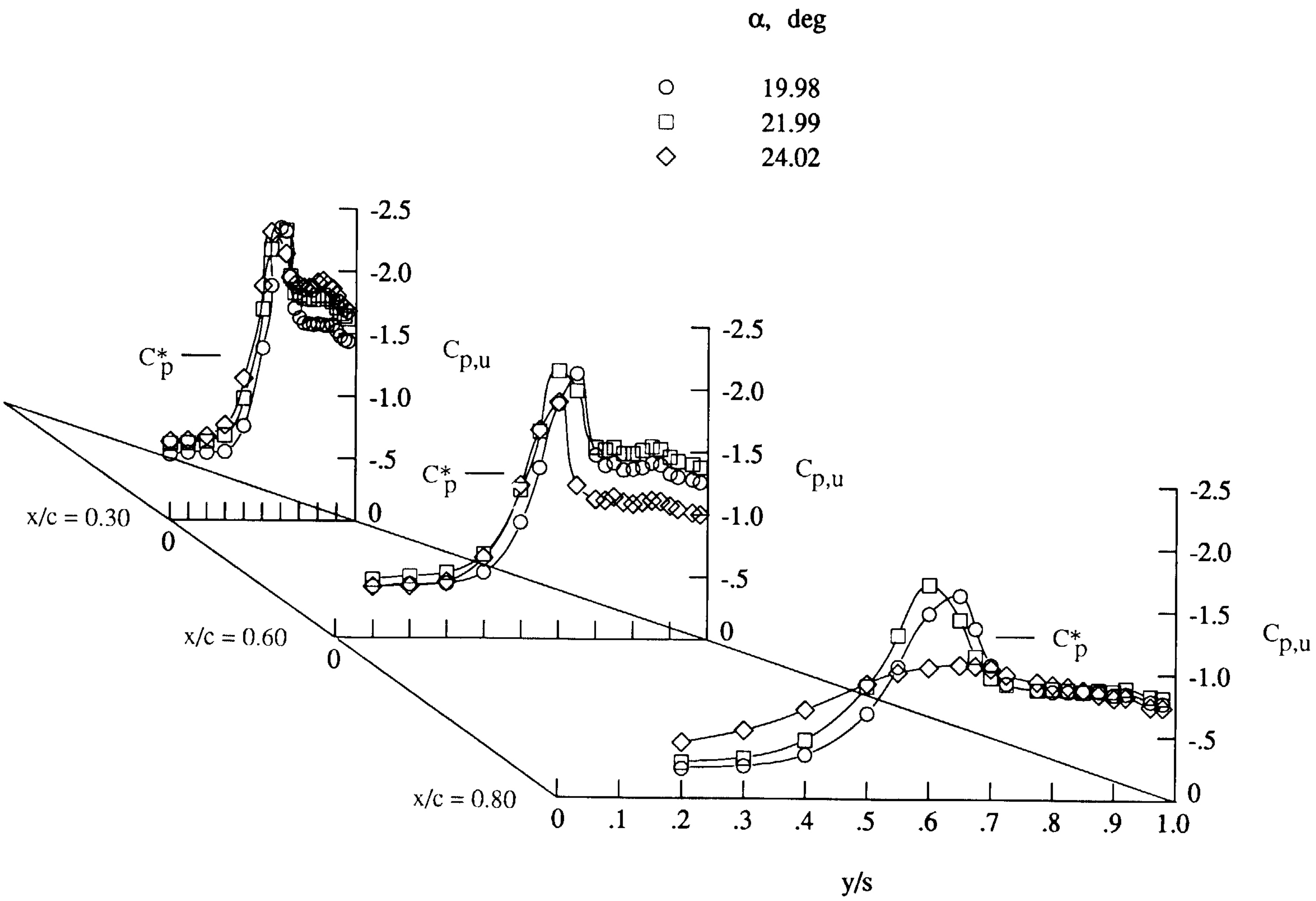

Figure 20. Wing upper surface static pressure distributions at $M_\infty = 0.60$ with LEX off.

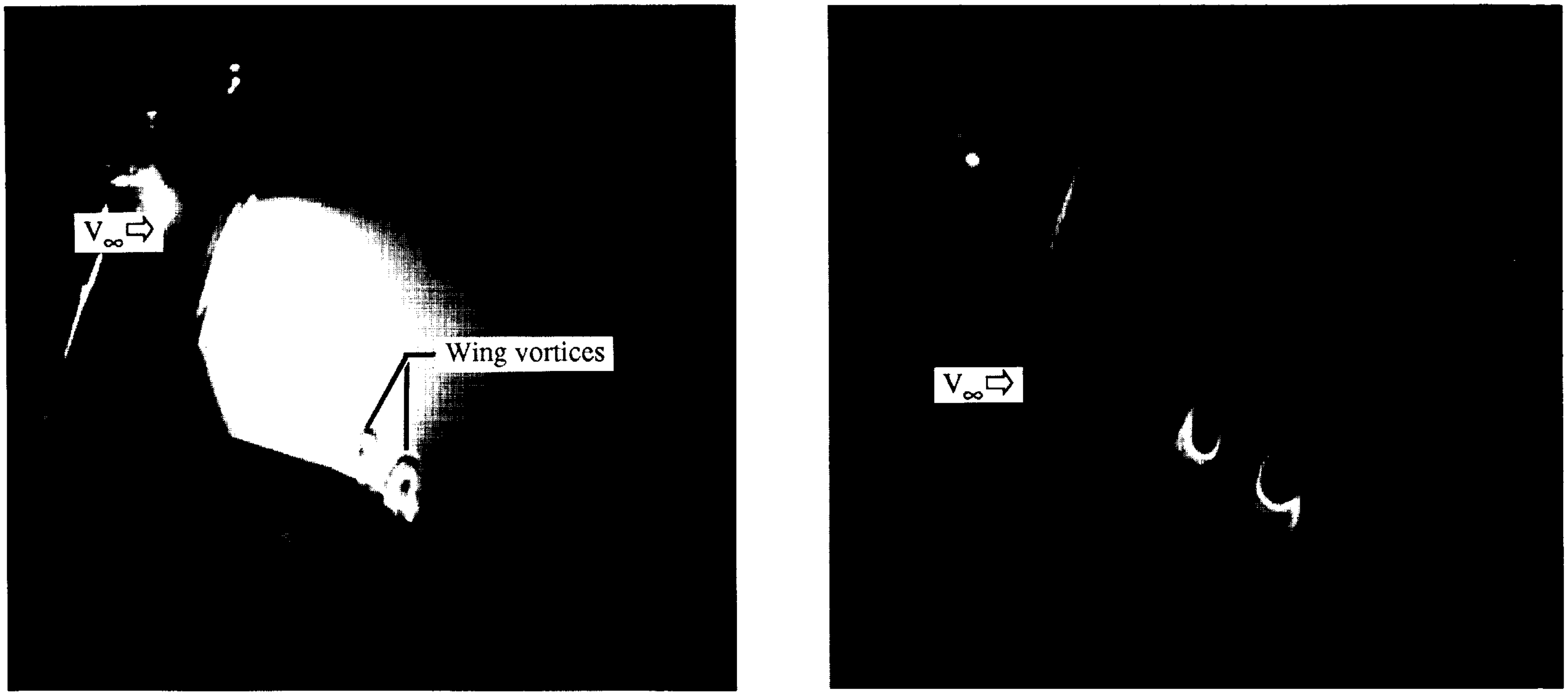

(a) $x/c = 0.40$.

(b) $x/c = 0.60$.

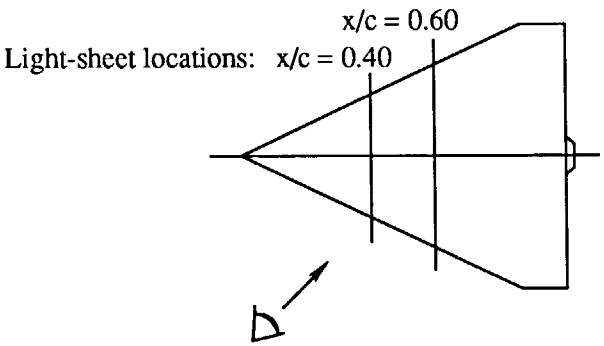

Figure 21. Laser vapor screen flow visualizations at $\alpha = 24°$ and $M_\infty = 0.60$ with LEX off.

ORIGINAL PAGE
BLACK AND WHITE PHOTOGRAPH

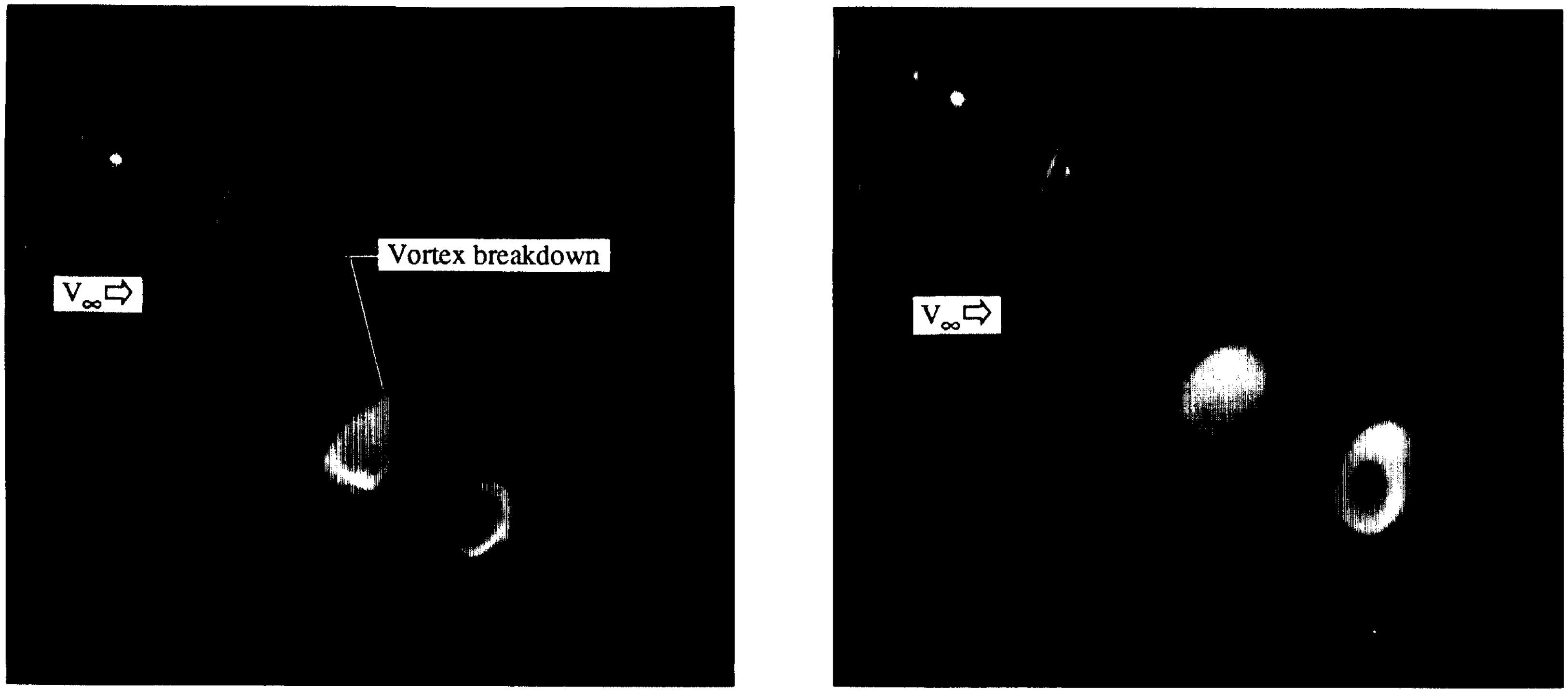

(c) $x/c = 0.80$.

(d) $x/c = 1.00$.

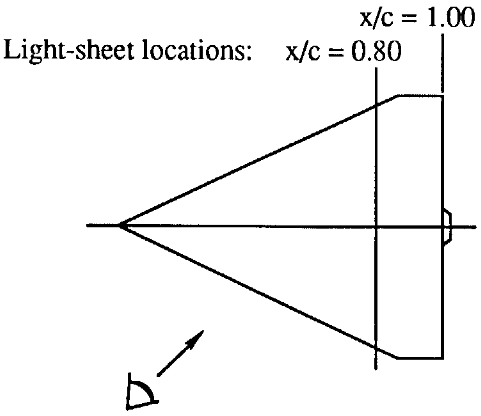

Figure 21. Concluded.

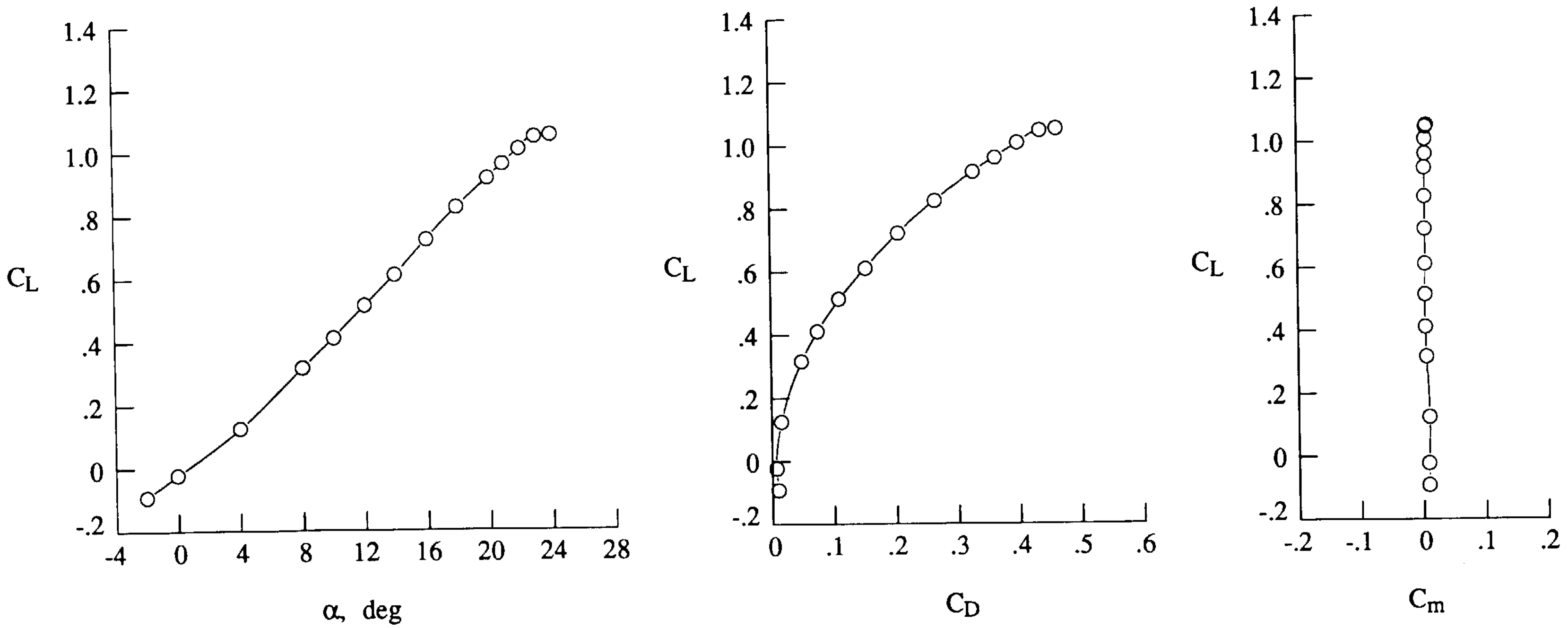

Figure 22. Lift, drag, and pitching-moment characteristics at $M_\infty = 0.60$ with LEX off.

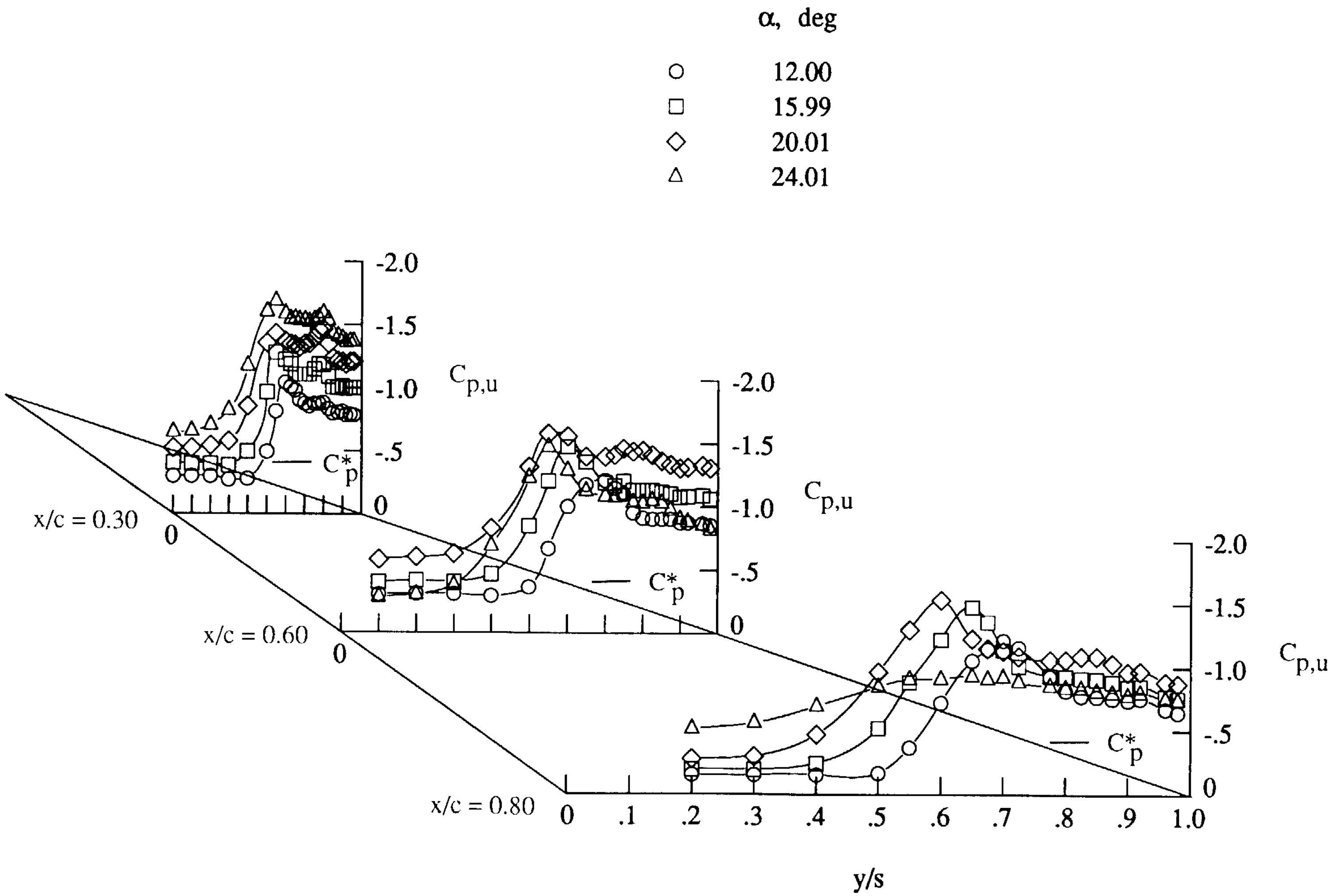

Figure 23. Wing upper surface static pressure distributions at $M_\infty = 0.80$ with LEX off.

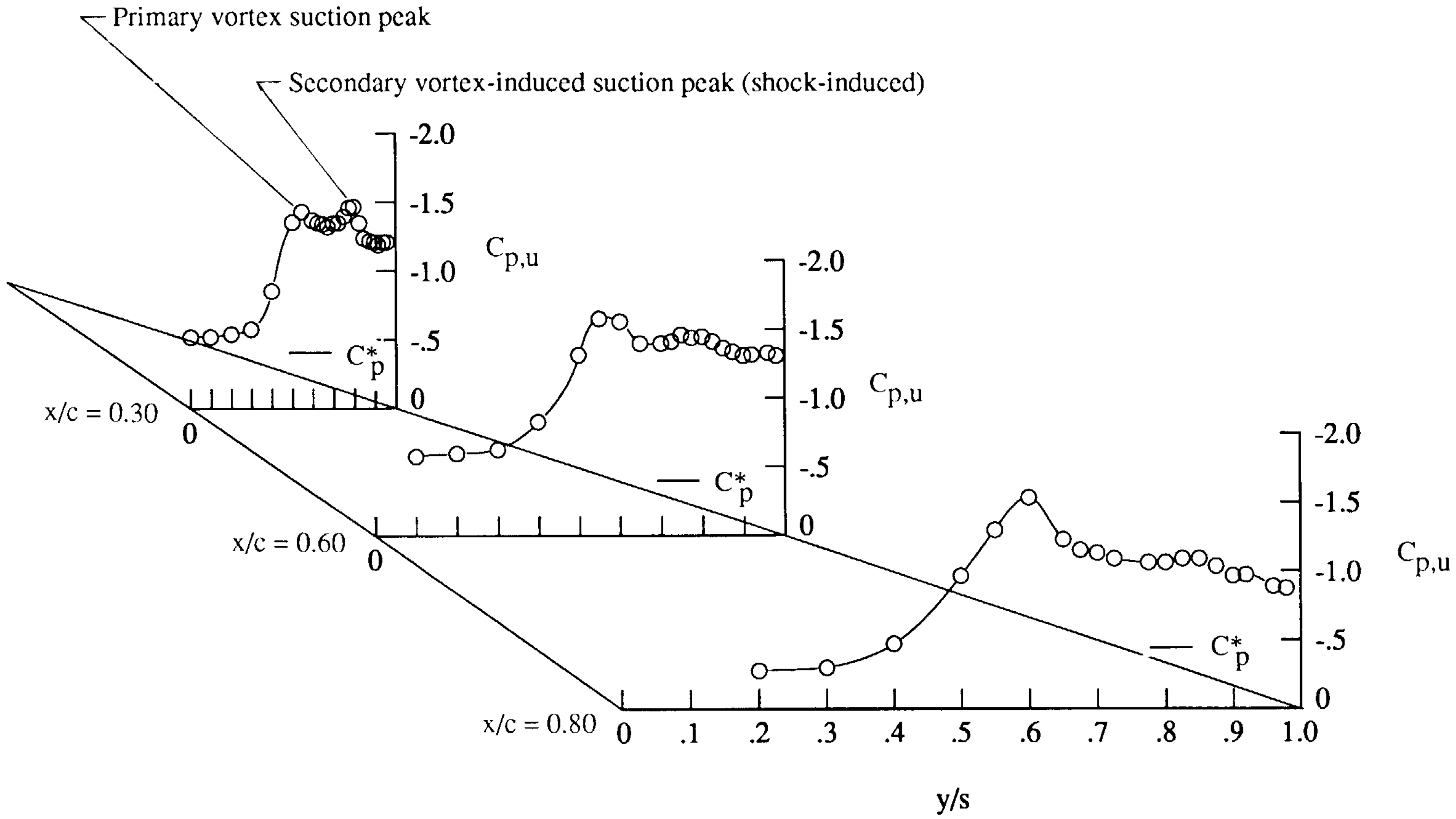

Figure 24. Wing upper surface static pressure distributions at $\alpha = 20°$ and $M_\infty = 0.80$ with LEX off.

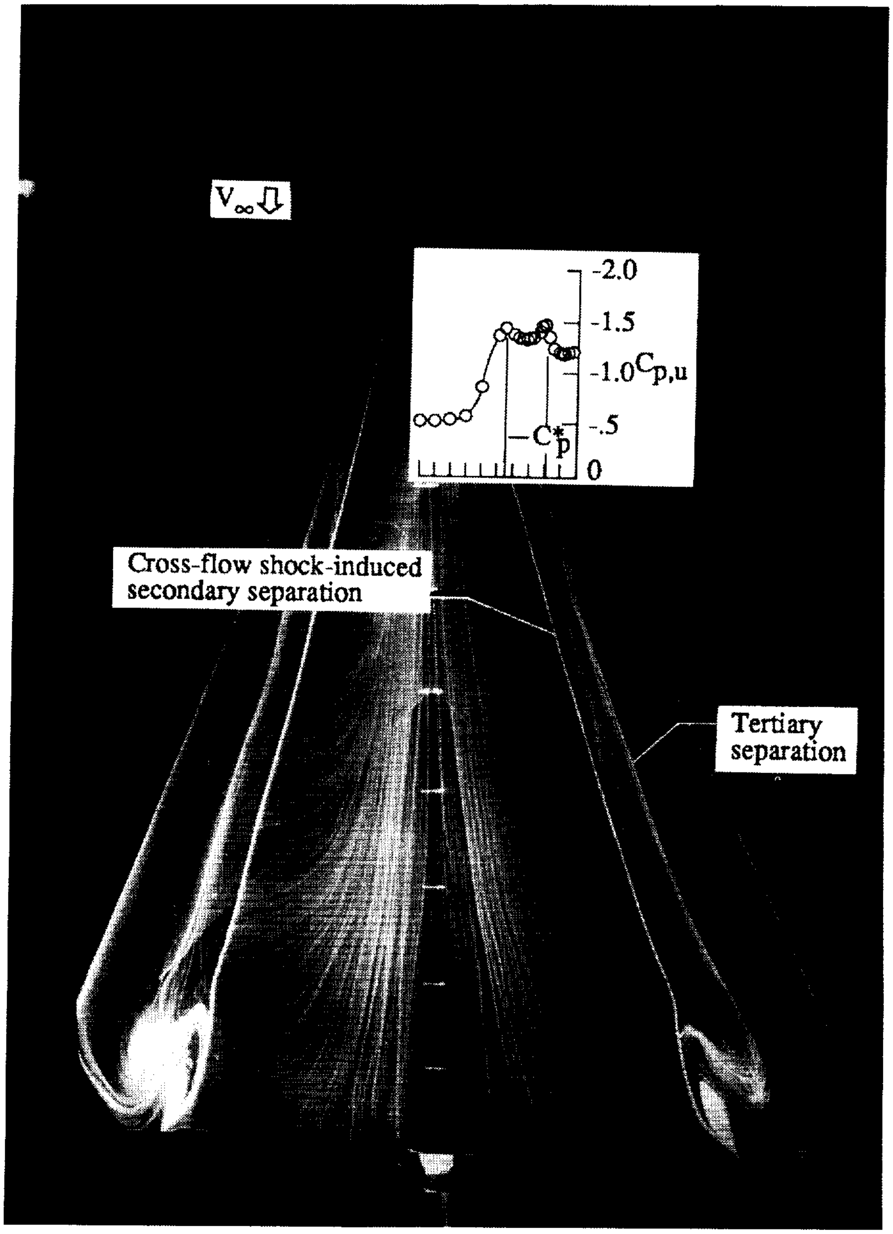

Figure 25. Wing upper surface oil flow pattern at $\alpha = 20°$ and $M_\infty = 0.80$ with LEX off.

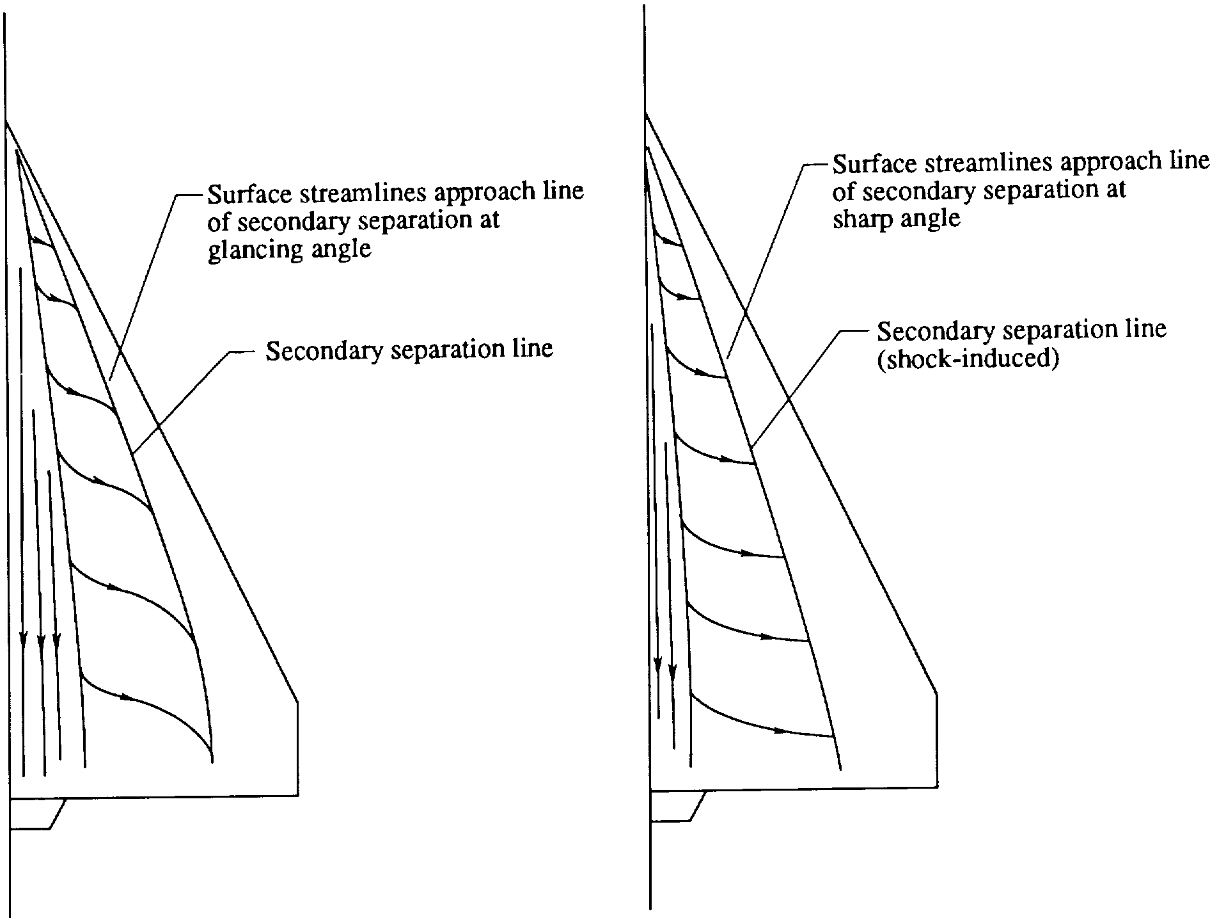

(a) Without shock.

(b) With shock.

Figure 26. Sketch of surface streamline patterns with and without shock-induced secondary boundary-layer separation.

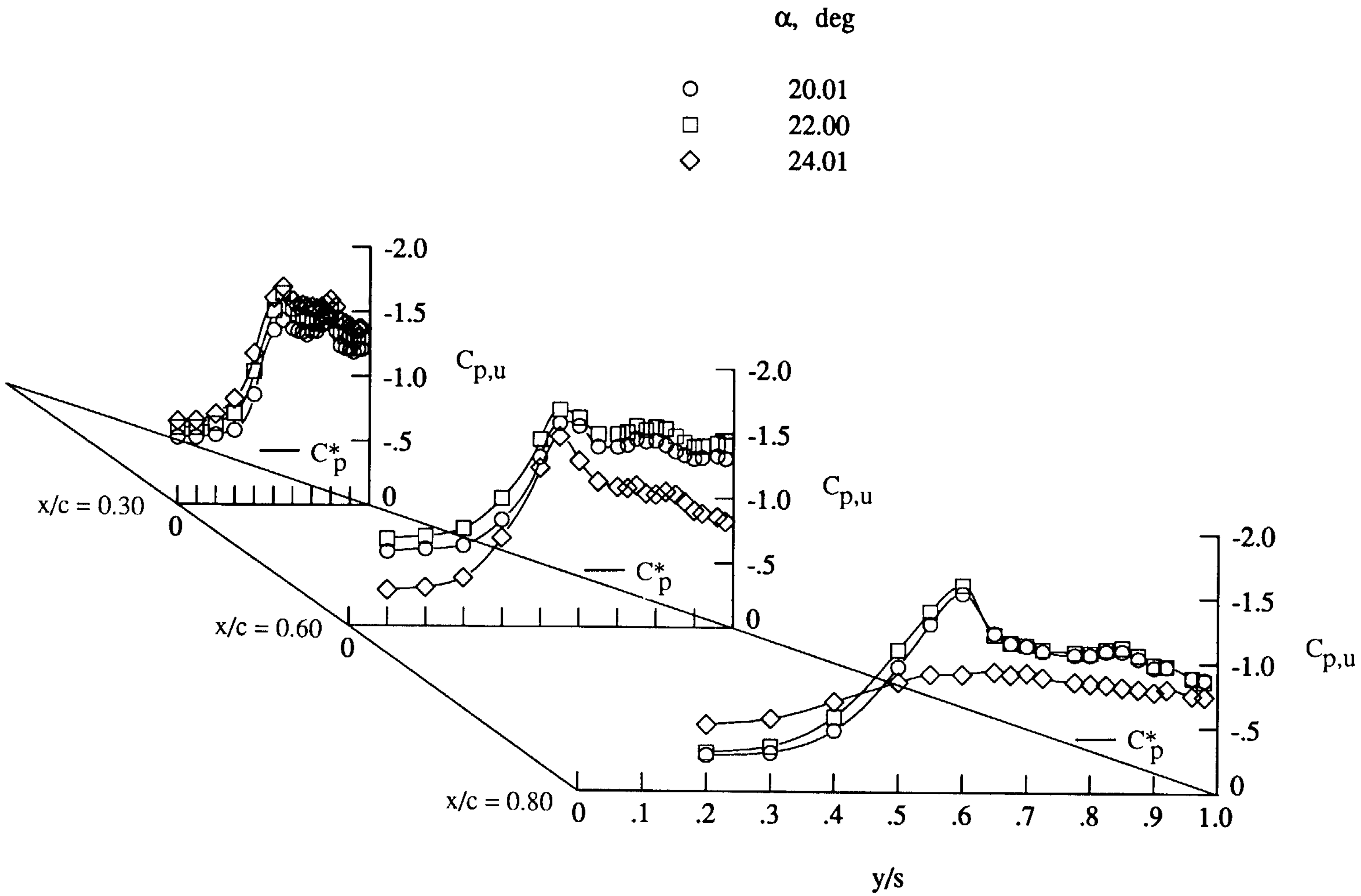

Figure 27. Wing upper surface static pressure distributions at $M_\infty = 0.80$ with LEX off.

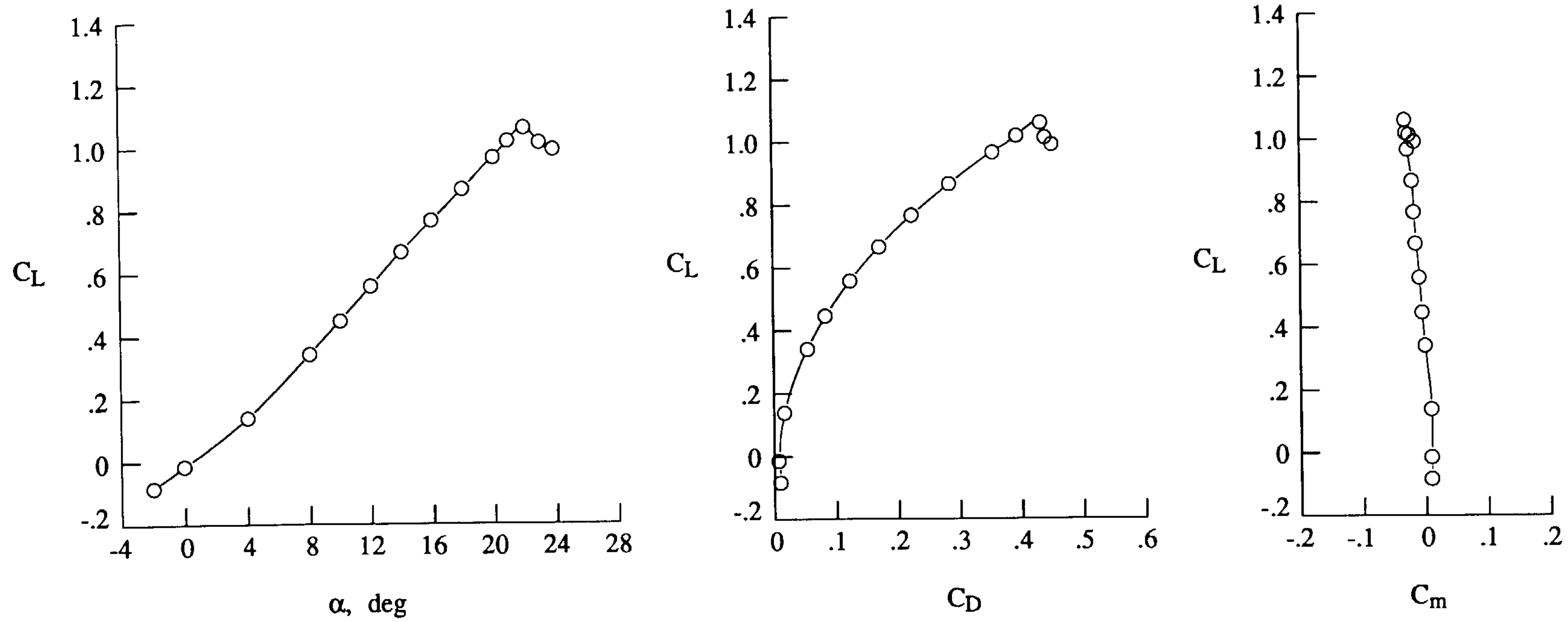

Figure 28. Lift, drag, and pitching-moment characteristics at $M_\infty = 0.80$ with LEX off.

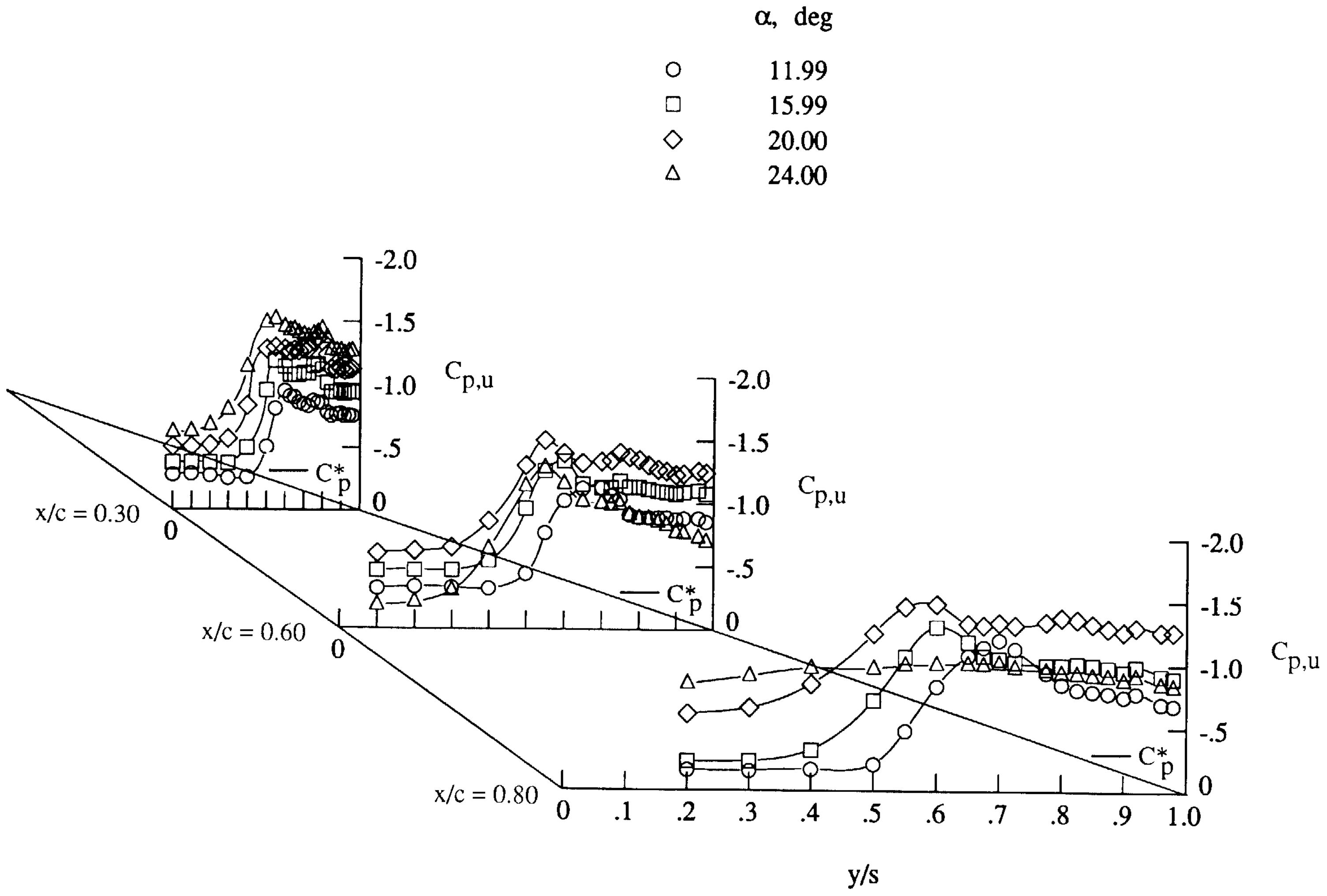

Figure 29. Wing upper surface static pressure distributions at $M_\infty = 0.85$ with LEX off.

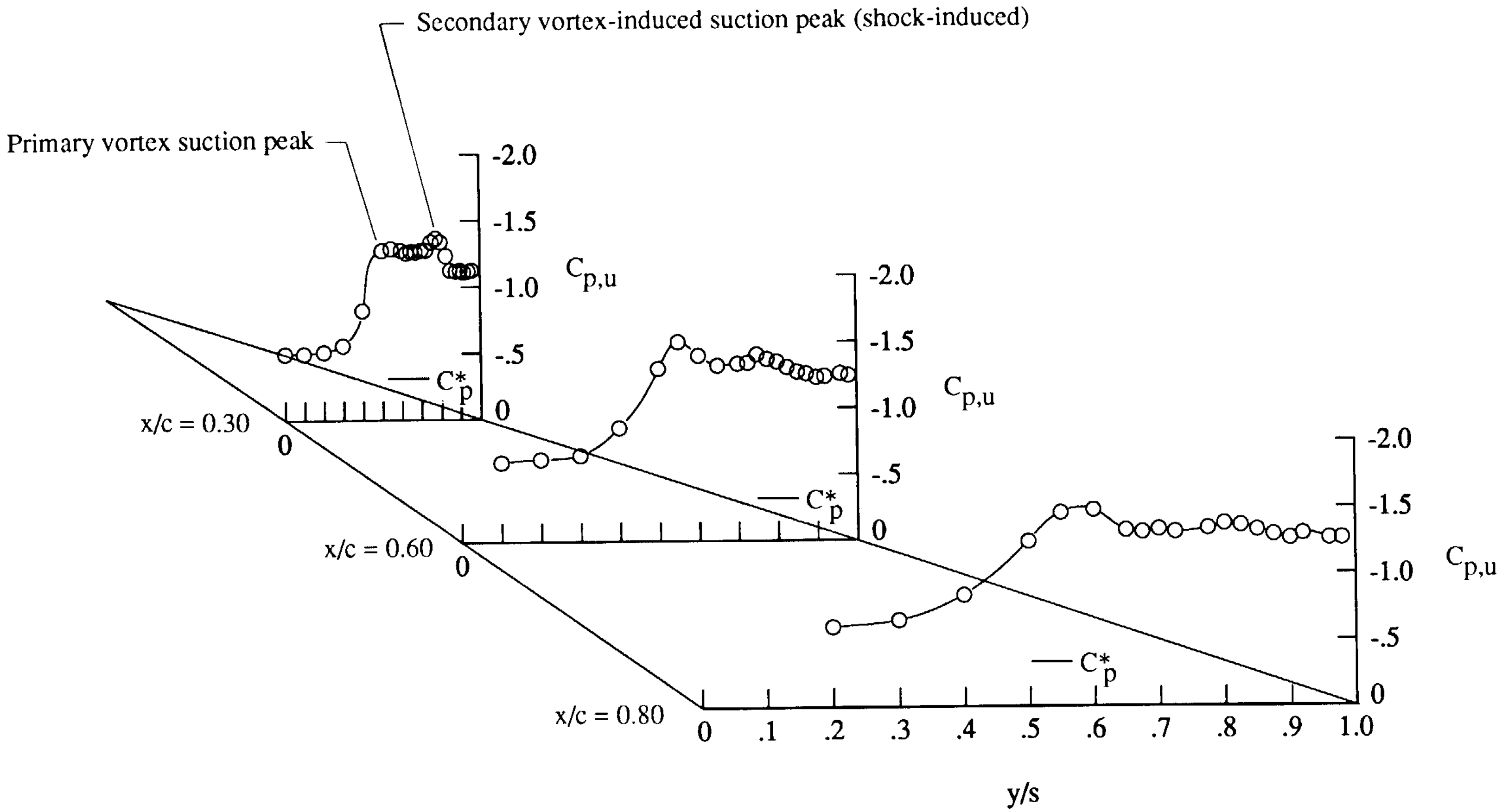

Figure 30. Wing upper surface static pressure distributions at $\alpha = 20°$ and $M_\infty = 0.85$ with LEX off.

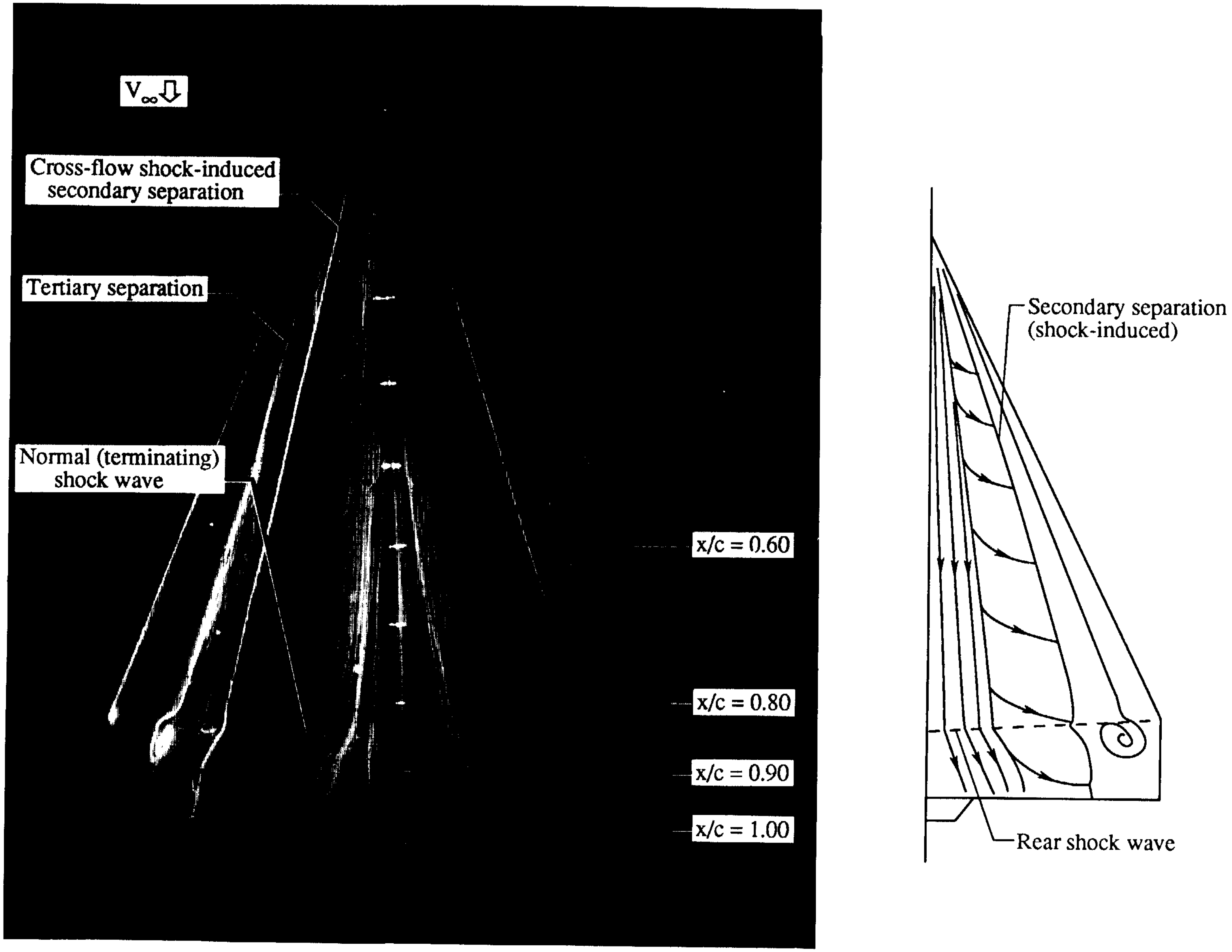

Figure 31. Wing upper surface oil flow pattern at $\alpha = 20°$ and $M_\infty = 0.85$ with LEX off.

ORIGINAL PAGE
BLACK AND WHITE PHOTOGRAPH

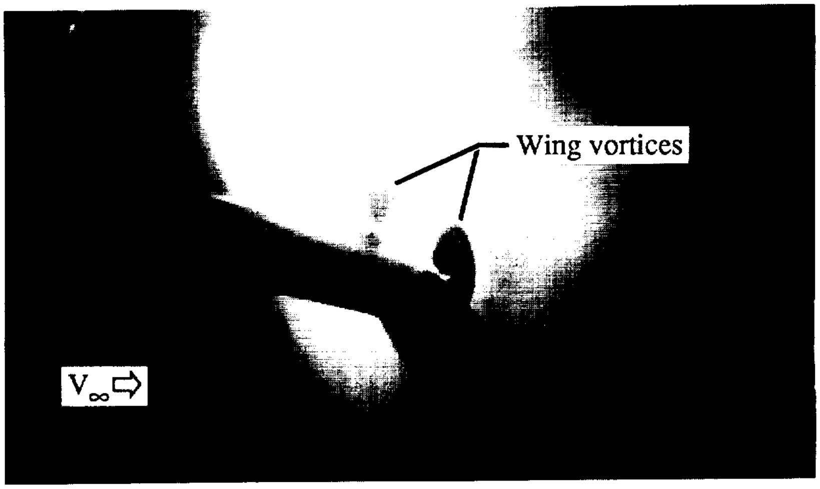

(a) $x/c = 0.60$.

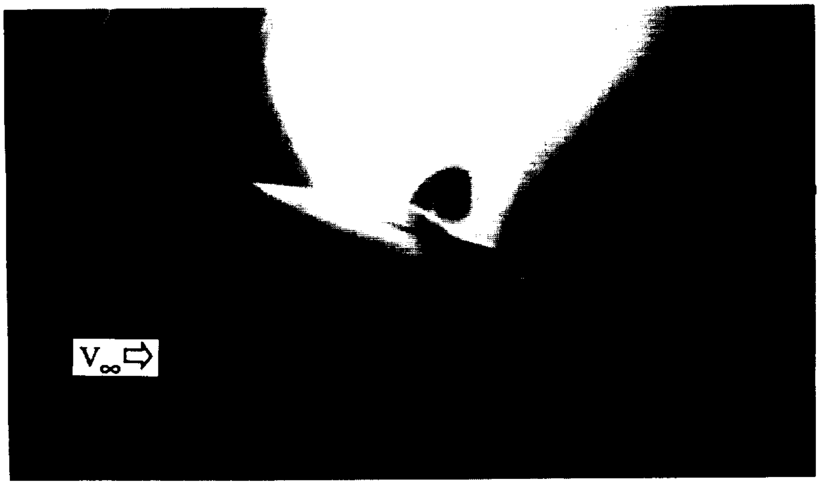

(b) $x/c = 0.80$.

Figure 32. Laser vapor screen flow visualizations at $\alpha = 20°$ and $M_\infty = 0.85$ with LEX off.

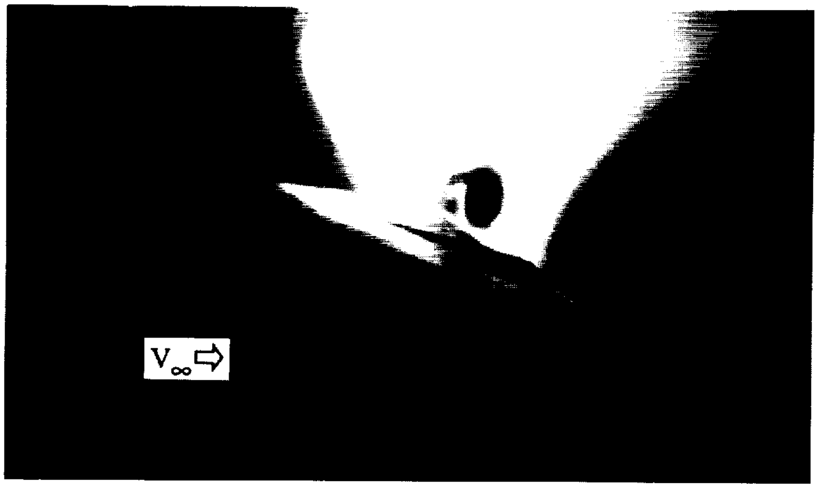

(c) $x/c = 0.90$.

(d) $x/c = 1.00$.

Figure 32. Concluded.

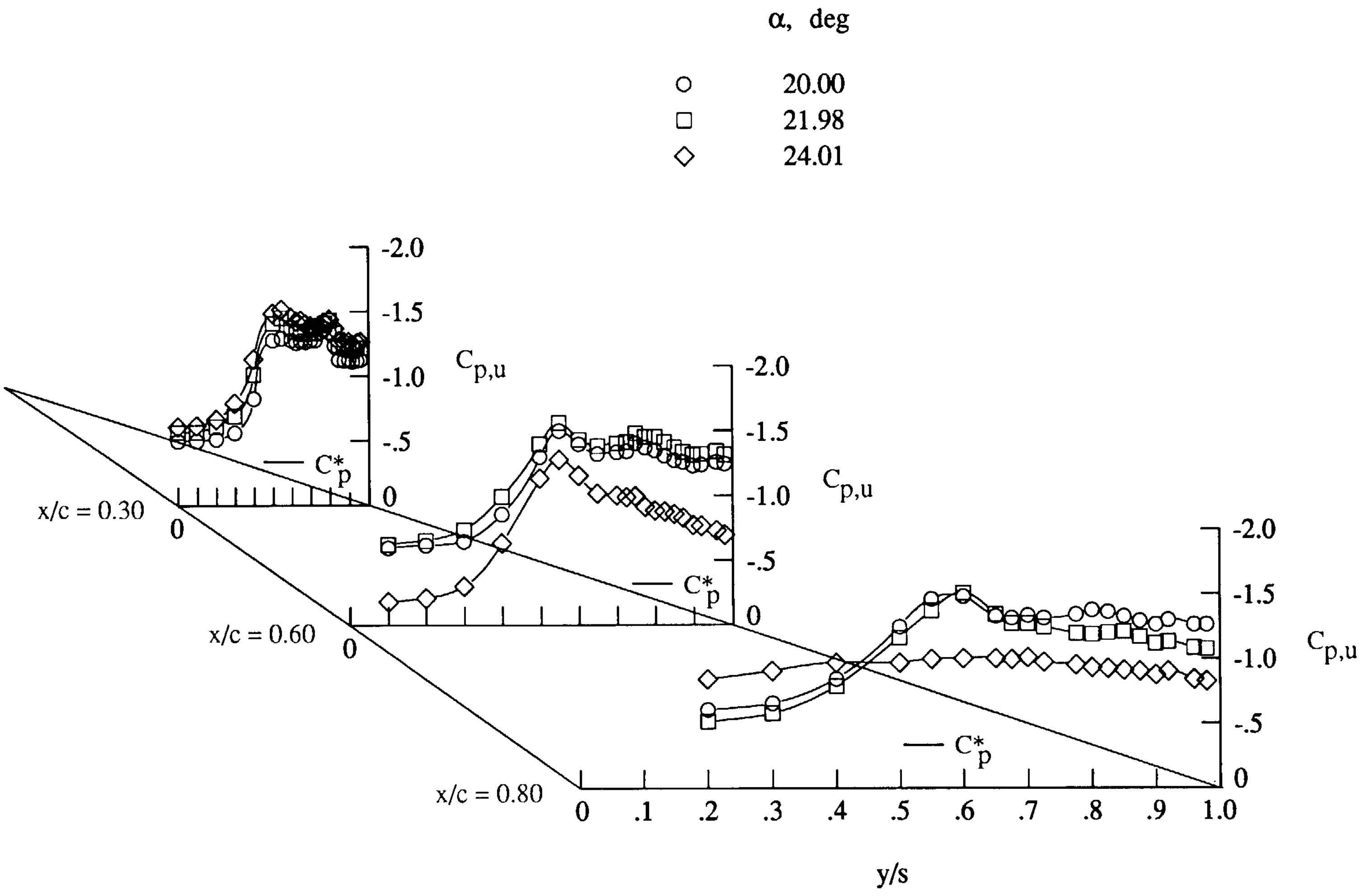

Figure 33. Wing upper surface static pressure distributions at $M_\infty = 0.85$ with LEX off.

ORIGINAL PAGE
BLACK AND WHITE PHOTOGRAPH

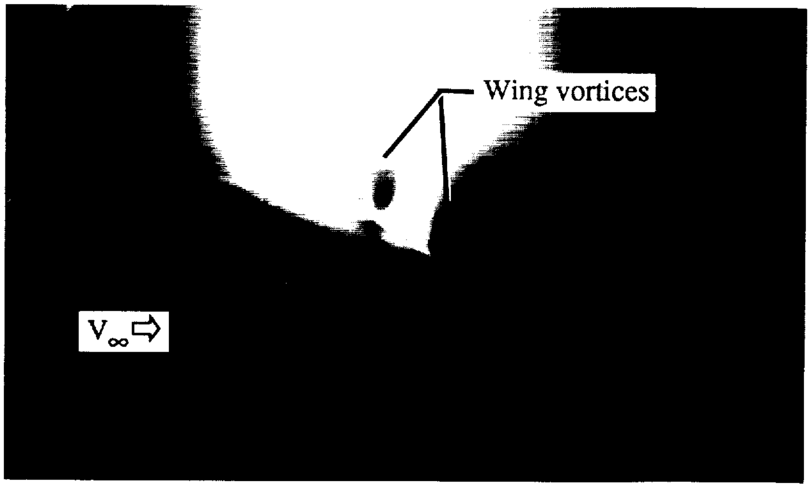

(a) $x/c = 0.60$.

(b) $x/c = 0.70$.

Figure 34. Laser vapor screen flow visualizations at $\alpha = 22°$ and $M_\infty = 0.85$ with LEX off.

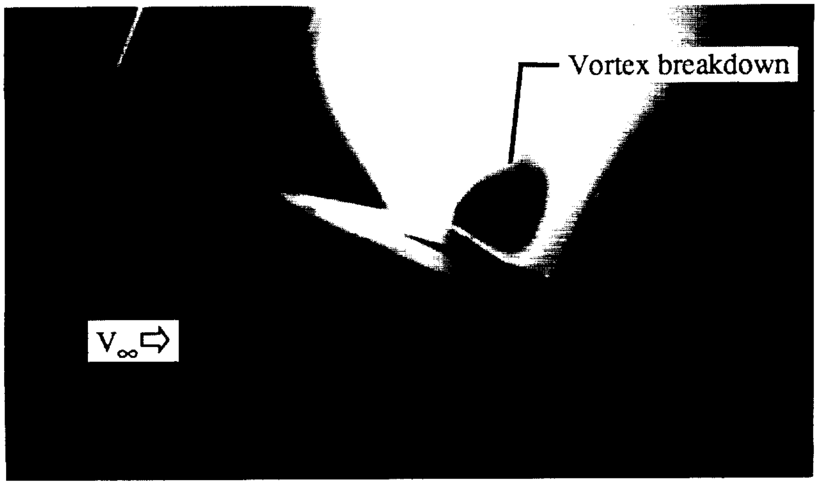

(c) $x/c = 0.90$.

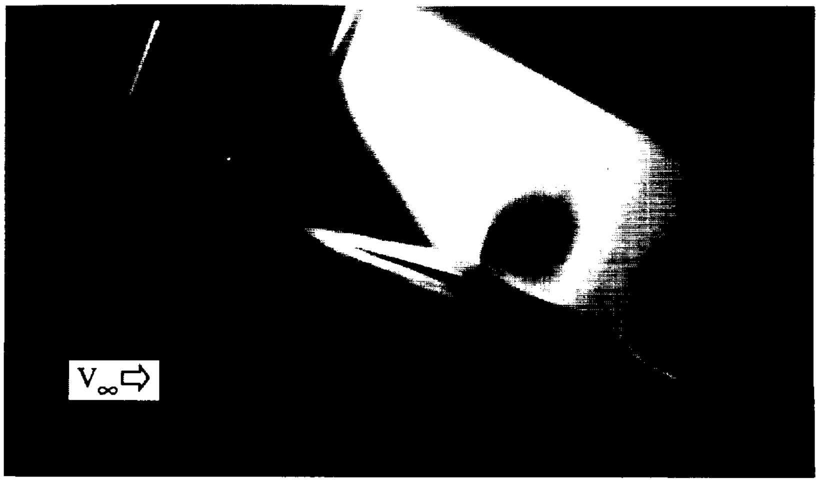

(d) $x/c = 1.00$.

Figure 34. Concluded.

ORIGINAL PAGE
BLACK AND WHITE PHOTOGRAPH

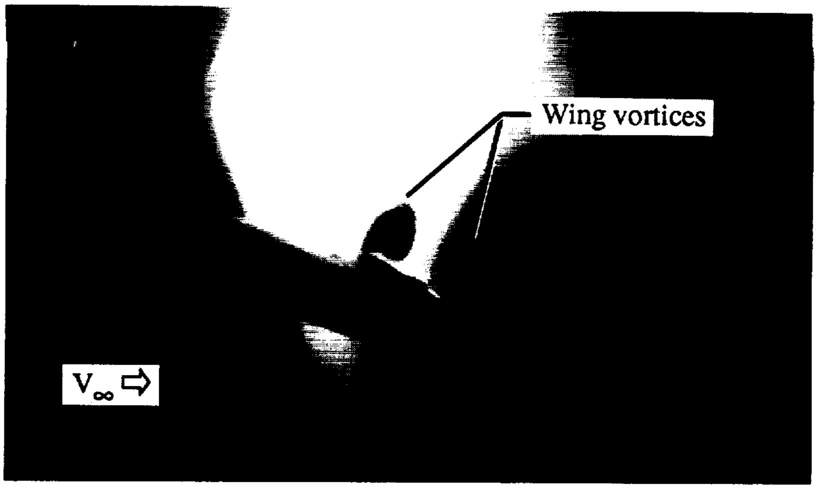

(a) $x/c = 0.60$.

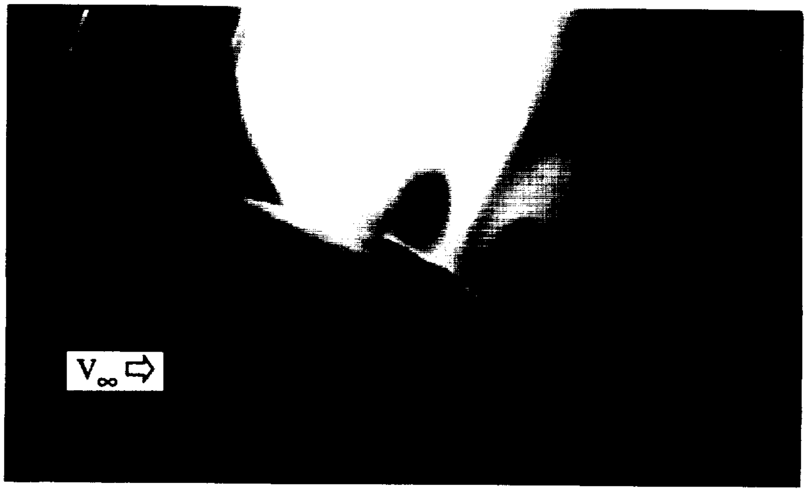

(b) $x/c = 0.70$.

Figure 35. Laser vapor screen flow visualizations at $\alpha = 24^\circ$ and $M_\infty = 0.85$ with LEX off.

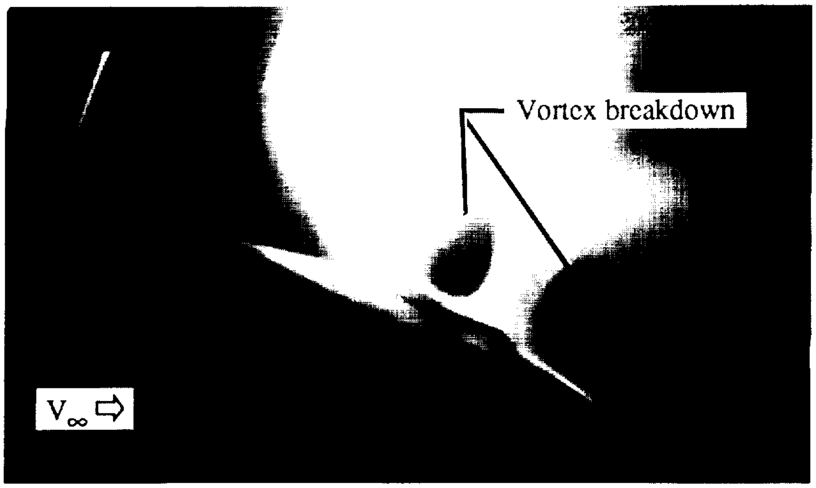

(c) $x/c = 0.80$.

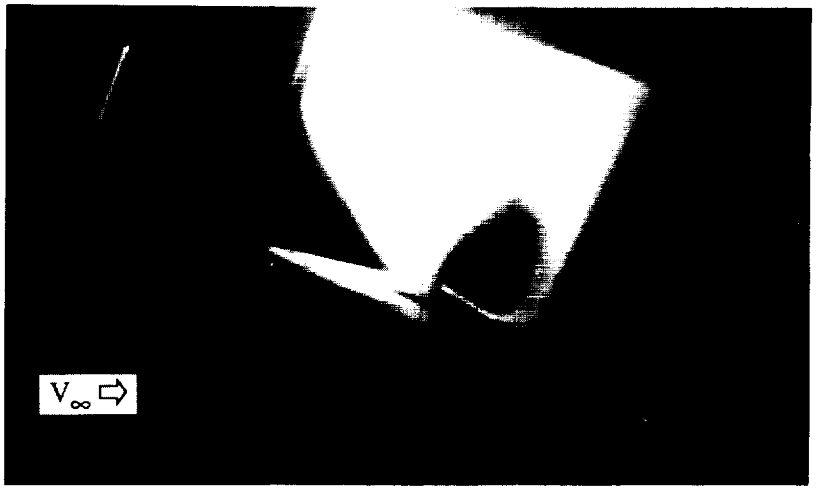

(d) $x/c = 0.90$.

Figure 35. Concluded.

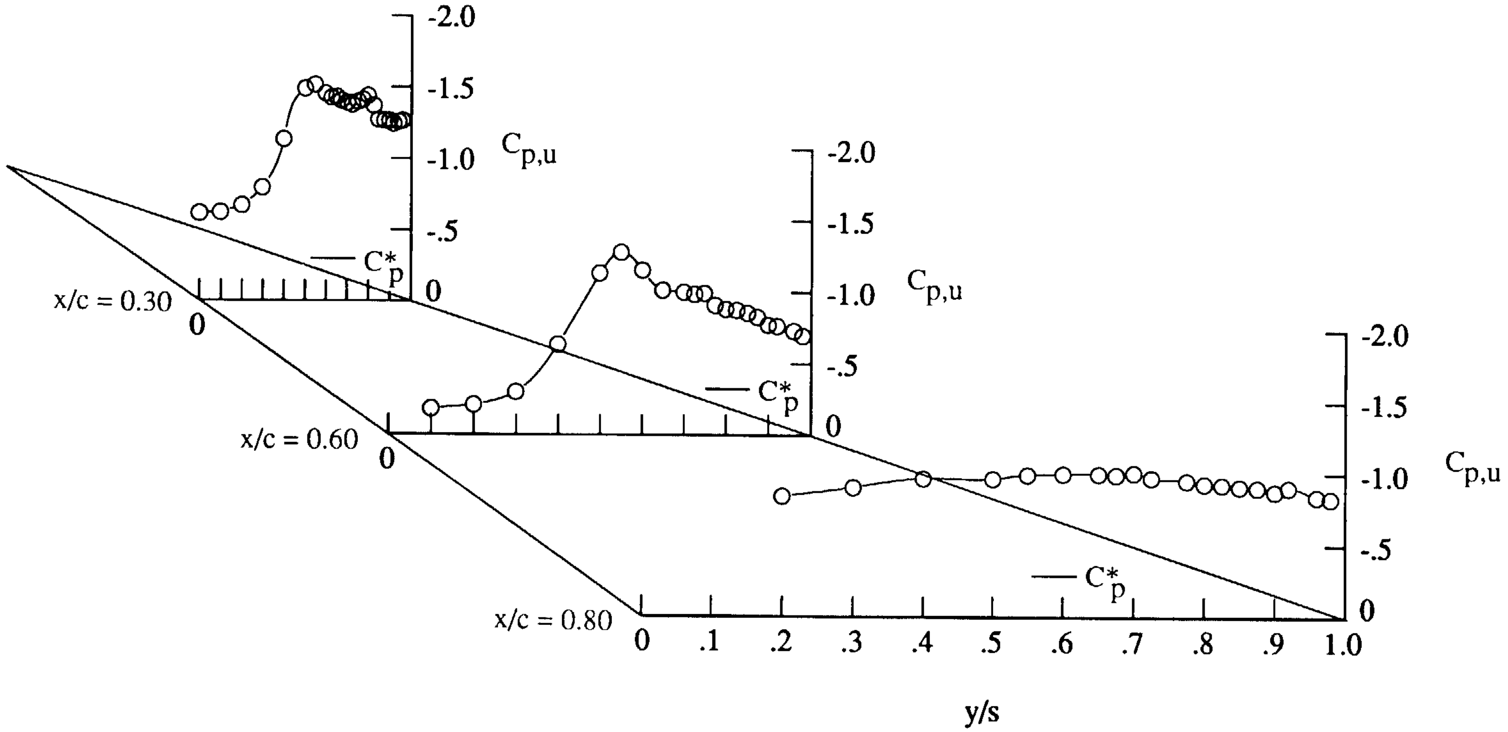

Figure 36. Wing upper surface static pressure distributions at $\alpha = 24°$ and $M_\infty = 0.85$ with LEX off.

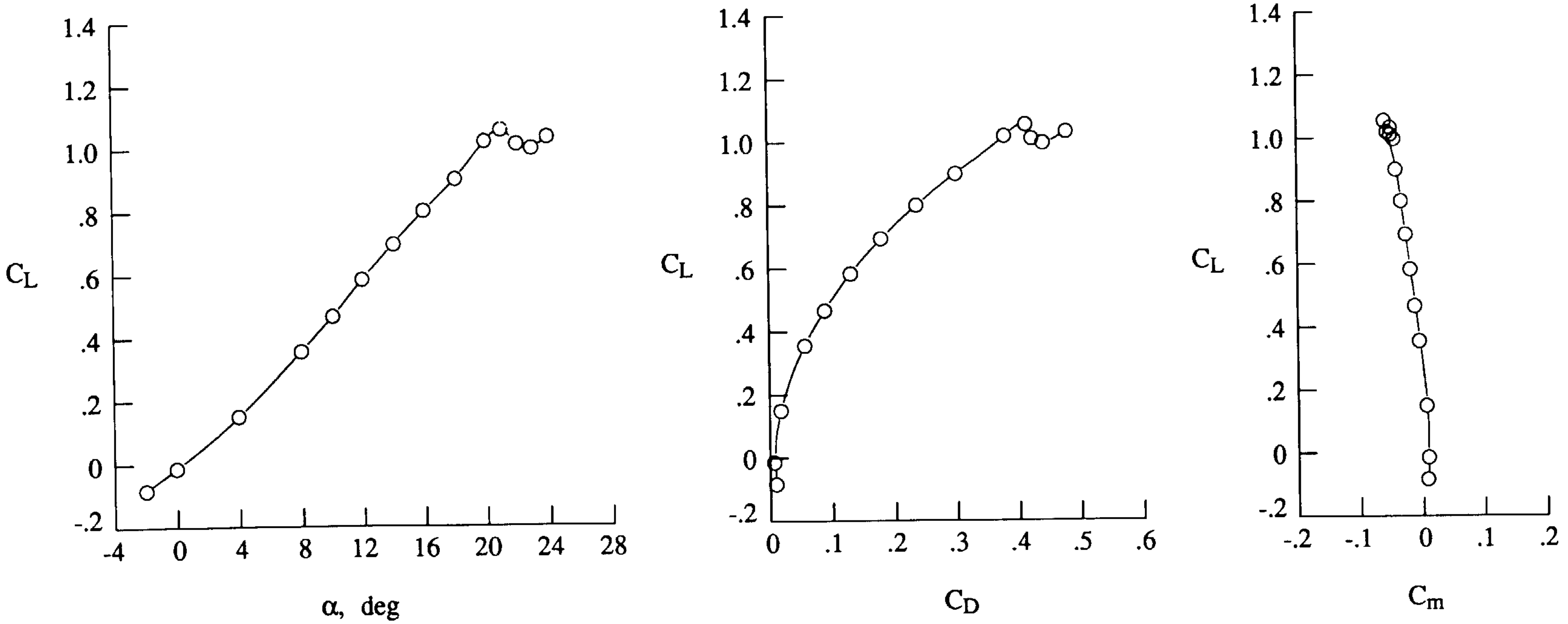

Figure 37. Lift, drag, and pitching-moment characteristics at $M_\infty = 0.85$ with LEX off.

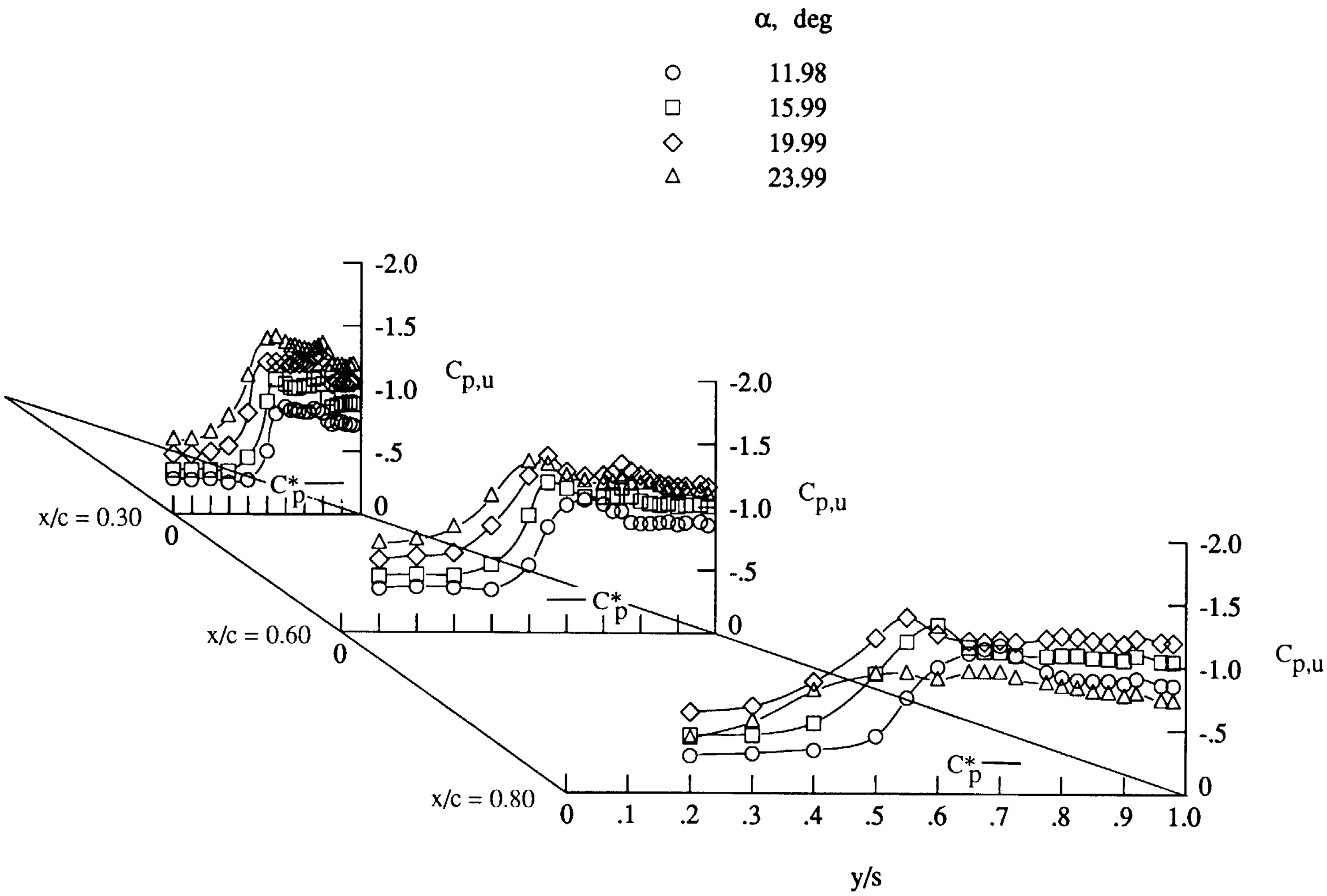

Figure 38. Wing upper surface static pressure distributions at $M_\infty = 0.90$ with LEX off.

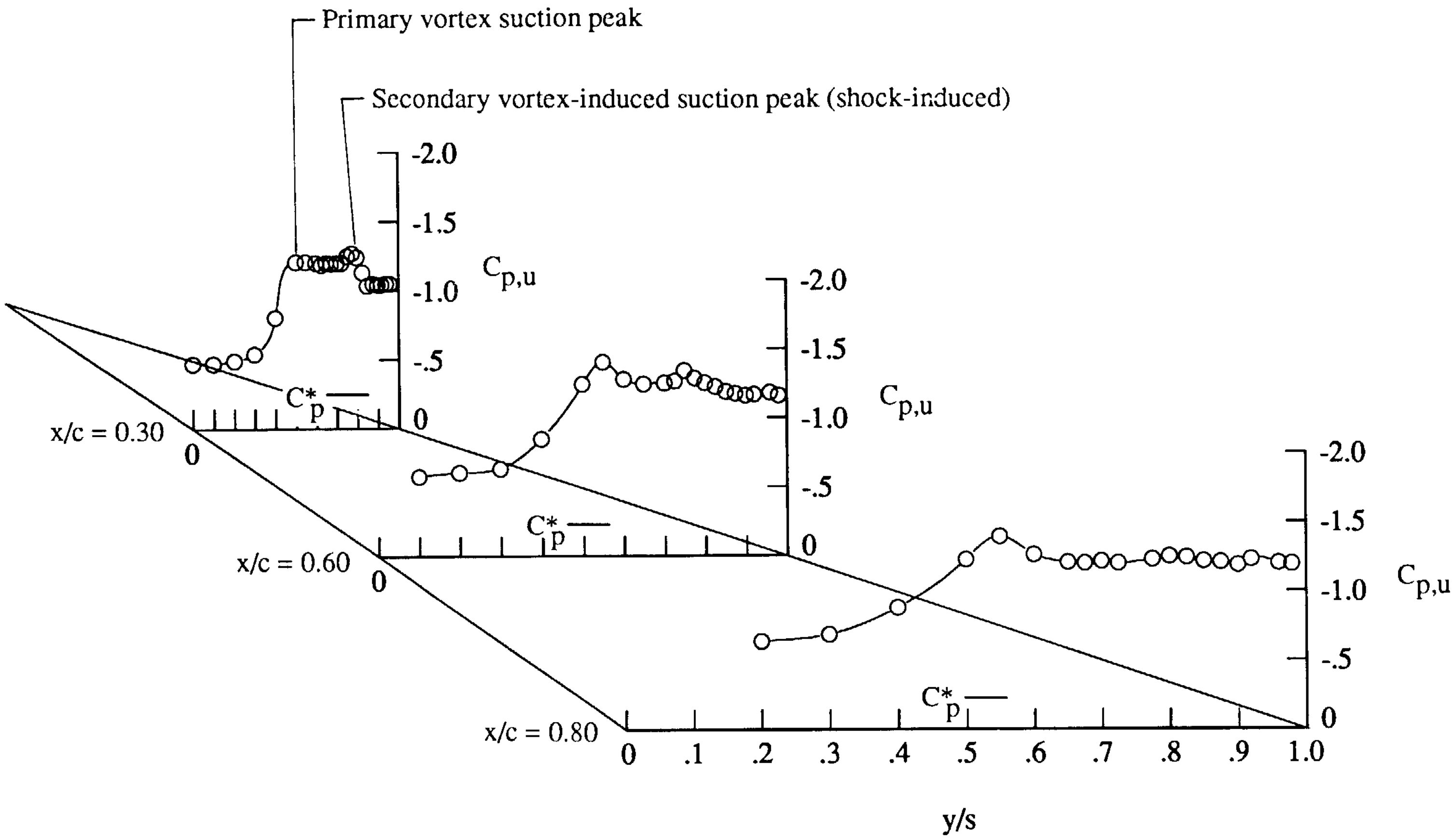

Figure 39. Wing upper surface static pressure distributions at $\alpha = 20°$ and $M_\infty = 0.90$ with LEX off.

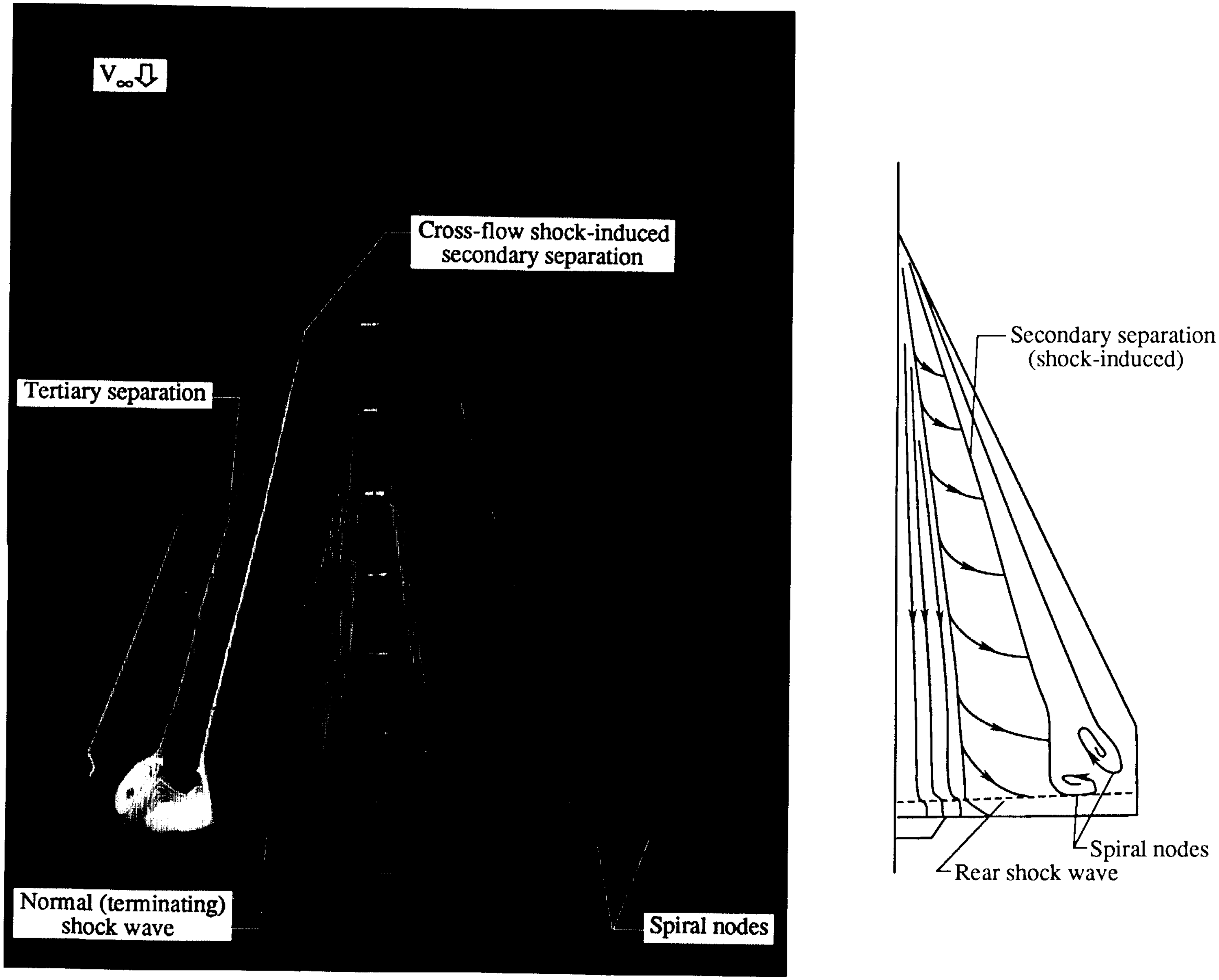

Figure 40. Wing upper surface oil flow pattern at $\alpha = 20^\circ$ and $M_\infty = 0.90$ with LEX off.

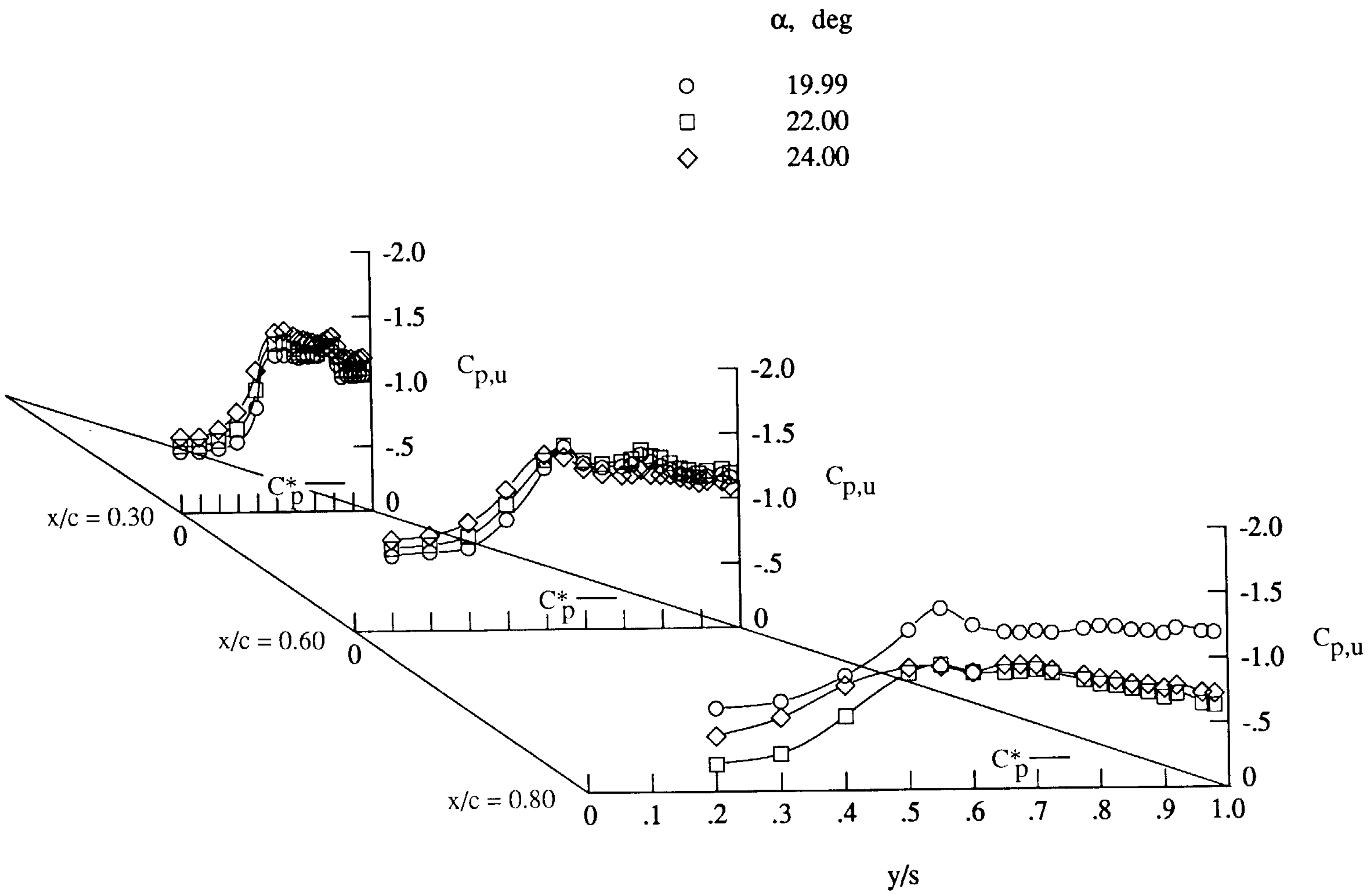

Figure 41. Wing upper surface static pressure distributions at $M_\infty = 0.90$ with LEX off.

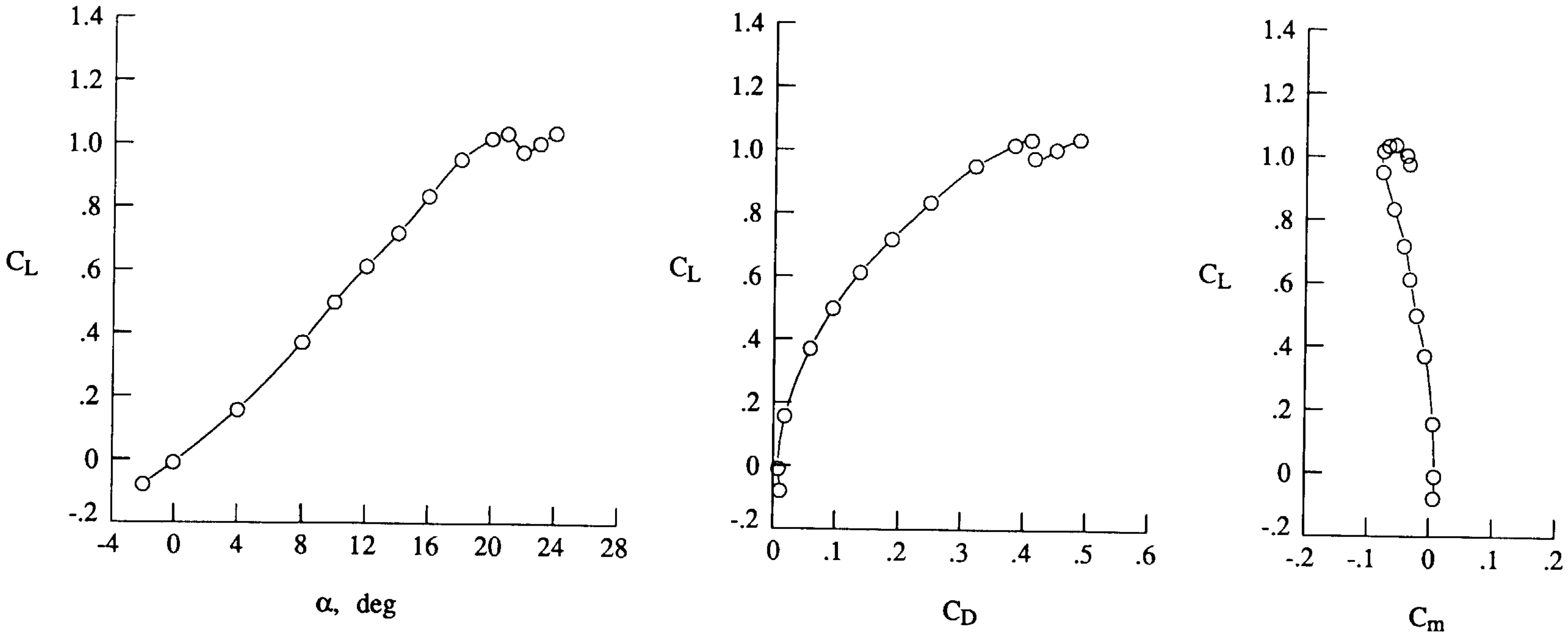

Figure 42. Lift, drag, and pitching-moment characteristics at $M_\infty = 0.90$ with LEX off.

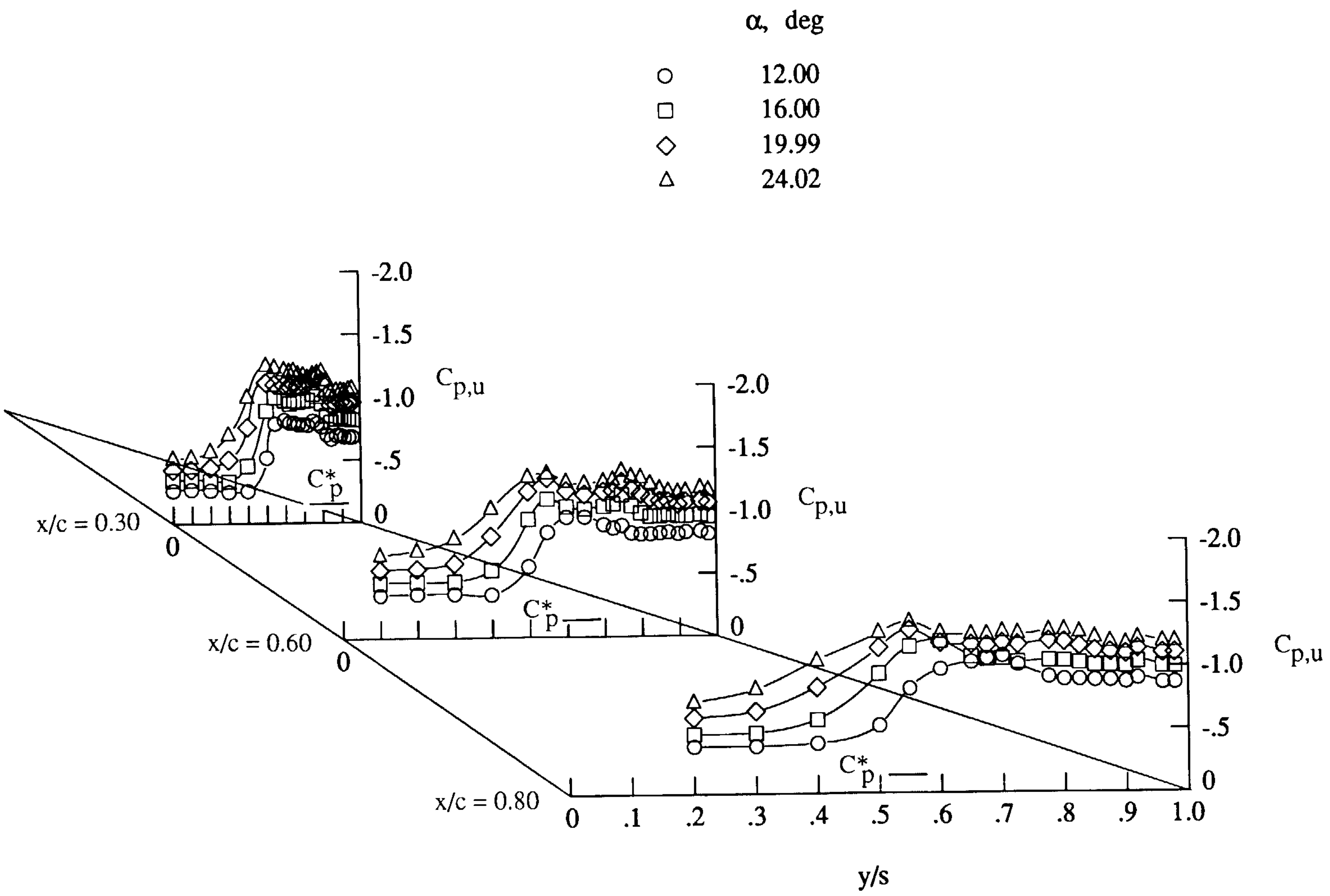

Figure 43. Wing upper surface static pressure distributions at $M_\infty = 0.95$ with LEX off.

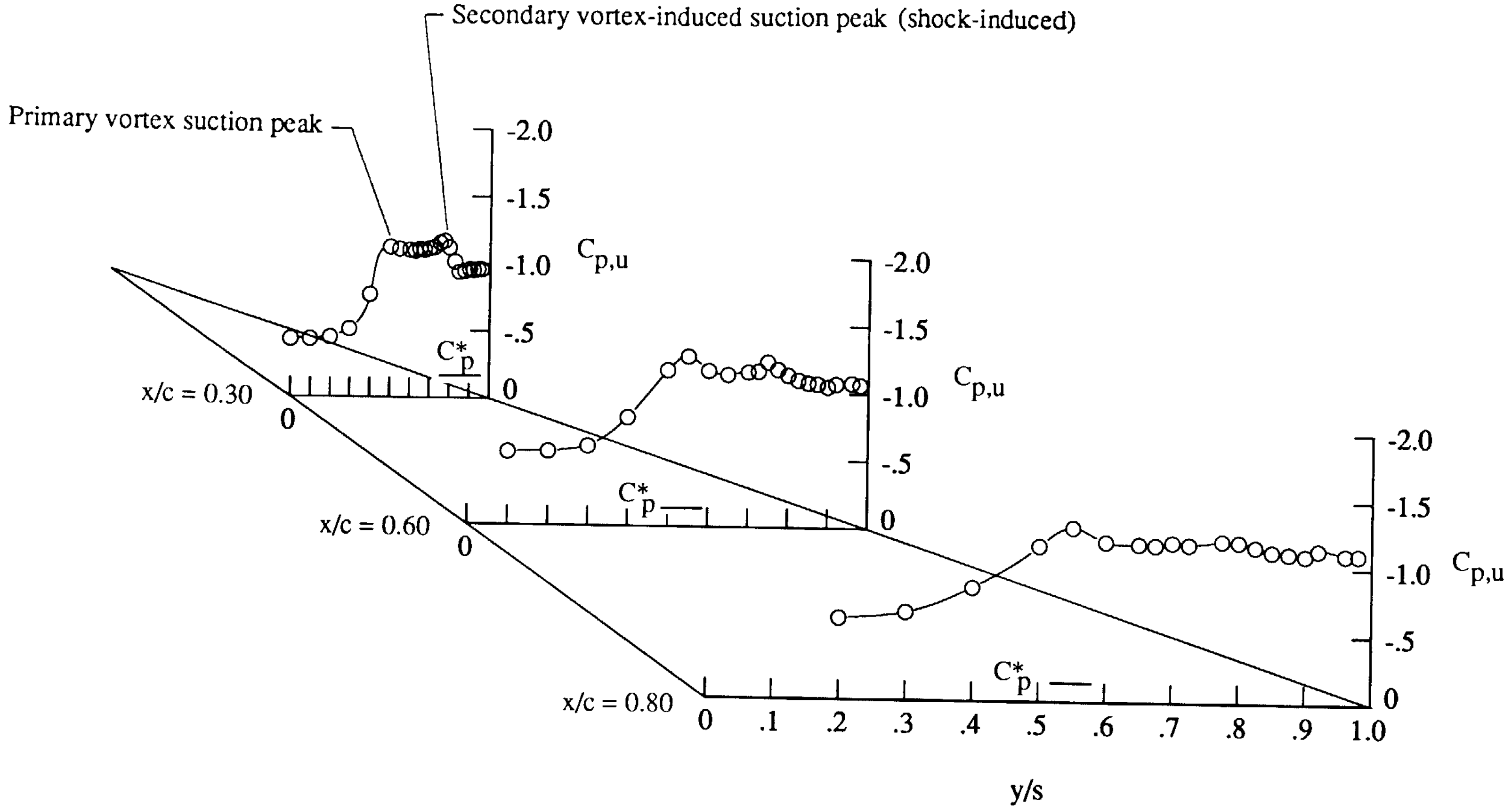

Figure 44. Wing upper surface static pressure distributions at $\alpha = 20°$ and $M_\infty = 0.95$ with LEX off.

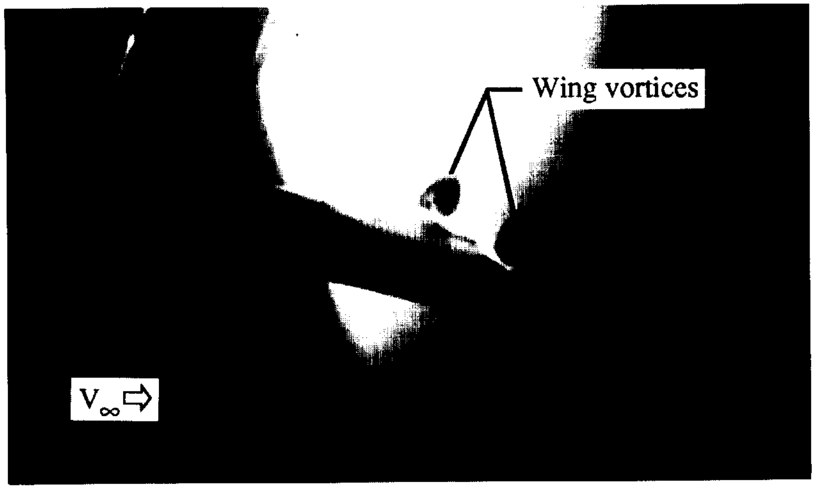

(a) $x/c = 0.60$.

(b) $x/c = 0.80$.

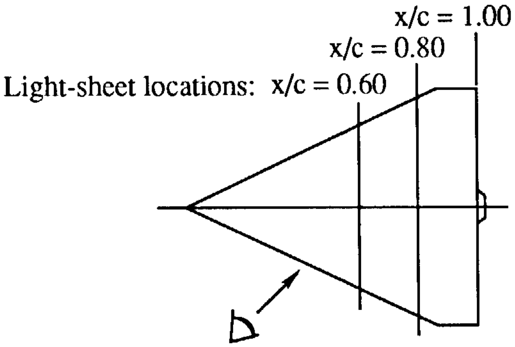

(c) $x/c = 1.00$.

Figure 45. Laser vapor screen flow visualizations at $\alpha = 20^\circ$ and $M_\infty = 0.95$ with LEX off.

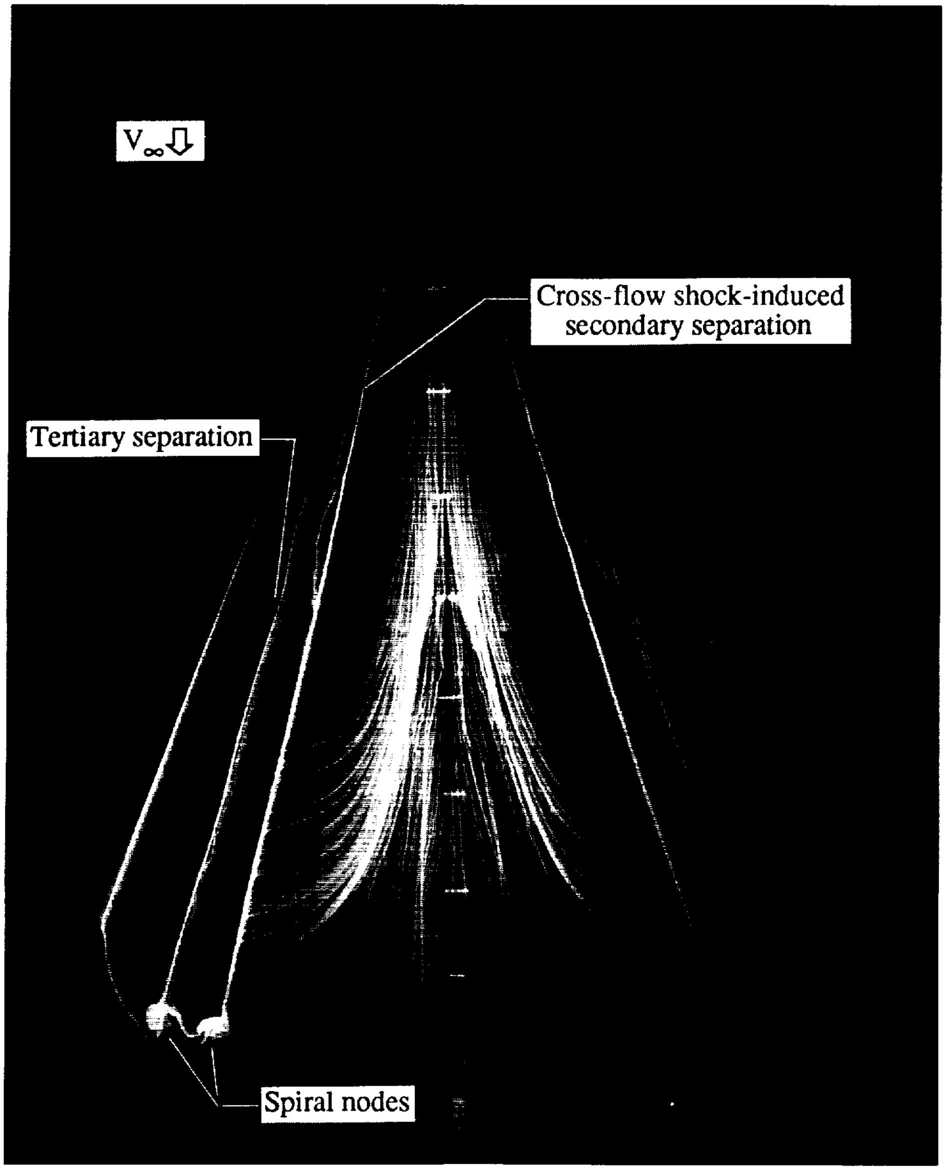

Figure 46. Wing upper surface oil flow pattern at $\alpha = 20°$ and $M_\infty = 0.95$ with LEX off.

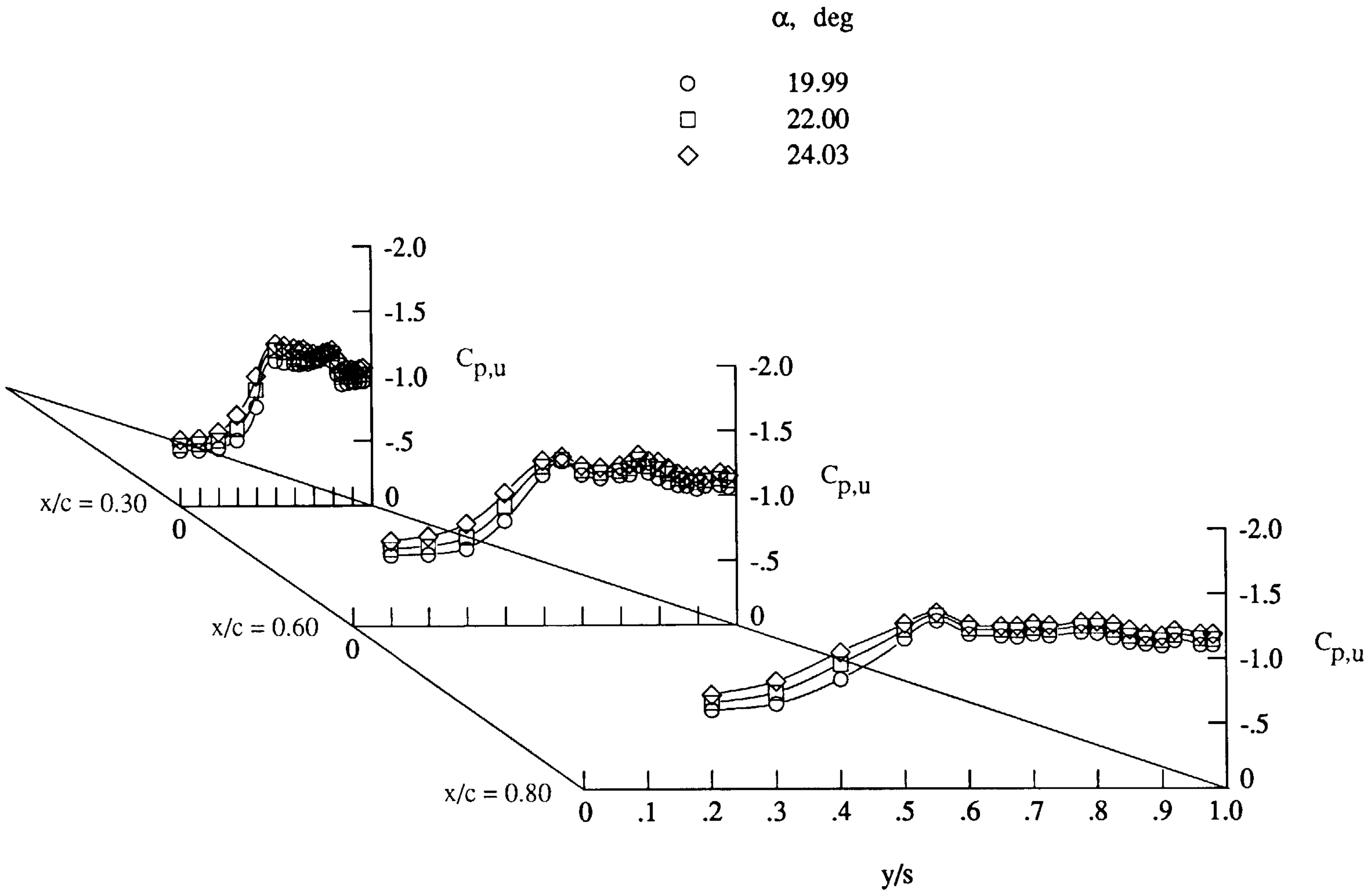

Figure 47. Wing upper surface static pressure distributions at $M_\infty = 0.95$ with LEX off.

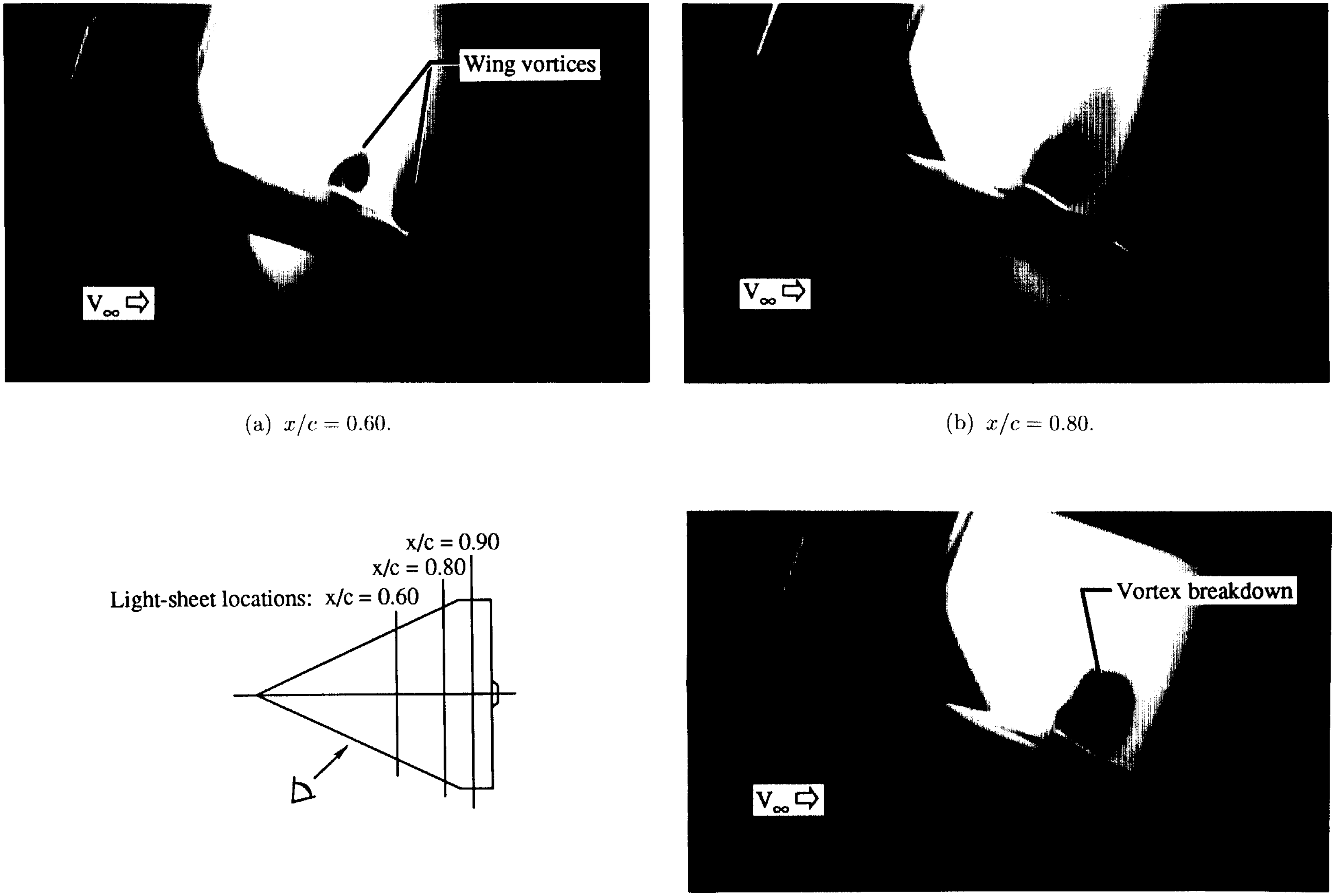

(a) $x/c = 0.60$.

(b) $x/c = 0.80$.

(c) $x/c = 0.90$.

Figure 48. Laser vapor screen flow visualizations at $\alpha = 24°$ and $M_\infty = 0.95$ with LEX off.

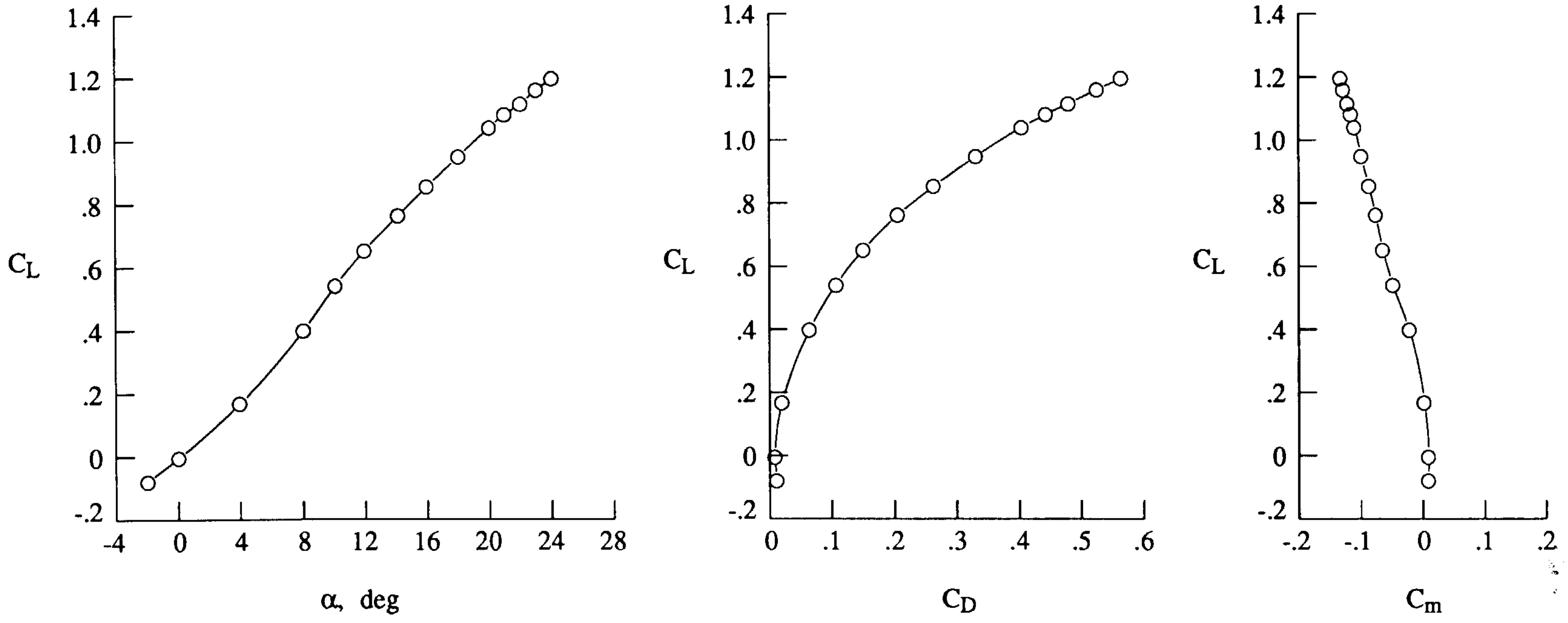

Figure 49. Lift, drag, and pitching-moment characteristics at $M_\infty = 0.95$ with LEX off.

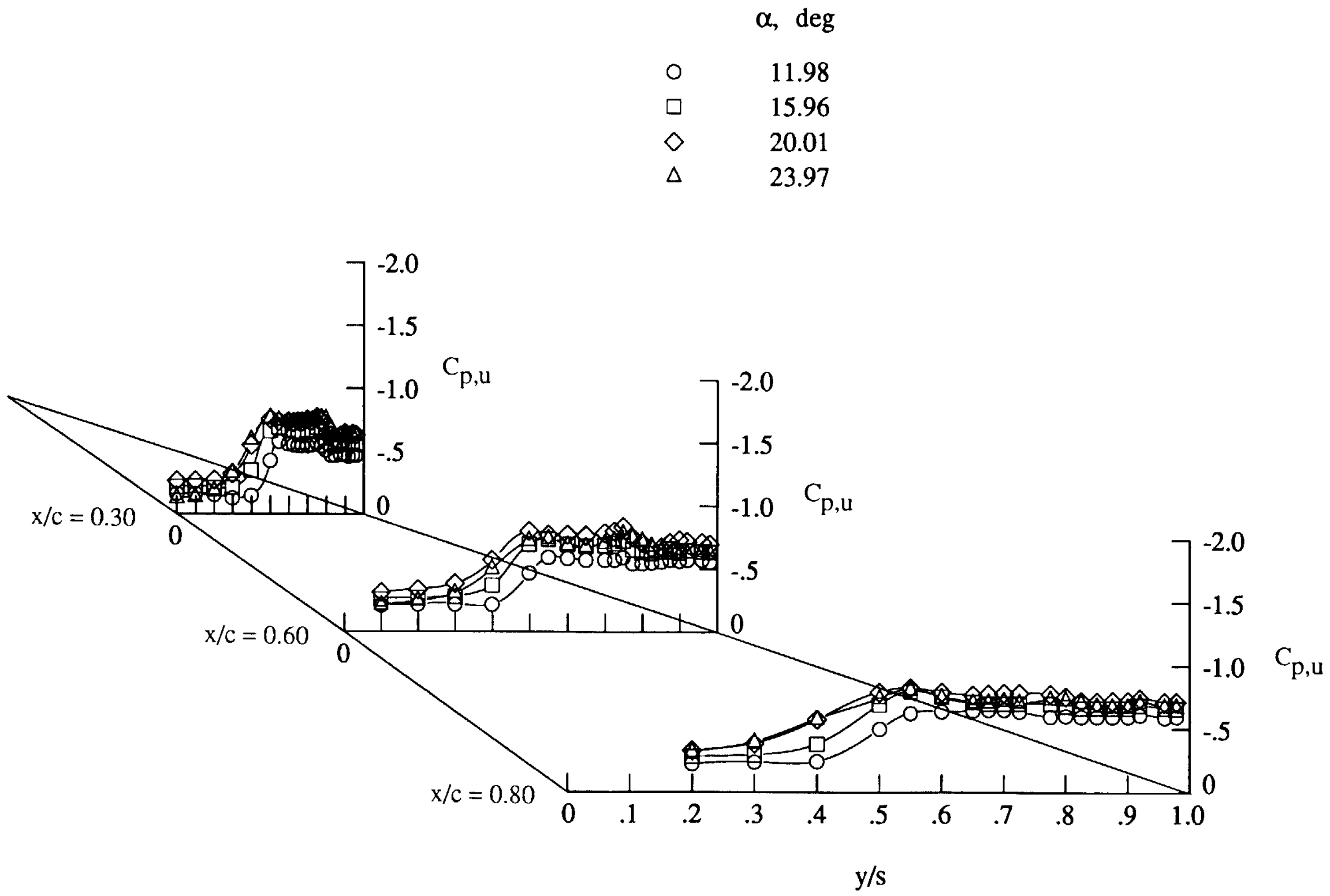

Figure 50. Wing upper surface static pressure distributions at $M_\infty = 1.20$ with LEX off.

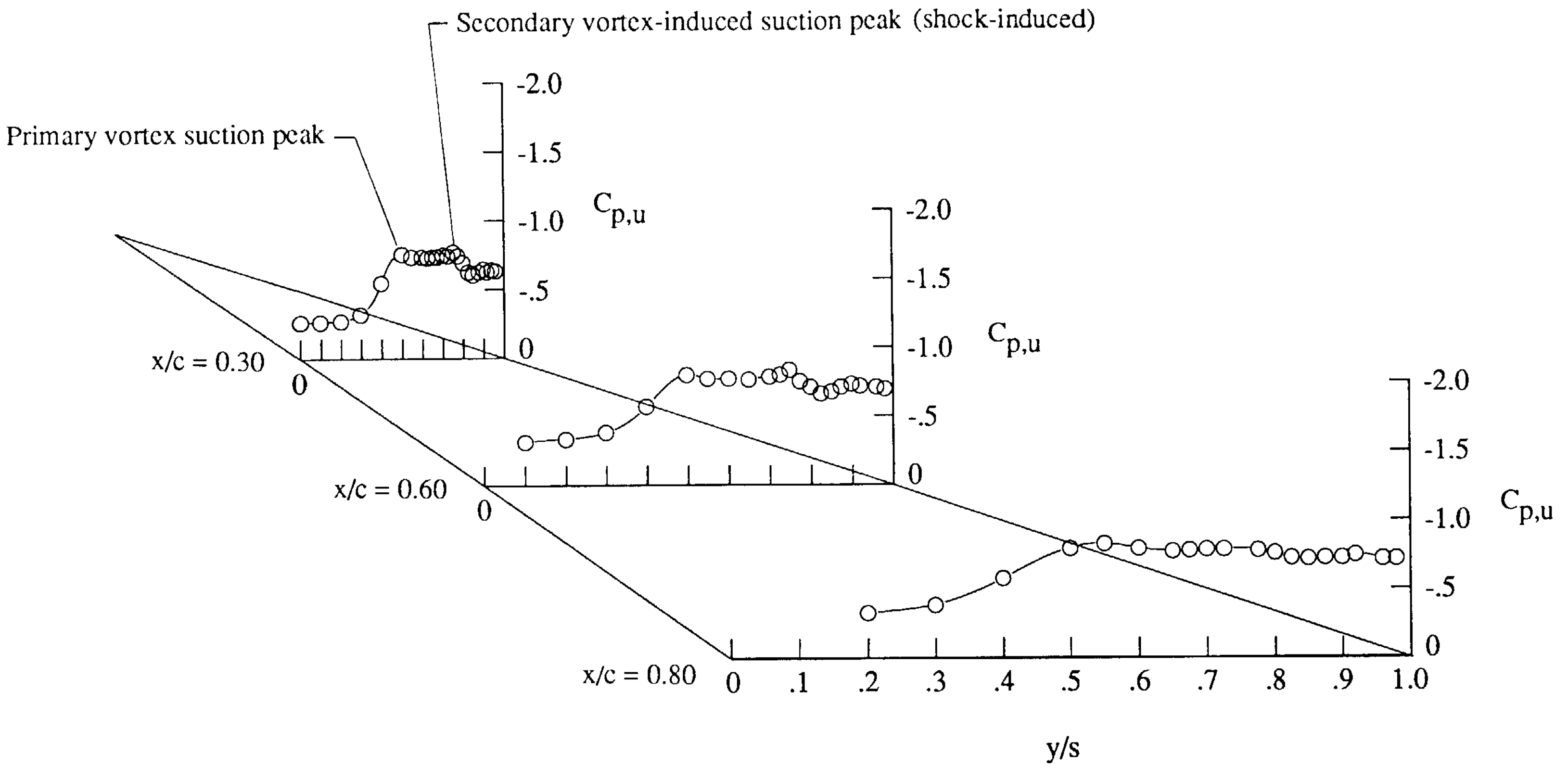

Figure 51. Wing upper surface static pressure distributions at $\alpha = 20°$ and $M_\infty = 1.20$ with LEX off.

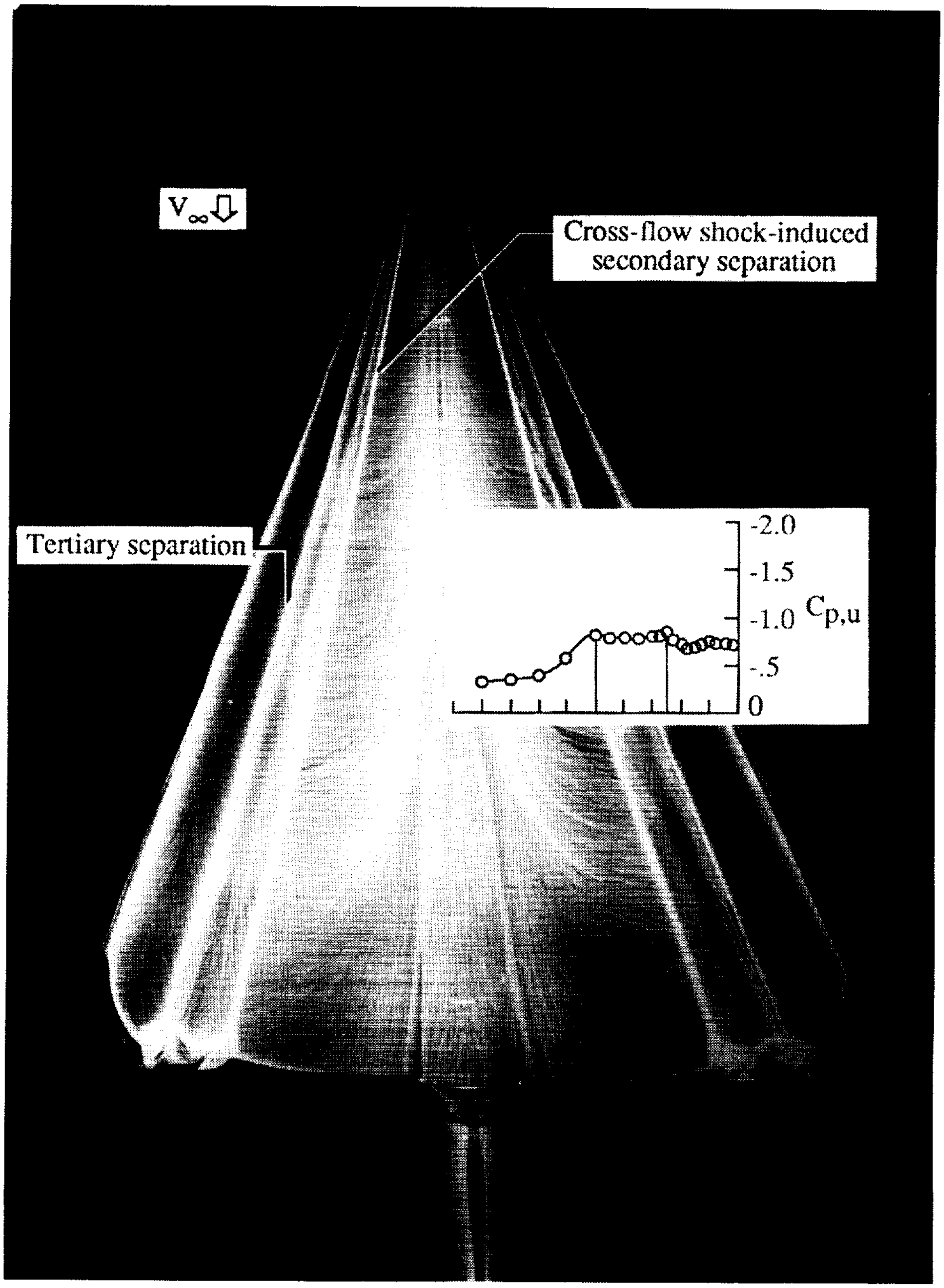

Figure 52. Wing upper surface oil flow pattern at $\alpha = 20°$ and $M_\infty = 1.20$ with LEX off.

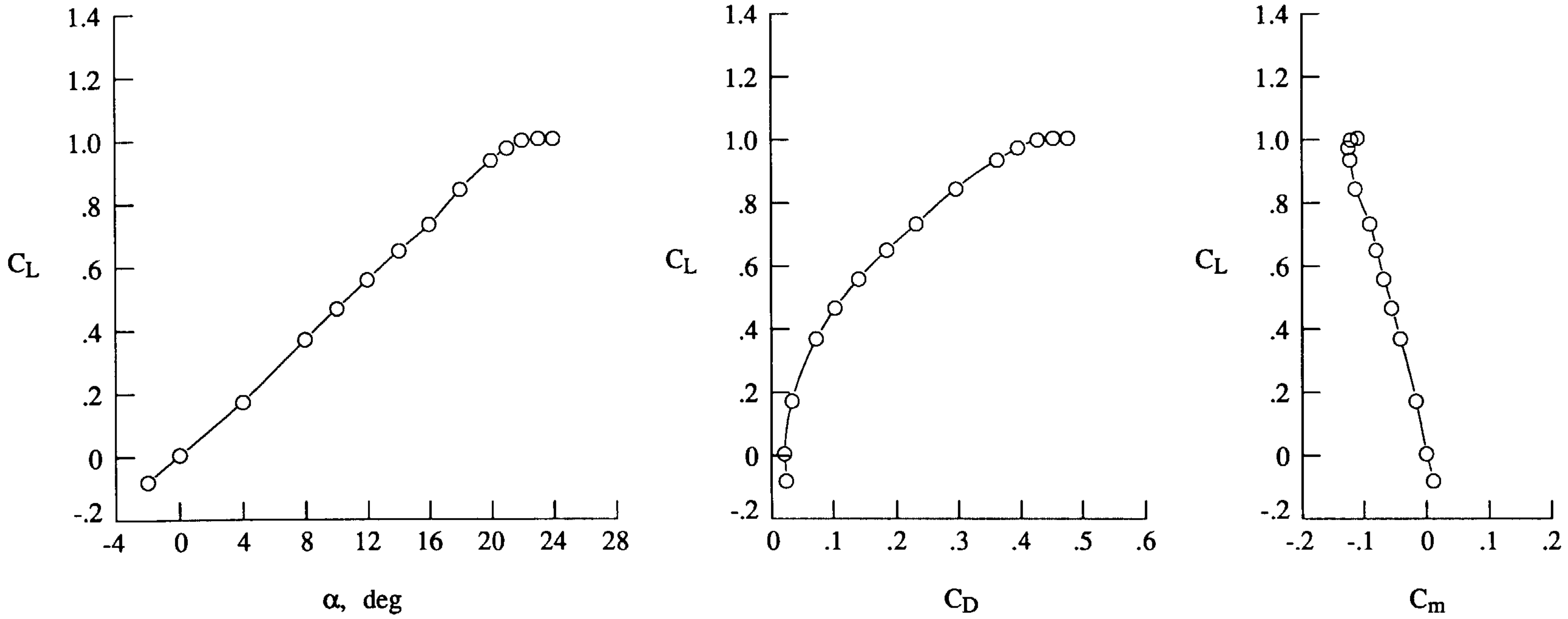

Figure 53. Lift, drag, and pitching-moment characteristics at $M_\infty = 1.20$ with LEX off.

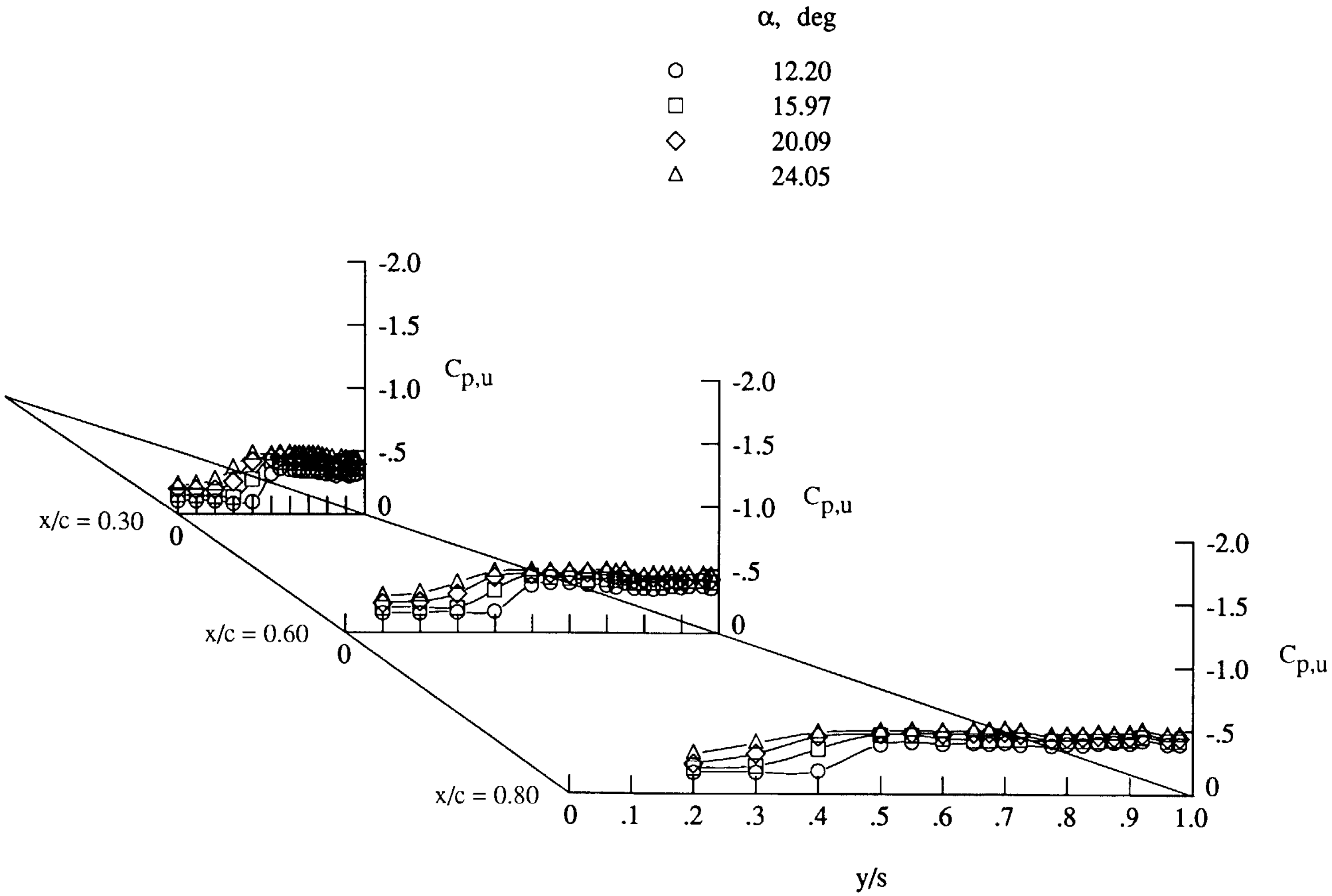

Figure 54. Wing upper surface static pressure distributions at $M_\infty = 1.60$ with LEX off.

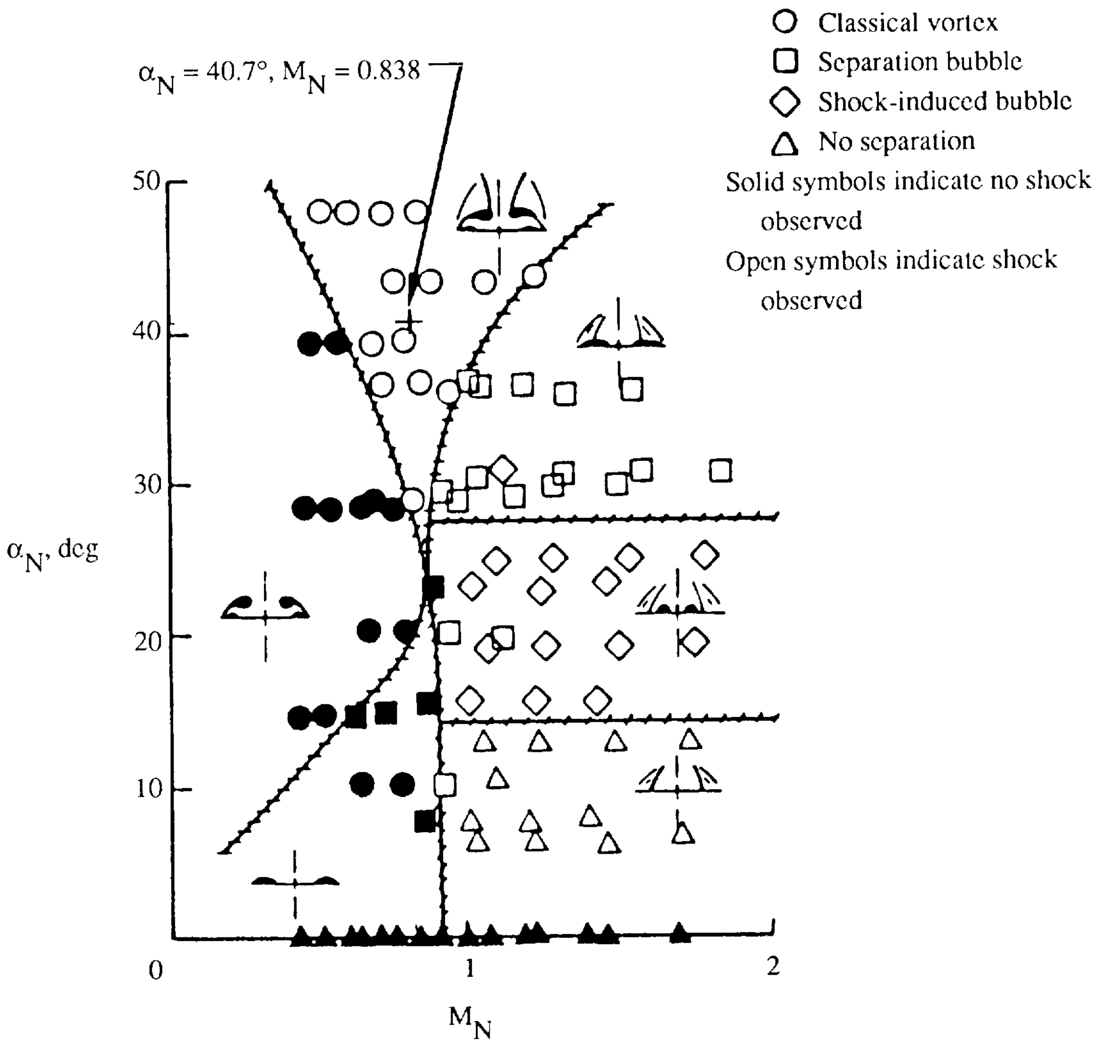

Figure 55. Classification of test data (ref. 18).

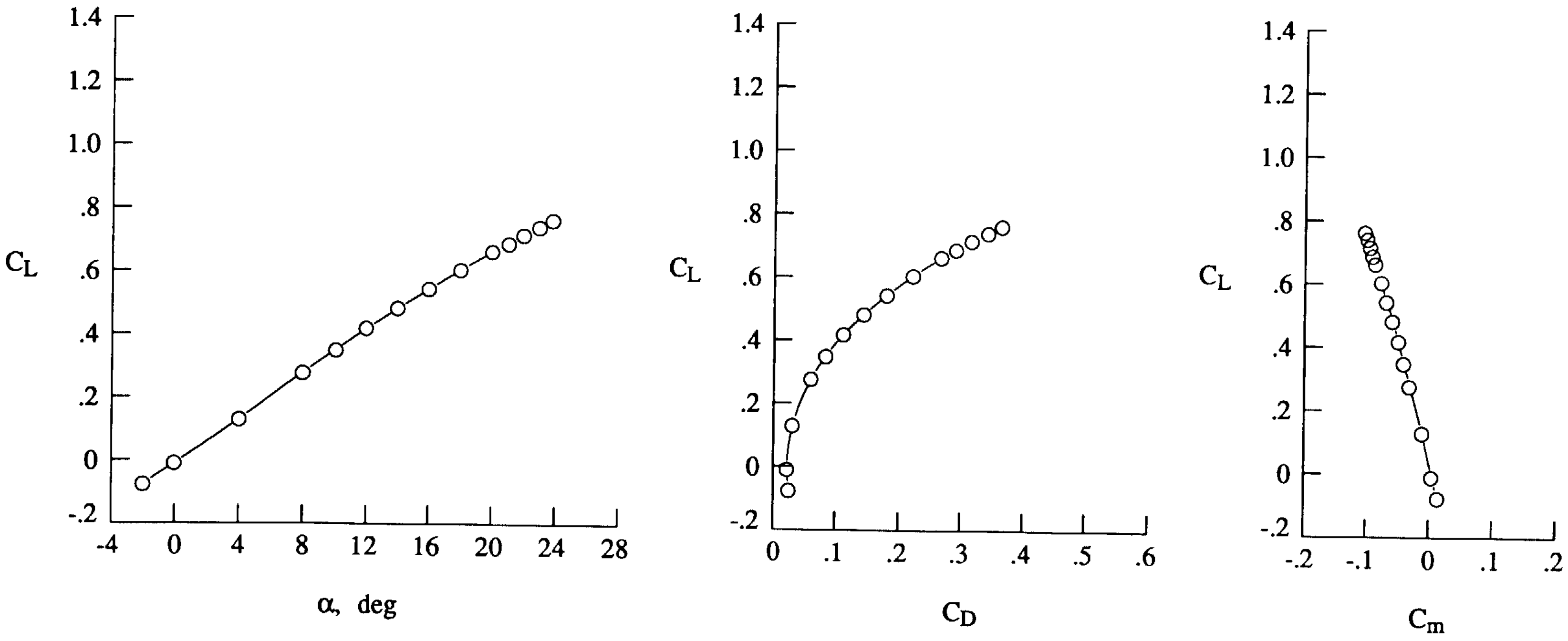

Figure 56. Lift, drag, and pitching-moment characteristics at $M_\infty = 1.60$ with LEX off.

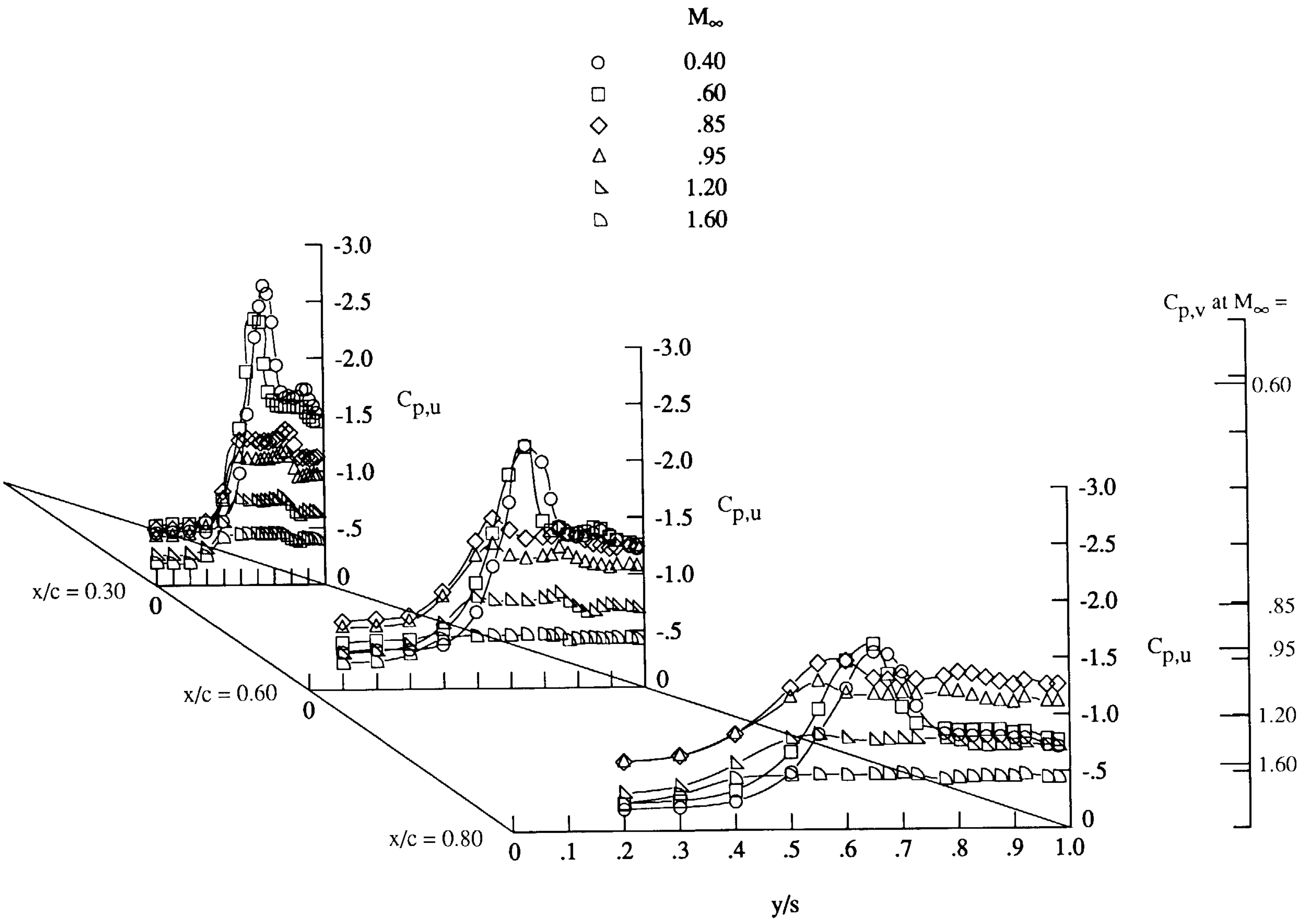

Figure 57. Mach number effect on wing upper surface static pressure distributions at $\alpha = 20°$ with LEX off.

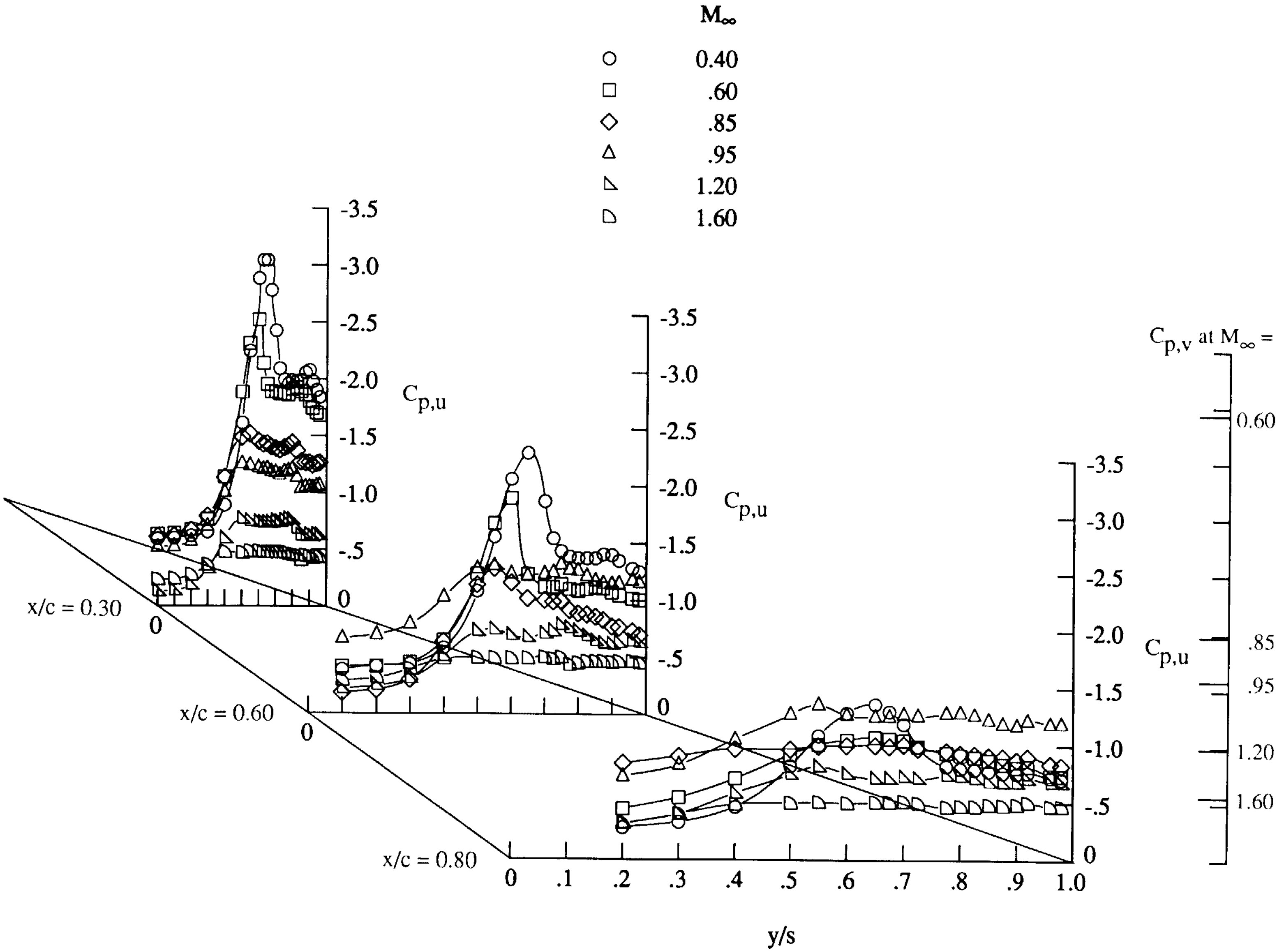

Figure 58. Mach number effect on wing upper surface static pressure distributions at $\alpha = 24°$ with LEX off.

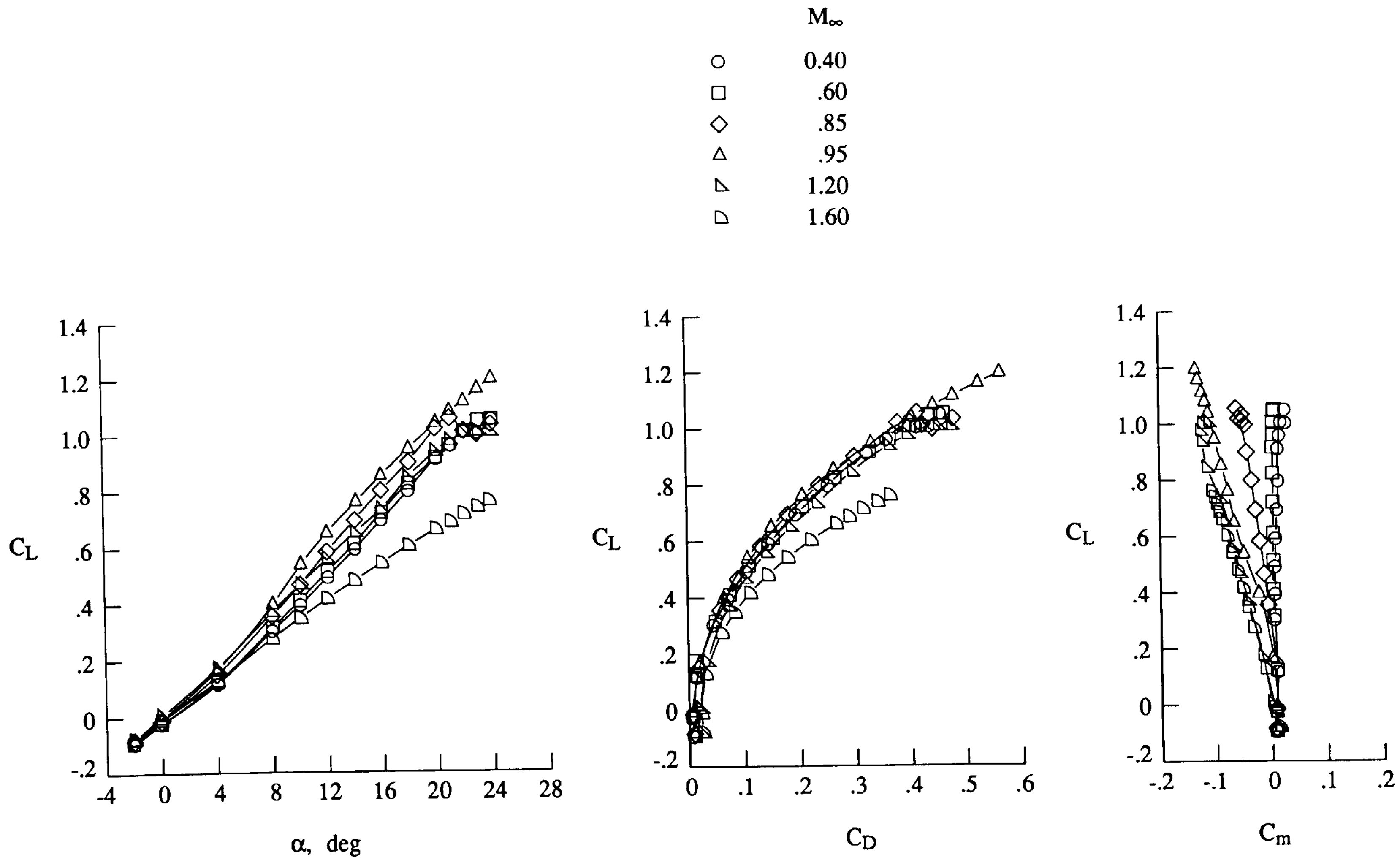

Figure 59. Mach number effect on lift, drag, and pitching-moment characteristics with LEX off.

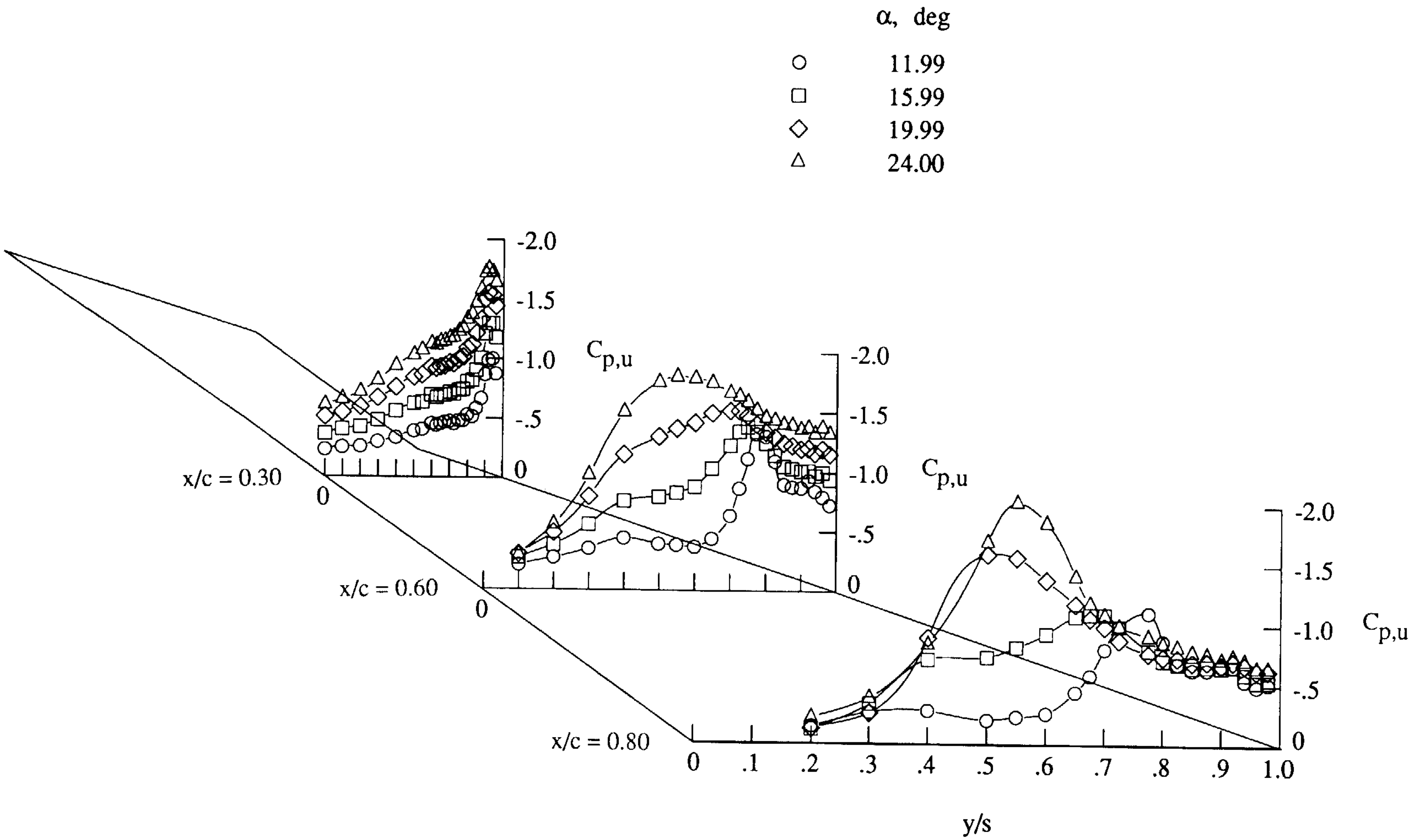

Figure 60. Wing upper surface static pressure distributions at $M_\infty = 0.40$ with LEX on.

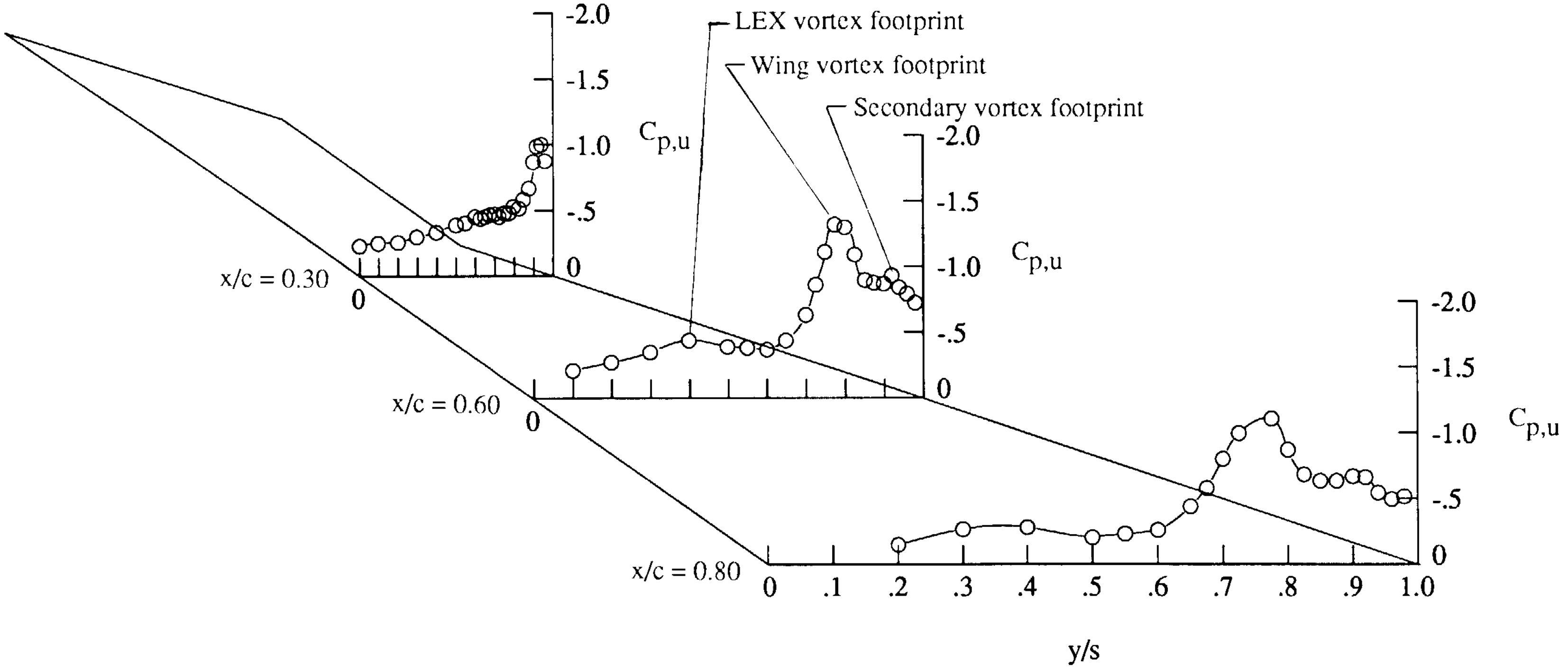

Figure 61. Wing upper surface static pressure distributions at $\alpha = 12°$ and $M_\infty = 0.40$ with LEX on.

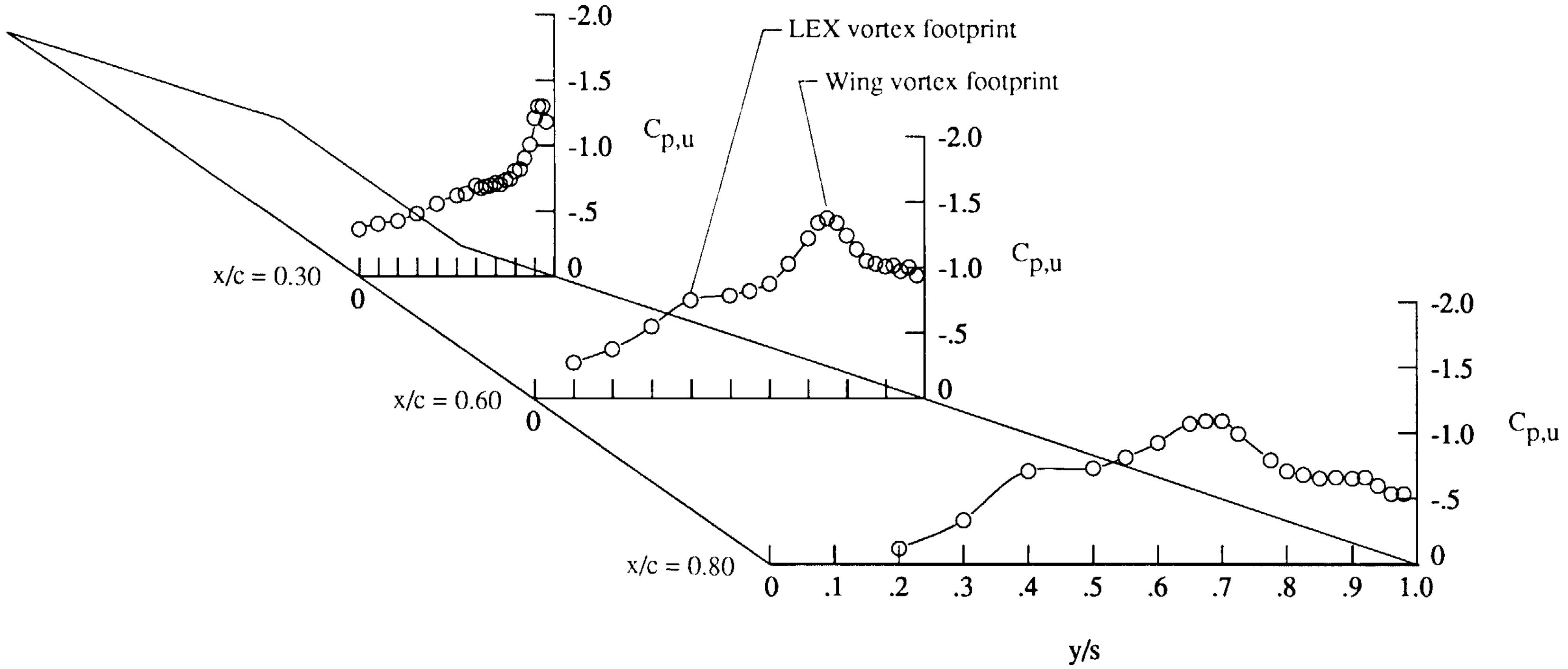

Figure 62. Wing upper surface static pressure distributions at $\alpha = 16°$ and $M_\infty = 0.40$ with LEX on.

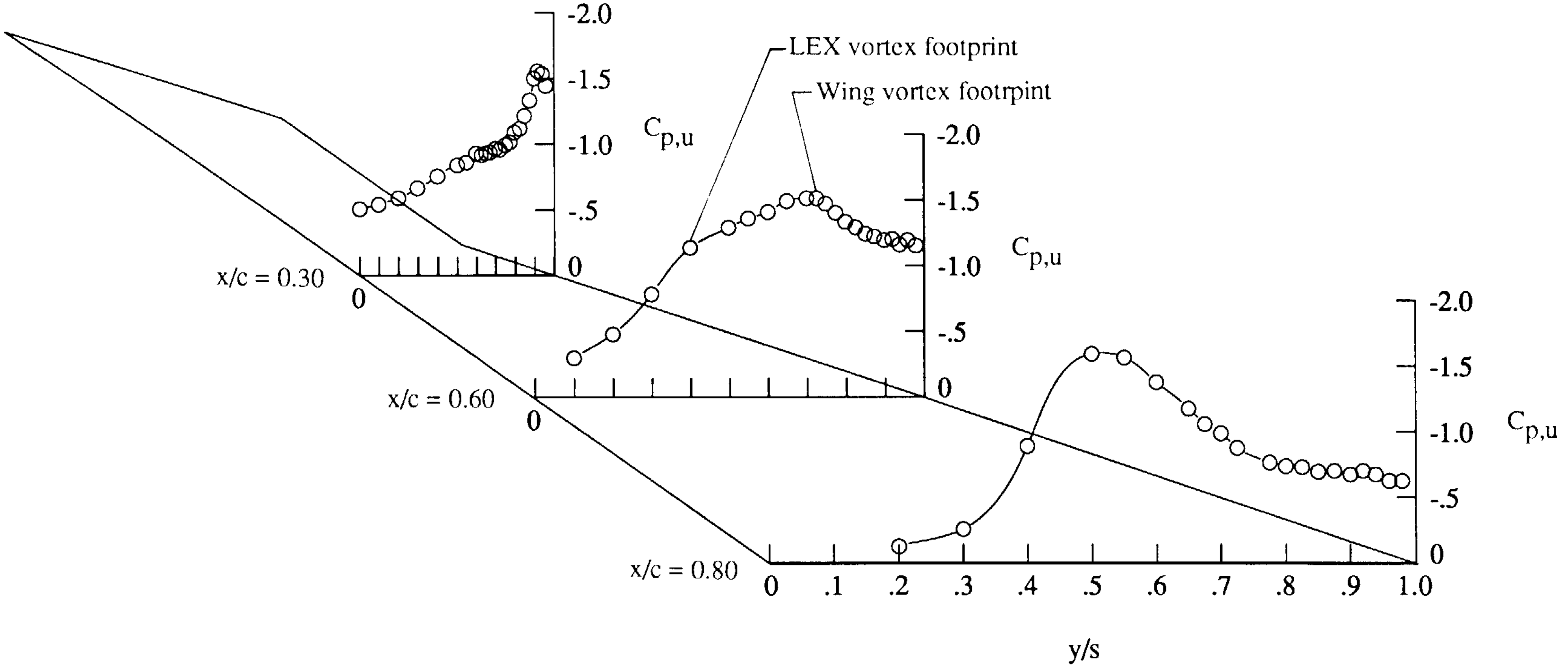

Figure 63. Wing upper surface static pressure distributions at $\alpha = 20°$ and $M_\infty = 0.40$ with LEX on.

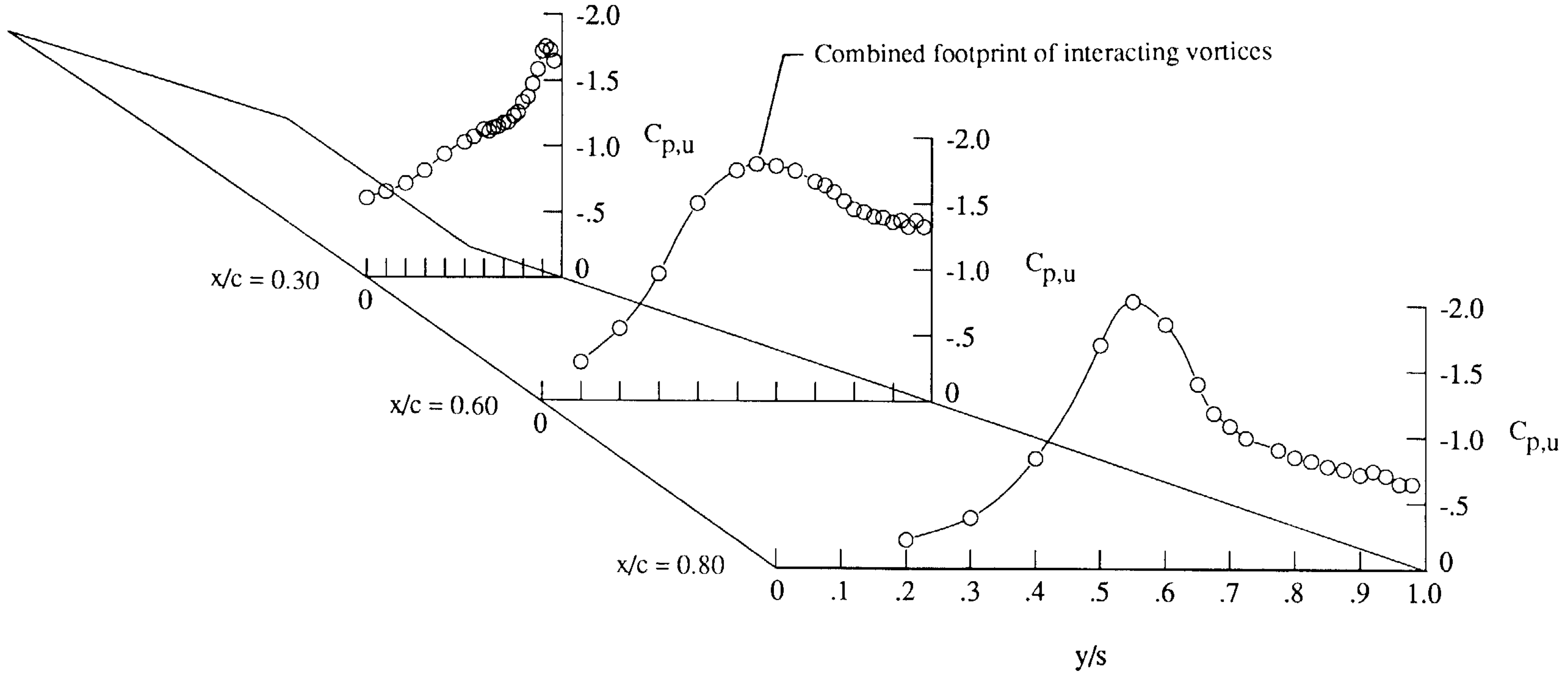

Figure 64. Wing upper surface static pressure distributions at $\alpha = 24°$ and $M_\infty = 0.40$ with LEX on.

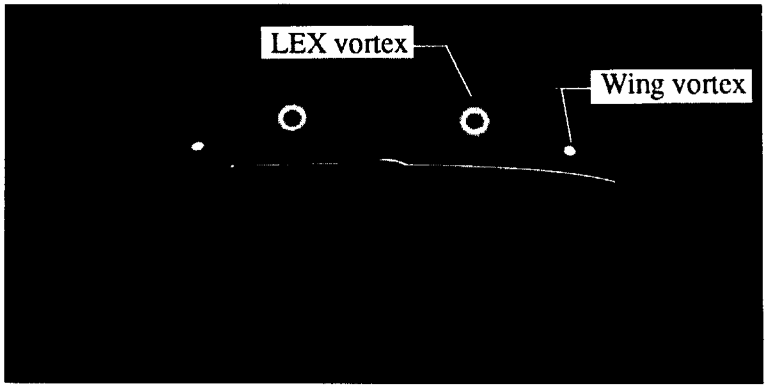

(a) $\alpha = 12°$.

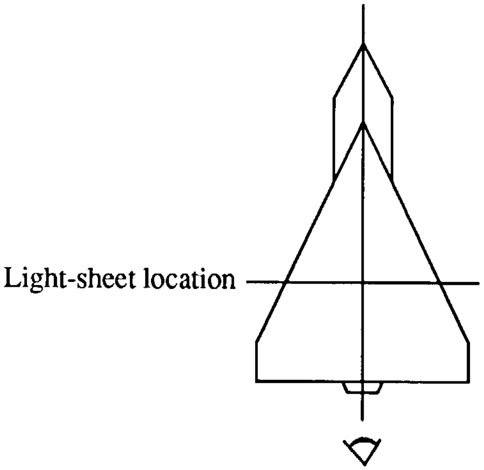

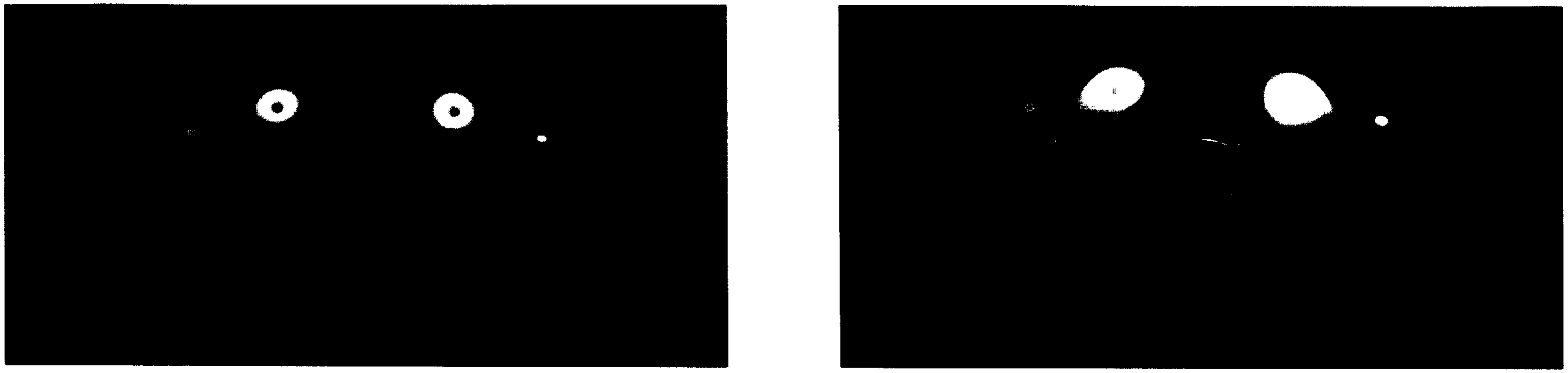

(b) $\alpha = 14°$.

(c) $\alpha = 16°$.

Figure 65. Laser vapor screen flow visualizations at $x/c = 0.60$ and $M_\infty = 0.40$ with LEX on.

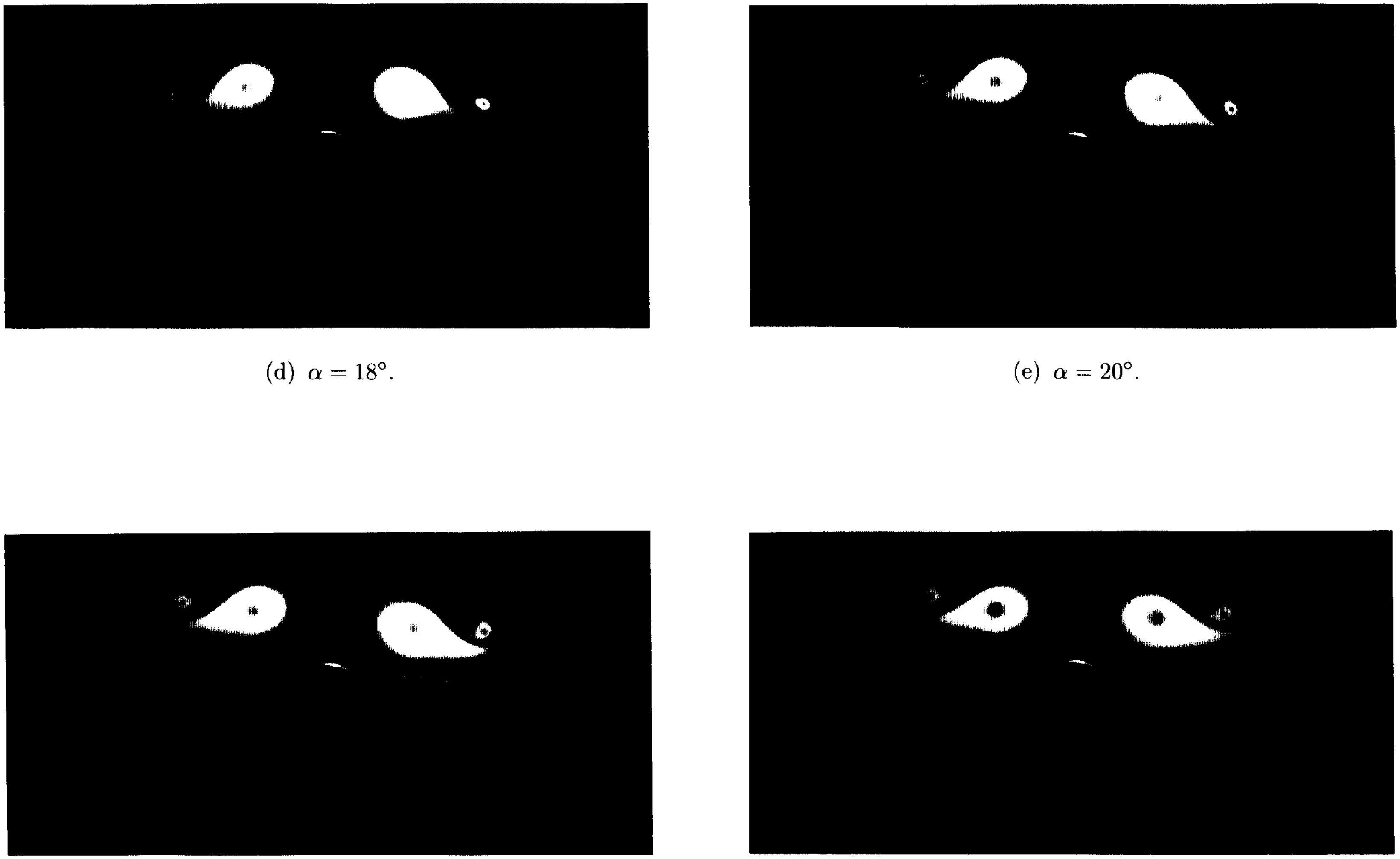

(d) $\alpha = 18°$.

(e) $\alpha = 20°$.

(f) $\alpha = 22°$.

(g) $\alpha = 24°$.

Figure 65. Concluded.

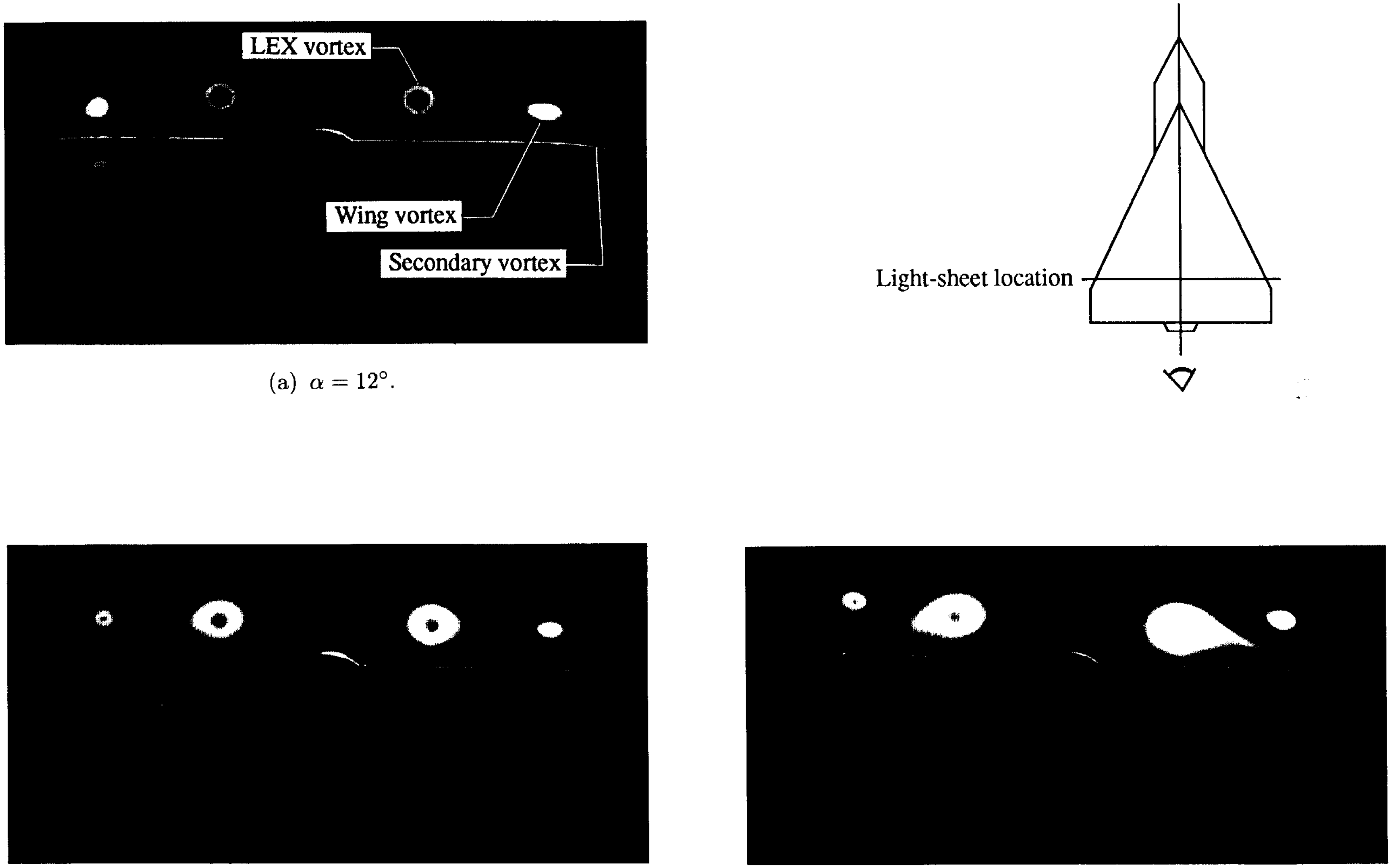

(a) $\alpha = 12^\circ$.

(b) $\alpha = 14^\circ$.

(c) $\alpha = 16^\circ$.

Figure 66. Laser vapor screen flow visualizations at $x/c = 0.80$ and $M_\infty = 0.40$ with LEX on.

ORIGINAL PAGE
BLACK AND WHITE PHOTOGRAPH

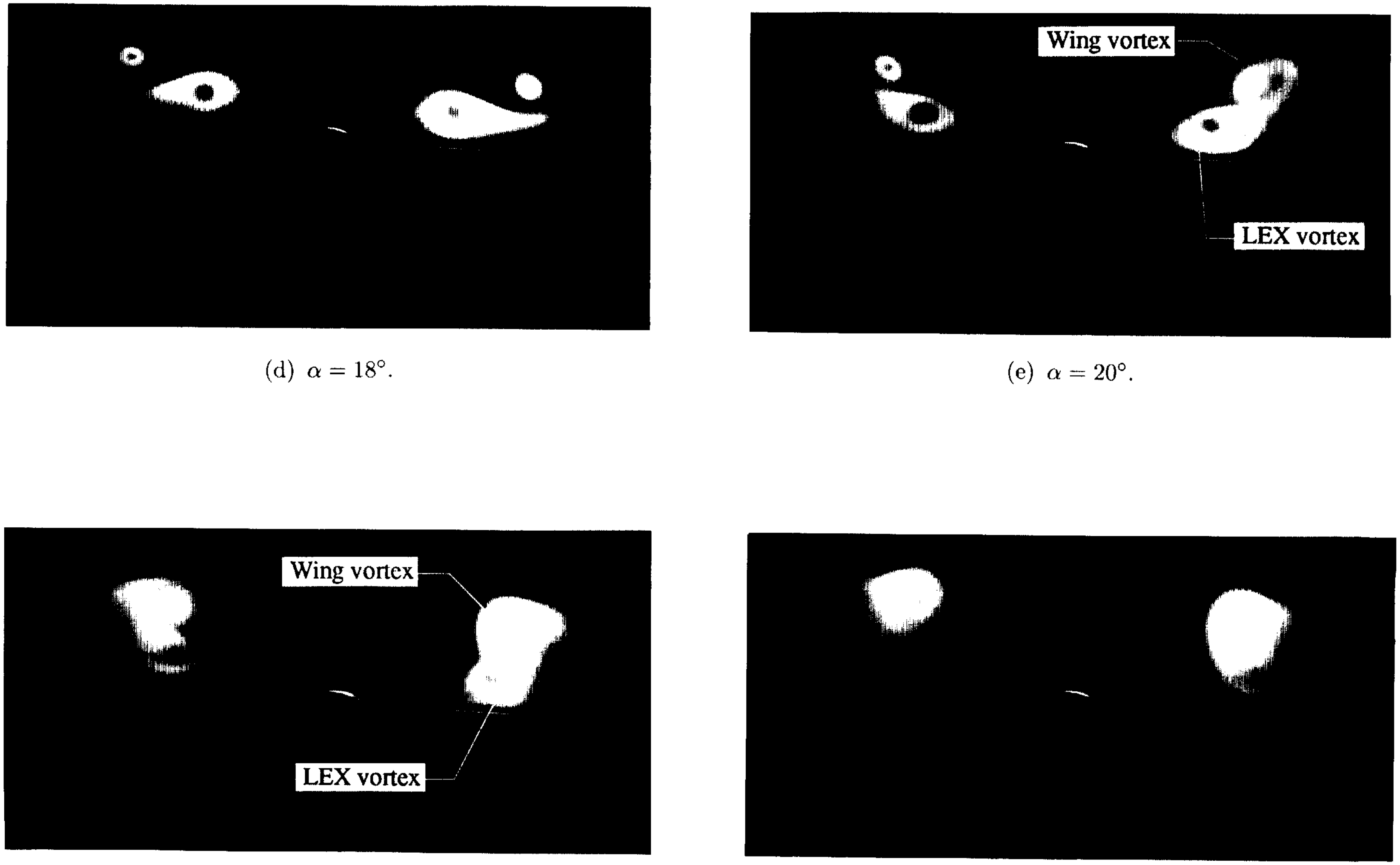

(d) $\alpha = 18°$.

(e) $\alpha = 20°$.

(f) $\alpha = 22°$.

(g) $\alpha = 24°$.

Figure 66. Concluded.

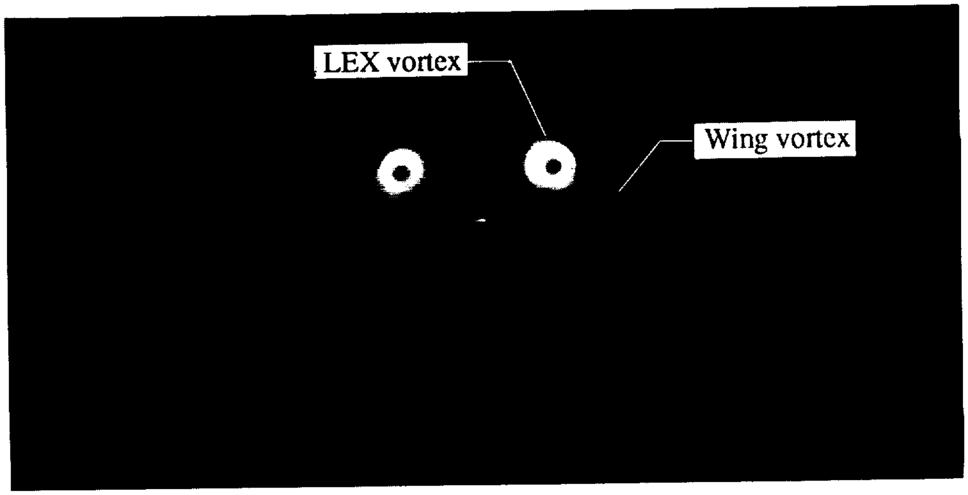

(a) $x/c = 0.50$.

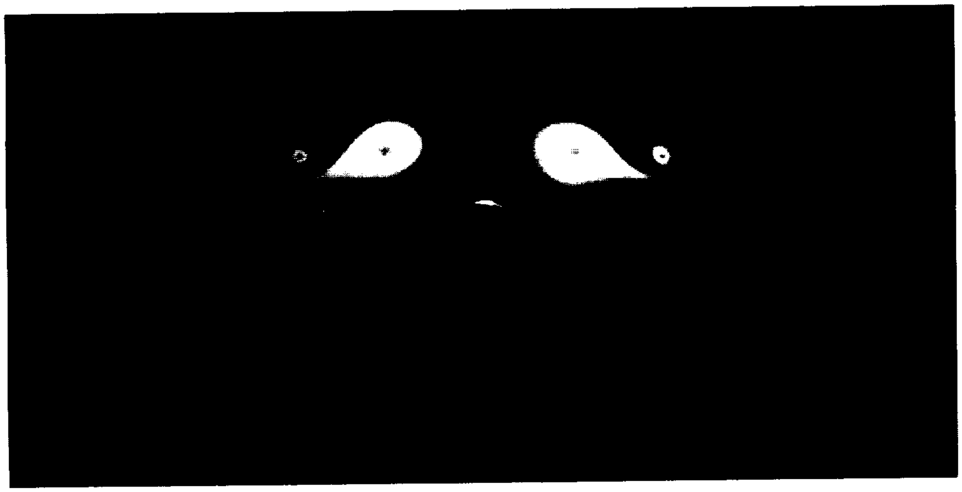

(b) $x/c = 0.60$.

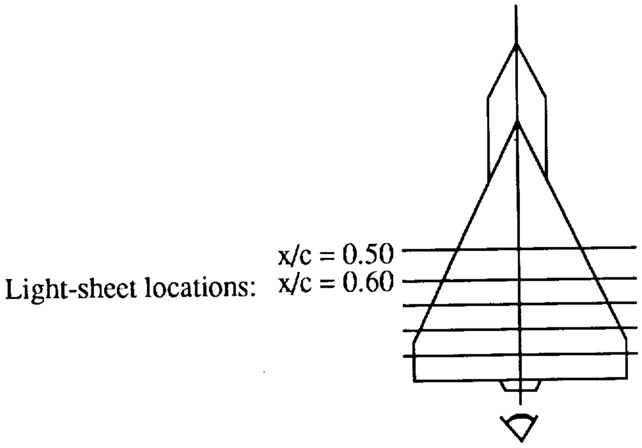

Figure 67. Laser vapor screen flow visualizations at $\alpha = 20^\circ$ and $M_\infty = 0.40$ with LEX on.

(c) $x/c = 0.70$.

(d) $x/c = 0.80$.

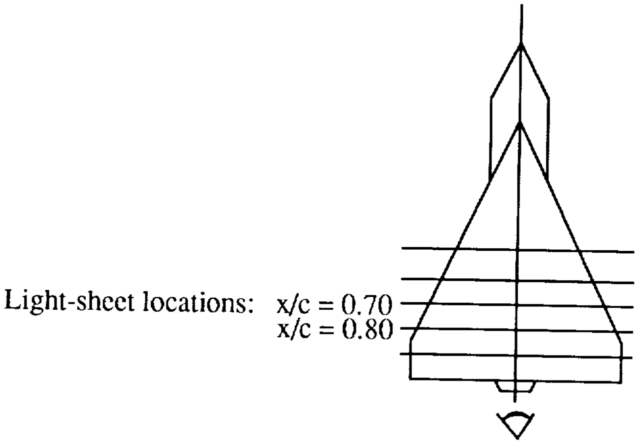

Figure 67. Continued.

C-2

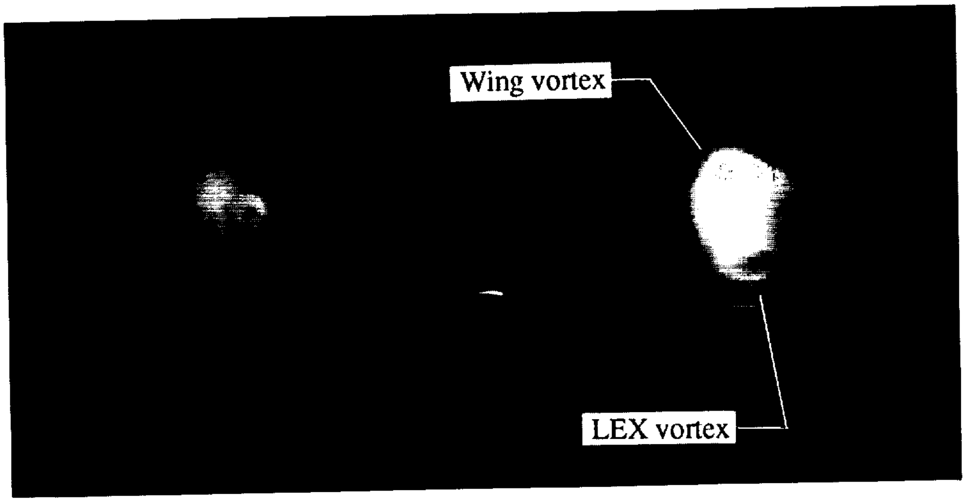

(e) $x/c = 0.90$.

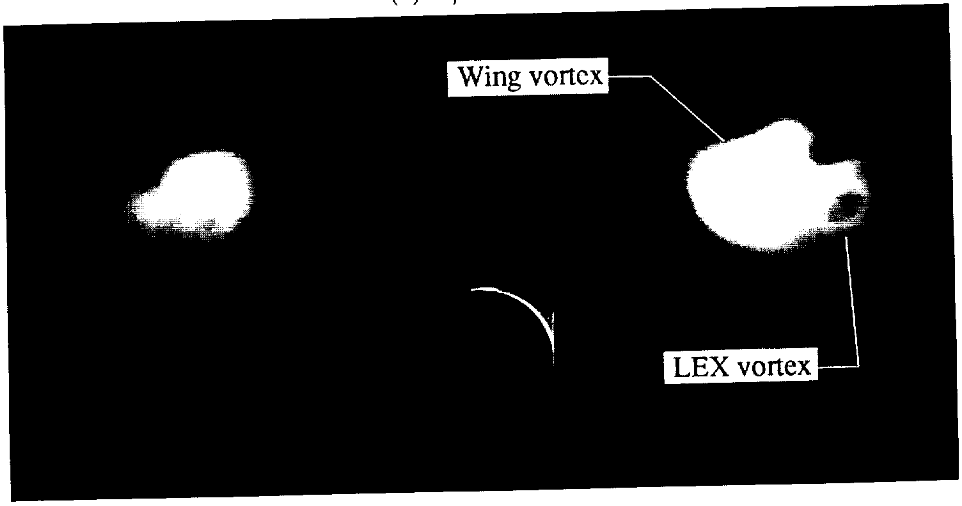

(f) $x/c = 1.00$.

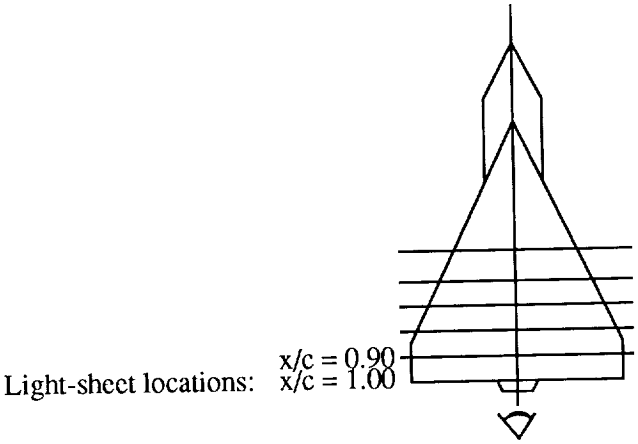

Figure 67. Concluded.

ORIGINAL PAGE
BLACK AND WHITE PHOTOGRAPH

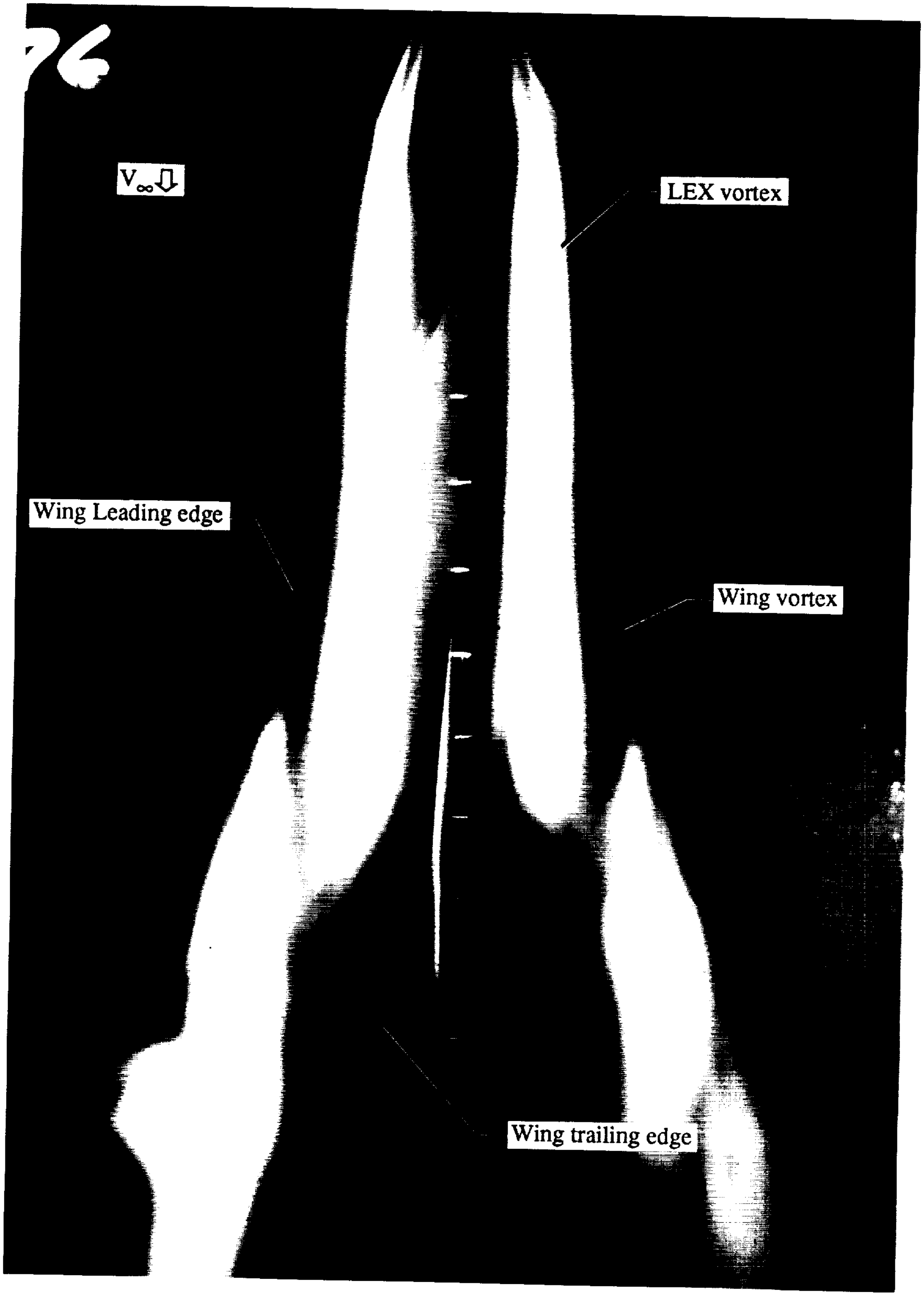

Figure 68. Laser vapor screen flow visualization at $\alpha = 20°$ and $M_\infty = 0.40$ with LEX on.

ORIGINAL PAGE
BLACK AND WHITE PHOTOGRAPH

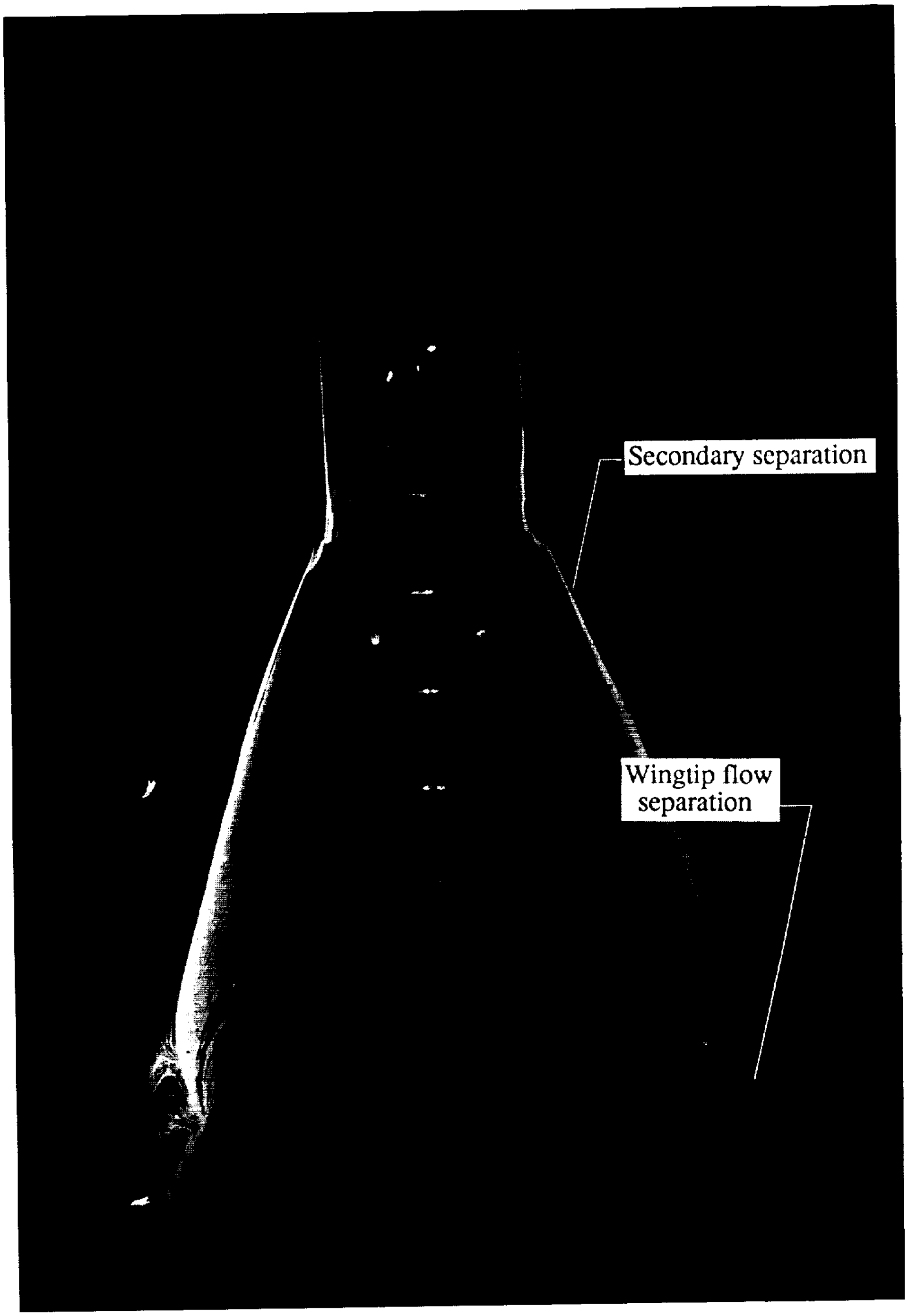

Figure 69. Wing upper surface oil flow pattern at $\alpha = 20°$ and $M_\infty = 0.40$ with LEX on.

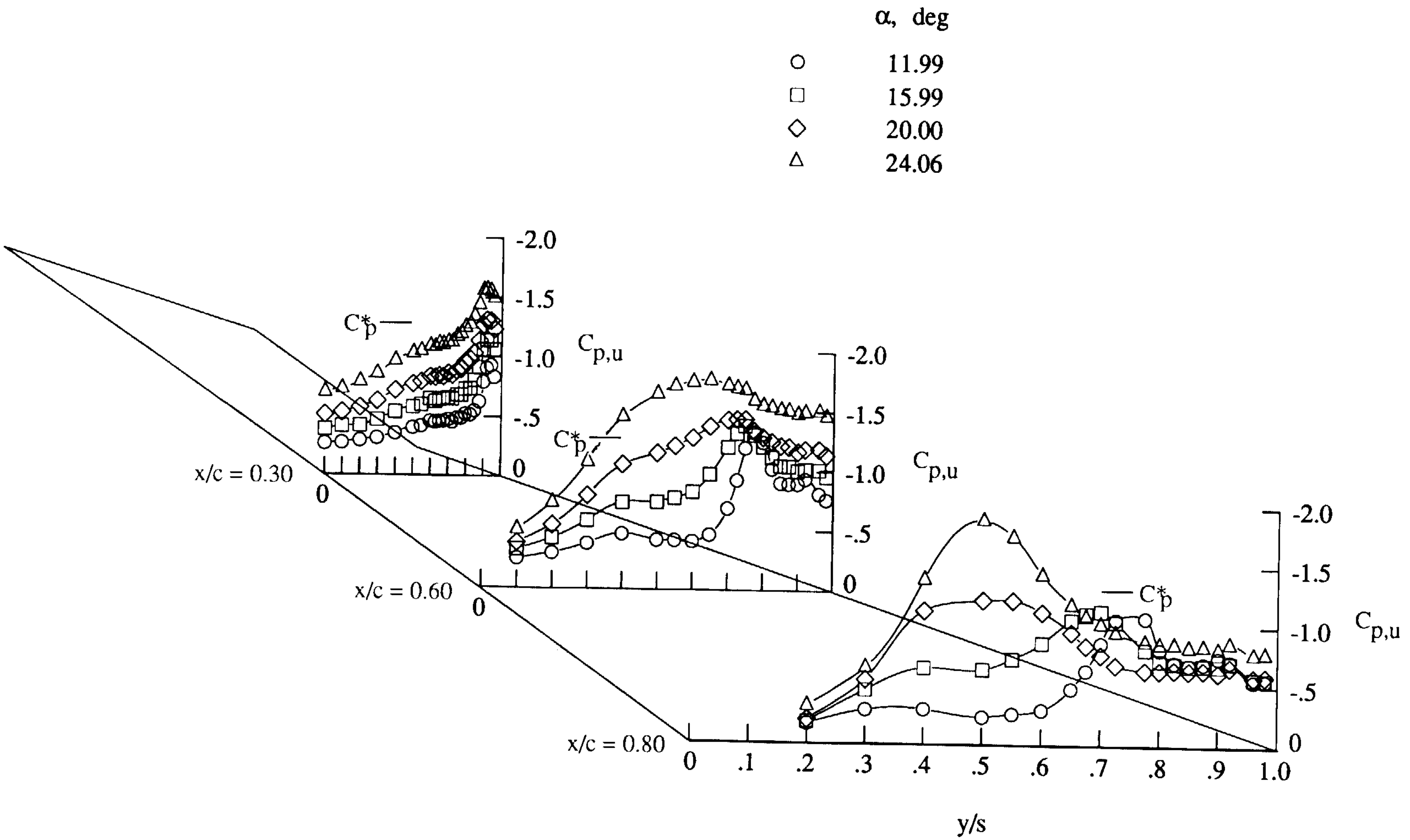

Figure 70. Wing upper surface static pressure distributions at $M_\infty = 0.60$ with LEX on.

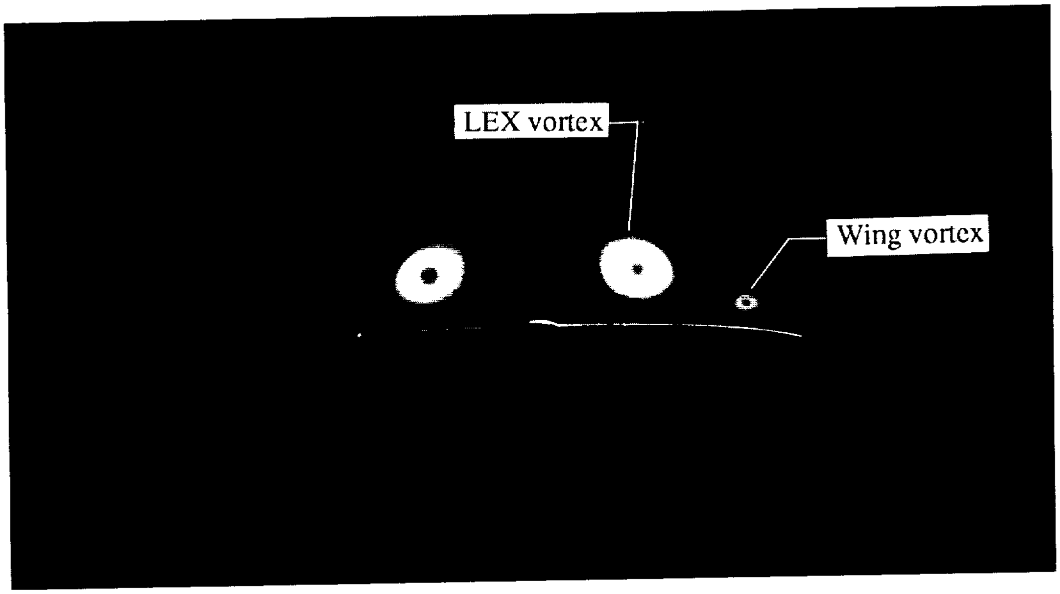

(a) $\alpha = 12°$.

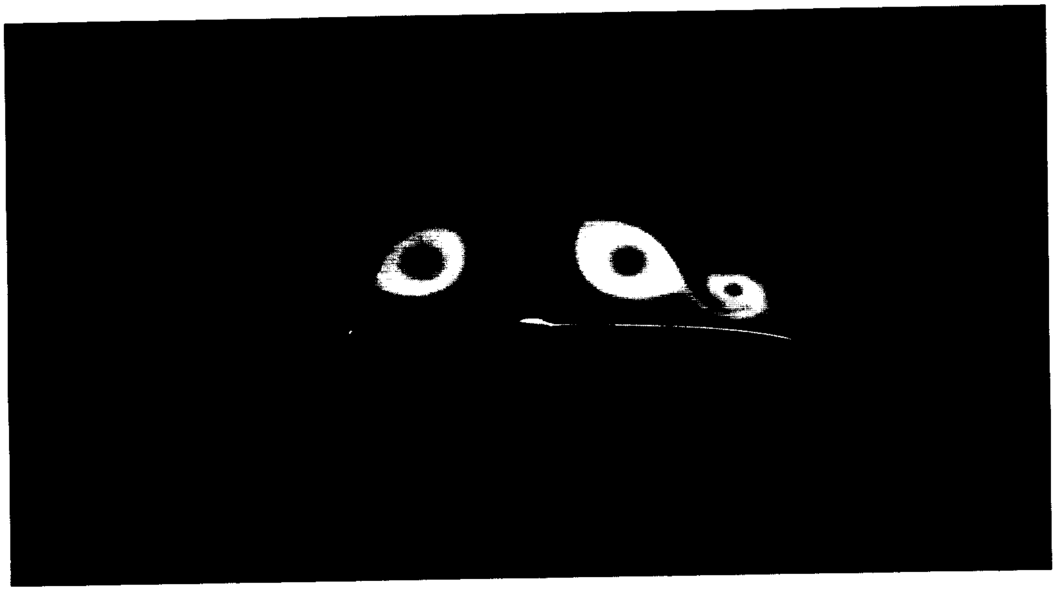

(b) $\alpha = 16°$.

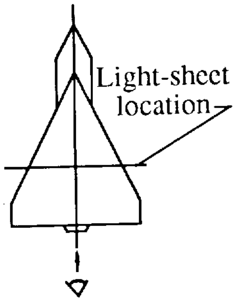

Figure 71. Laser vapor screen flow visualizations at $x/c = 0.60$ and $M_\infty = 0.60$ with LEX on.

(c) $\alpha = 20°$.

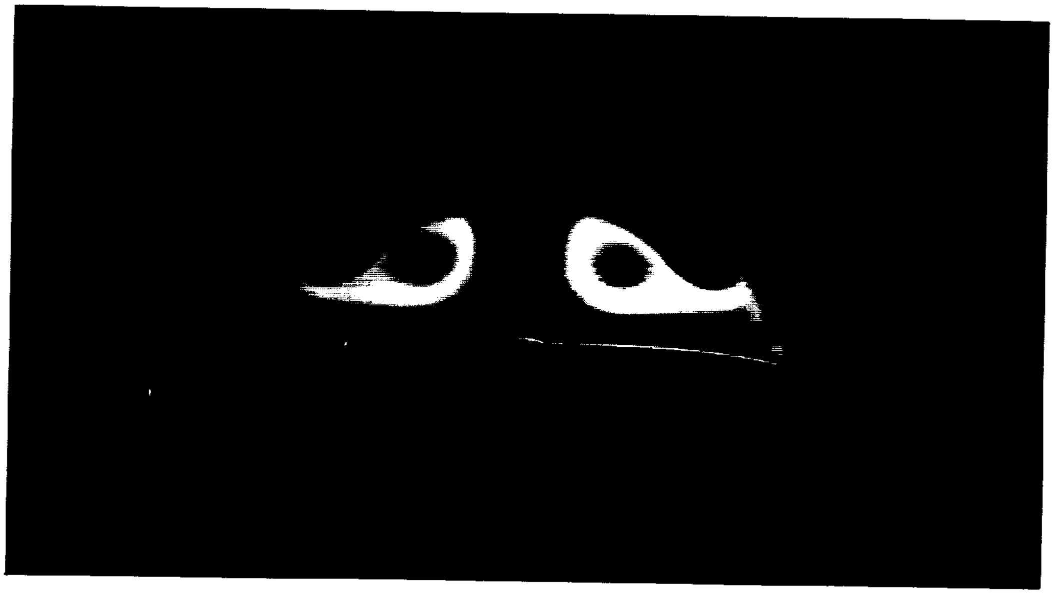

(d) $\alpha = 24°$.

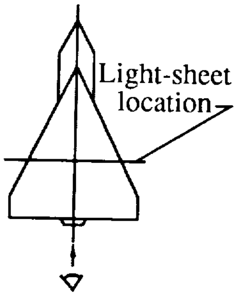

Figure 71. Concluded.

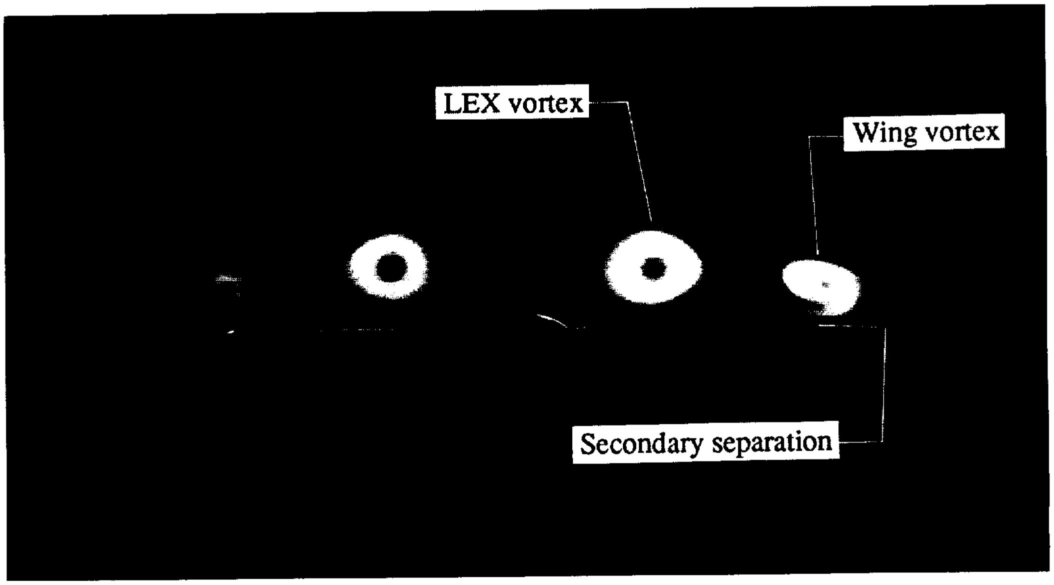

(a) $\alpha = 12°$.

(b) $\alpha = 16°$.

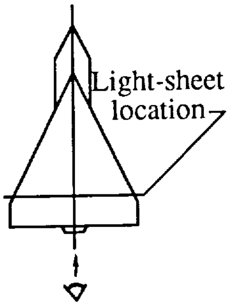

Figure 72. Laser vapor screen flow visualizations at $x/c = 0.80$ and $M_\infty = 0.60$ with LEX on.

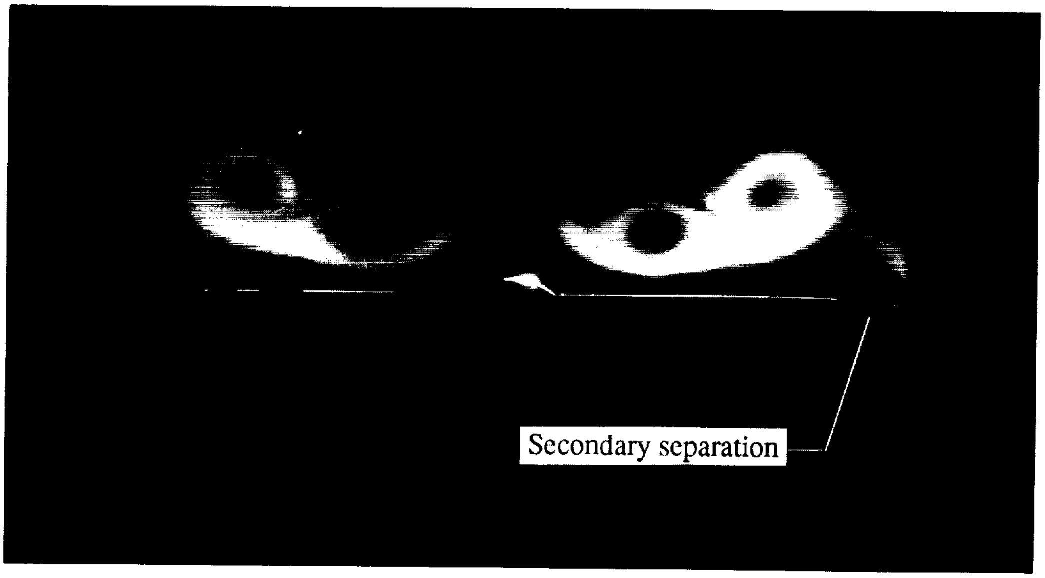

(c) $\alpha = 20^\circ$.

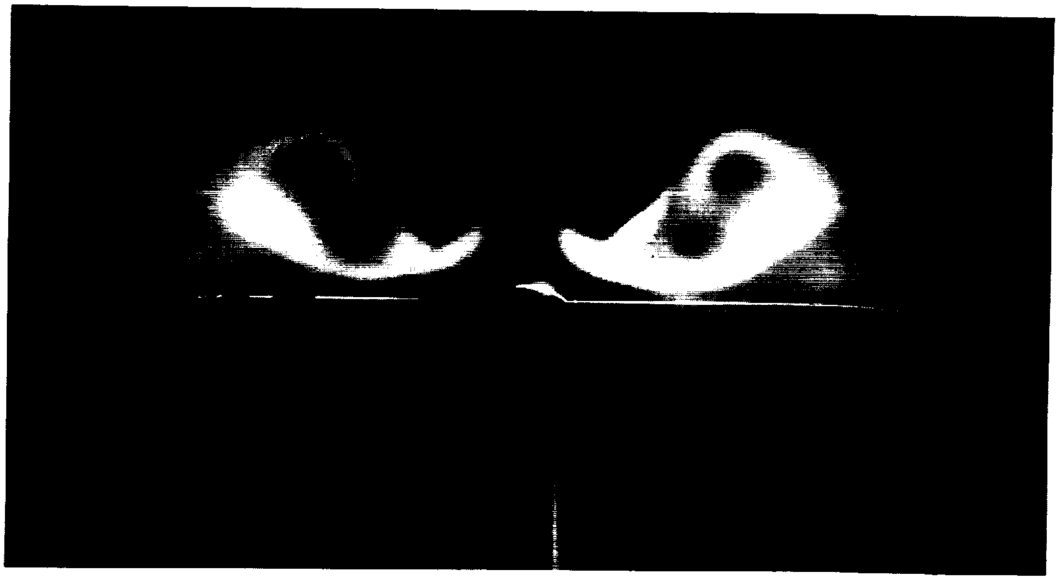

(d) $\alpha = 24^\circ$.

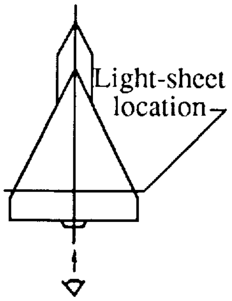

Figure 72. Concluded.

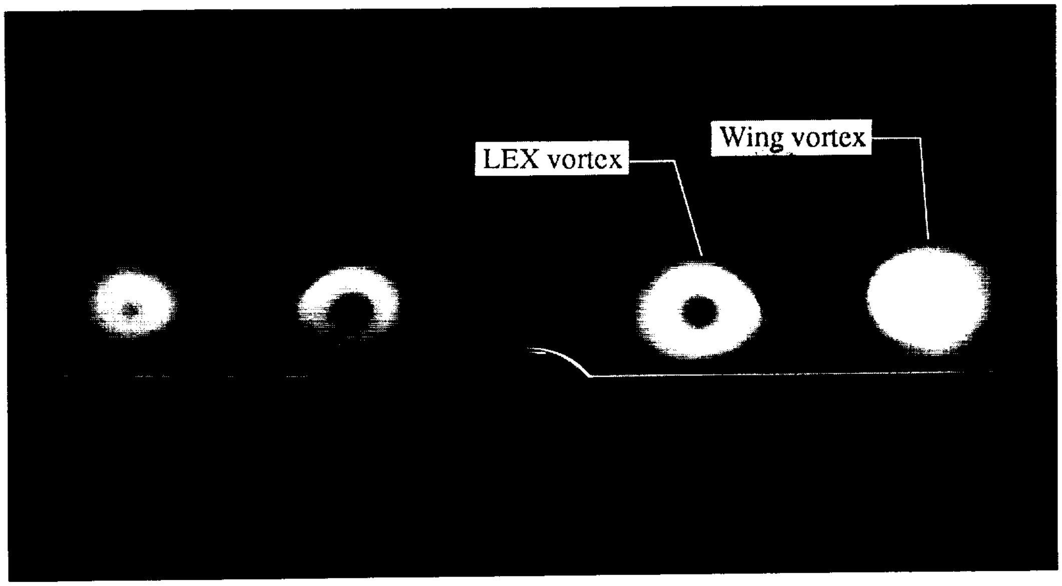

(a) $\alpha = 12°$.

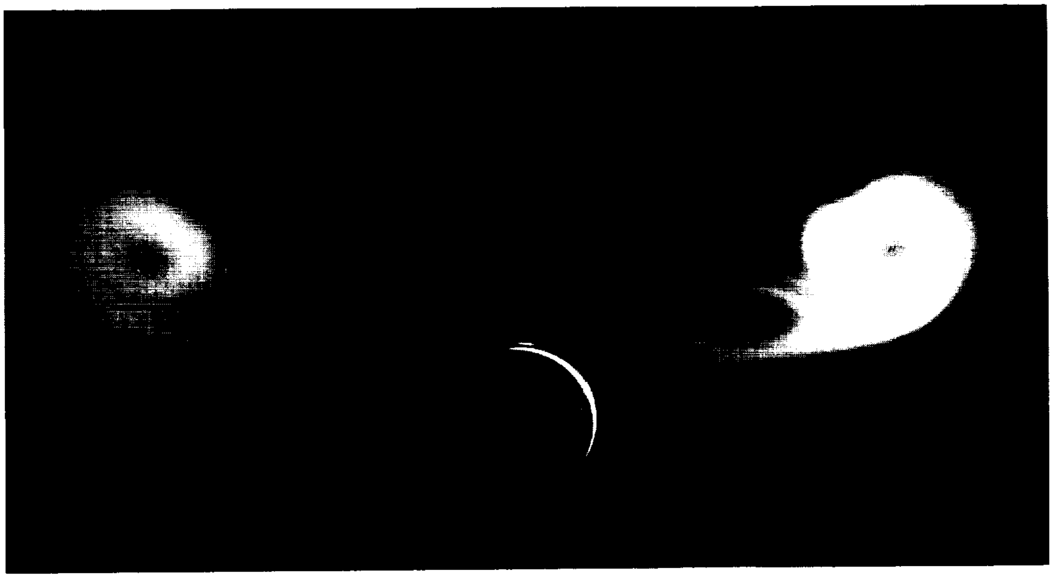

(b) $\alpha = 16°$.

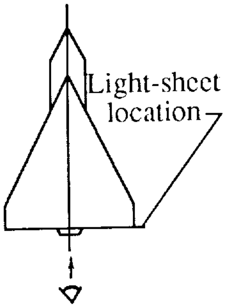

Figure 73. Laser vapor screen flow visualizations at $x/c = 1.00$ and $M_\infty = 0.60$ with LEX on.

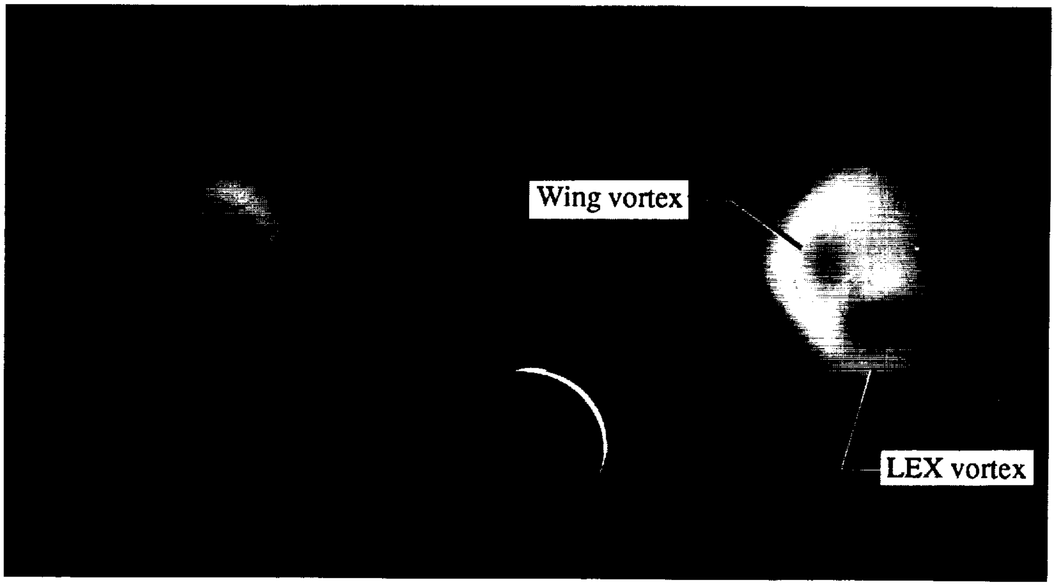

(c) $\alpha = 20°$.

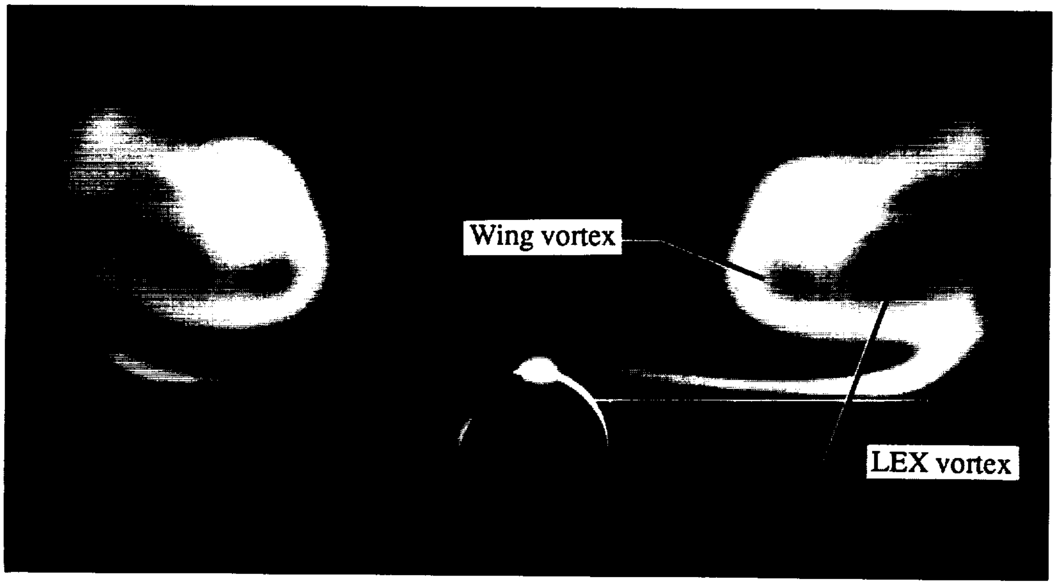

(d) $\alpha = 24°$.

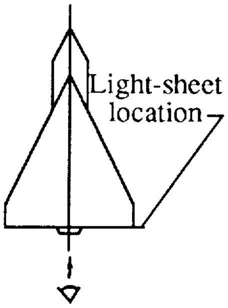

Figure 73. Concluded.

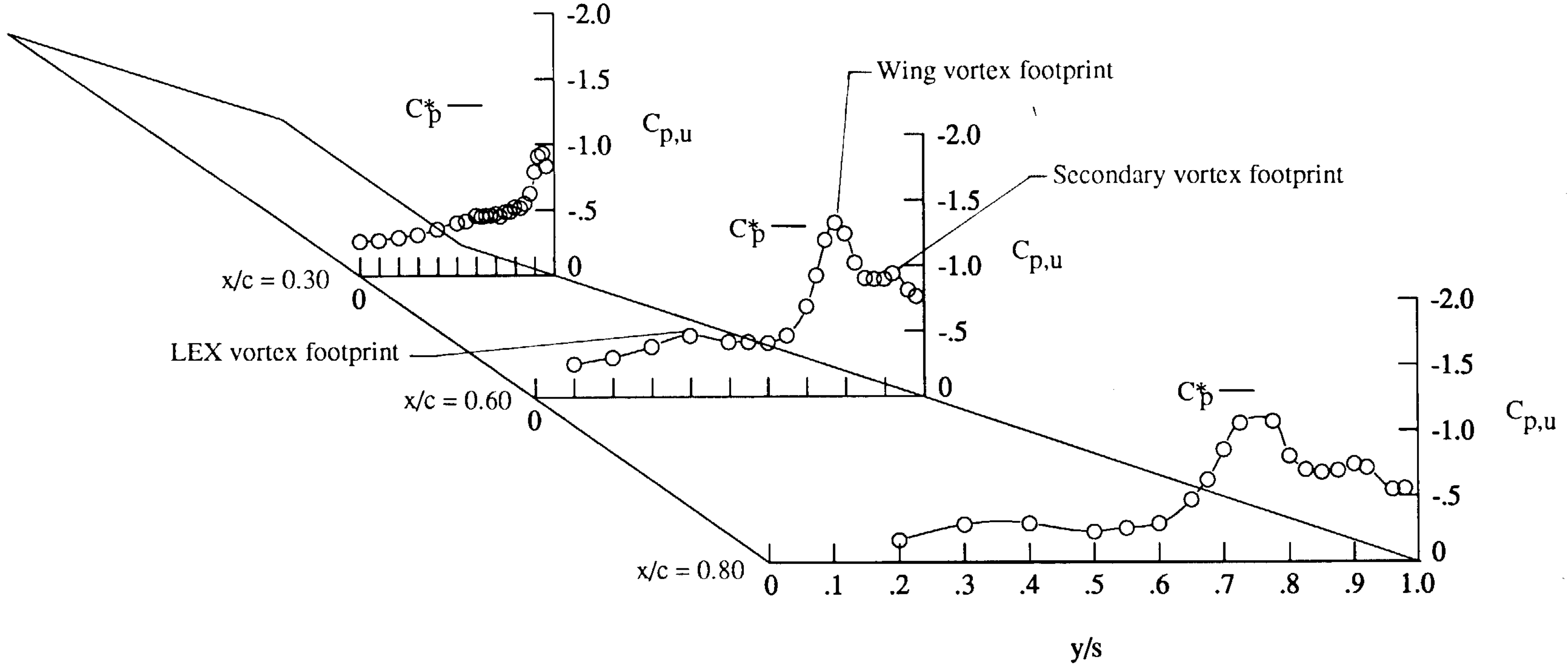

Figure 74. Wing upper surface static pressure distributions at $\alpha = 12°$ and $M_\infty = 0.60$ with LEX on.

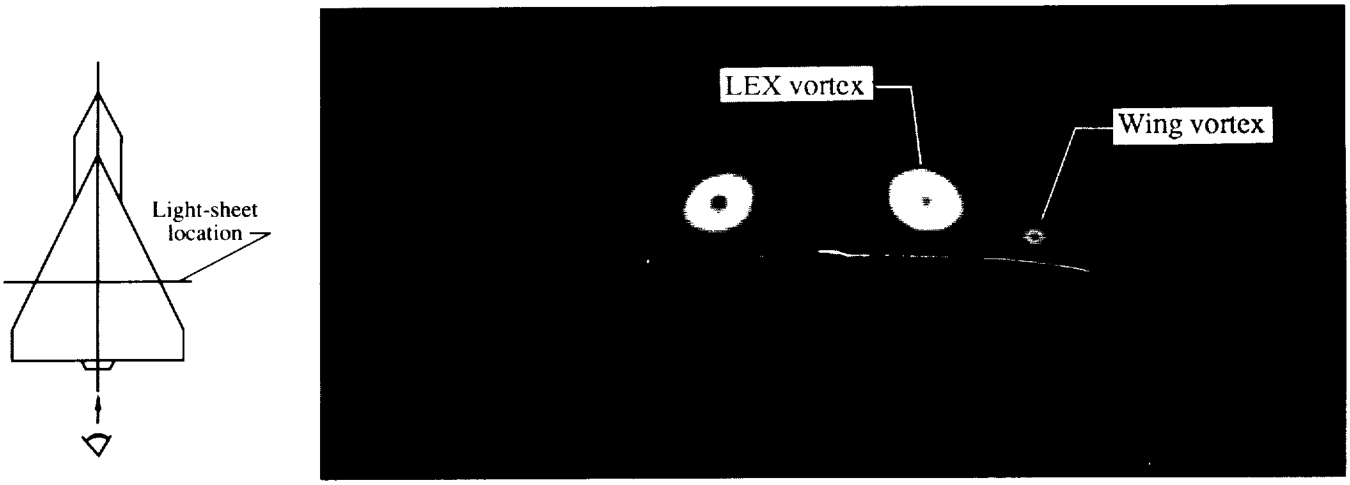

(a) $x/c = 0.60$.

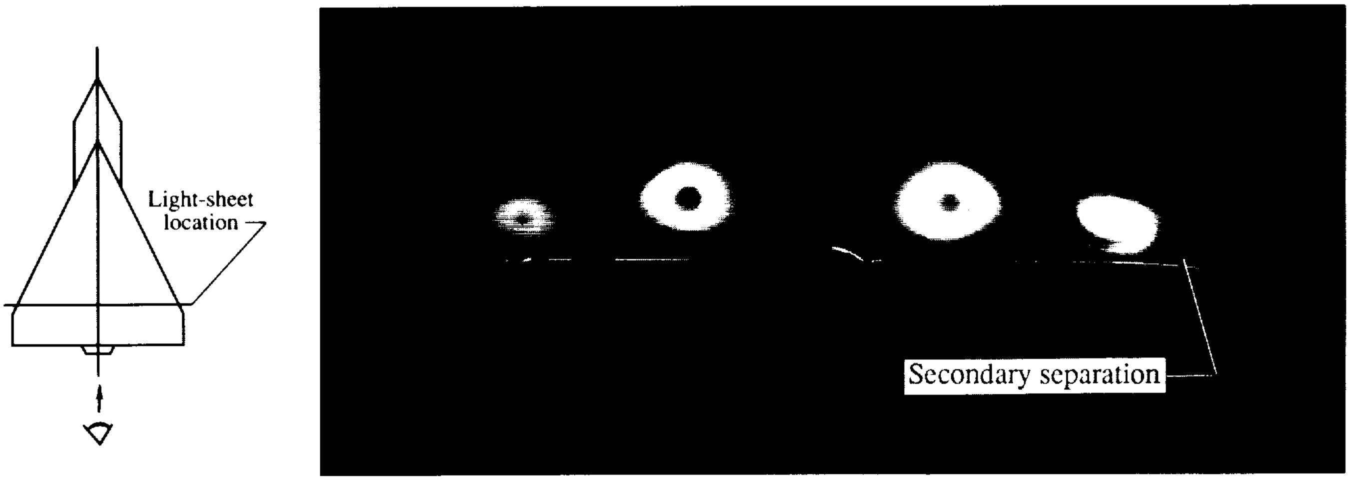

(b) $x/c = 0.80$.

(c) $x/c = 1.00$.

Figure 75. Laser vapor screen flow visualizations at $\alpha = 12^\circ$ and $M_\infty = 0.60$ with LEX on.

ORIGINAL PAGE
BLACK AND WHITE PHOTOGRAPH

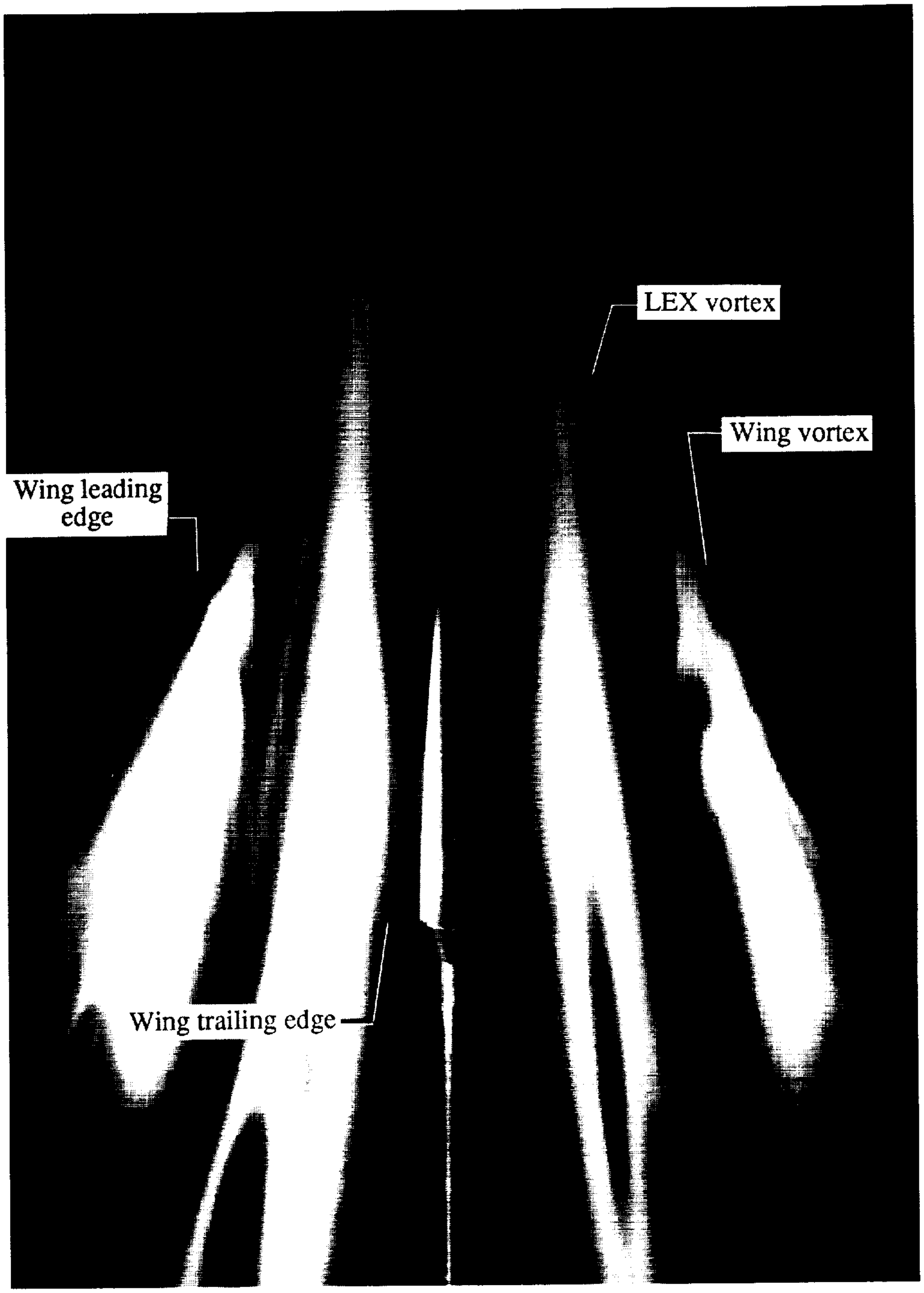

Figure 76. Laser vapor screen flow visualization at $\alpha = 12°$ and $M_\infty = 0.60$ with LEX on.

ORIGINAL PAGE
BLACK AND WHITE PHOTOGRAPH

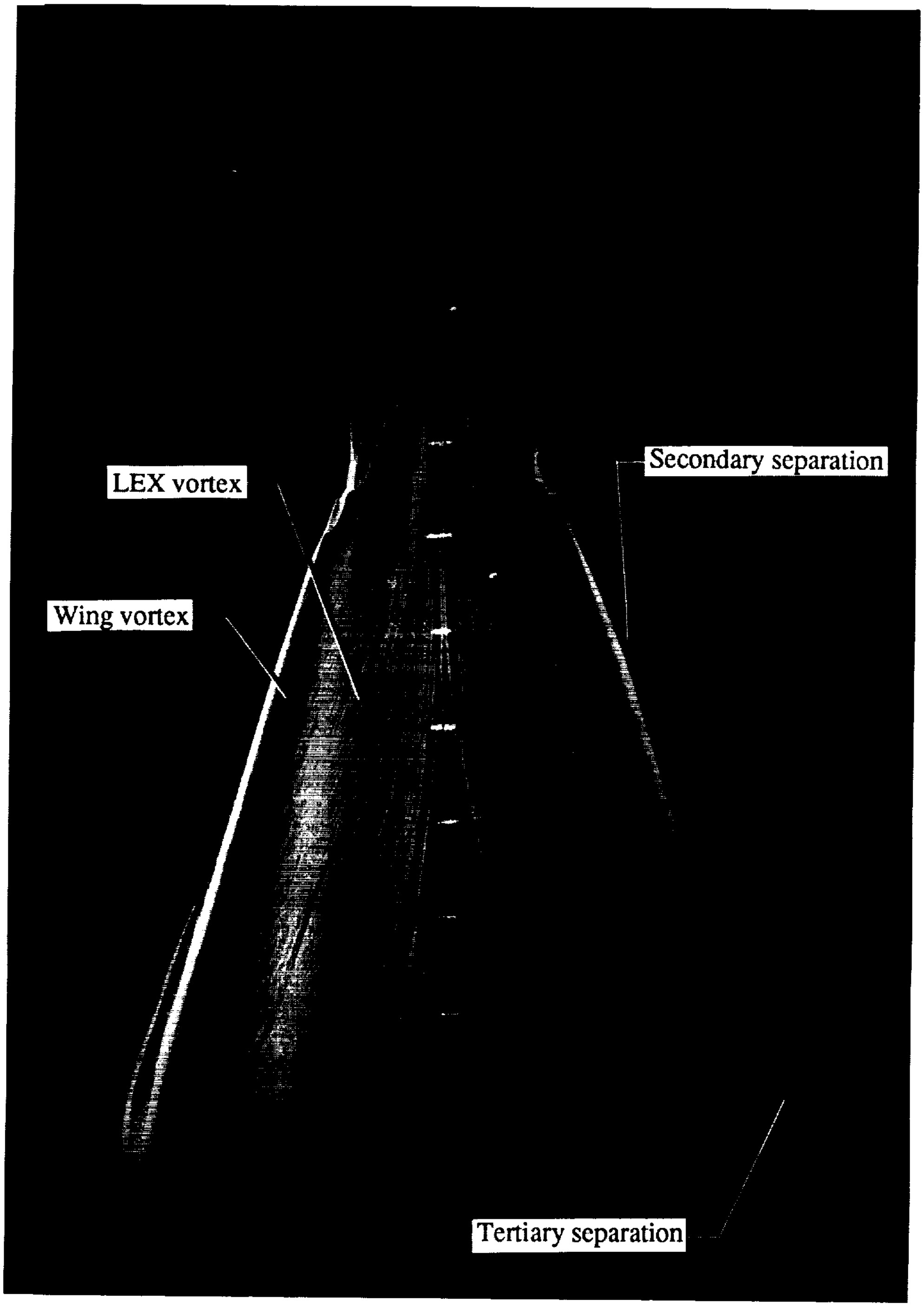

Figure 77. Wing upper surface oil flow pattern at $\alpha = 12^\circ$ and $M_\infty = 0.60$ with LEX on.

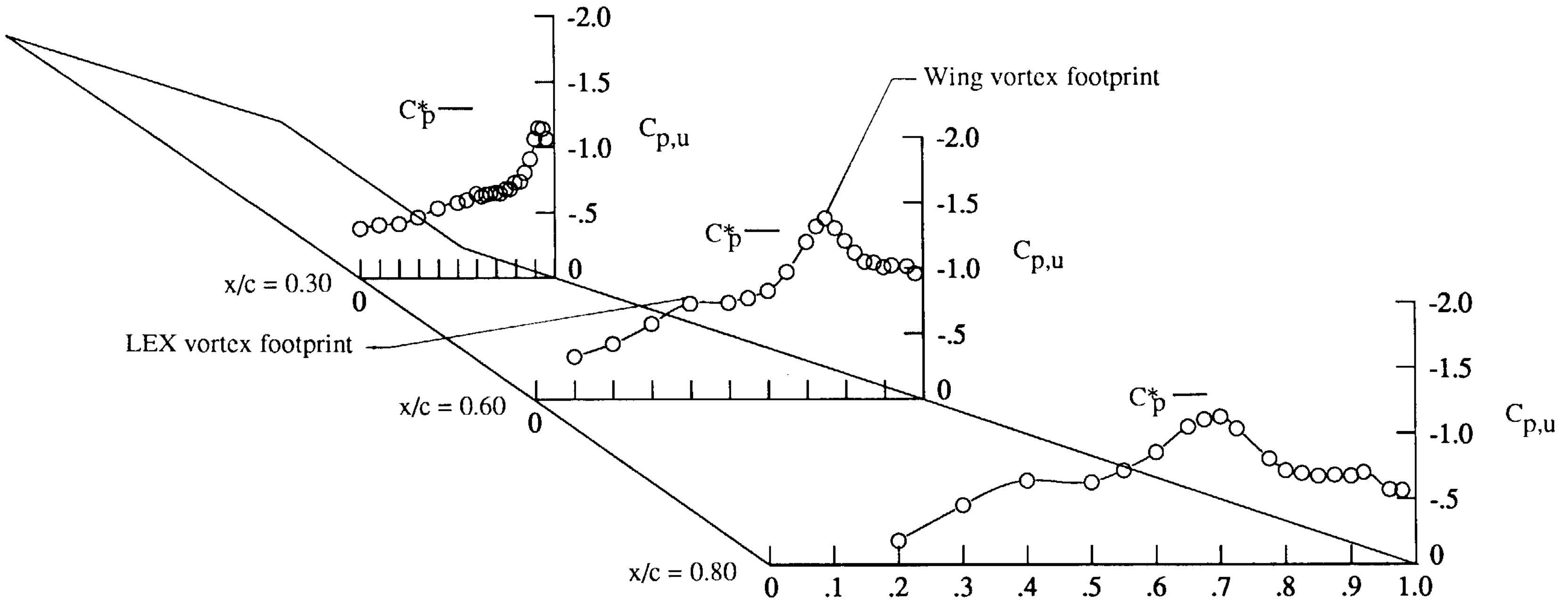

Figure 78. Wing upper surface static pressure distributions at $\alpha = 16°$ and $M_\infty = 0.60$ with LEX on.

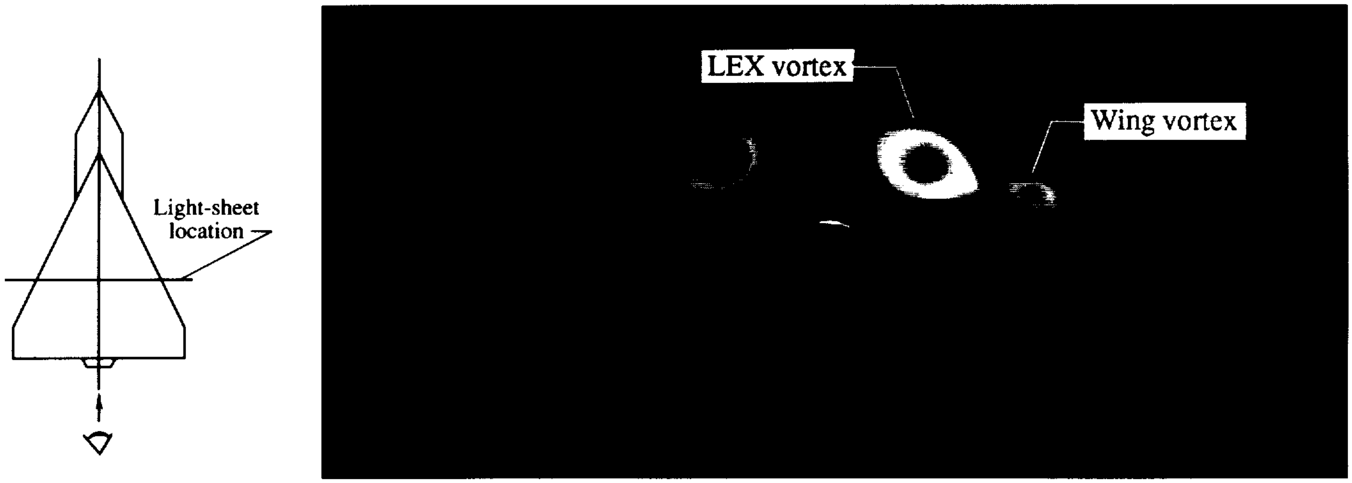

(a) $x/c = 0.60$.

(b) $x/c = 0.80$.

(c) $x/c = 1.00$.

Figure 79. Laser vapor screen flow visualizations at $\alpha = 16^\circ$ and $M_\infty = 0.60$ with LEX on.

ORIGINAL PAGE
BLACK AND WHITE PHOTOGRAPH

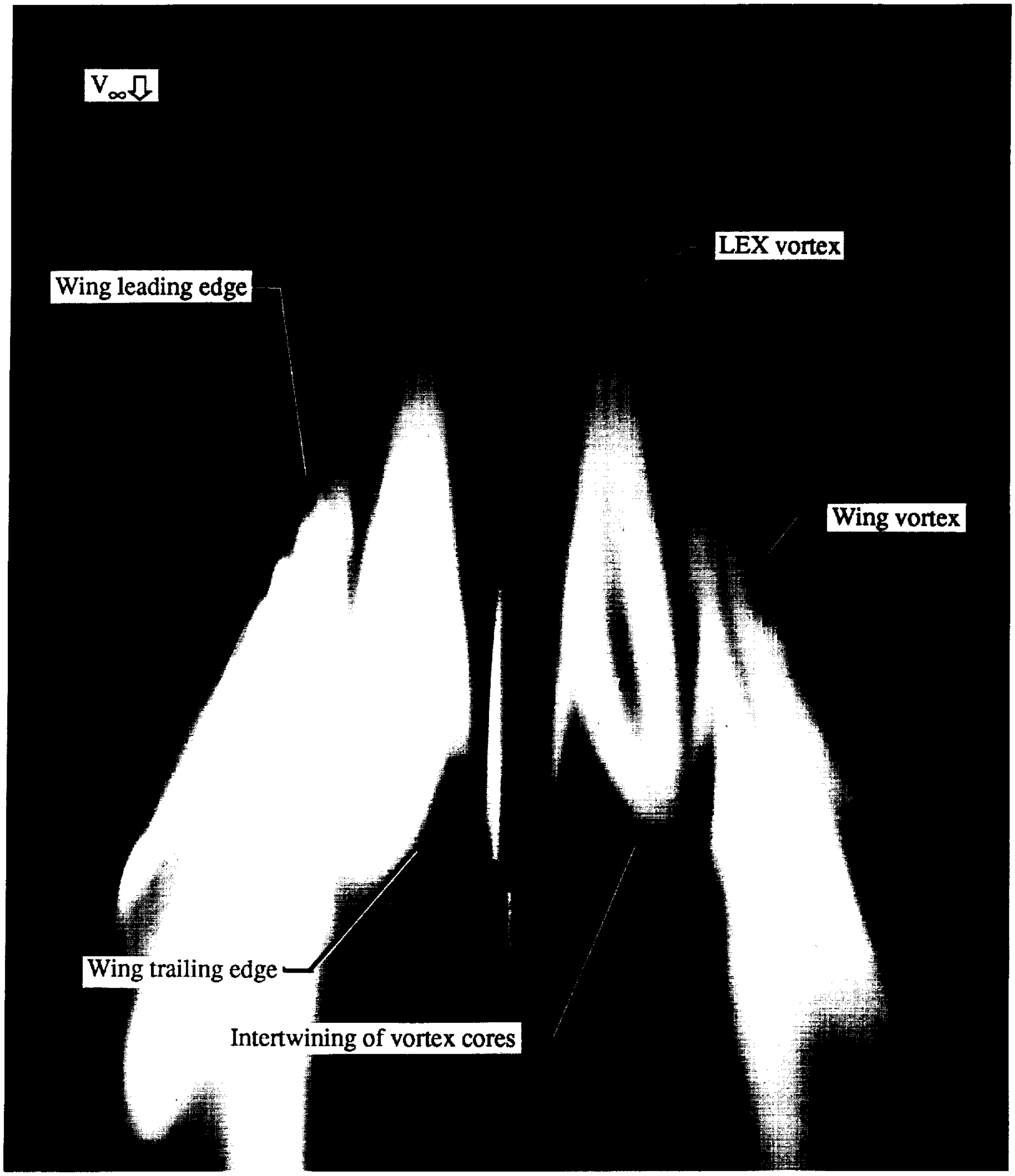

Figure 80. Laser vapor screen flow visualization at $\alpha = 16°$ and $M_\infty = 0.60$ with LEX on.

ORIGINAL PAGE
BLACK AND WHITE PHOTOGRAPH

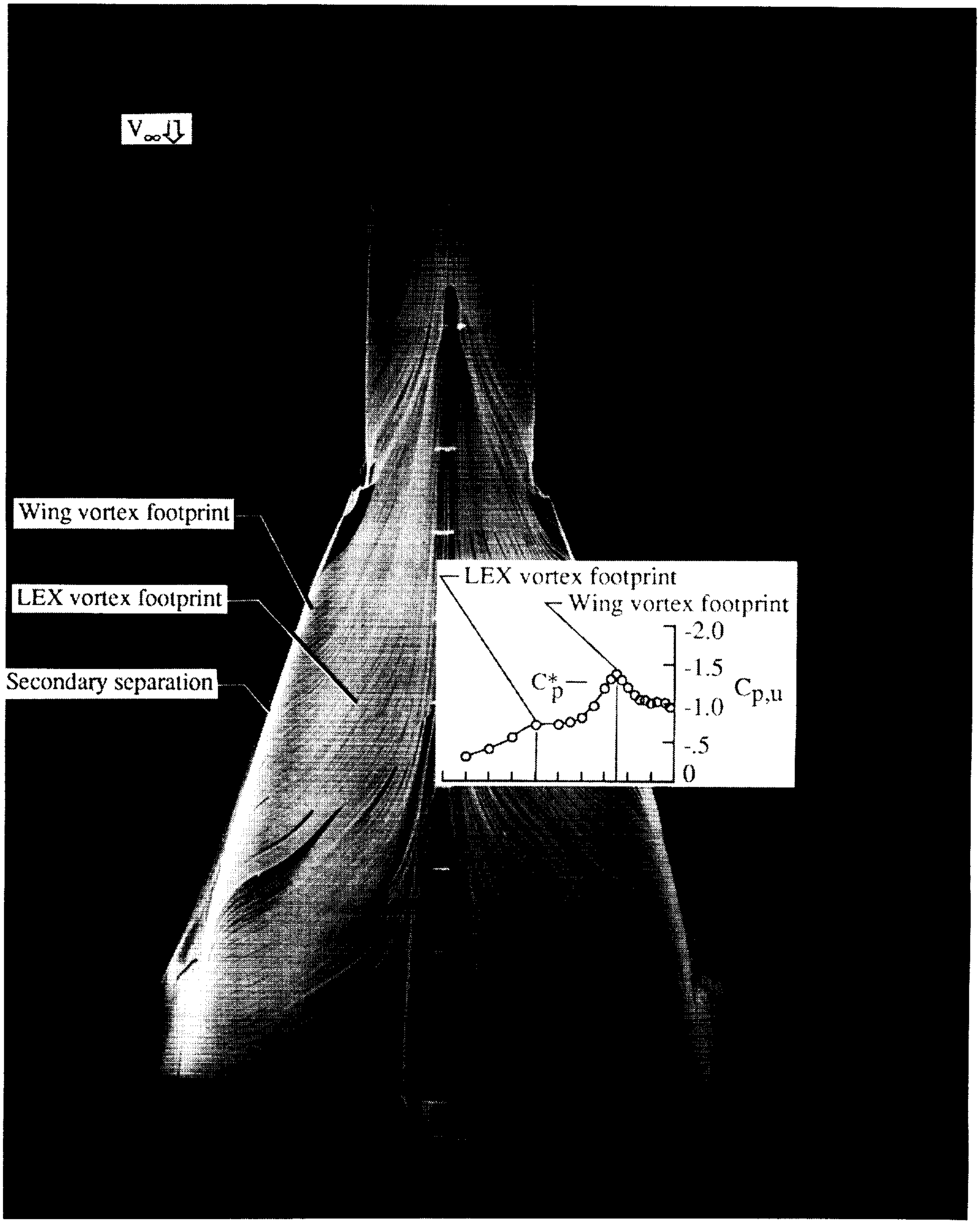

Figure 81. Wing upper surface oil flow pattern at $\alpha = 16°$ and $M_\infty = 0.60$ with LEX on.

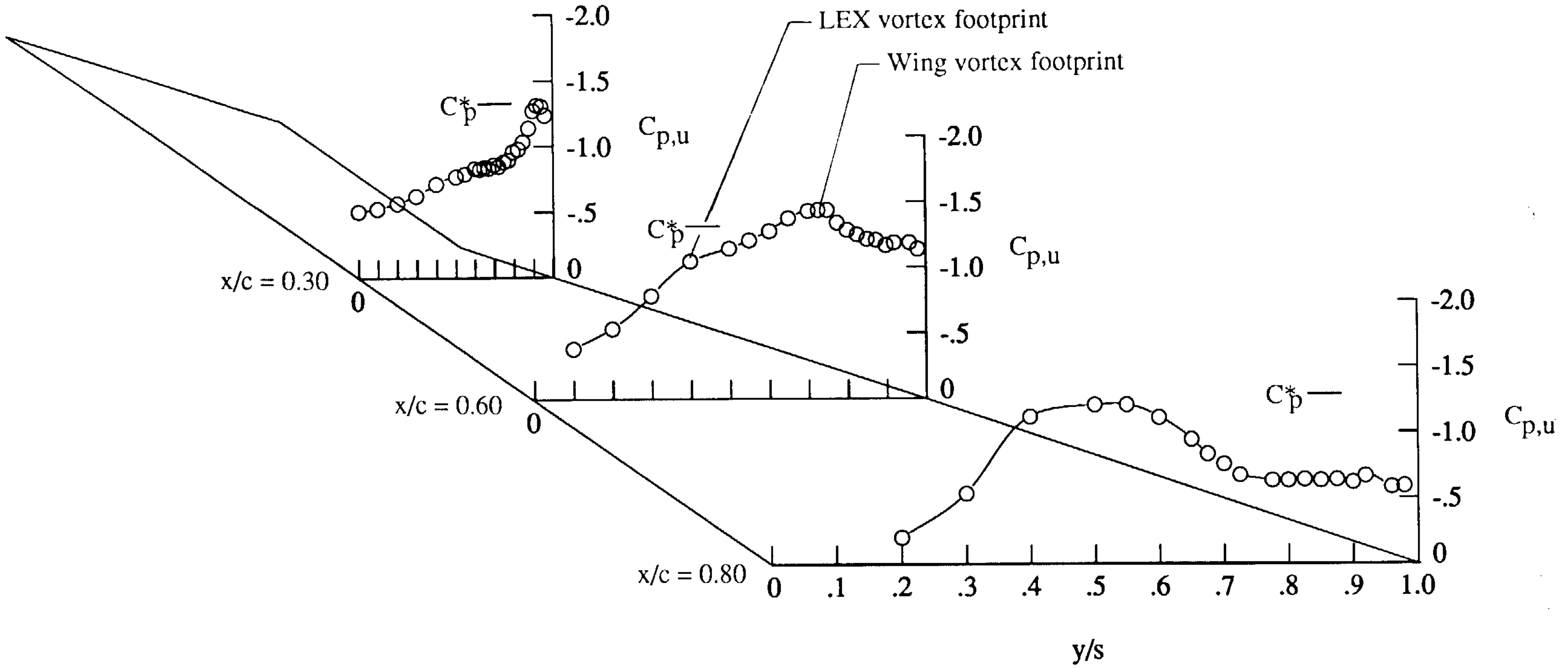

Figure 82. Wing upper surface static pressure distributions at $\alpha = 20°$ and $M_\infty = 0.60$ with LEX on.

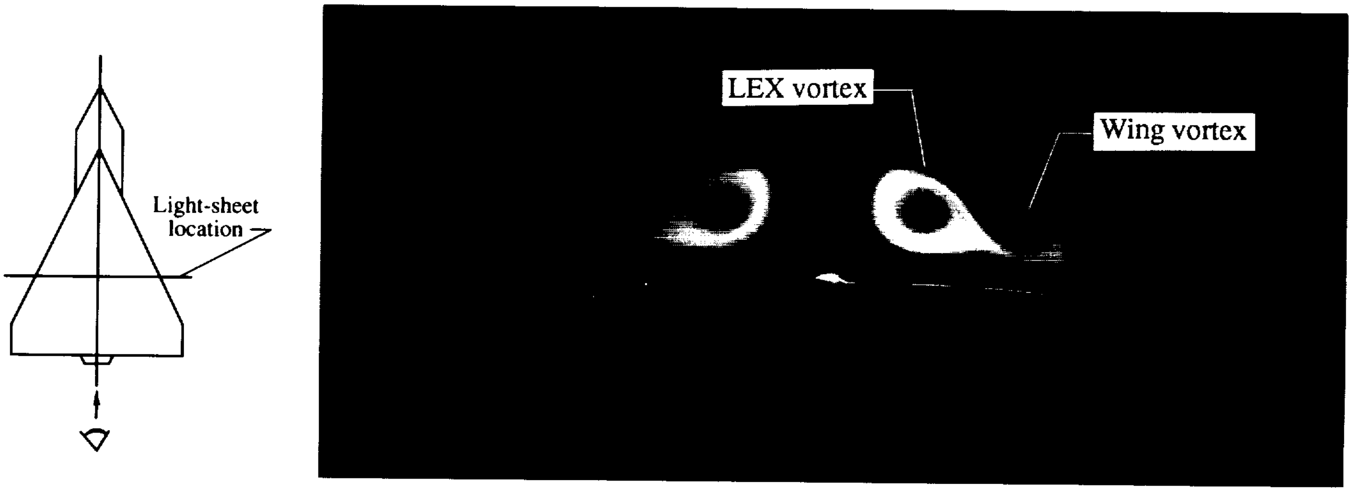

(a) $x/c = 0.60$.

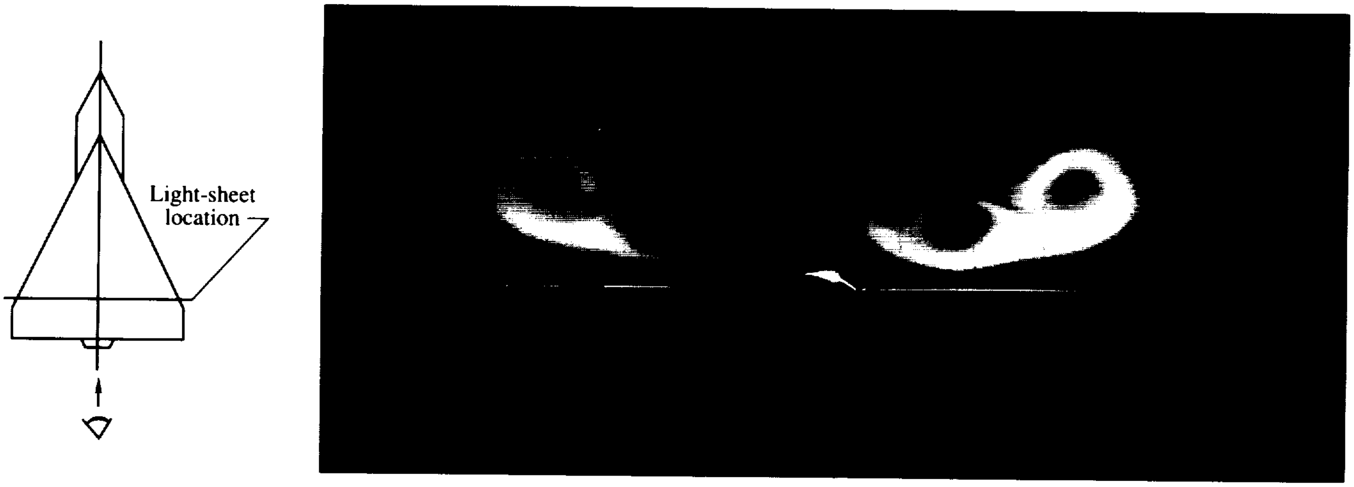

(b) $x/c = 0.80$.

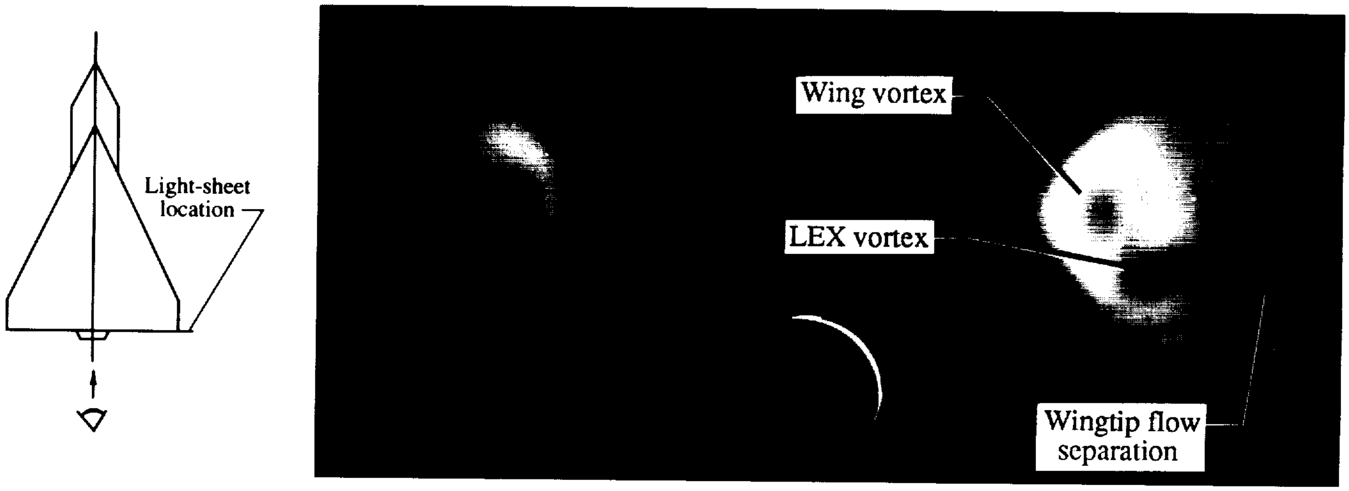

(c) $x/c = 1.00$.

Figure 83. Laser vapor screen flow visualizations at $\alpha = 20°$ and $M_\infty = 0.60$ with LEX on.

ORIGINAL PAGE
BLACK AND WHITE PHOTOGRAPH

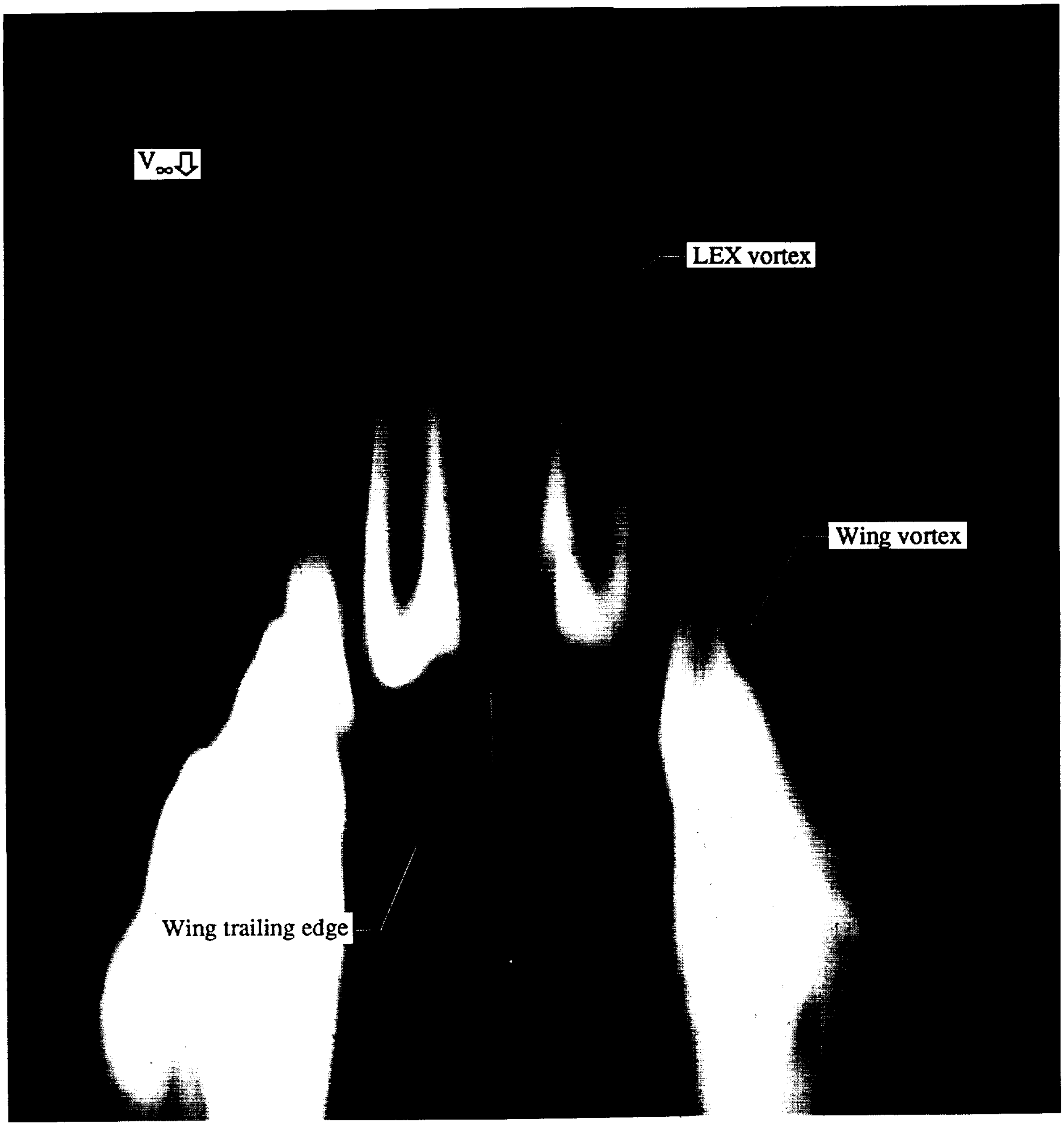

Figure 84. Laser vapor screen flow visualization at $\alpha = 20^\circ$ and $M_\infty = 0.60$ with LEX on.

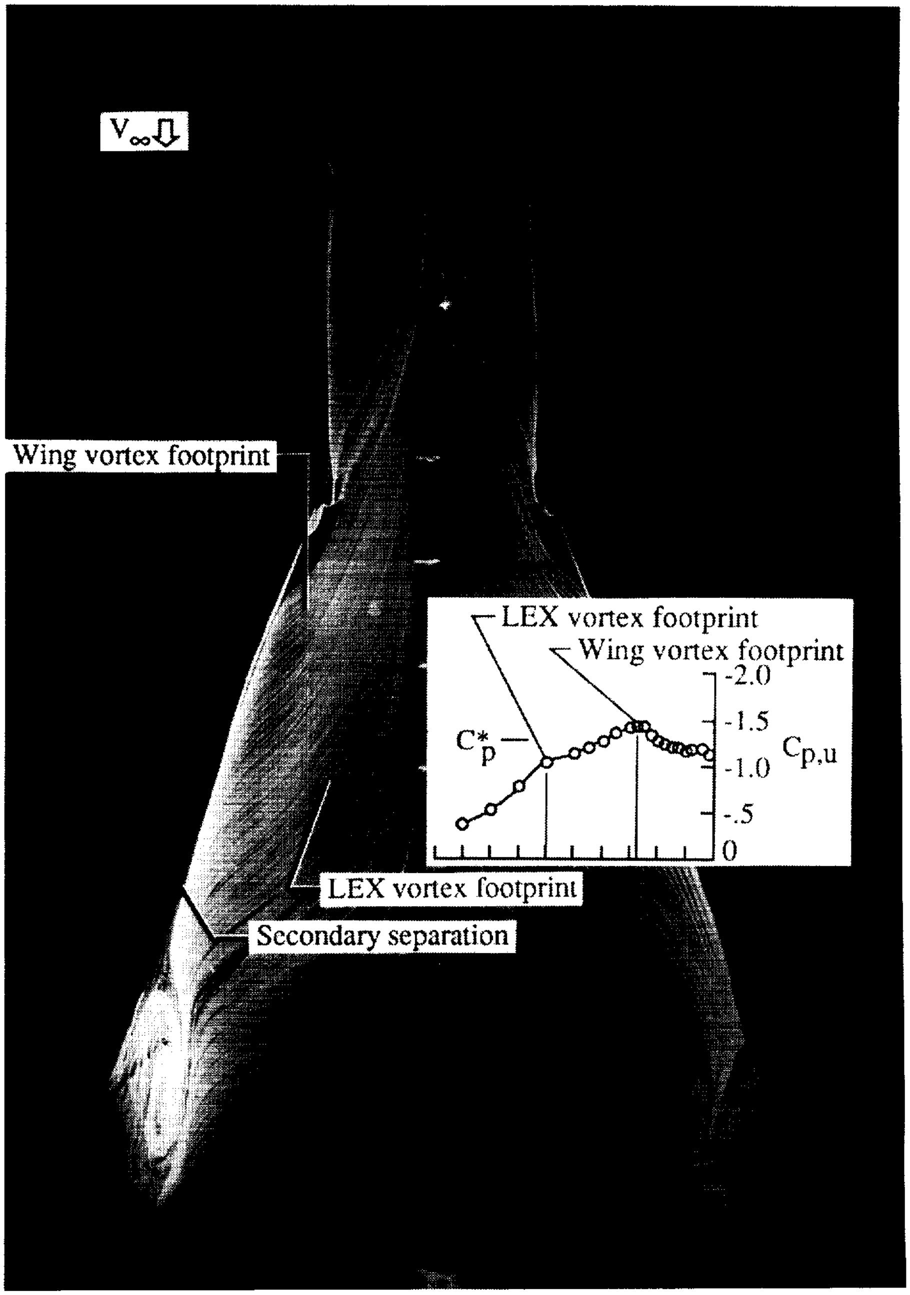

Figure 85. Wing upper surface oil flow pattern at $\alpha = 20°$ and $M_\infty = 0.60$ with LEX on.

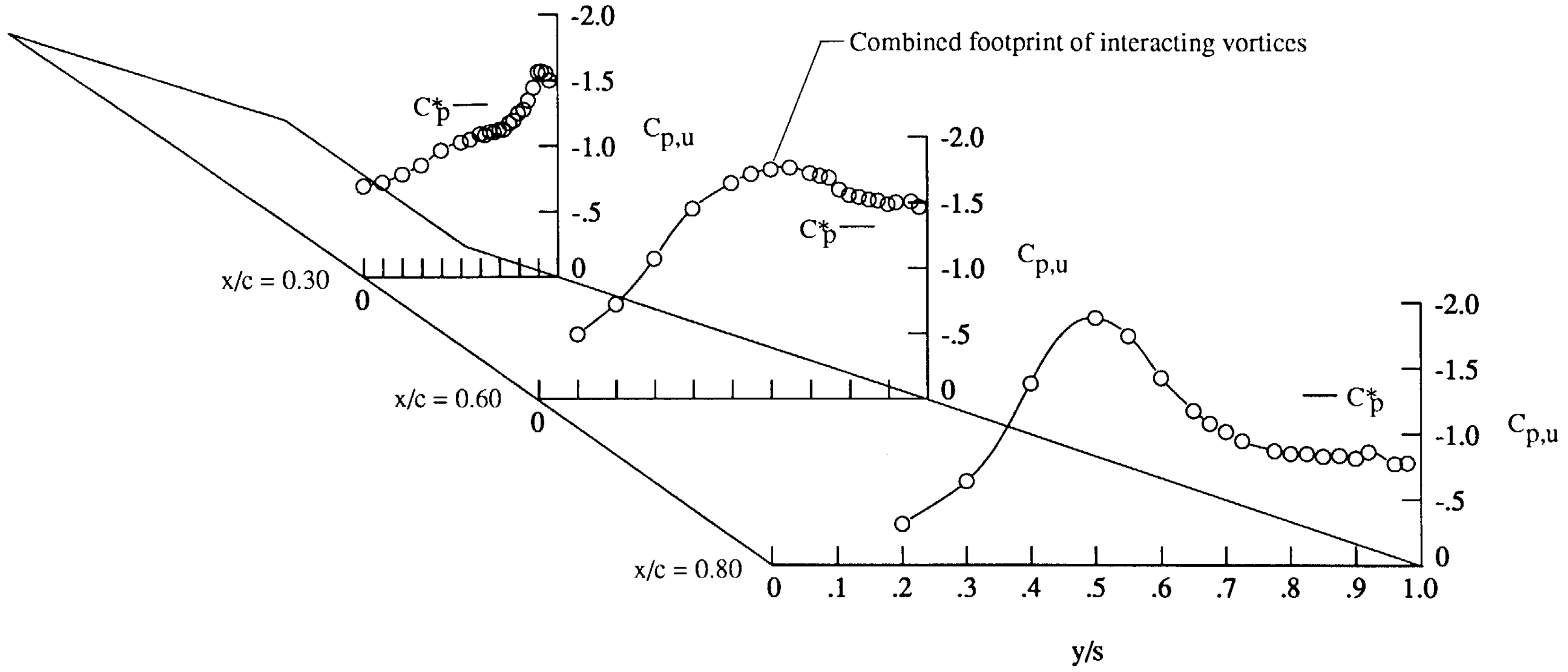

Figure 86. Wing upper surface static pressure distributions at $\alpha = 24°$ and $M_\infty = 0.60$ with LEX on.

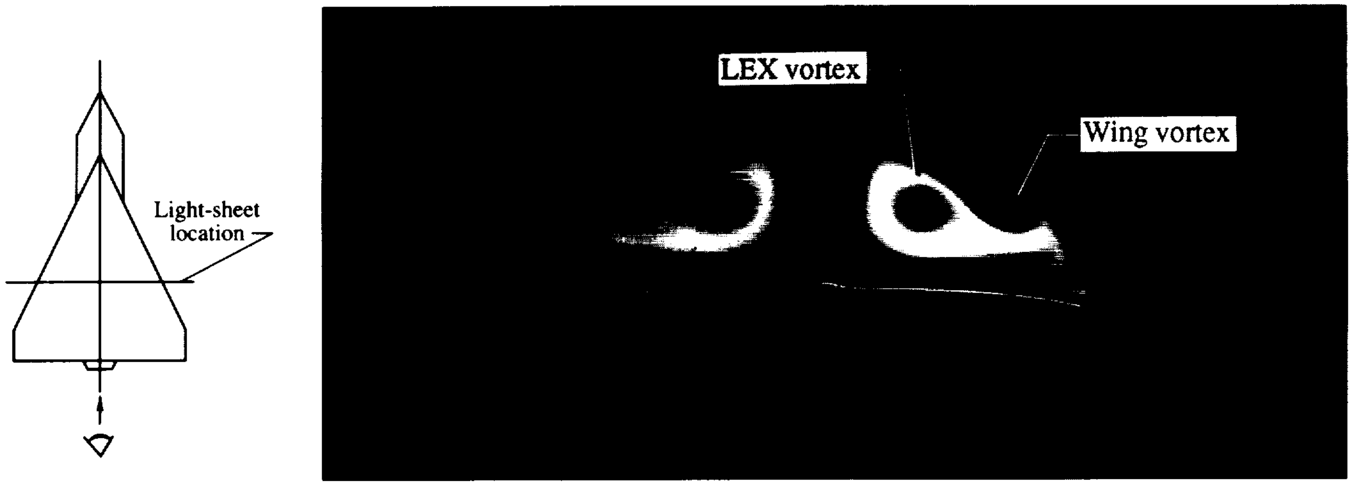

(a) $x/c = 0.60$.

(b) $x/c = 0.80$.

(c) $x/c = 1.00$.

Figure 87. Laser vapor screen flow visualizations at $\alpha = 24^\circ$ and $M_\infty = 0.60$ with LEX on.

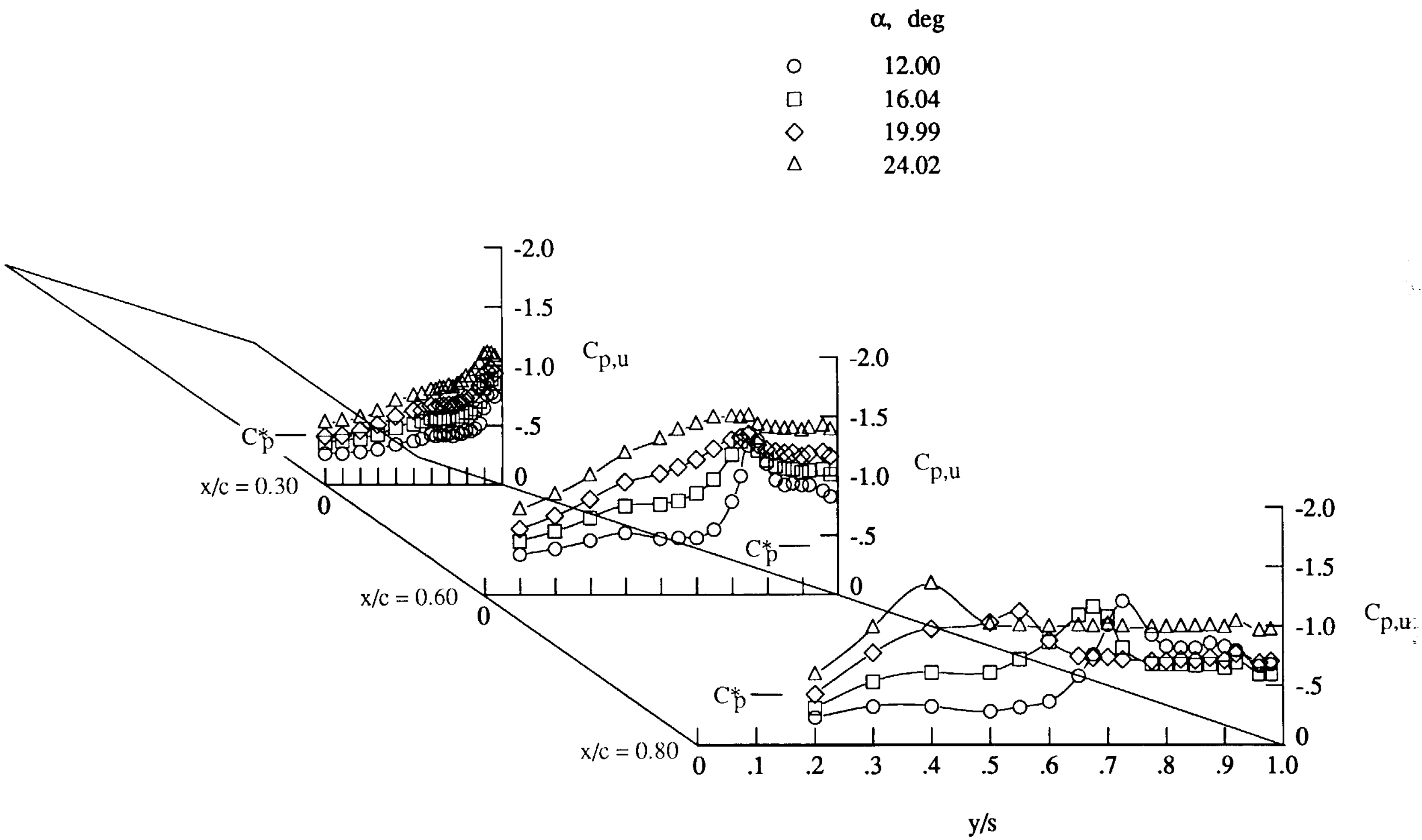

Figure 88. Wing upper surface static pressure distributions at $M_\infty = 0.80$ with LEX on.

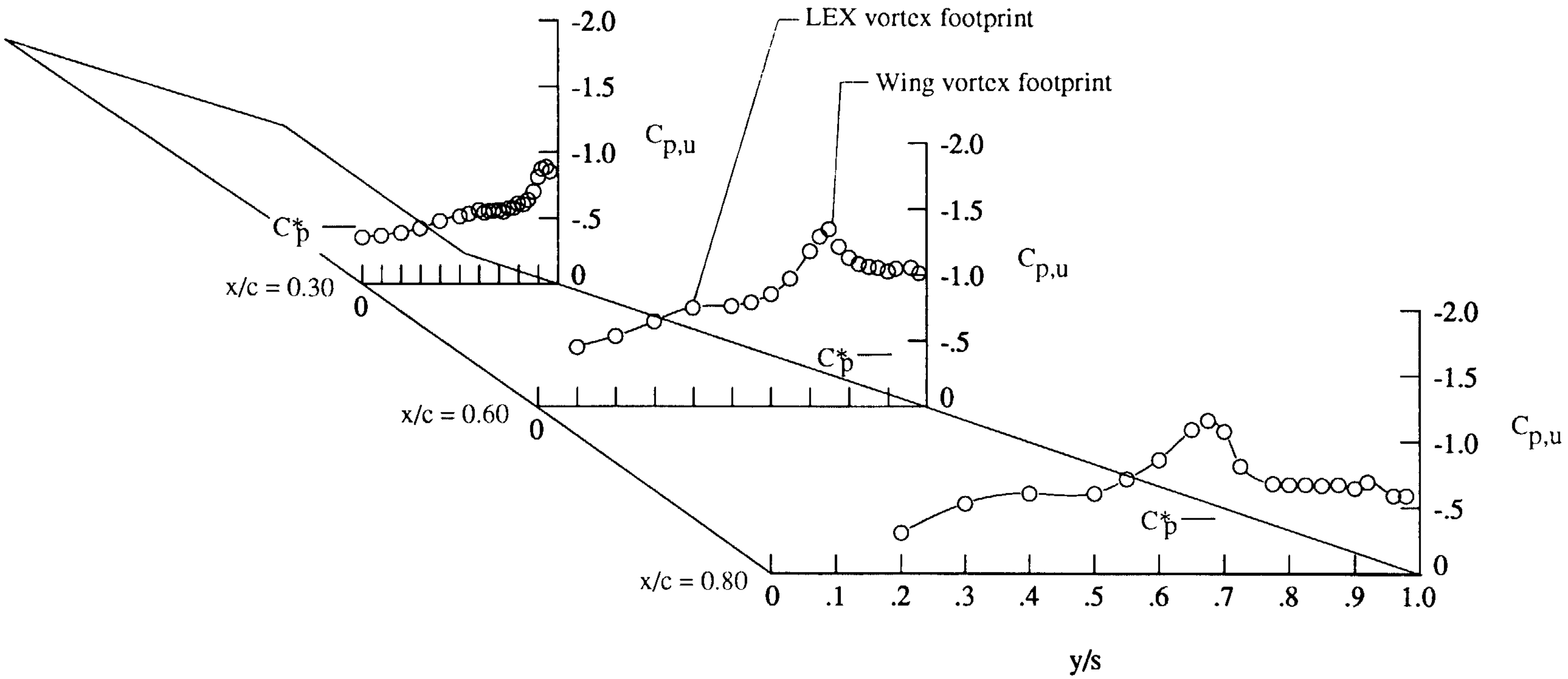

Figure 89. Wing upper surface static pressure distributions at $\alpha = 16°$ and $M_\infty = 0.80$ with LEX on.

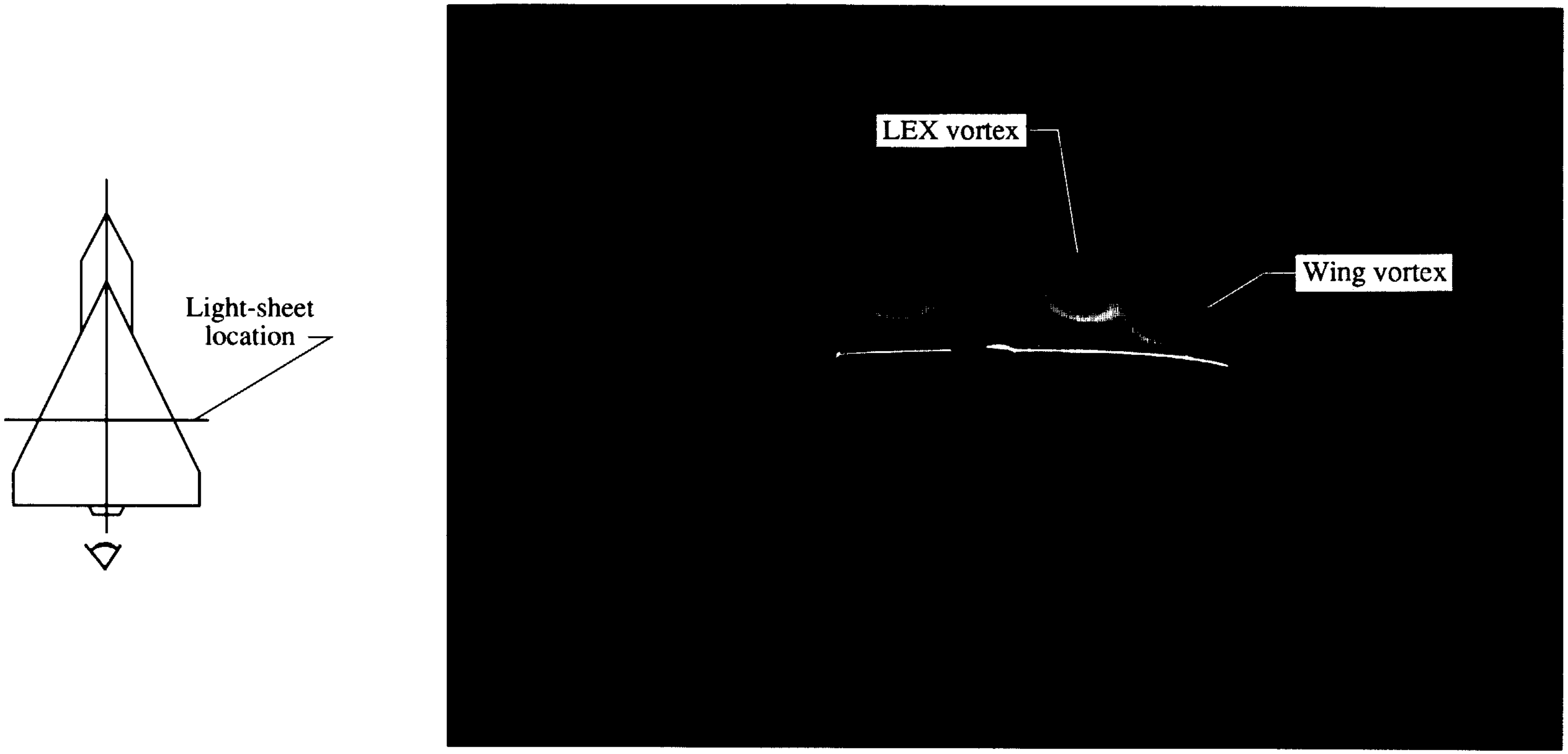

(a) $x/c = 0.60$.

Figure 90. Laser vapor screen flow visualizations at $\alpha = 16°$ and $M_\infty = 0.80$ with LEX on.

(b) $x/c = 0.80$.

Figure 90. Continued.

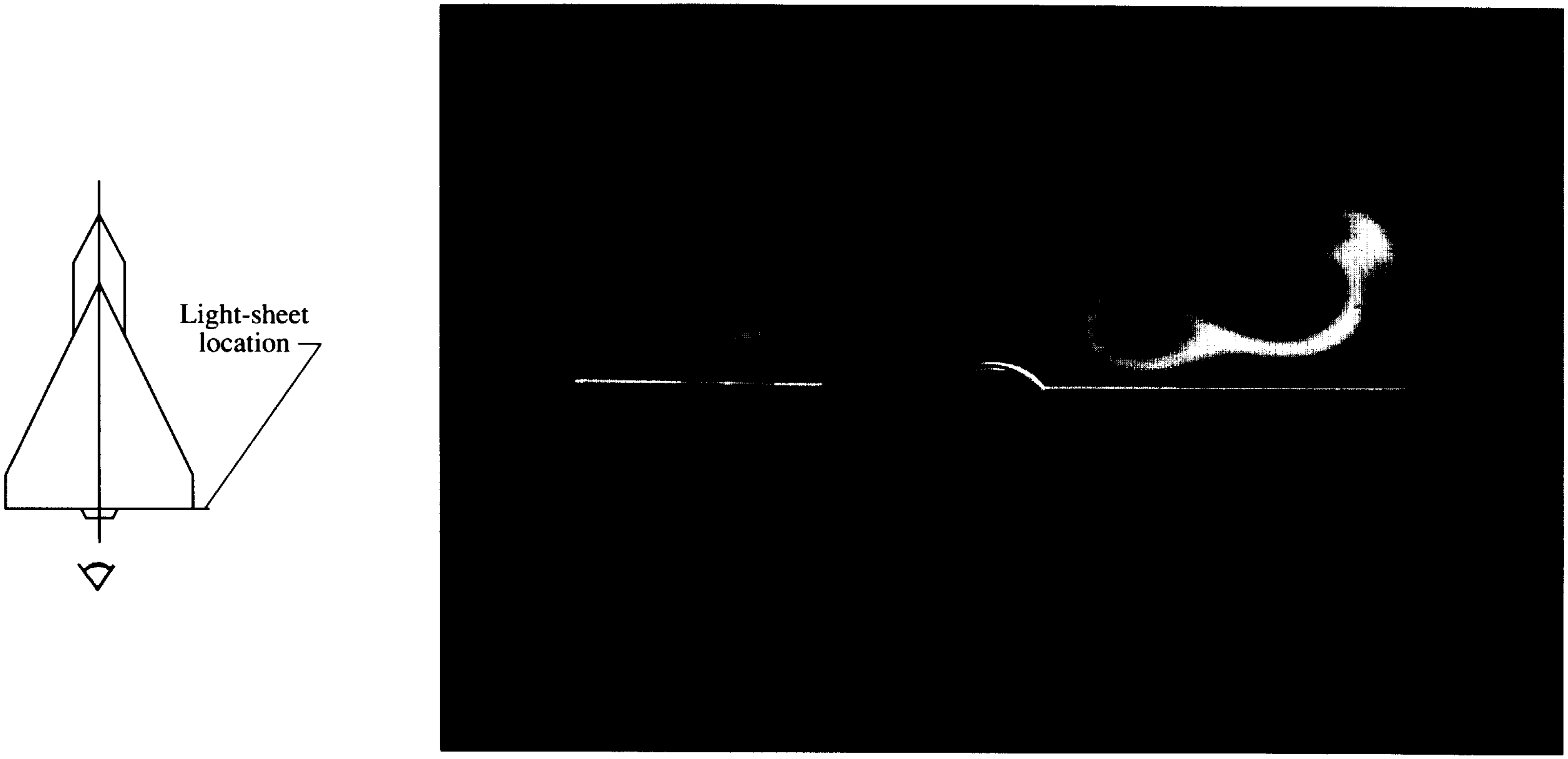

(c) $x/c = 1.00$.

Figure 90. Continued.

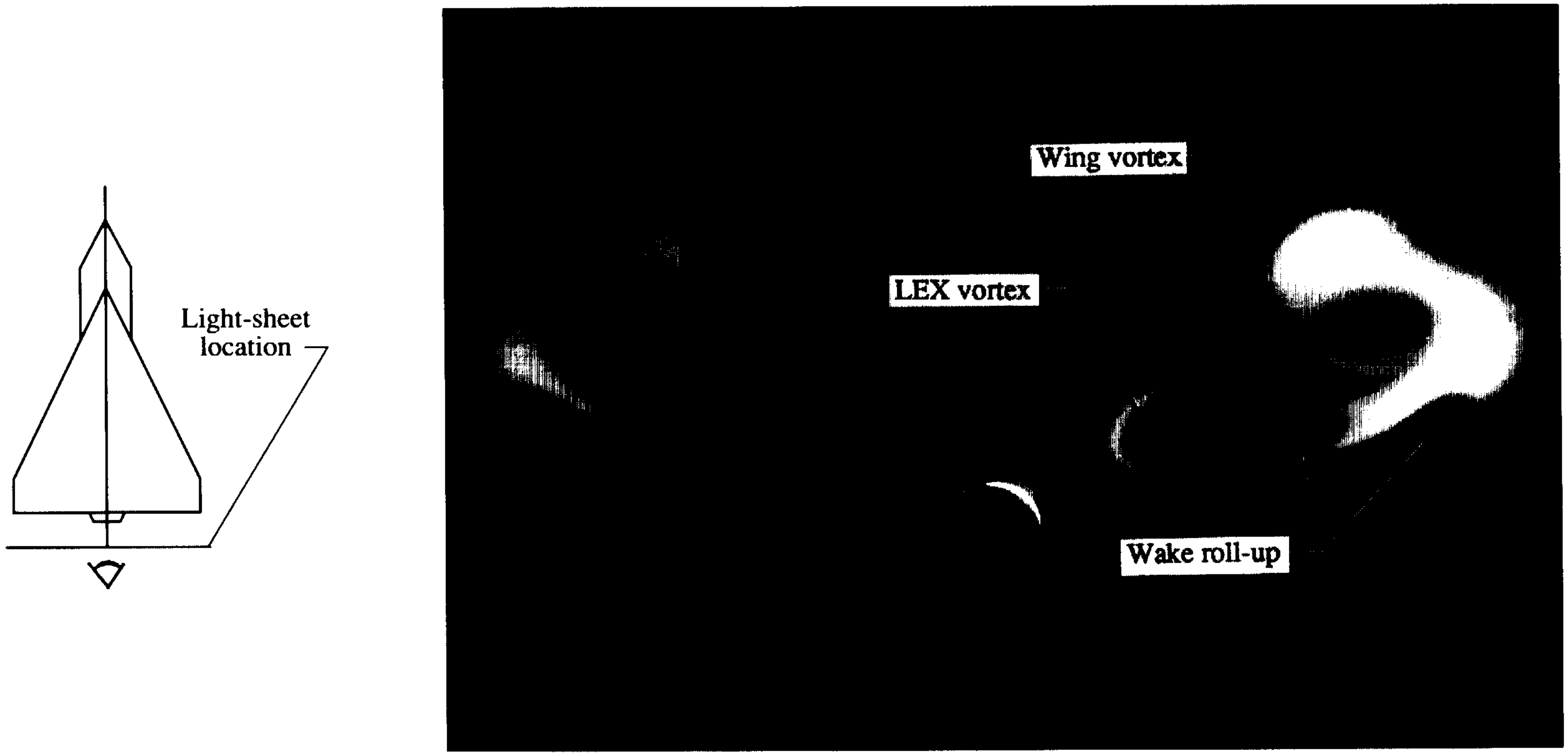

(d) $x/c = 1.20$.

Figure 90. Concluded.

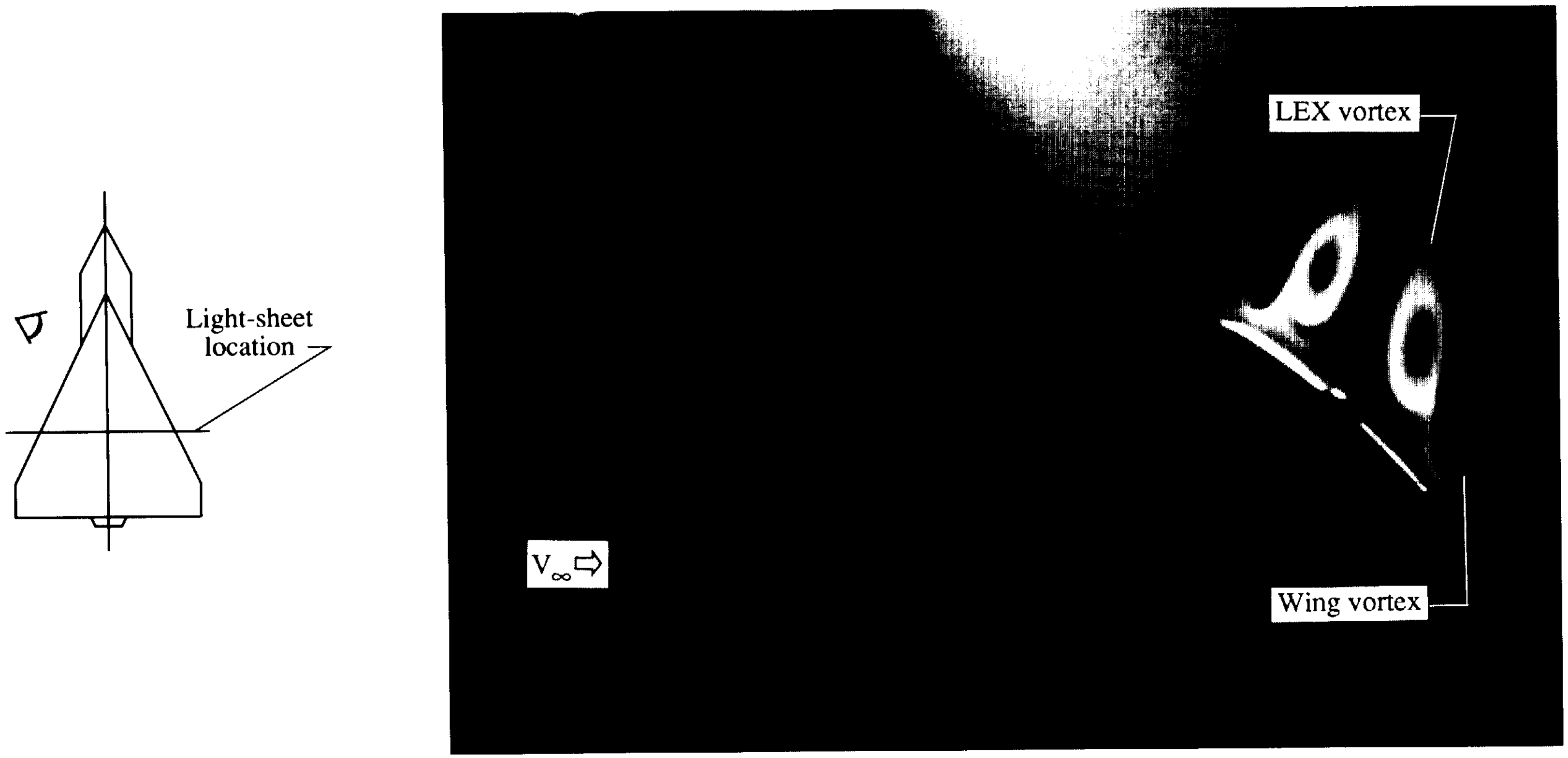

(a) $x/c = 0.60$.

Figure 91. Laser vapor screen flow visualizations at $\alpha = 16°$ and $M_\infty = 0.80$ with LEX on.

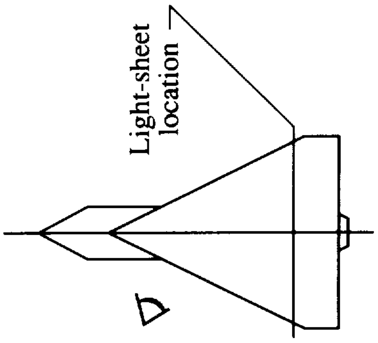

(b) $x/c = 0.80$.

Figure 91. Continued.

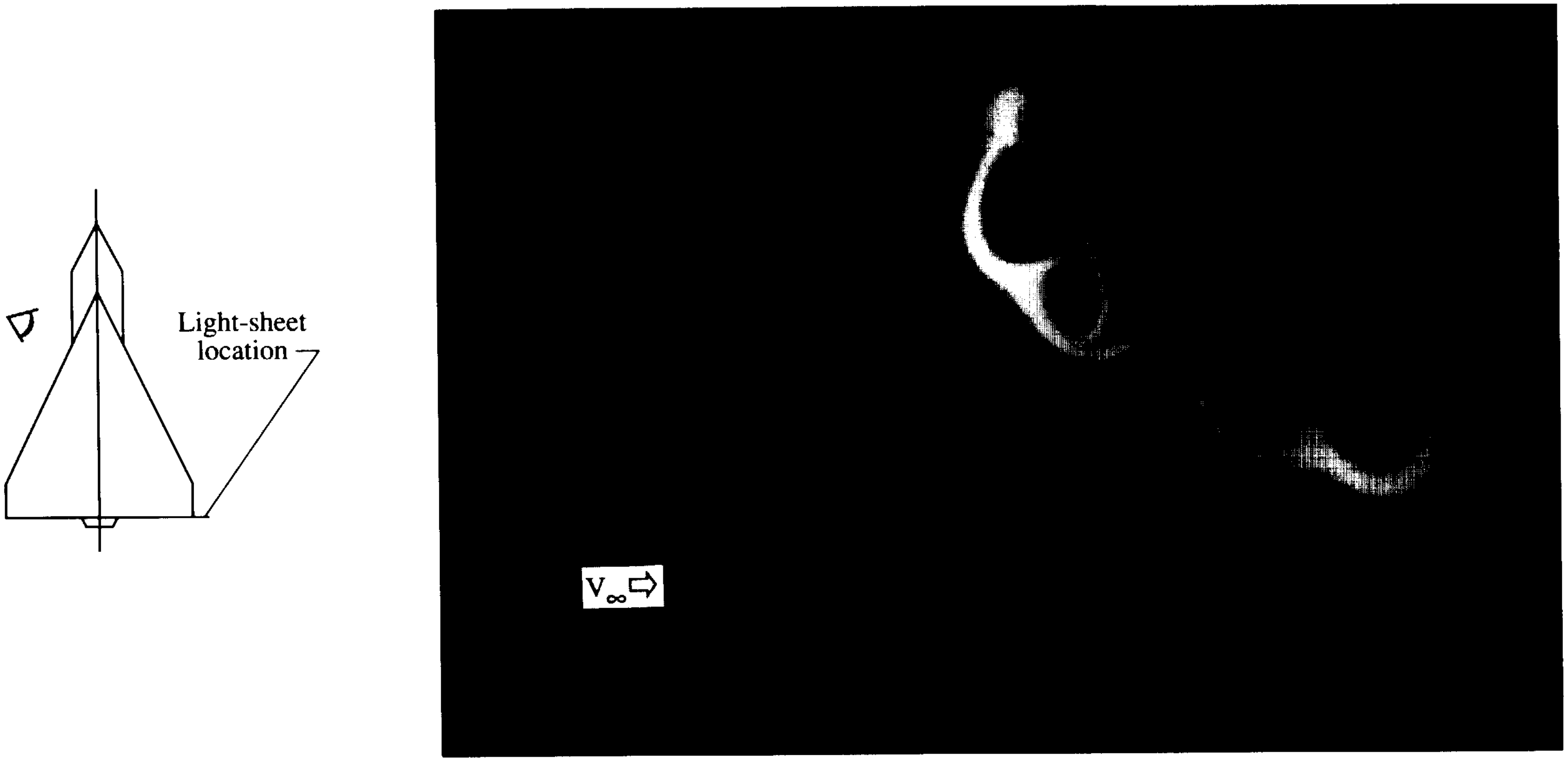

(c) $x/c = 1.00$.

Figure 91. Continued.

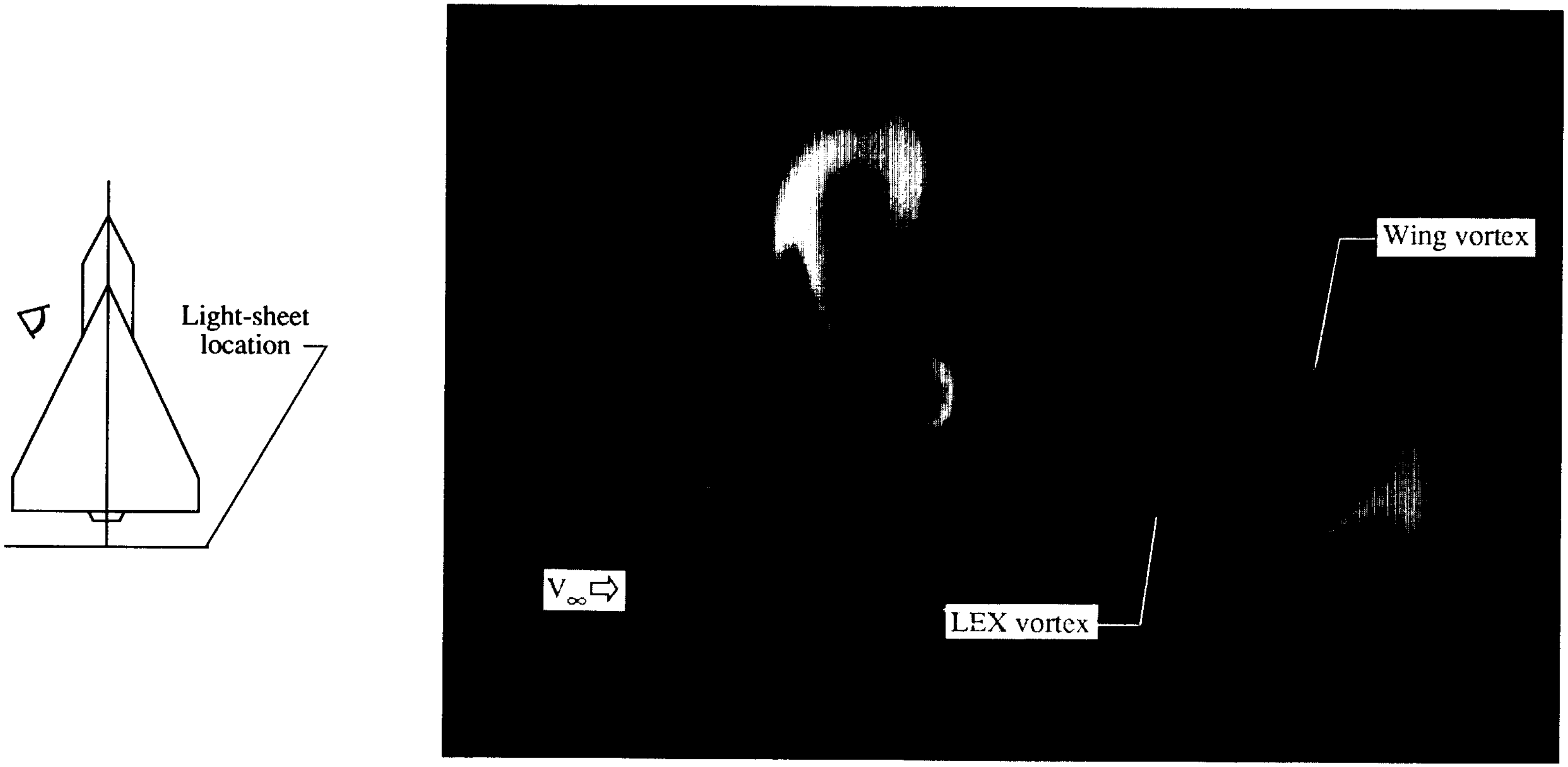

(d) $x/c = 1.20$.

Figure 91. Concluded.

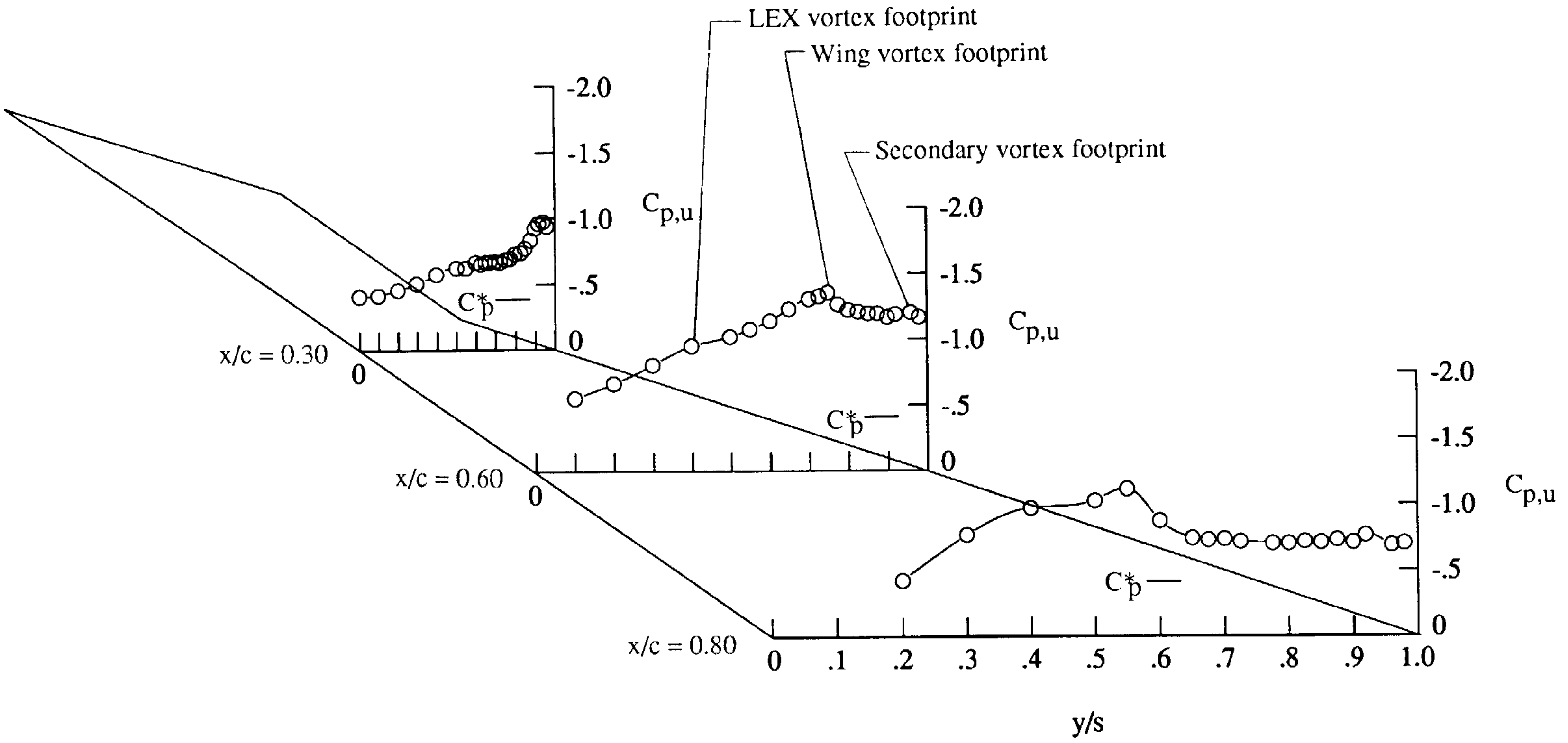

Figure 92. Wing upper surface static pressure distributions at $\alpha = 20°$ and $M_\infty = 0.80$ with LEX on.

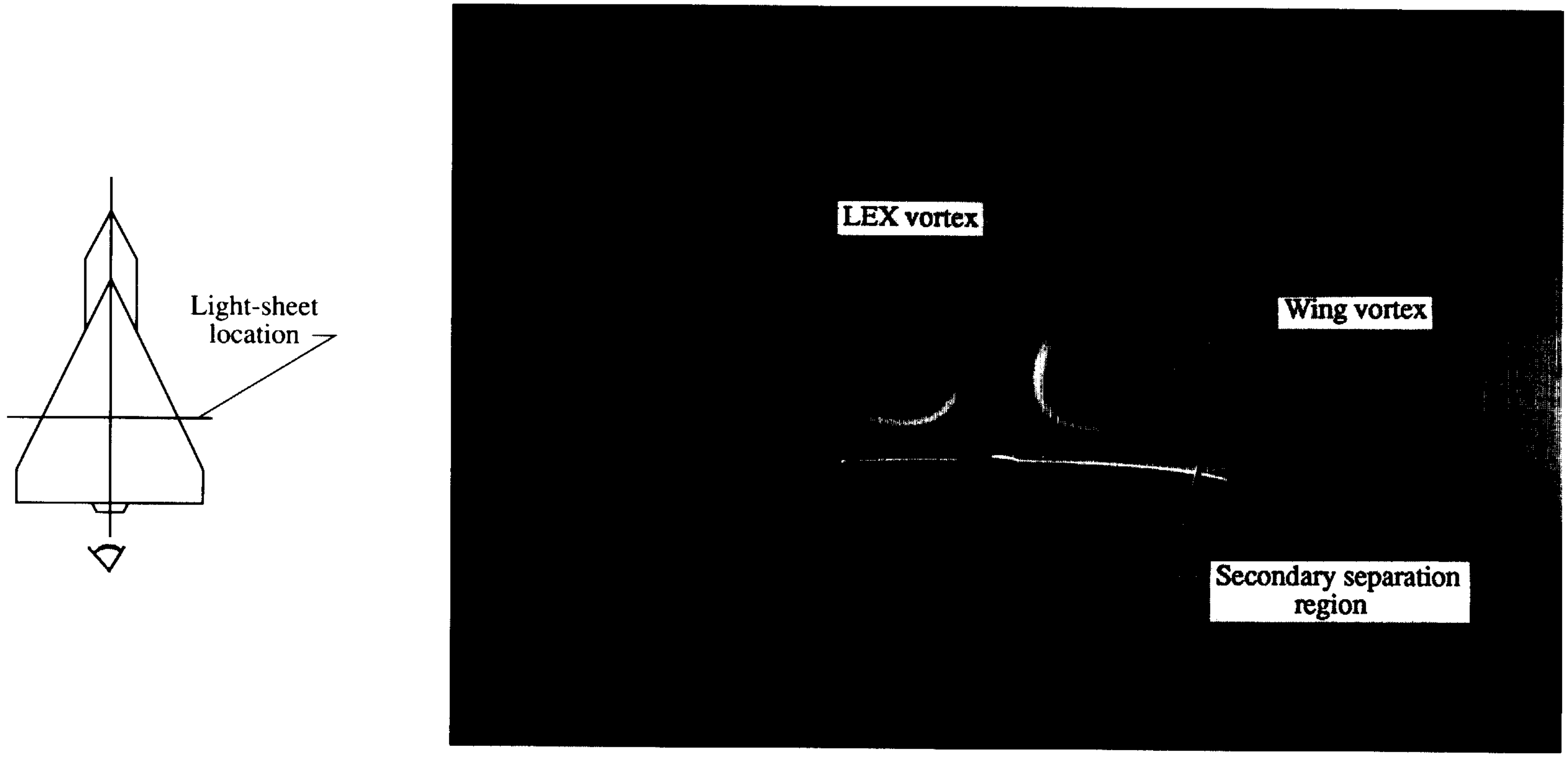

(a) $x/c = 0.60$.

Figure 93. Laser vapor screen flow visualizations at $\alpha = 20°$ and $M_\infty = 0.80$ with LEX on.

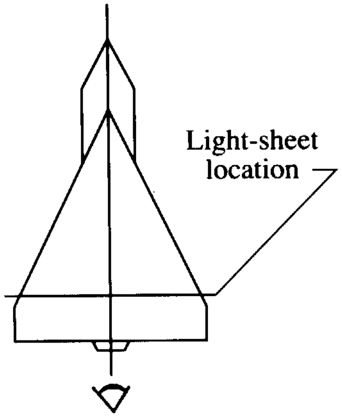

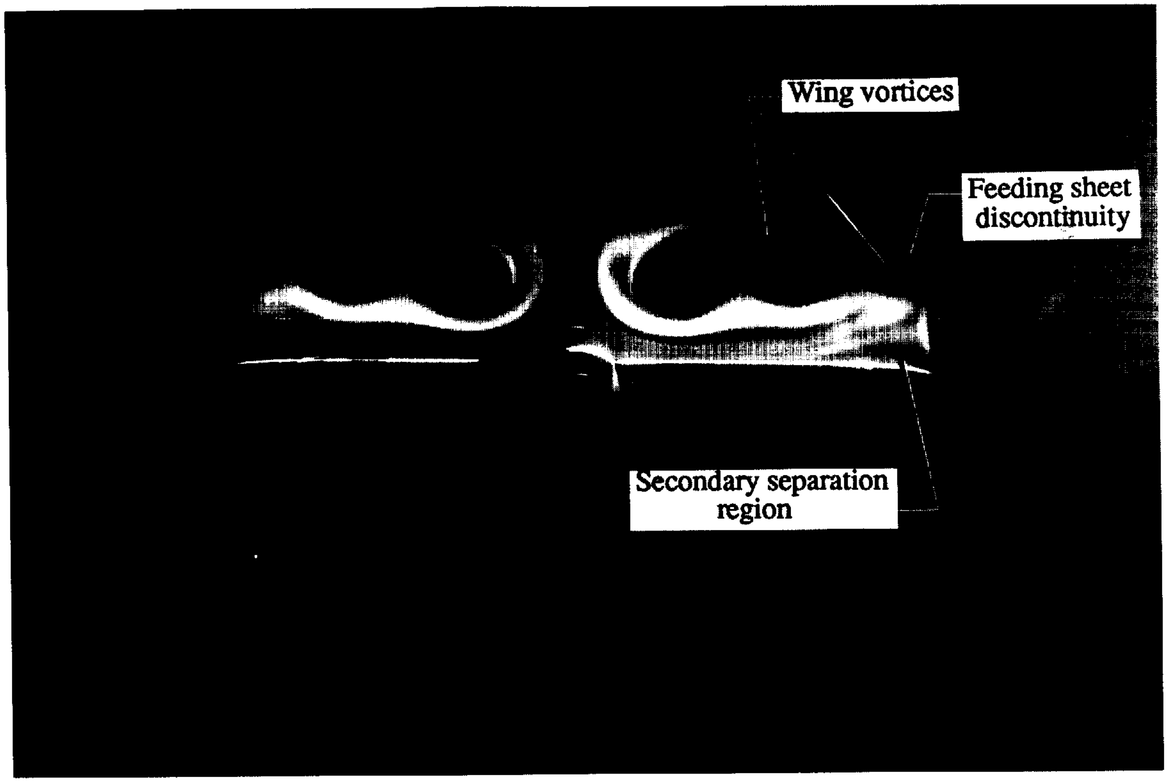

(b) $x/c = 0.80$.

Figure 93. Continued.

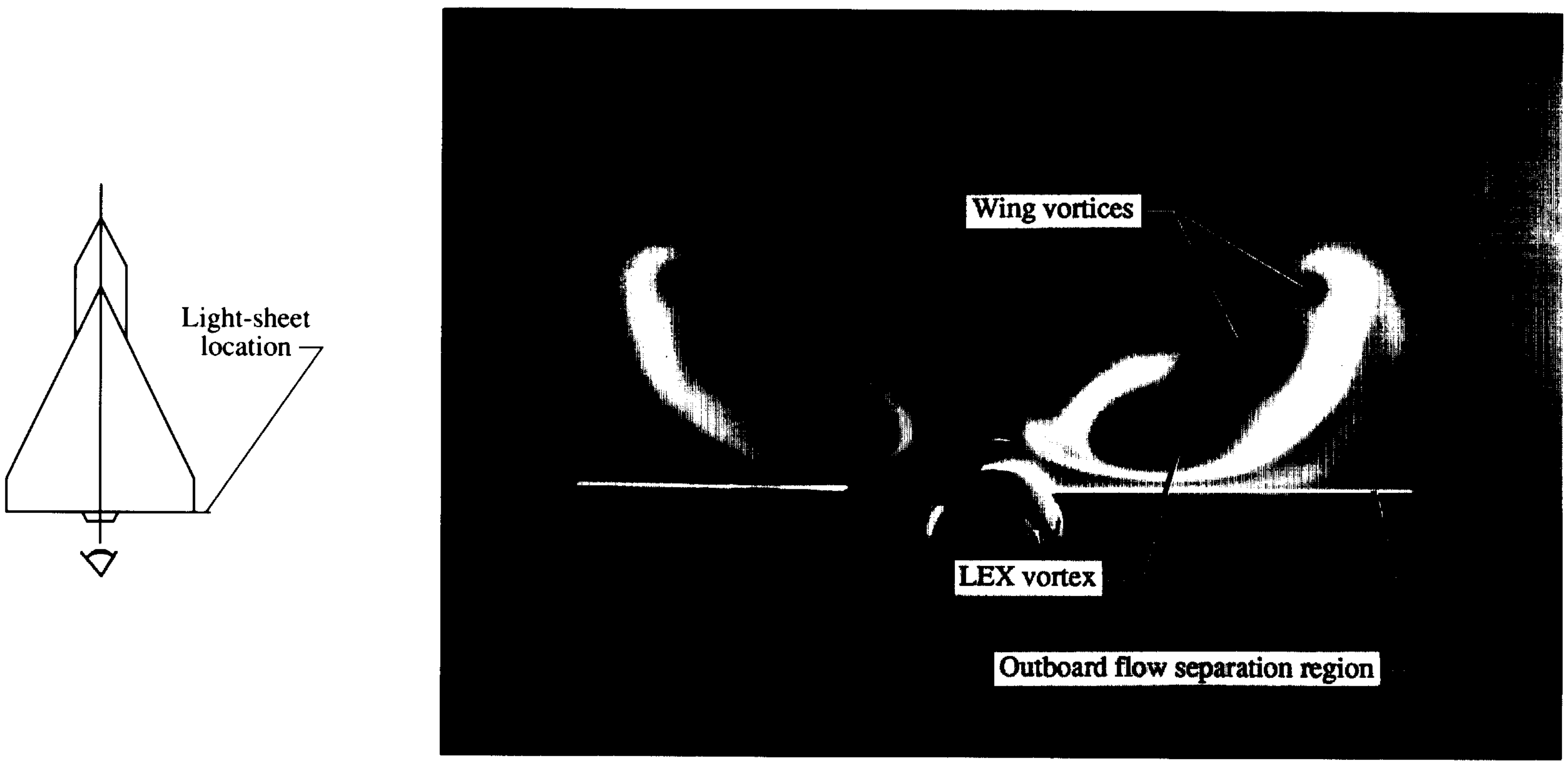

(c) $x/c = 1.00$.

Figure 93. Continued.

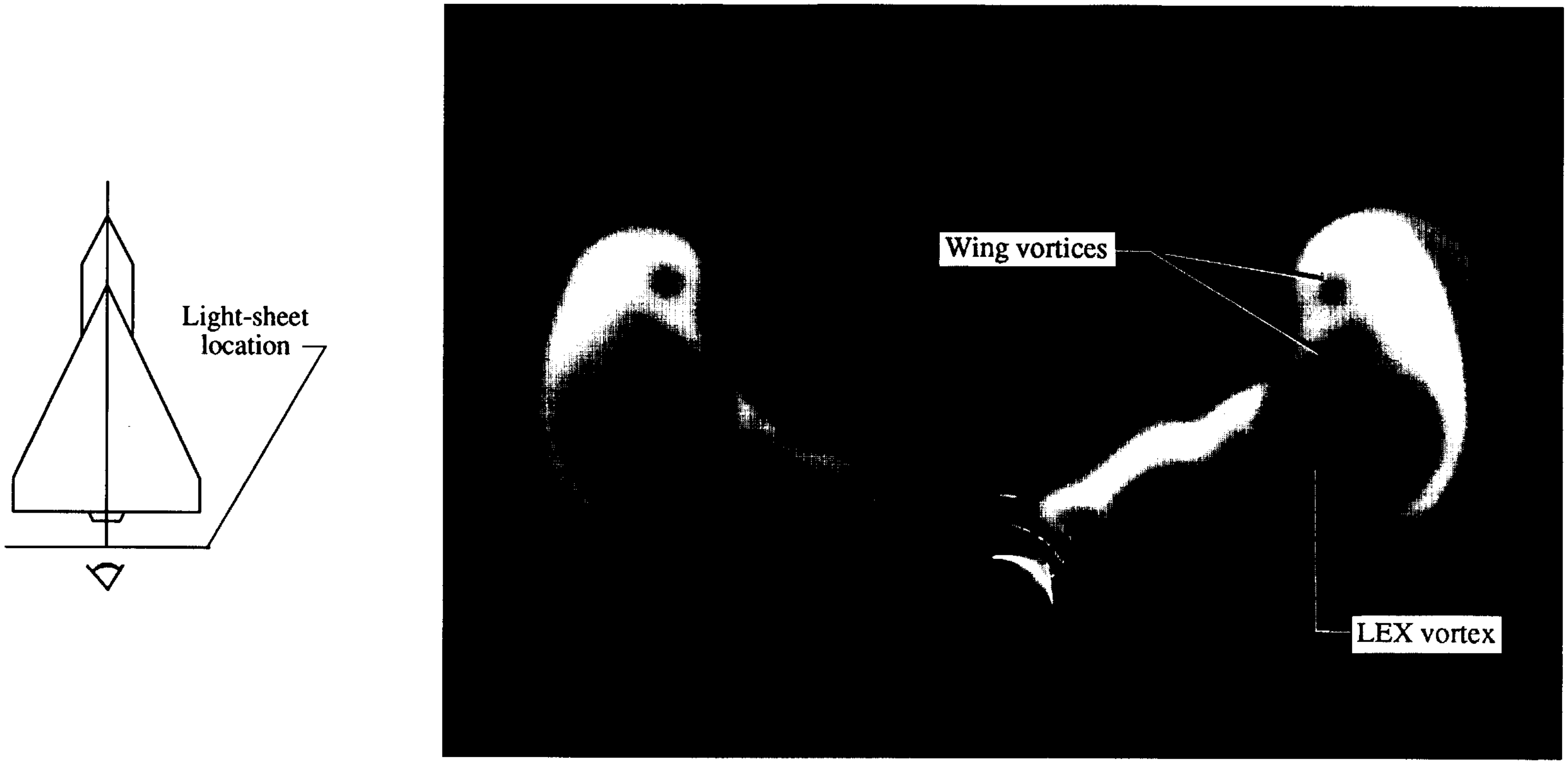

(d) $x/c = 1.20$.

Figure 93. Concluded.

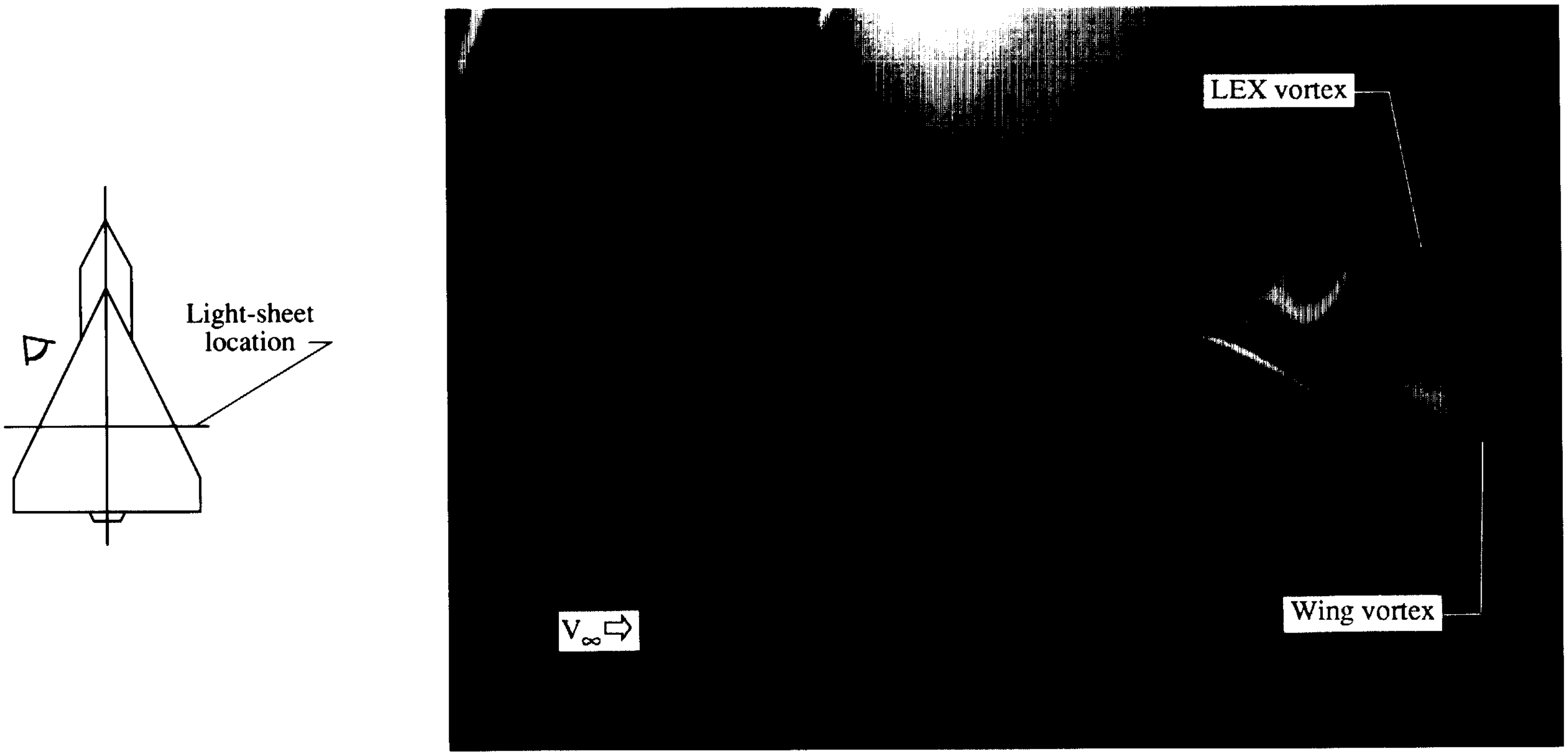

(a) $x/c = 0.60$.

Figure 94. Laser vapor screen flow visualizations at $\alpha = 20°$ and $M_\infty = 0.80$ with LEX on.

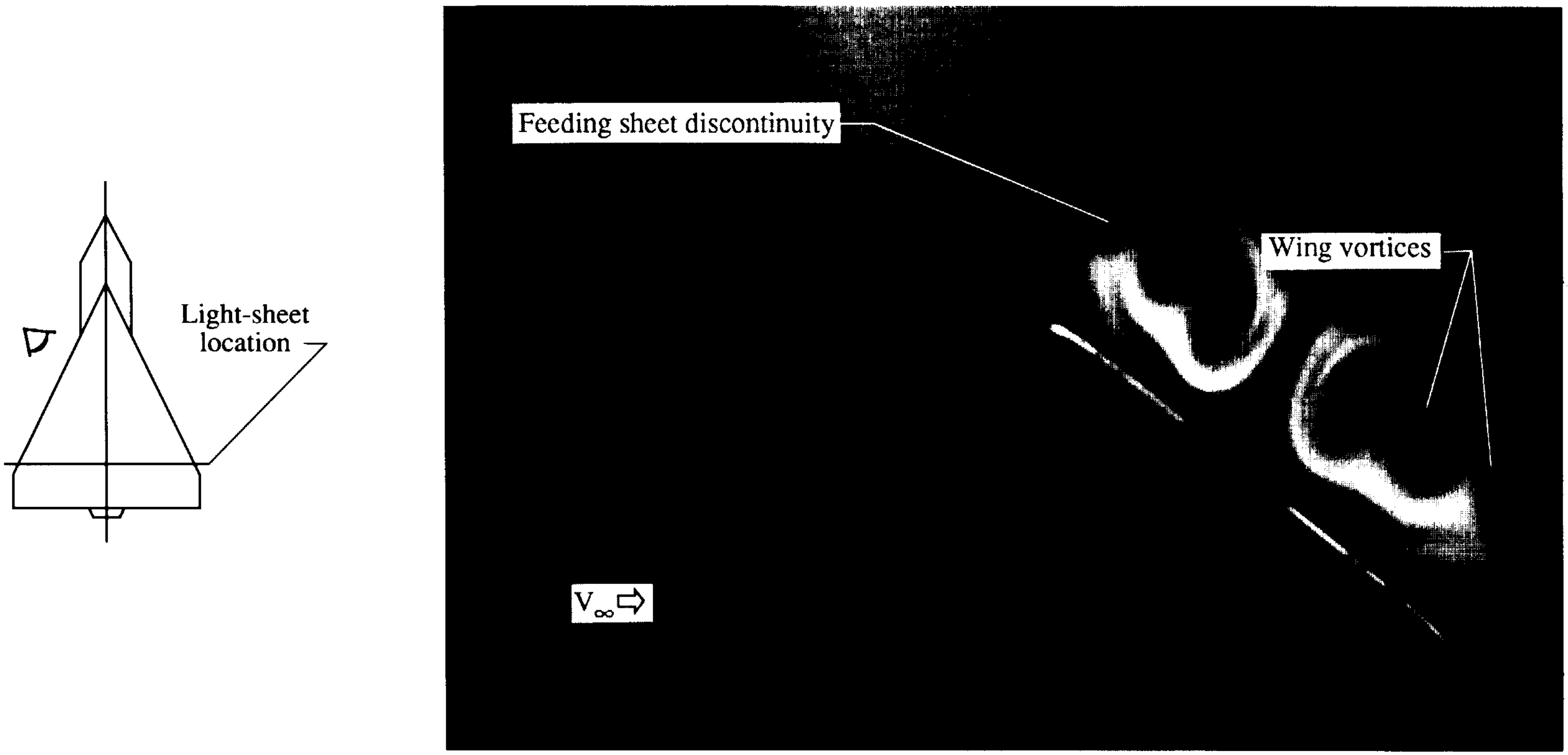

(b) $x/c = 0.80$.

Figure 94. Continued.

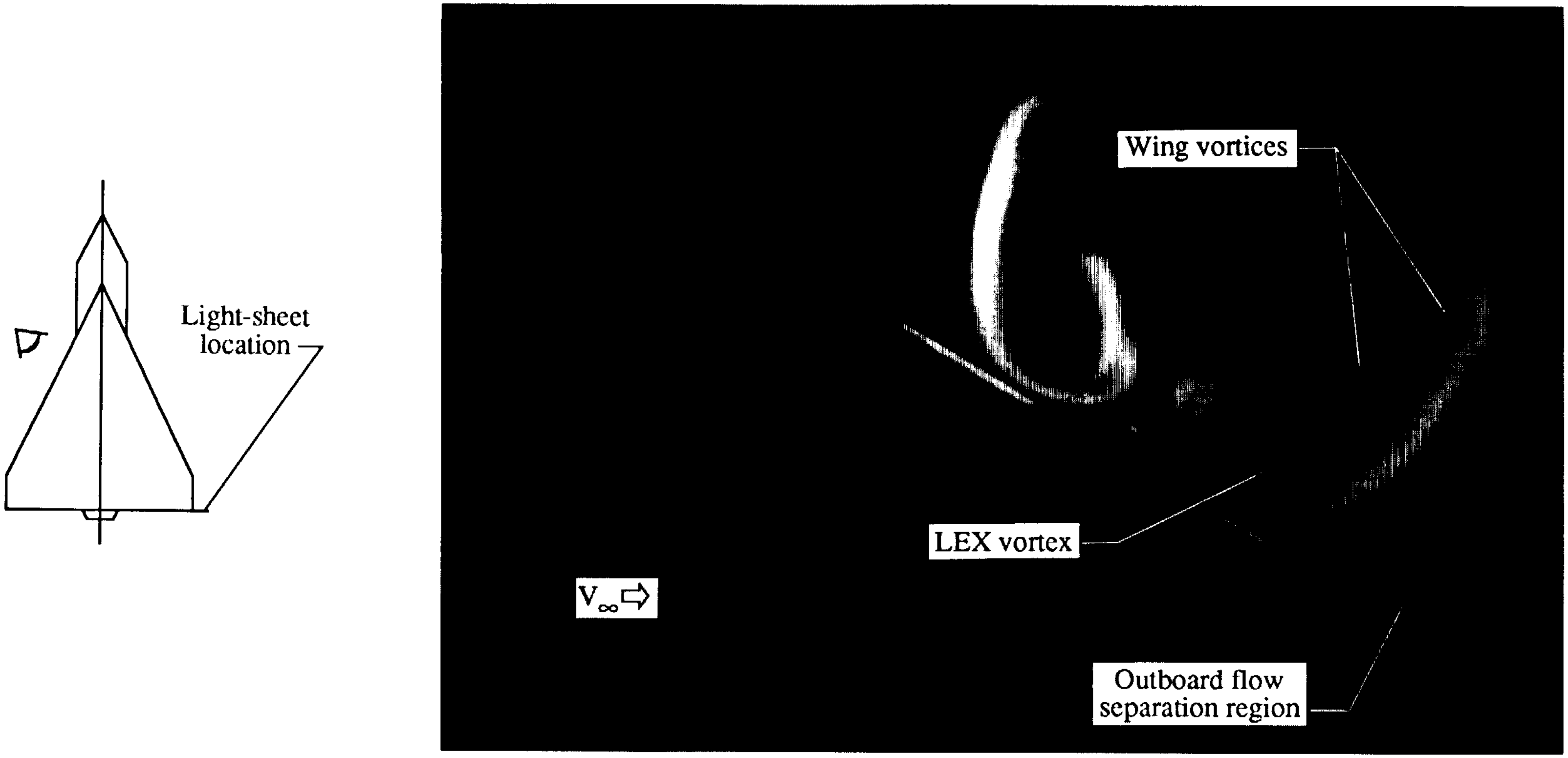

(c) $x/c = 1.00$.

Figure 94. Continued.

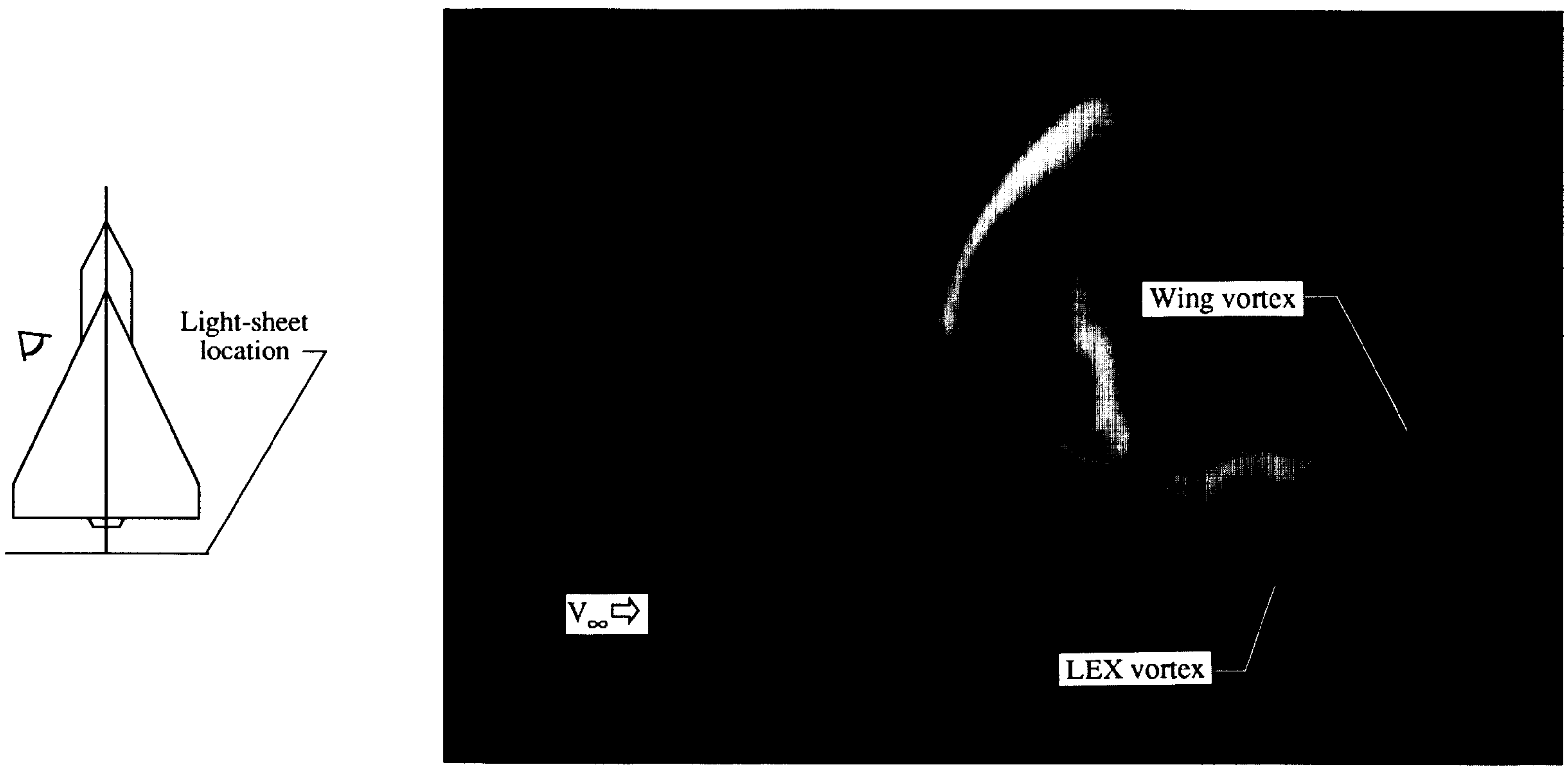

(d) $x/c = 1.20$.

Figure 94. Concluded.

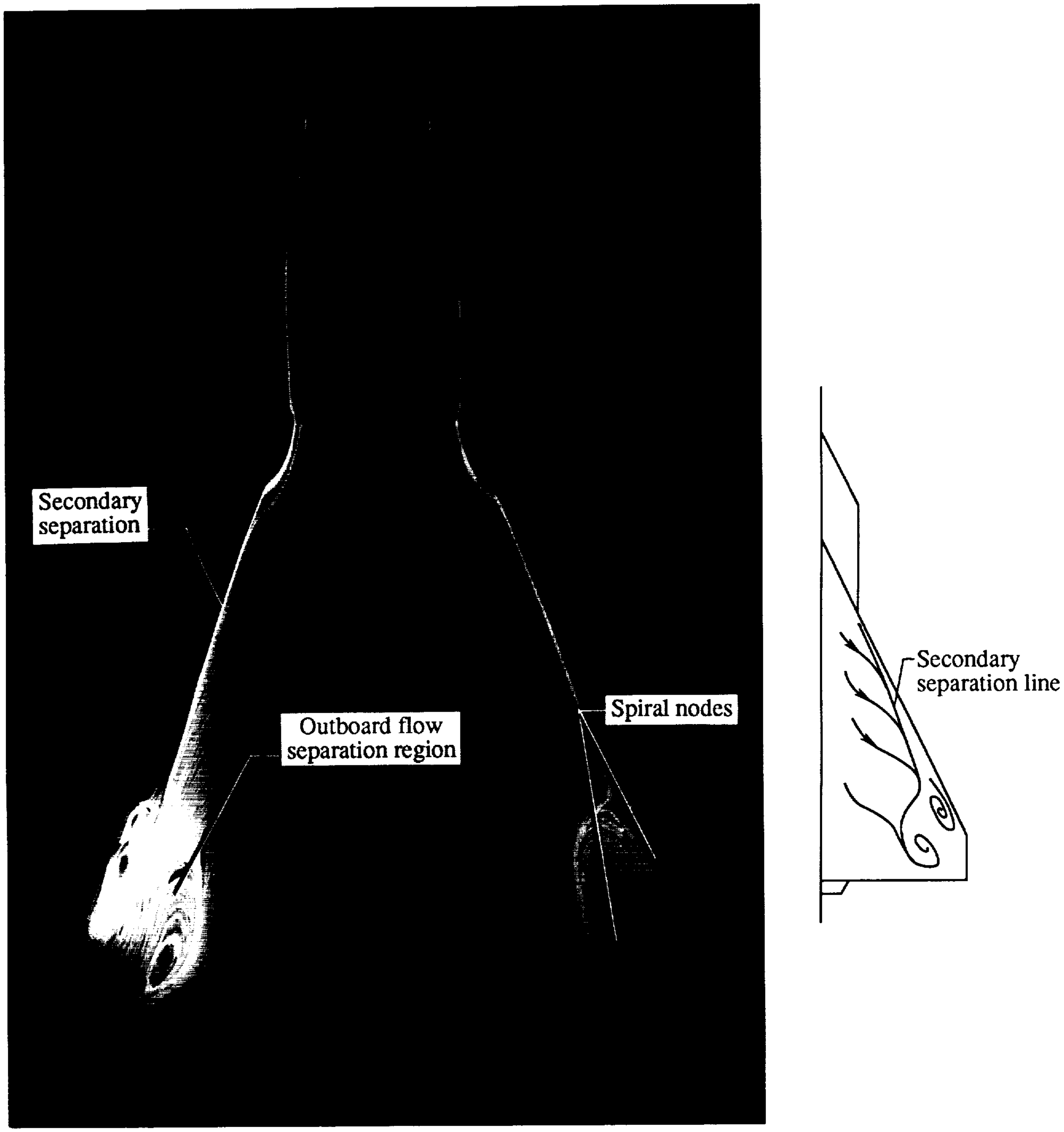

Figure 95. Wing upper surface oil flow pattern at $\alpha = 20^\circ$ and $M_\infty = 0.80$ with LEX on.

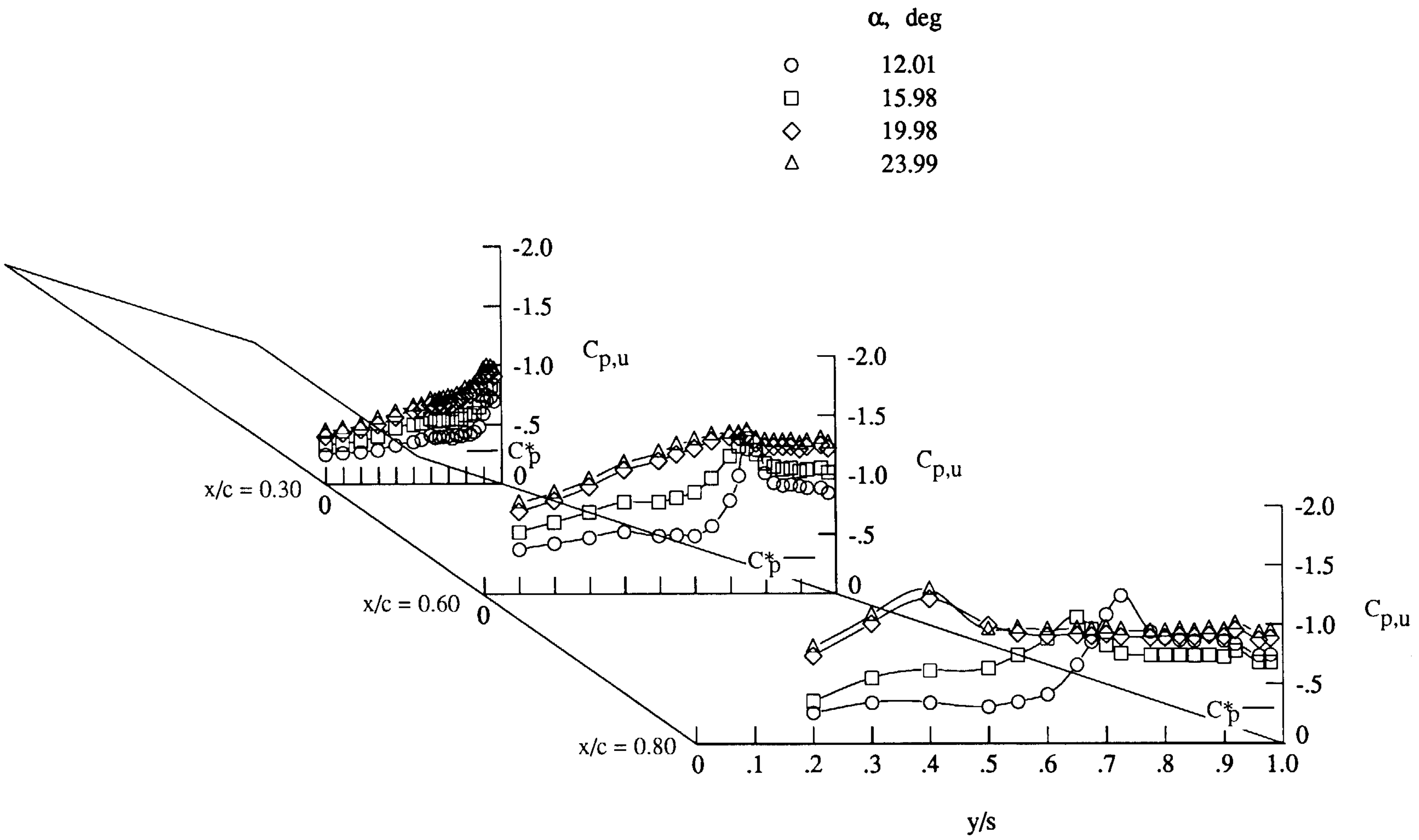

Figure 96. Wing upper surface static pressure distributions at $M_\infty = 0.85$ with LEX on.

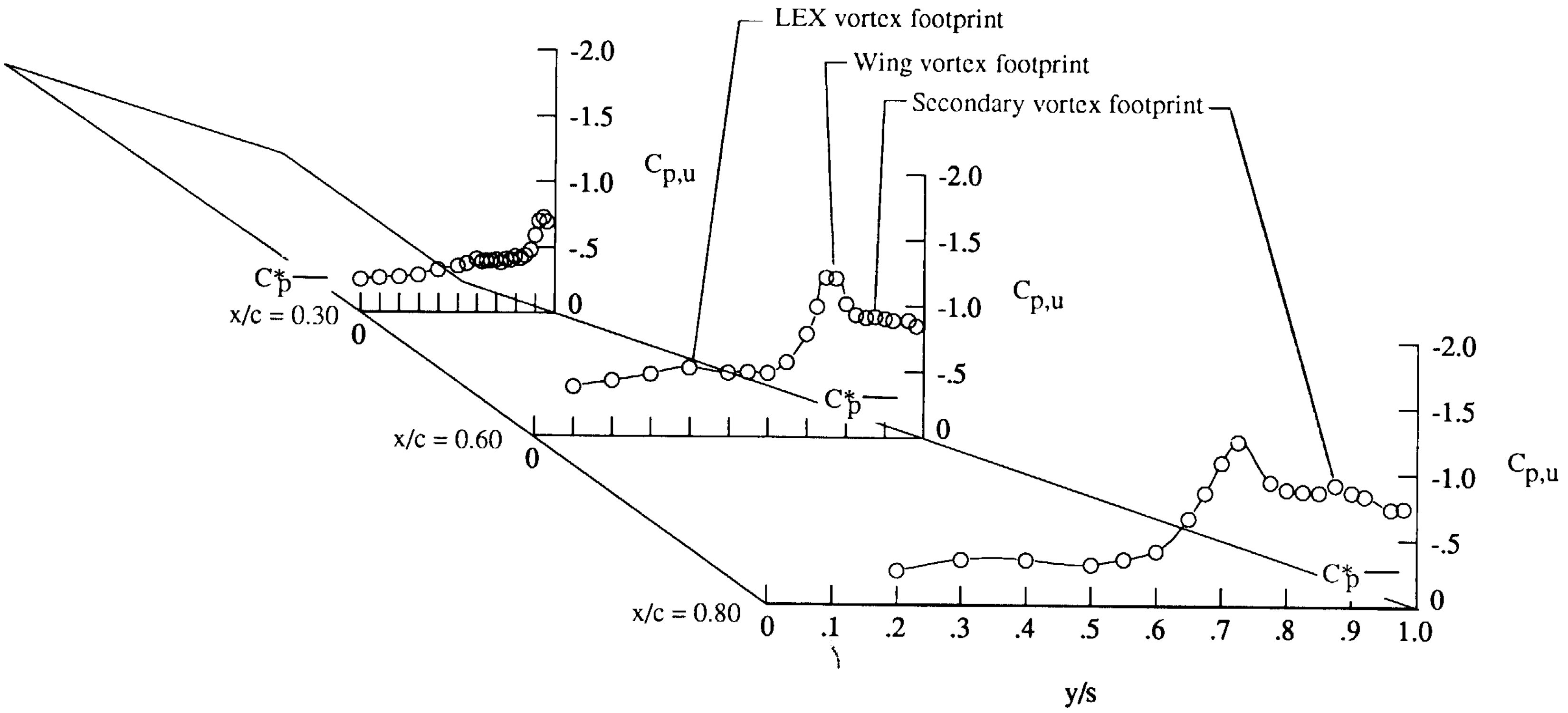

Figure 97. Wing upper surface static pressure distributions at $\alpha = 12°$ and $M_\infty = 0.85$ with LEX on.

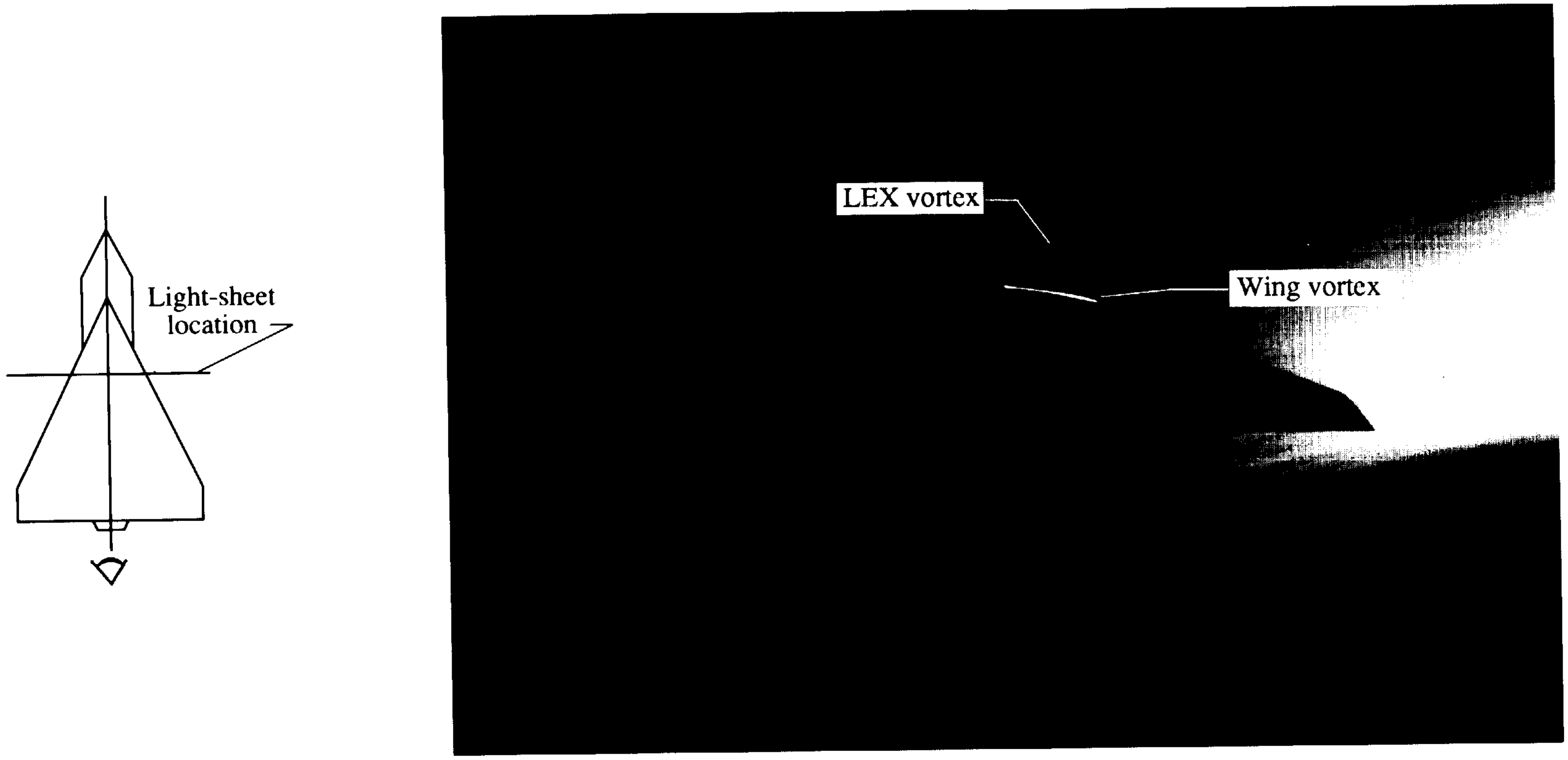

(a) $x/c = 0.30$.

Figure 98. Laser vapor screen flow visualizations at $\alpha = 12°$ and $M_\infty = 0.85$ with LEX on.

(b) $x/c = 0.60$.

Figure 98. Continued.

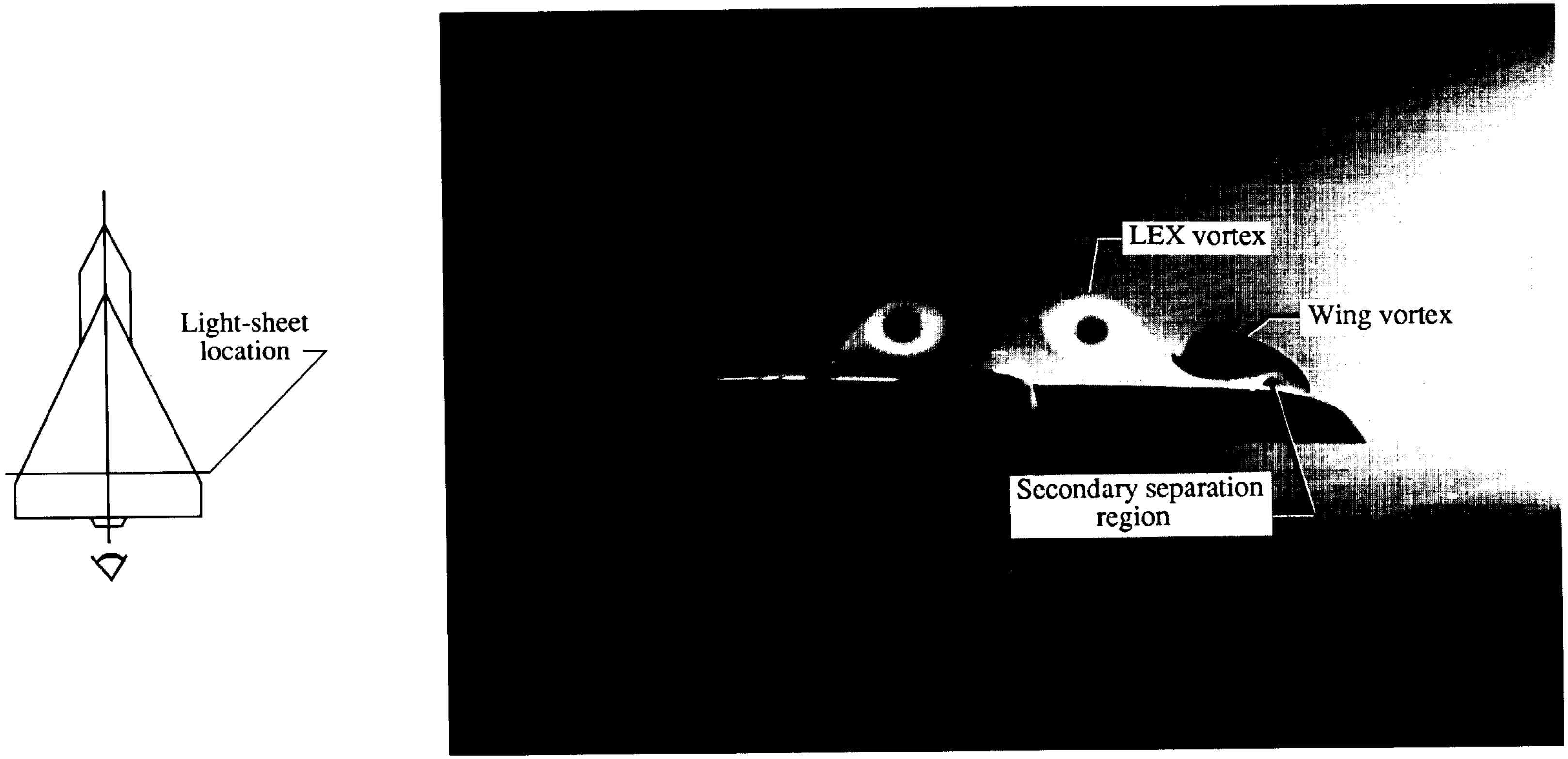

(c) $x/c = 0.80$.

Figure 98. Continued.

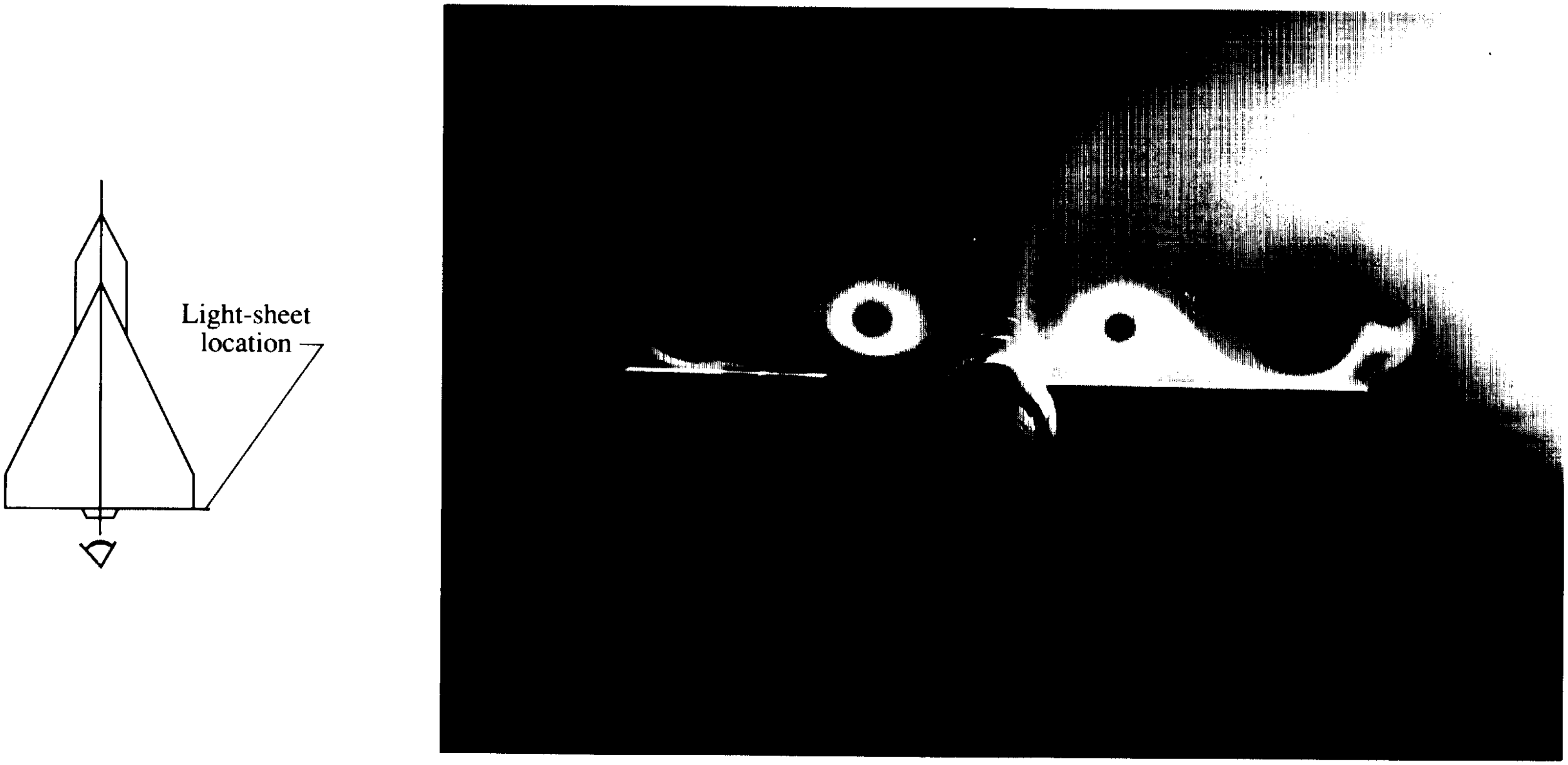

(d) $x/c = 1.00$.

Figure 98. Concluded.

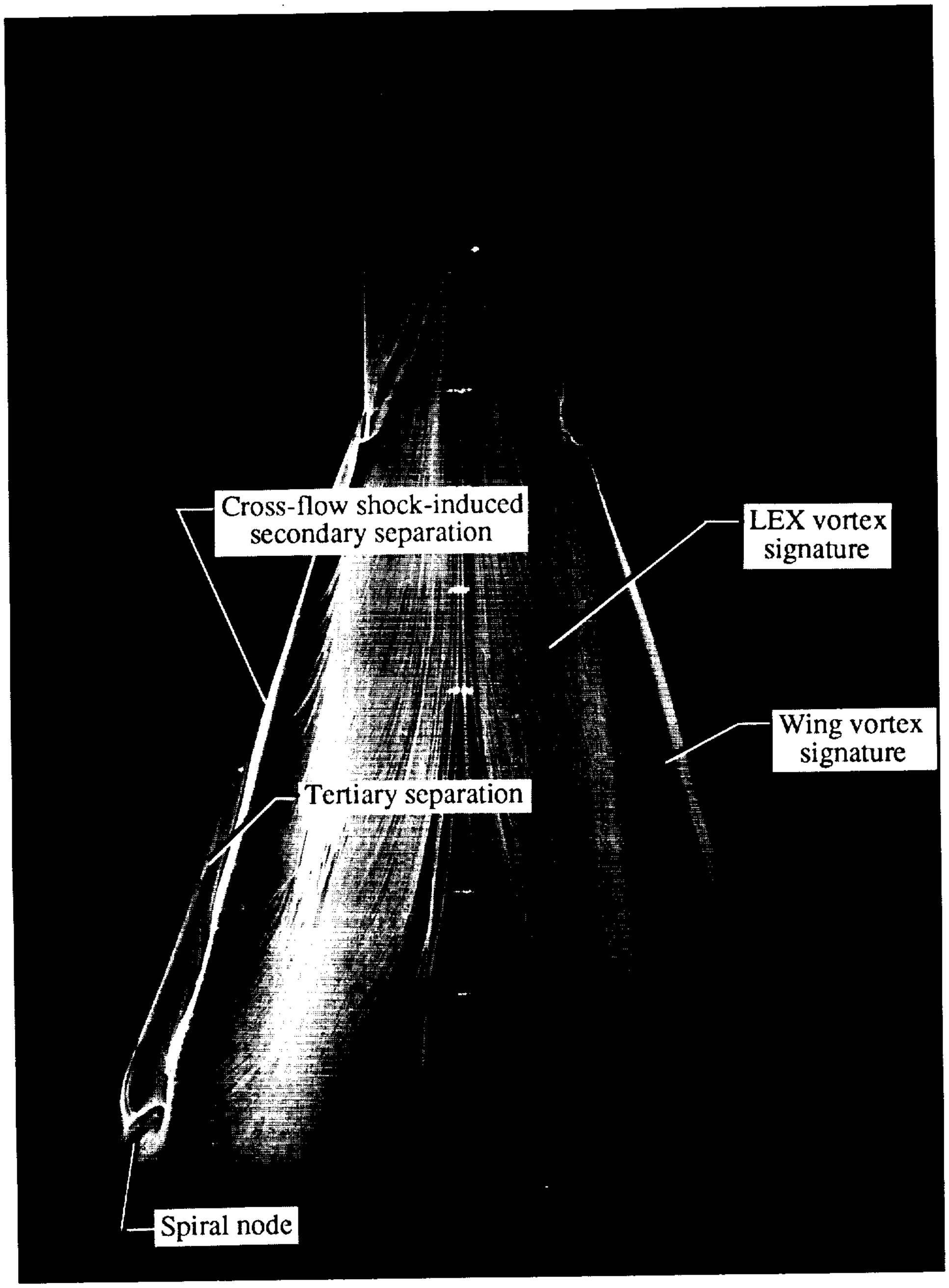

Figure 99. Wing upper surface oil flow pattern at $\alpha = 12^\circ$ and $M_\infty = 0.85$ with LEX on.

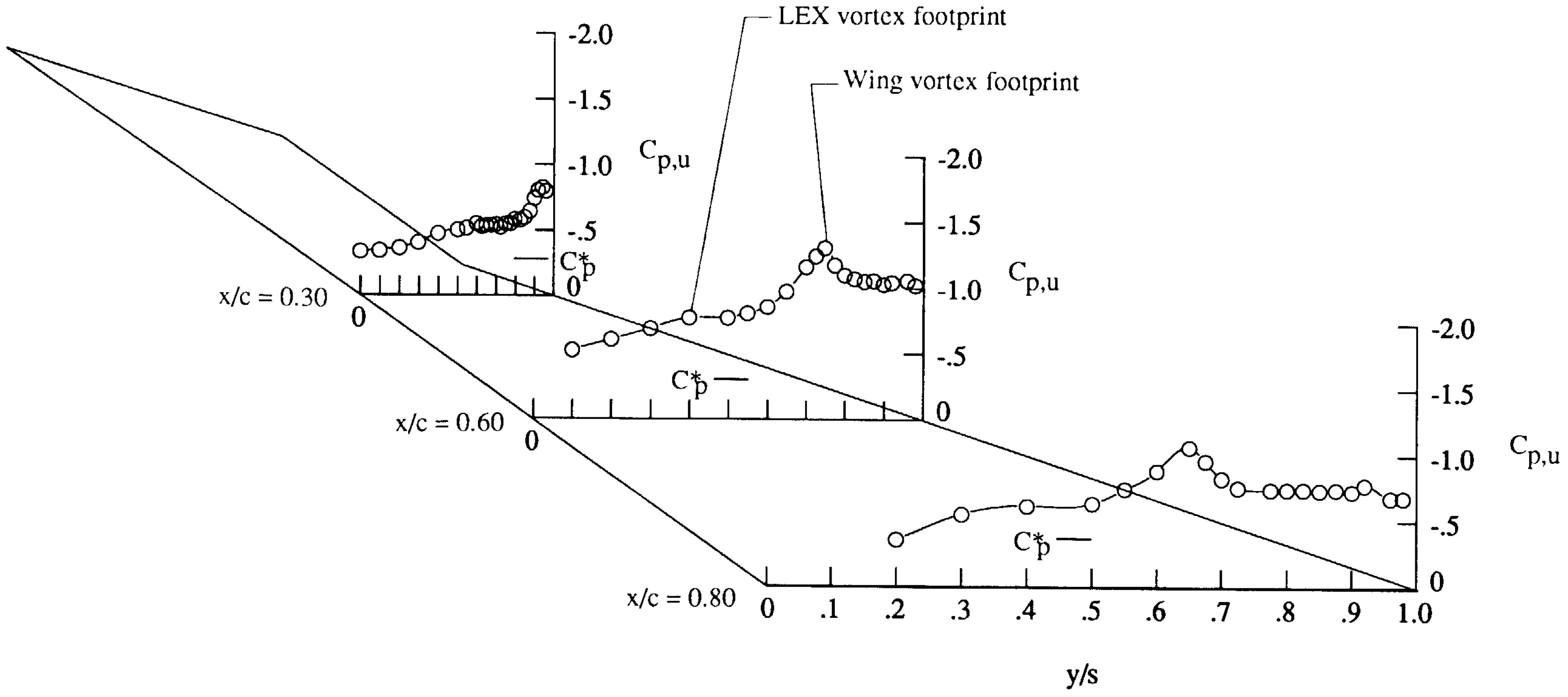

Figure 100. Wing upper surface static pressure distributions at $\alpha = 16°$ and $M_\infty = 0.85$ with LEX on.

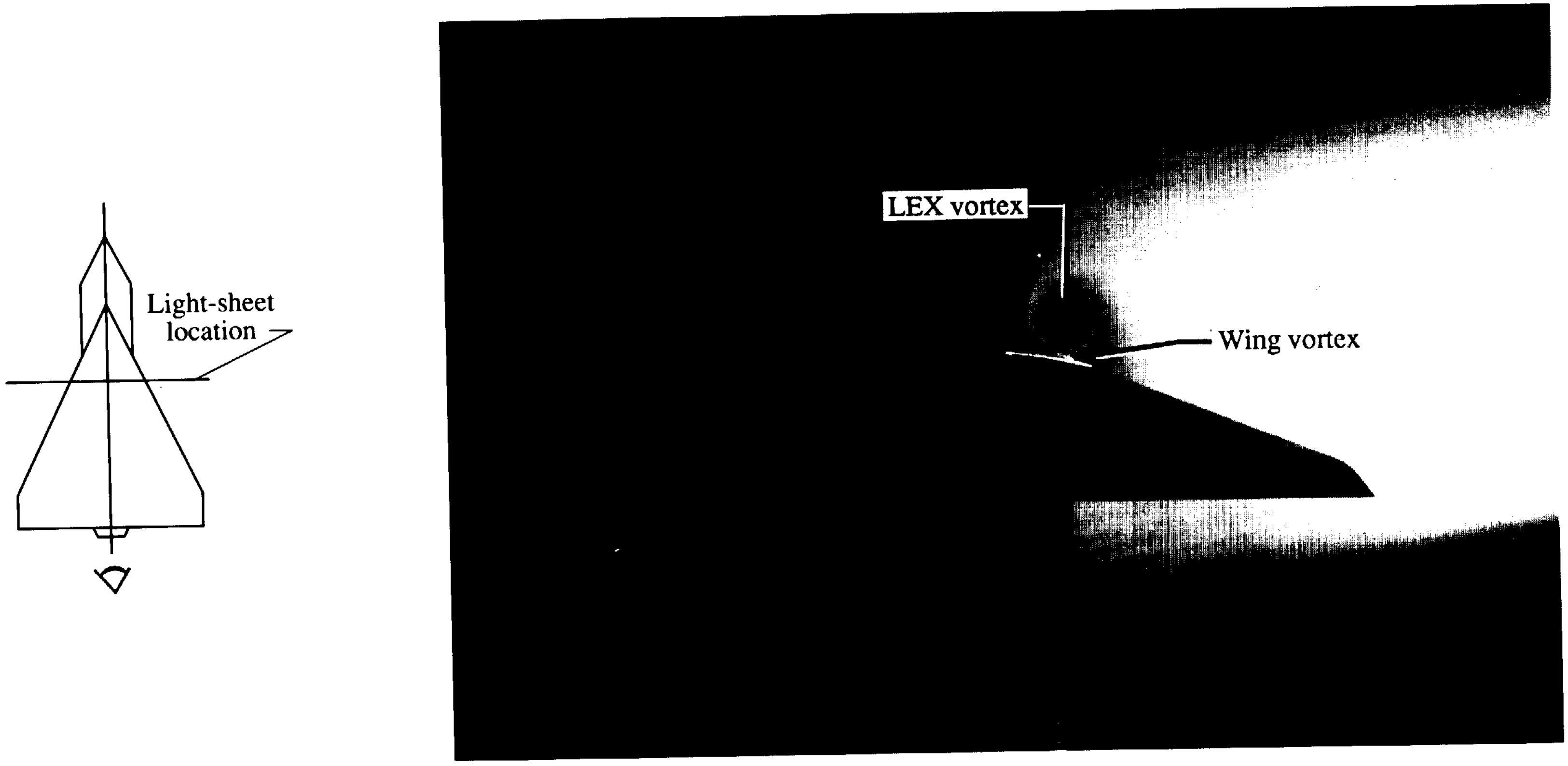

(a) $x/c = 0.30$.

Figure 101. Laser vapor screen flow visualizations at $\alpha = 16°$ and $M_\infty = 0.85$ with LEX on.

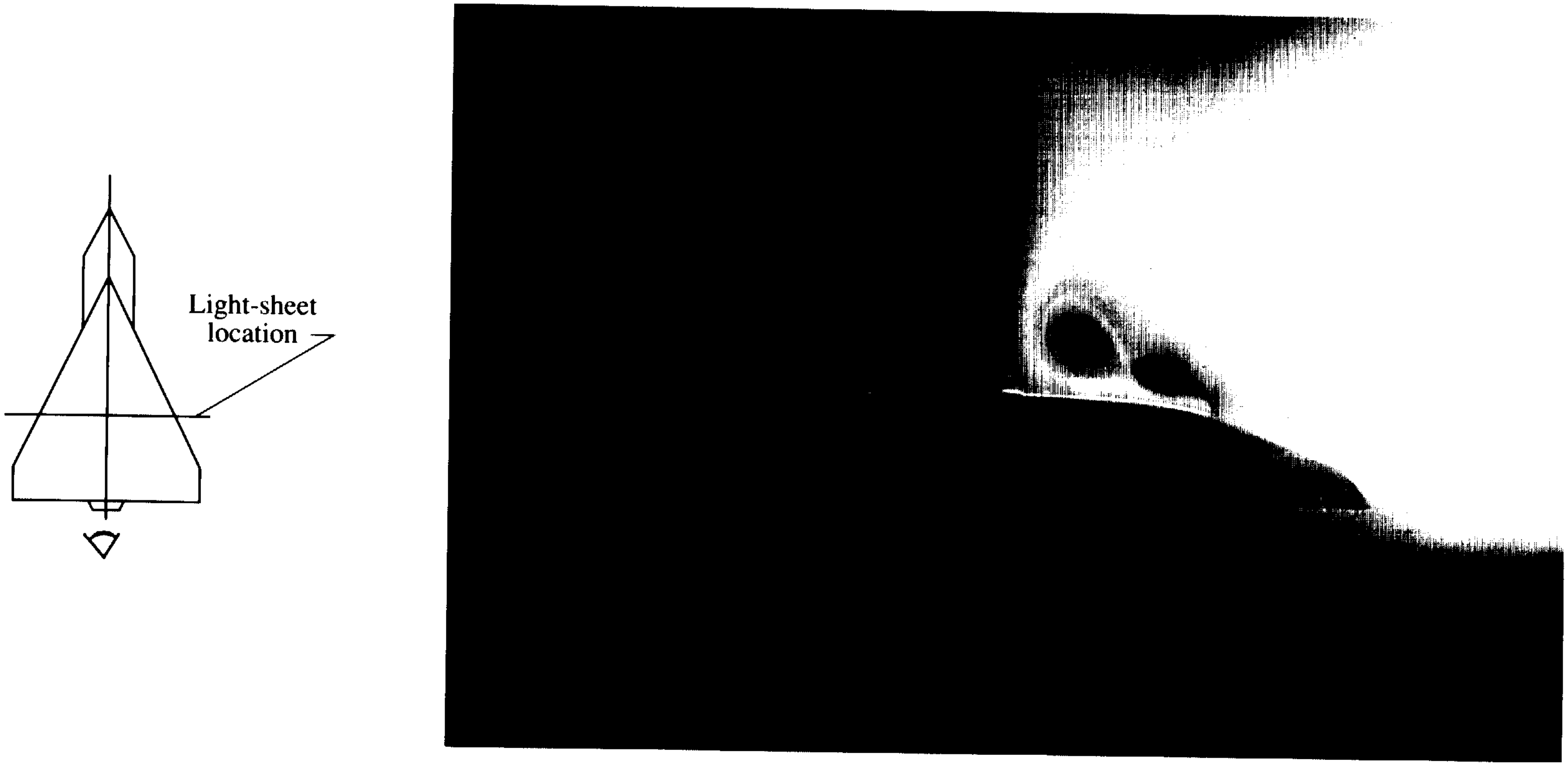

(b) $x/c = 0.60$.

Figure 101. Continued.

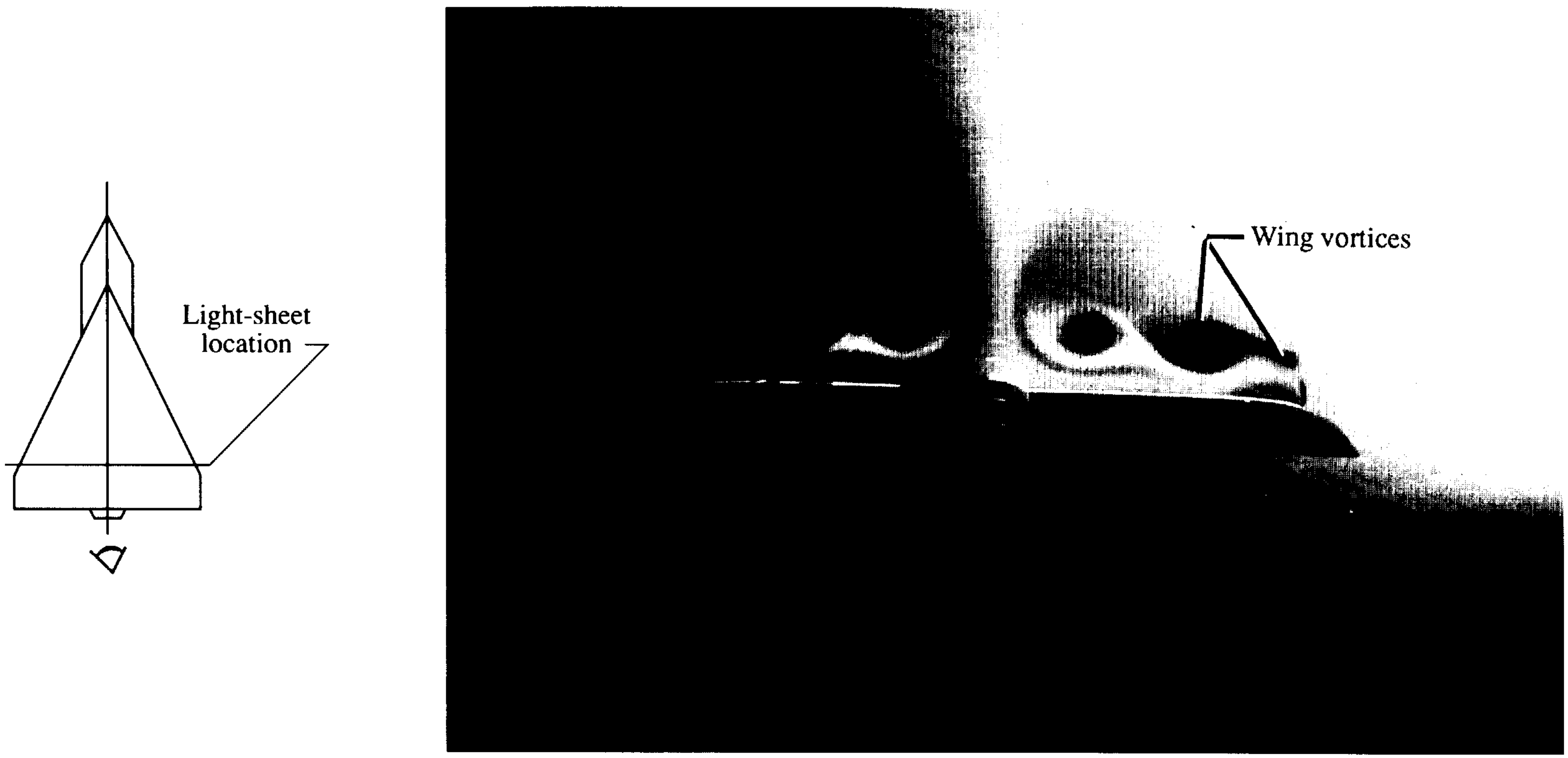

(c) $x/c = 0.80$.

Figure 101. Continued.

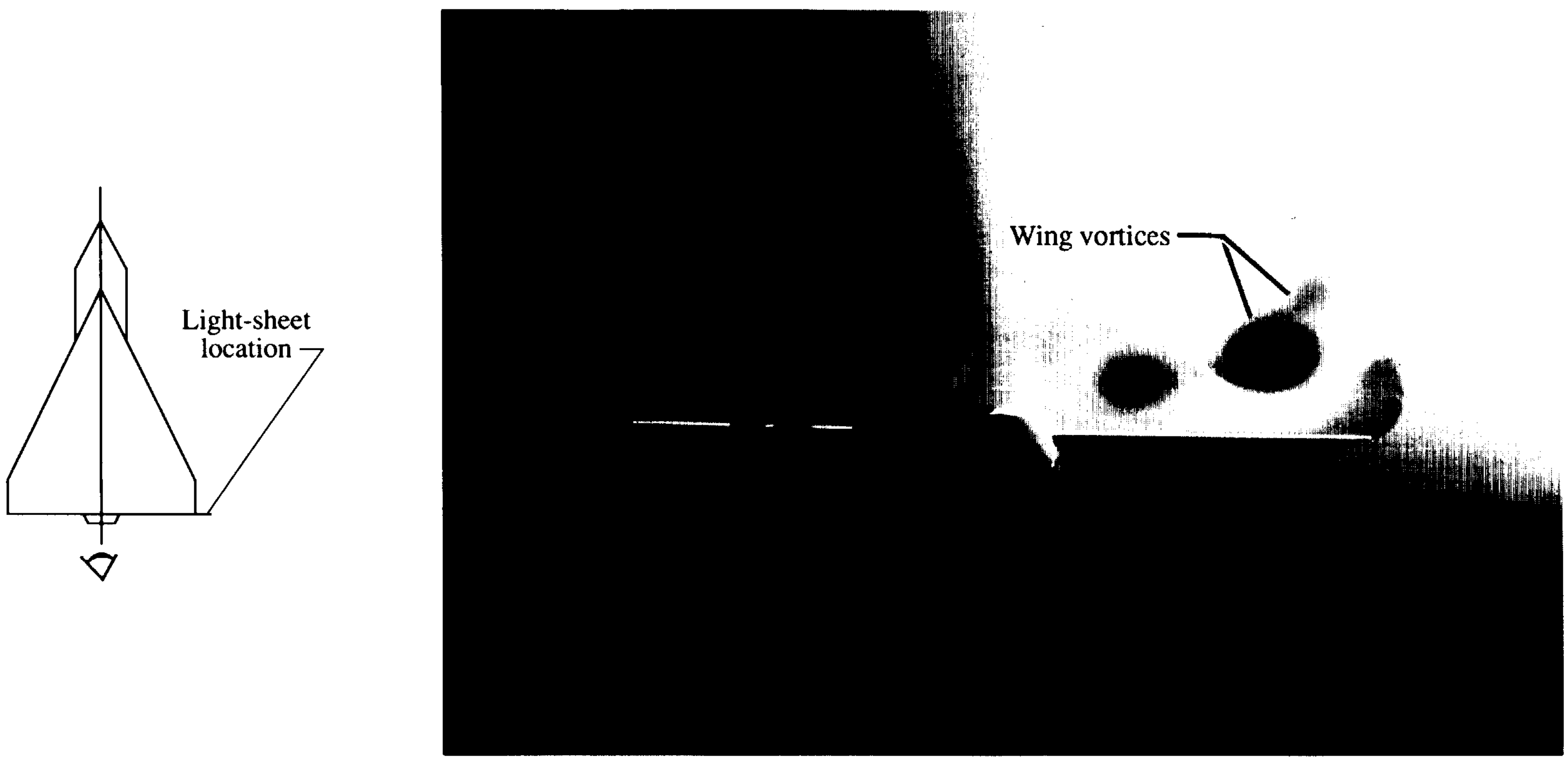

(d) $x/c = 1.00$.

Figure 101. Concluded.

ORIGINAL PAGE
BLACK AND WHITE PHOTOGRAPH

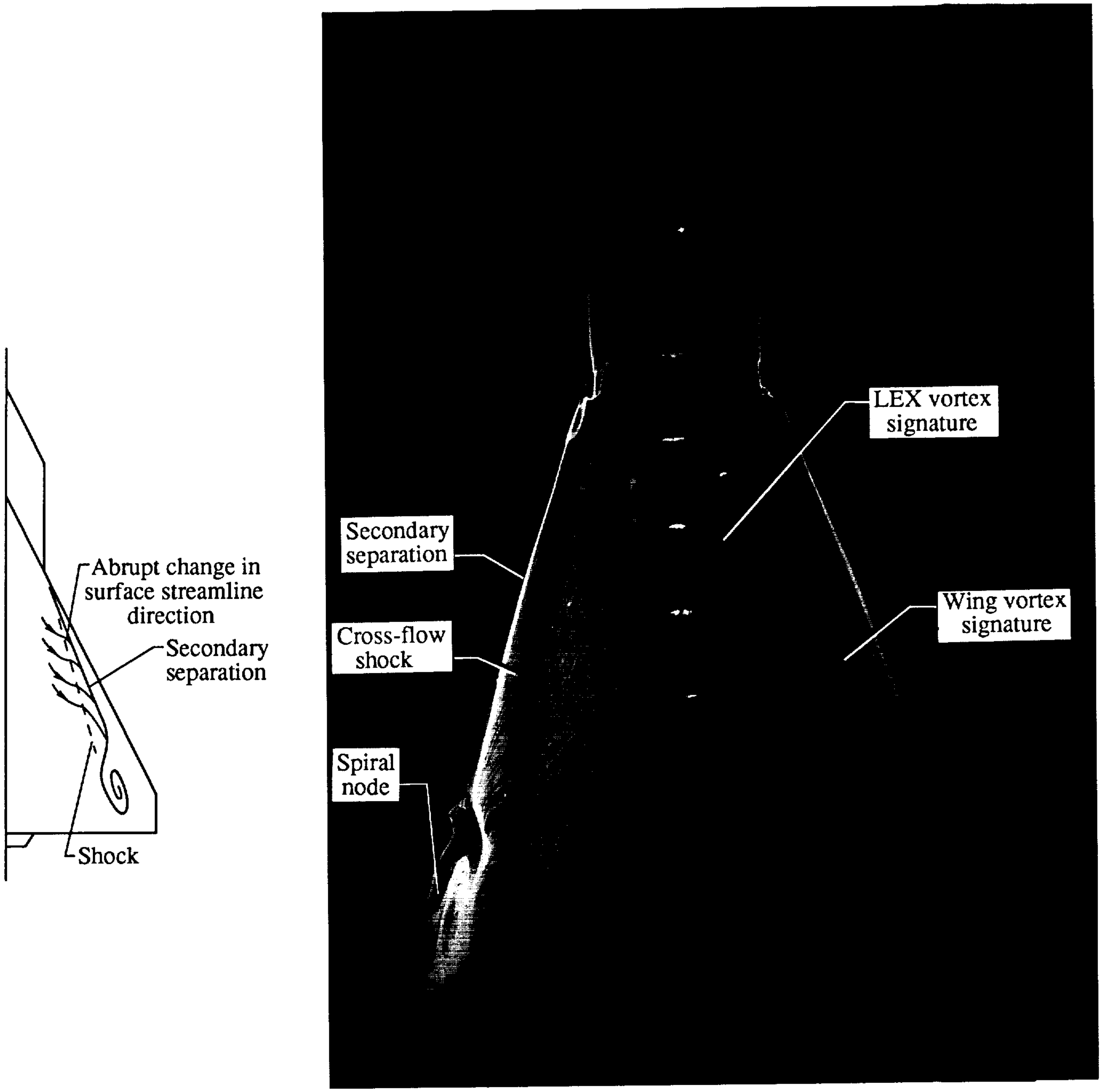

Figure 102. Wing upper surface oil flow pattern at $\alpha = 16^\circ$ and $M_\infty = 0.85$ with LEX on.

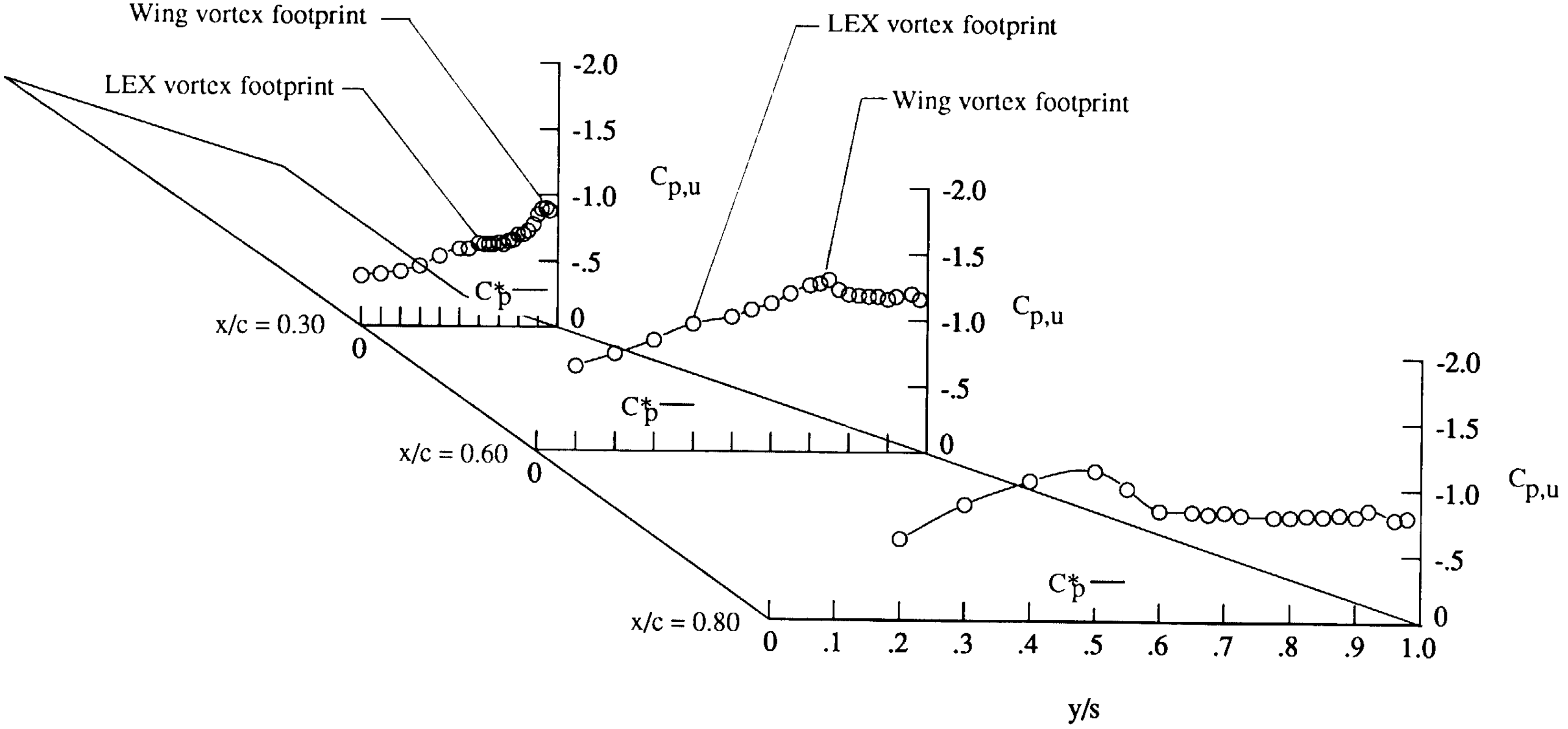

Figure 103. Wing upper surface static pressure distributions at $\alpha = 20°$ and $M_\infty = 0.85$ with LEX on.

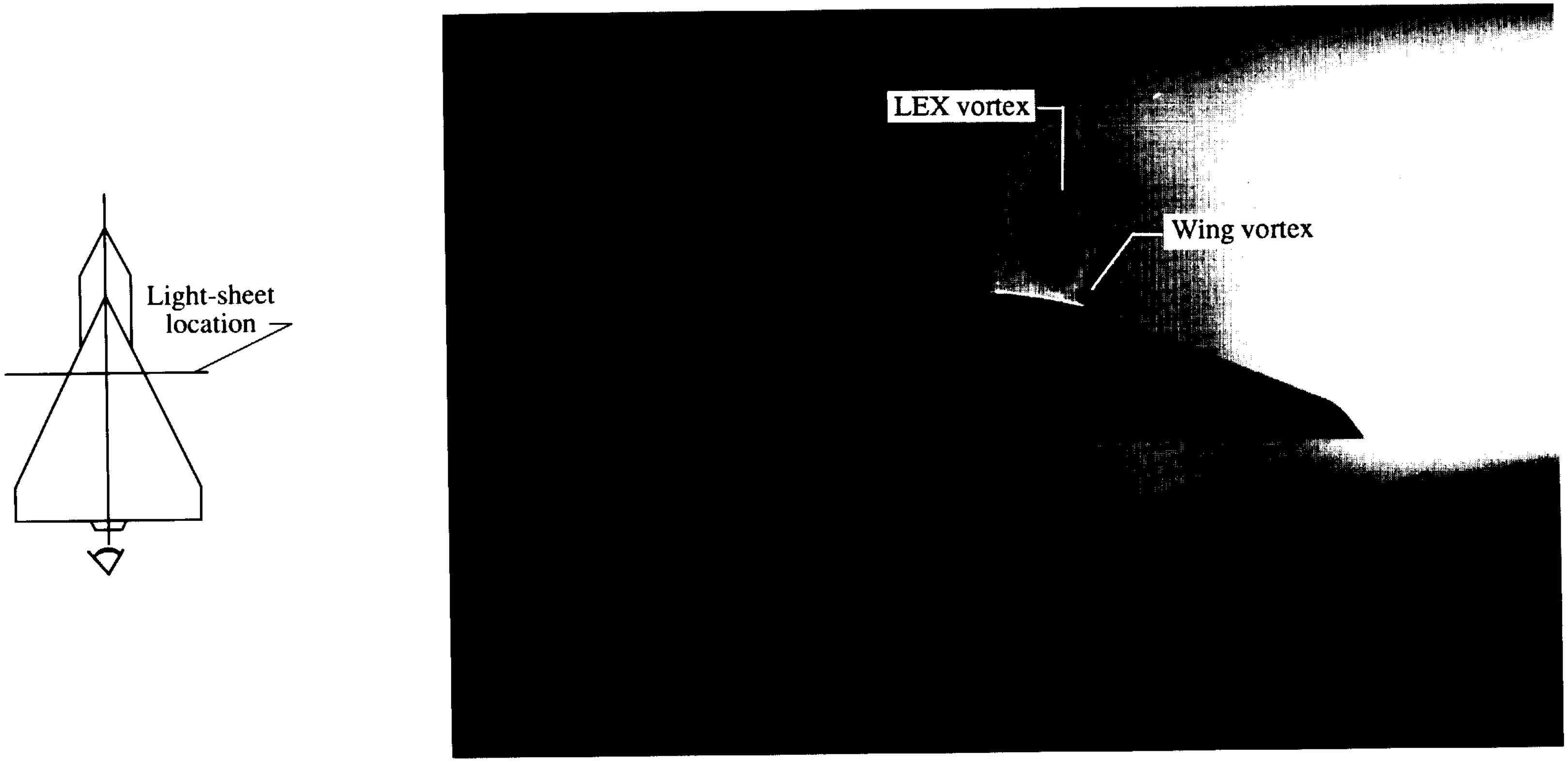

(a) $x/c = 0.30$.

Figure 104. Laser vapor screen flow visualizations at $\alpha = 20°$ and $M_\infty = 0.85$ with LEX on.

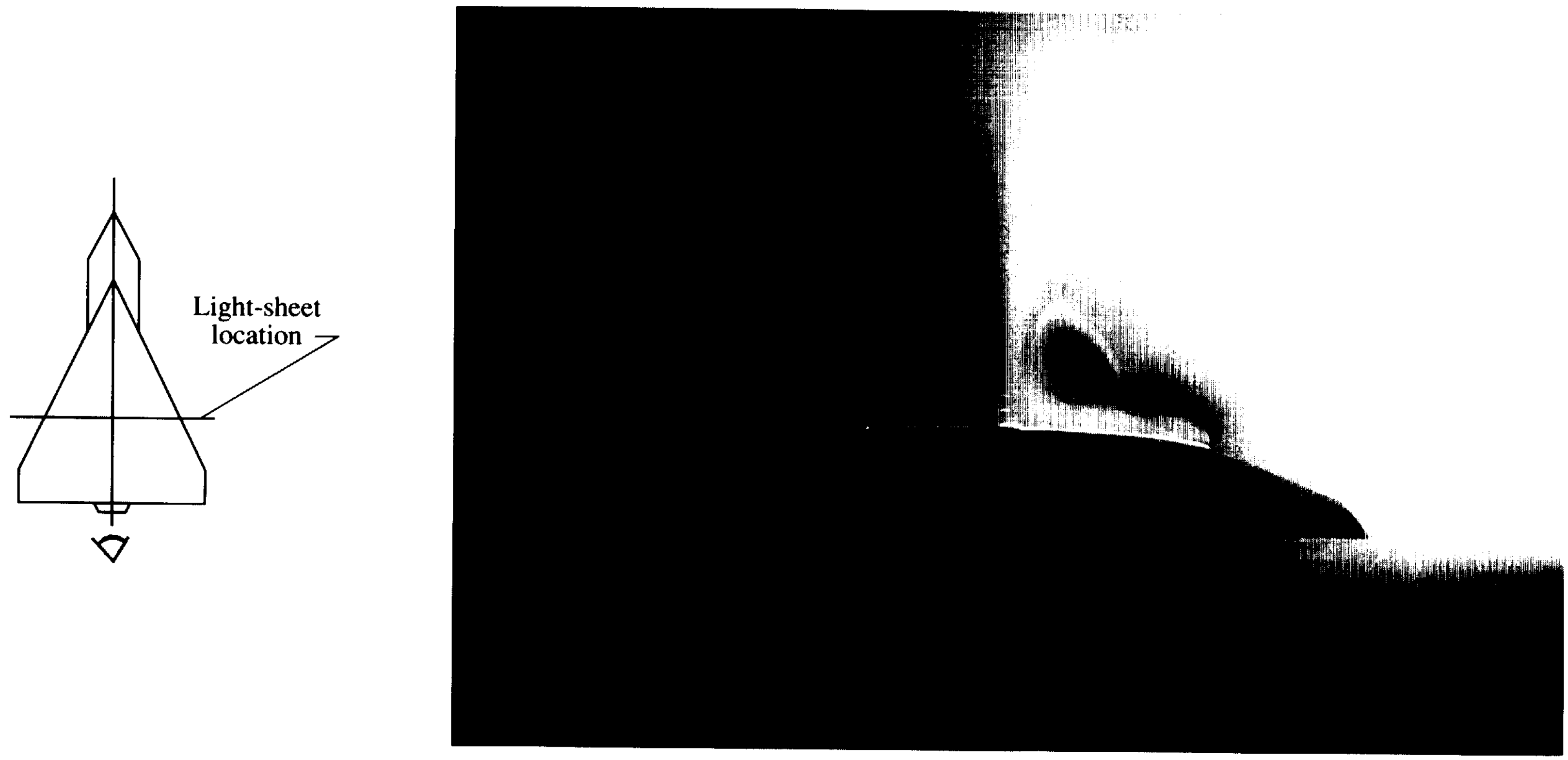

(b) $x/c = 0.60$.

Figure 104. Continued.

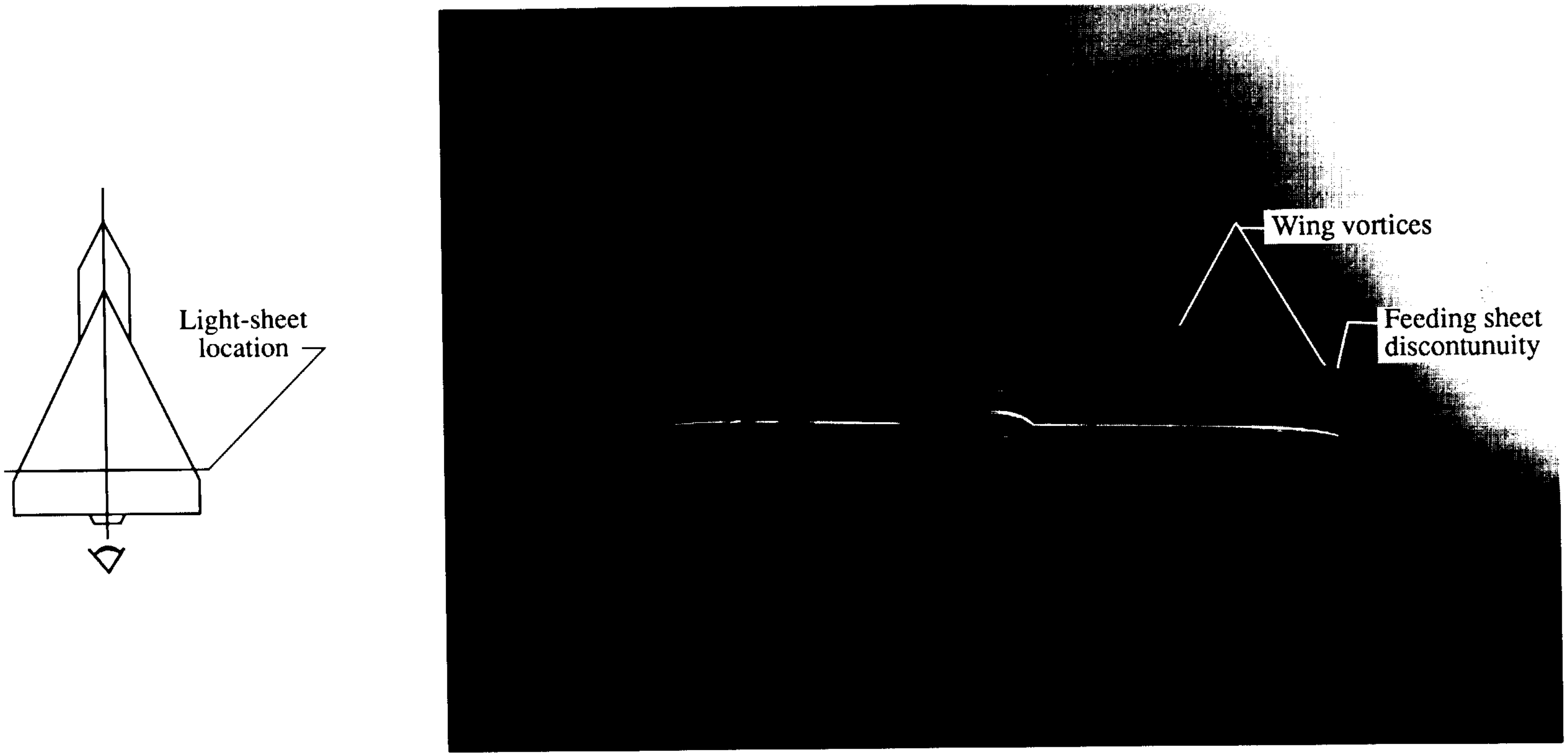

(c) $x/c = 0.80$.

Figure 104. Continued.

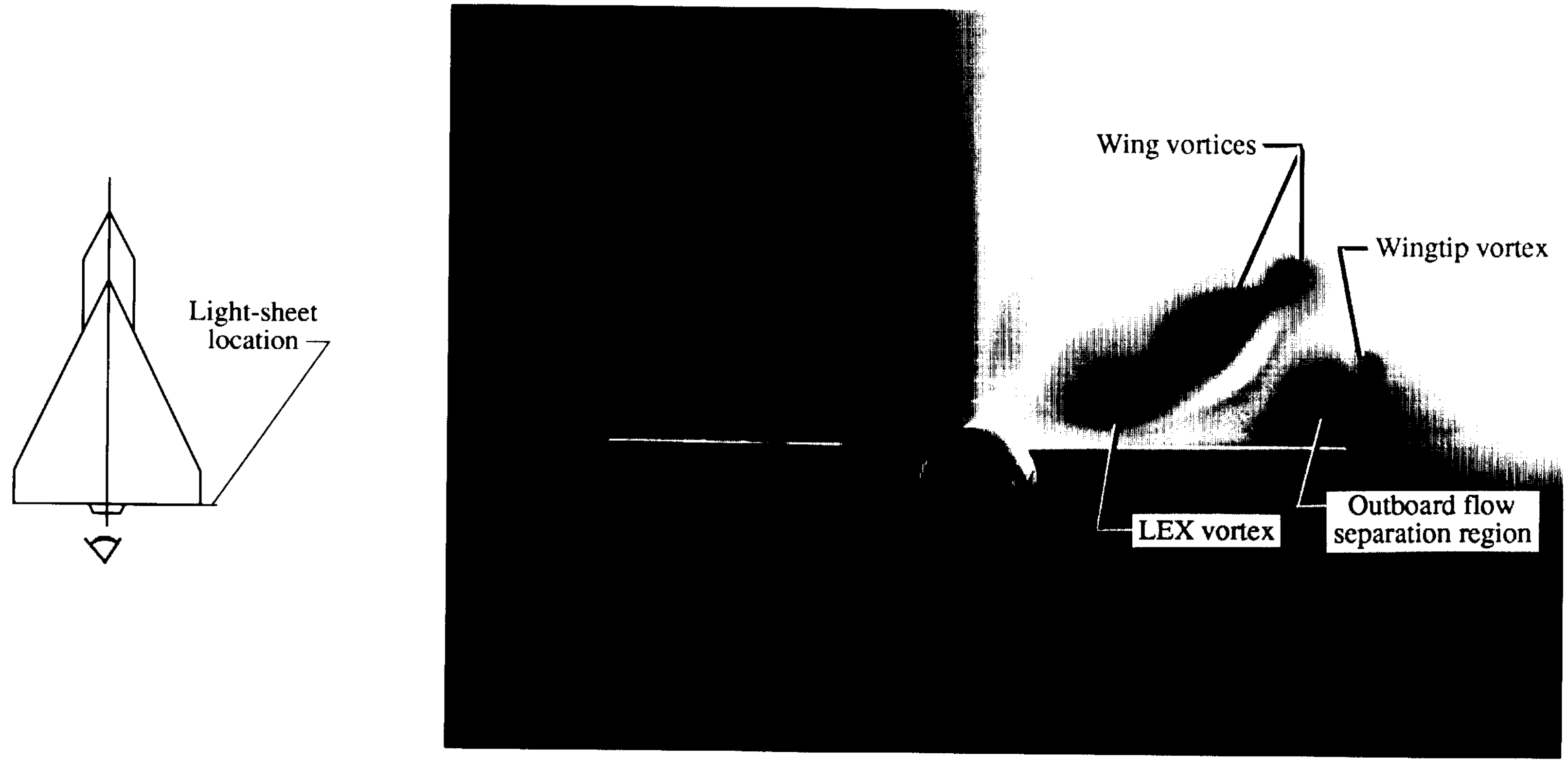

(d) $x/c = 1.00$.

Figure 104. Concluded.

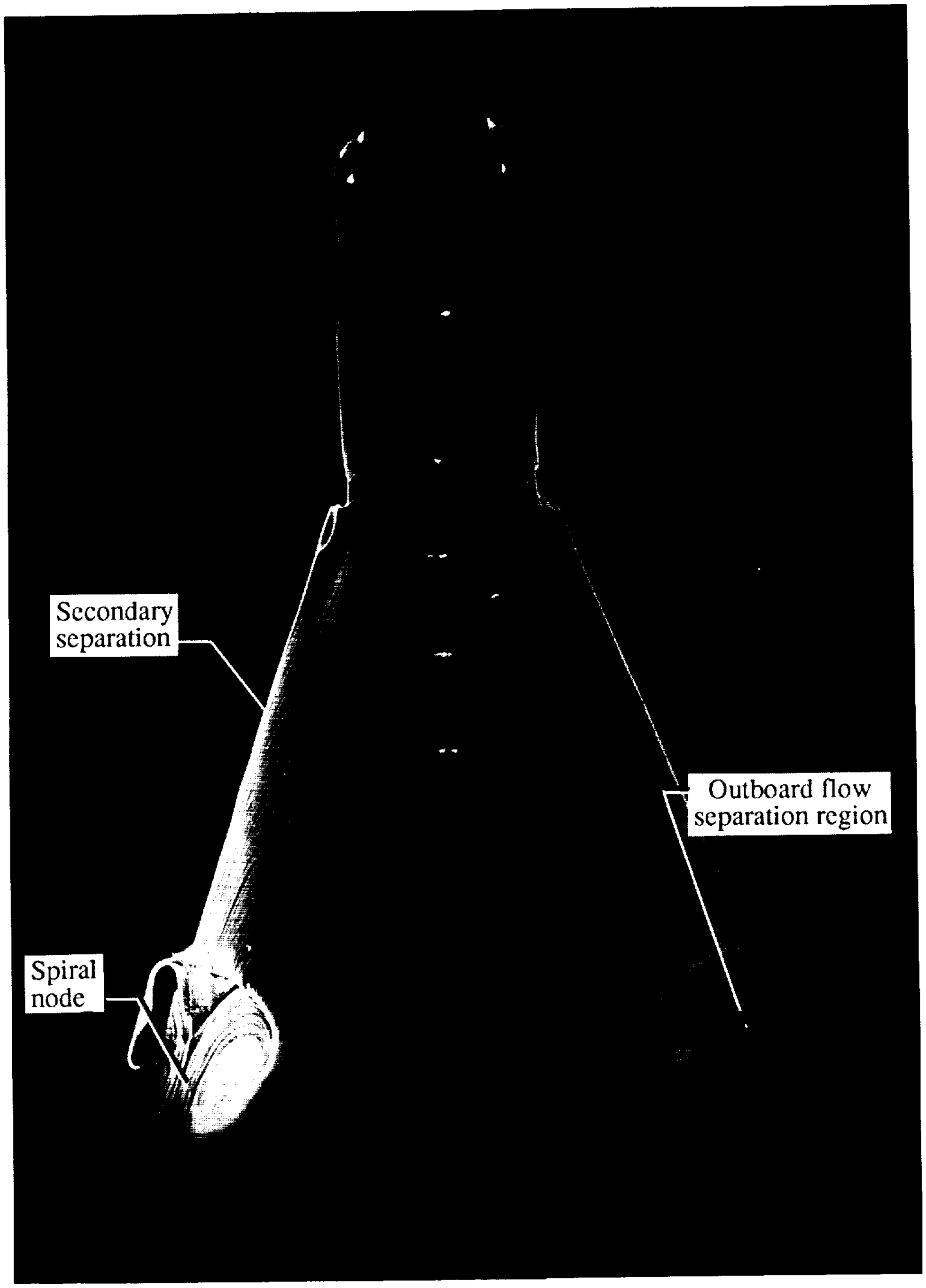

Figure 105. Wing upper surface oil flow pattern at $\alpha = 20^\circ$ and $M_\infty = 0.85$ with LEX on.

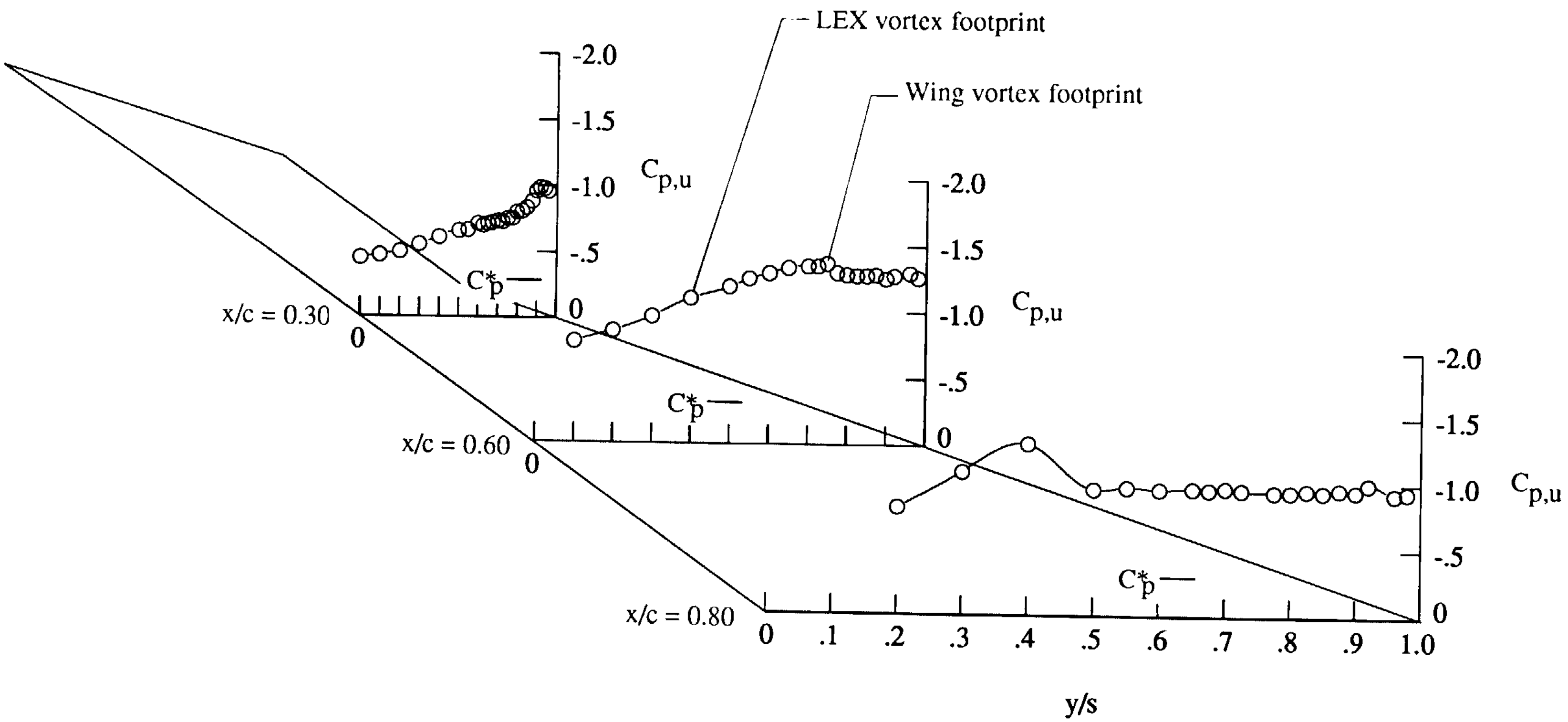

Figure 106. Wing upper surface static pressure distributions at $\alpha = 24°$ and $M_\infty = 0.85$ with LEX on.

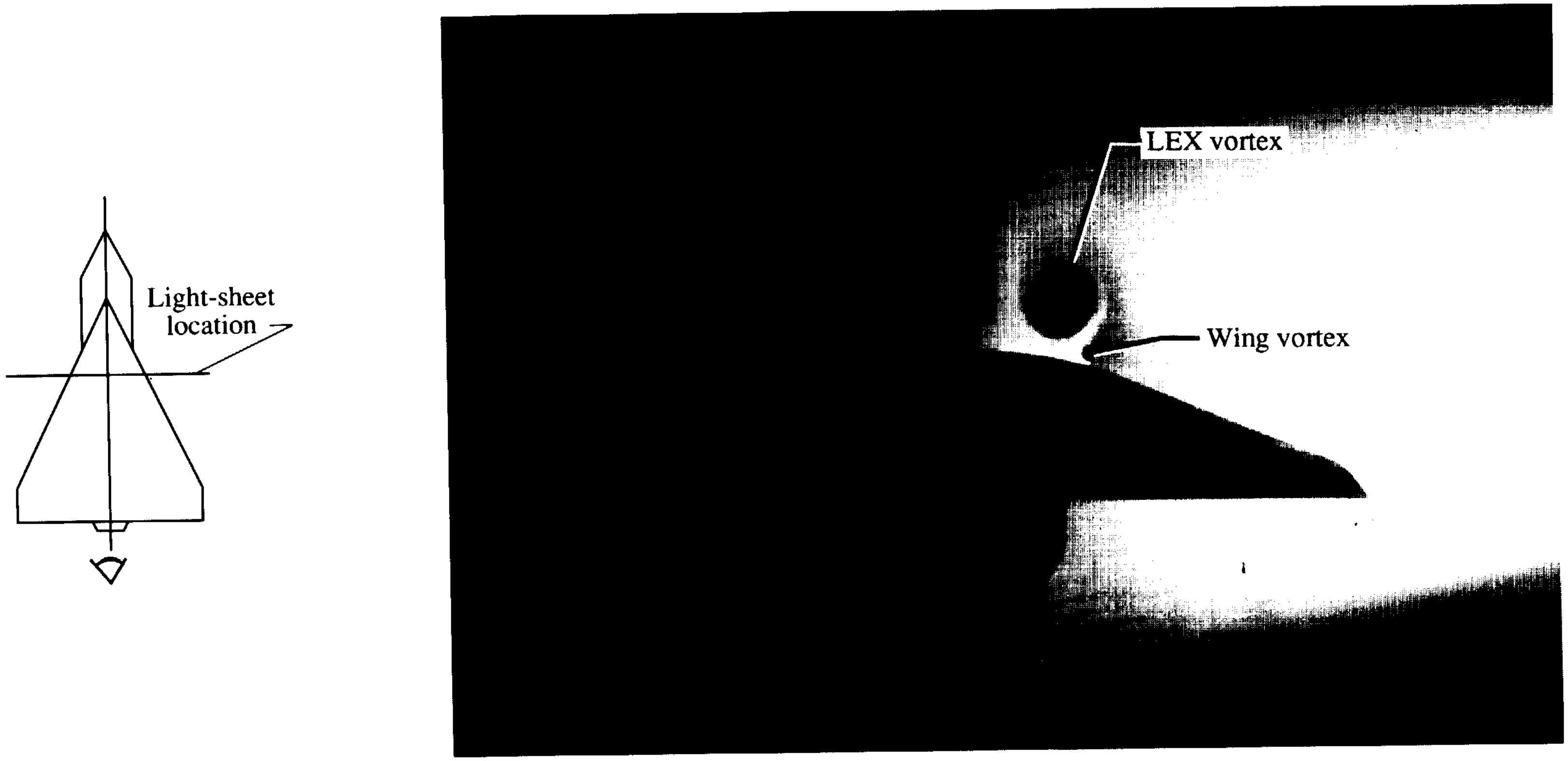

(a) $x/c = 0.30$.

Figure 107. Laser vapor screen flow visualizations at $\alpha = 24°$ and $M_\infty = 0.85$ with LEX on.

(b) $x/c = 0.60$.

Figure 107. Continued.

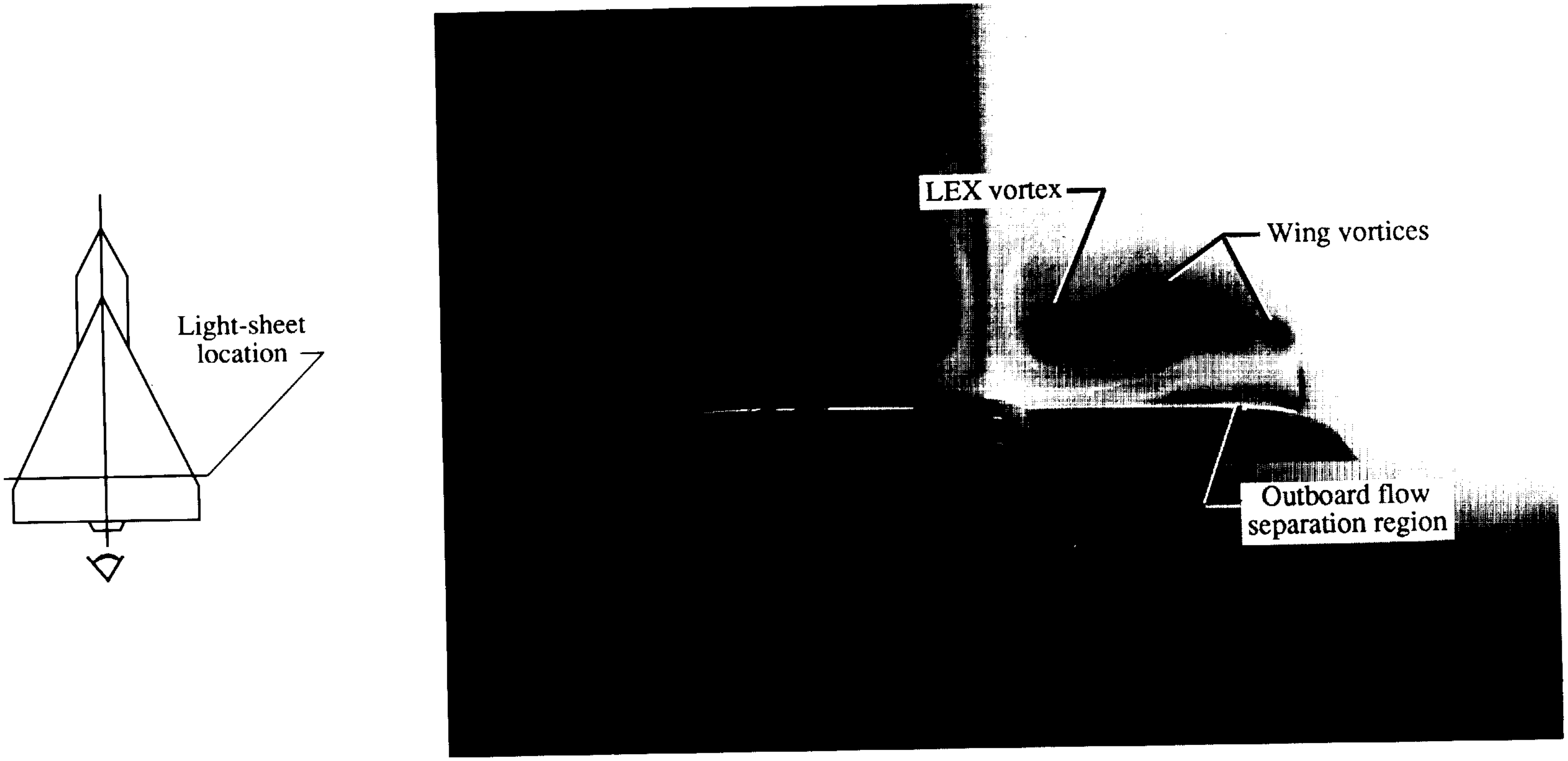

(c) $x/c = 0.80$.

Figure 107. Continued.

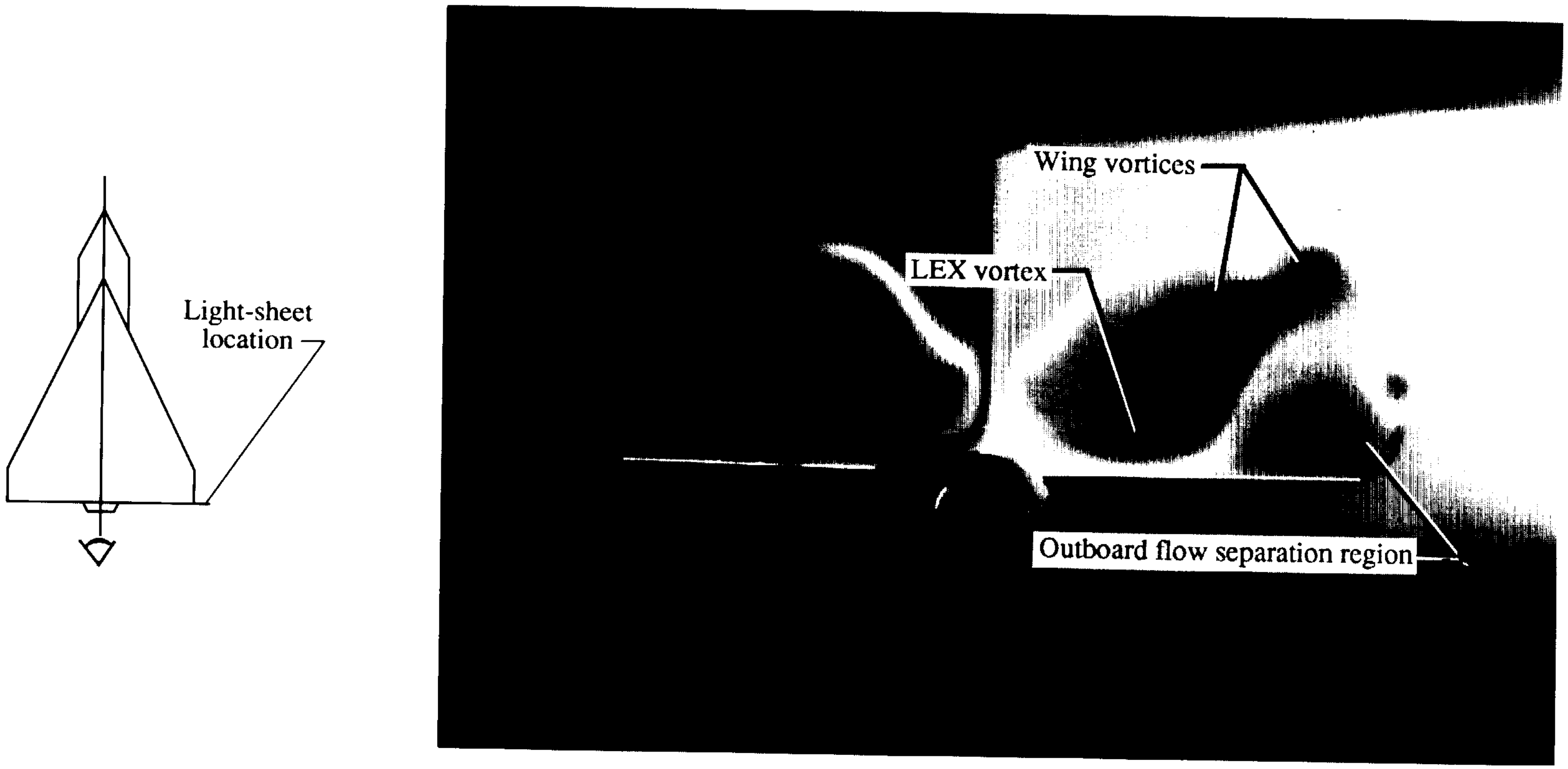

(d) $x/c = 1.00$.

Figure 107. Concluded.

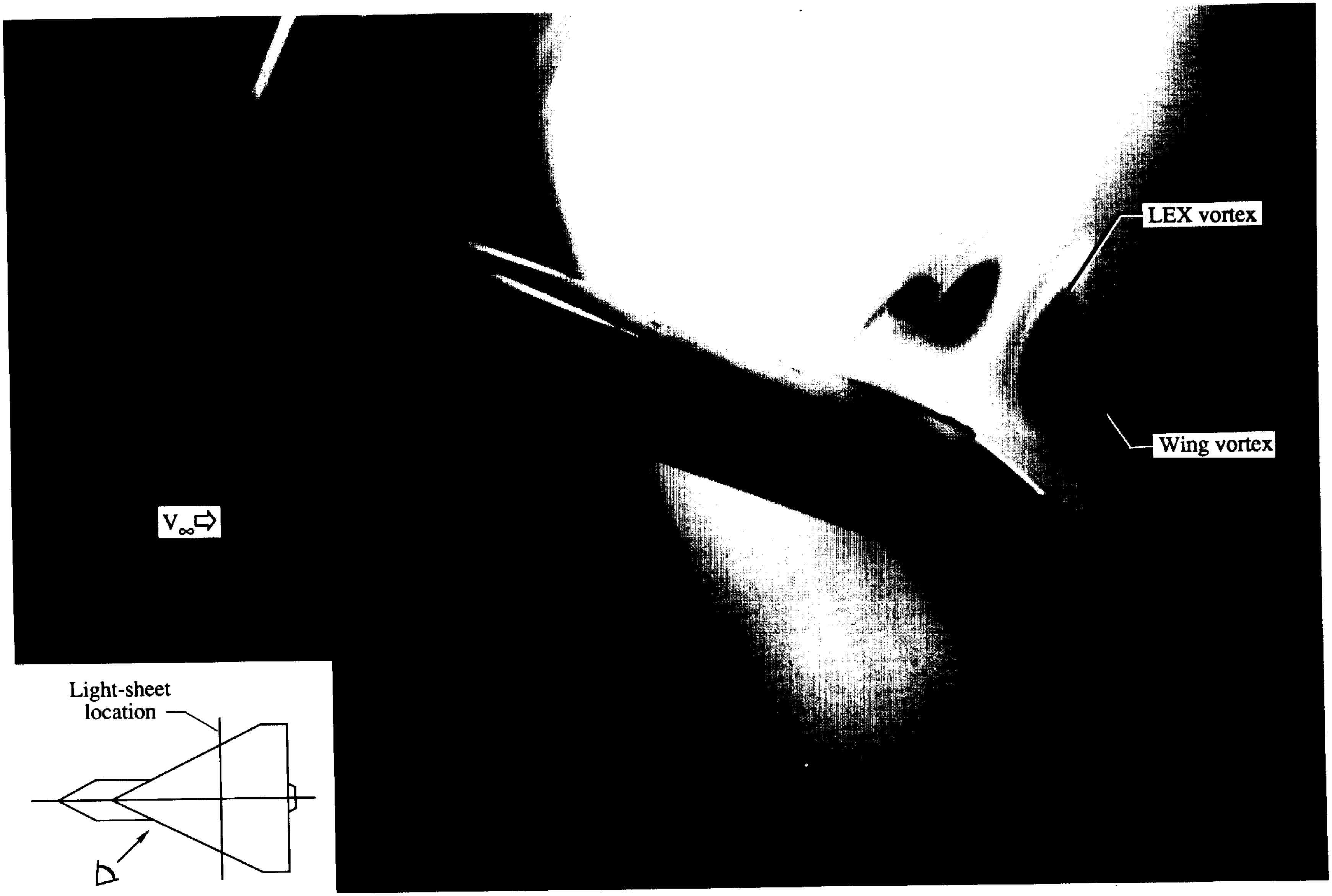

(a) $x/c = 0.60$.

Figure 108. Laser vapor screen flow visualizations at $\alpha = 24°$ and $M_\infty = 0.85$ with LEX on.

(b) $x/c = 0.80$.

Figure 108. Continued.

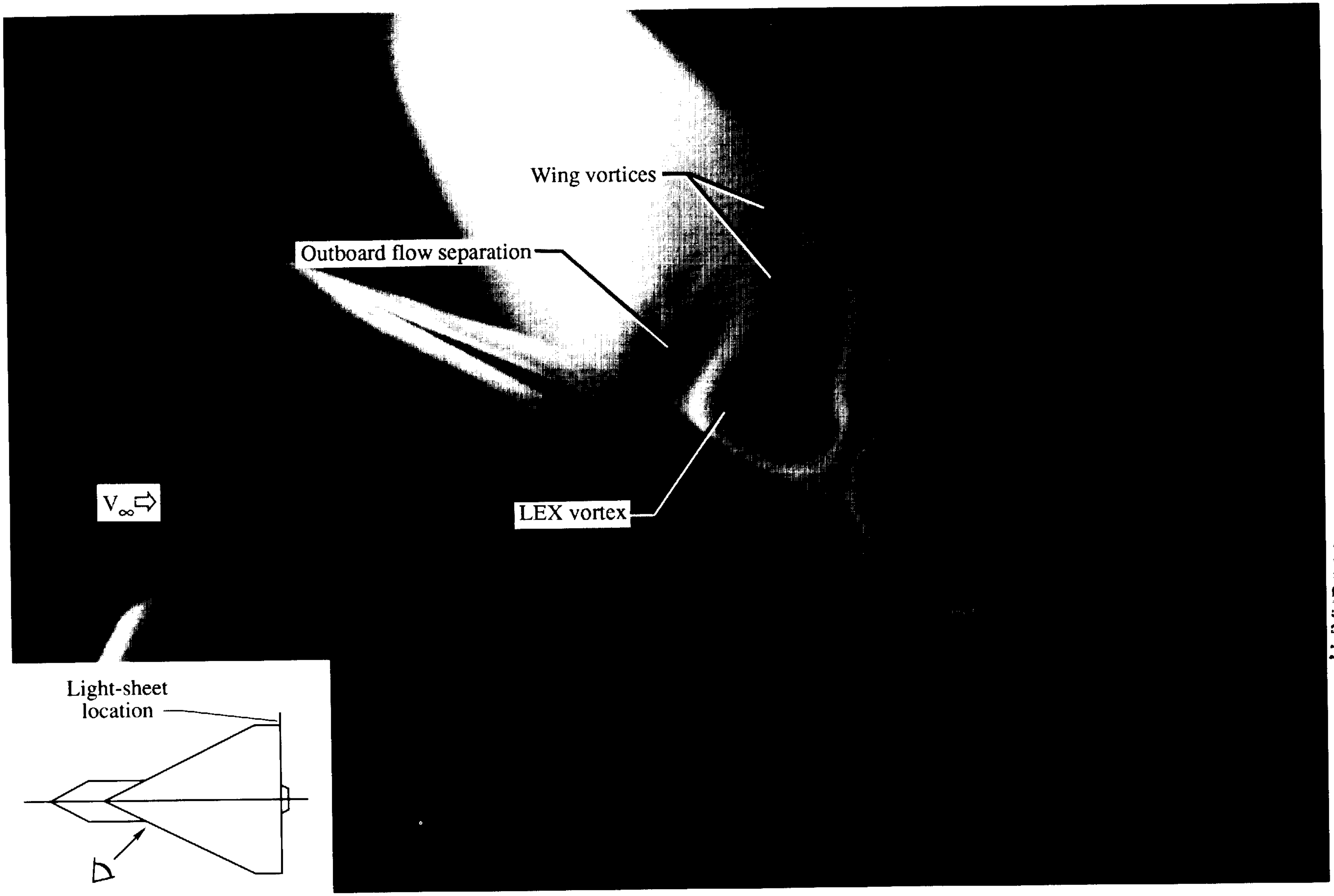

(c) $x/c = 1.00$.

Figure 108. Concluded.

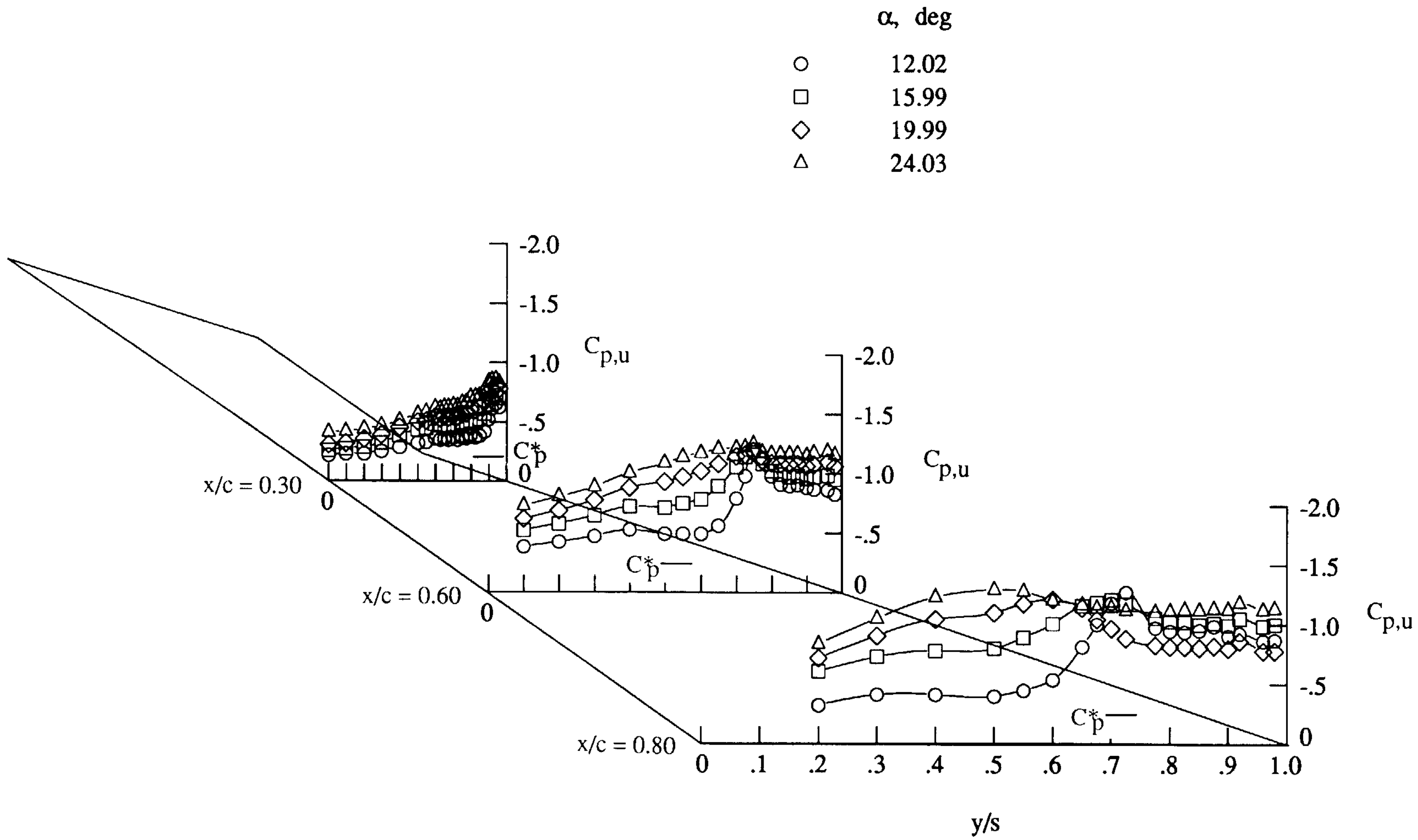

Figure 109. Wing upper surface static pressure distributions at $M_\infty = 0.90$ with LEX on.

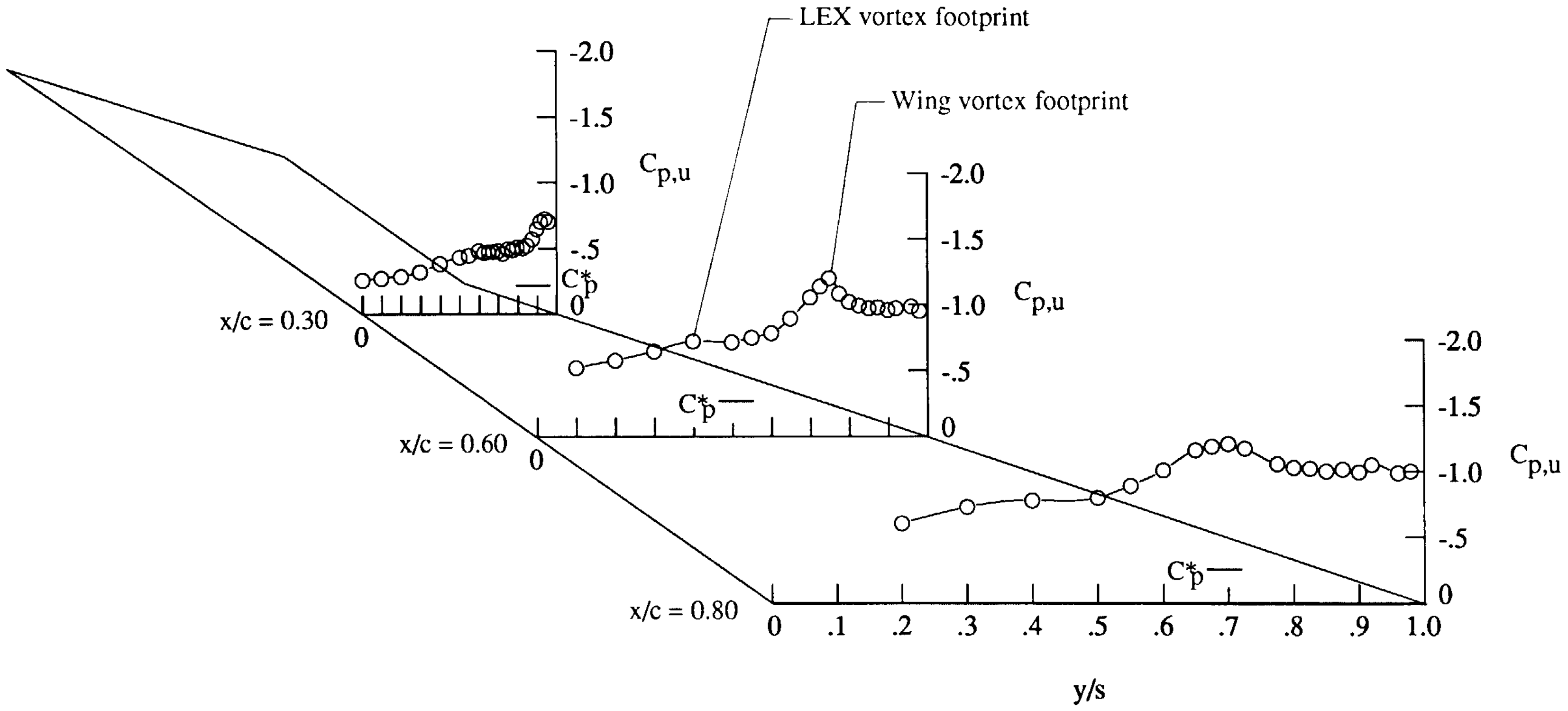

Figure 110. Wing upper surface static pressure distributions at $\alpha = 16°$ and $M_\infty = 0.90$ with LEX on.

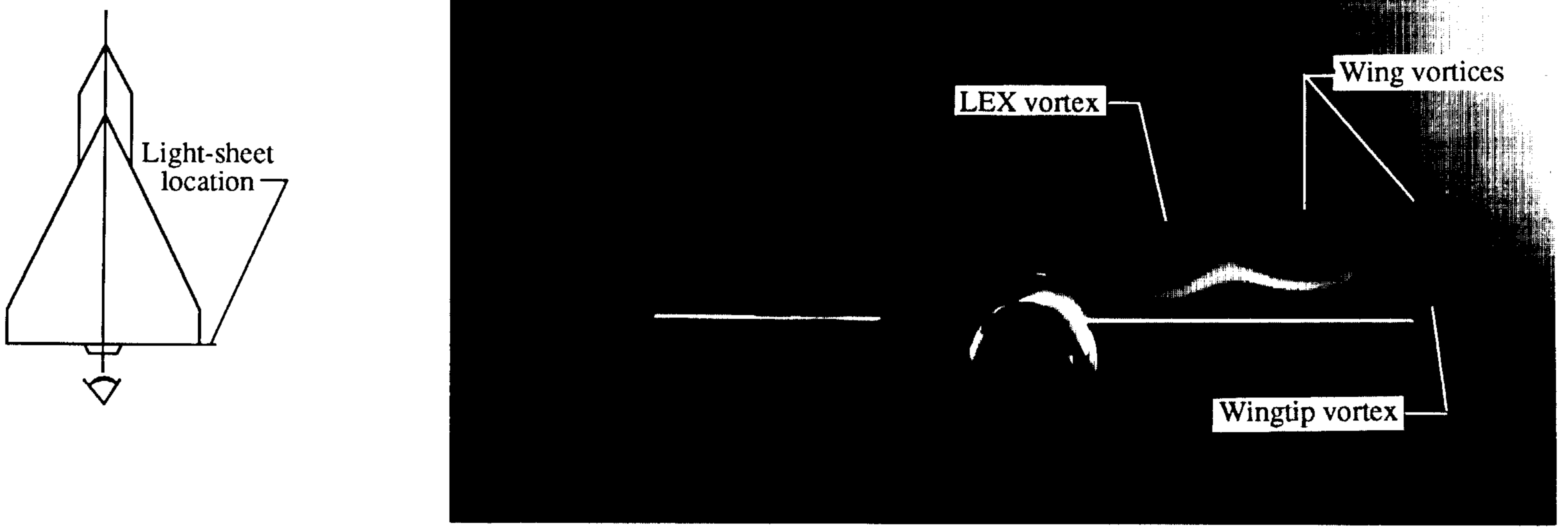

Figure 111. Laser vapor screen flow visualizations at $\alpha = 16^\circ$ and $M_\infty = 0.90$ with LEX on.

(a) $x/c = 0.60$.

Figure 112. Laser vapor screen flow visualizations at $\alpha = 16°$ and $M_\infty = 0.90$ with LEX on.

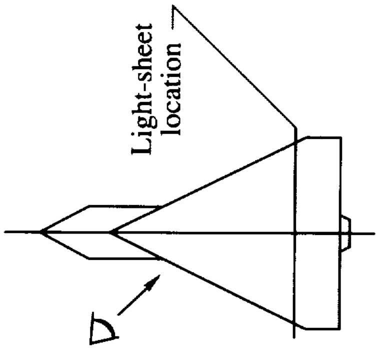

(b) $x/c = 0.80$.

Figure 112. Continued.

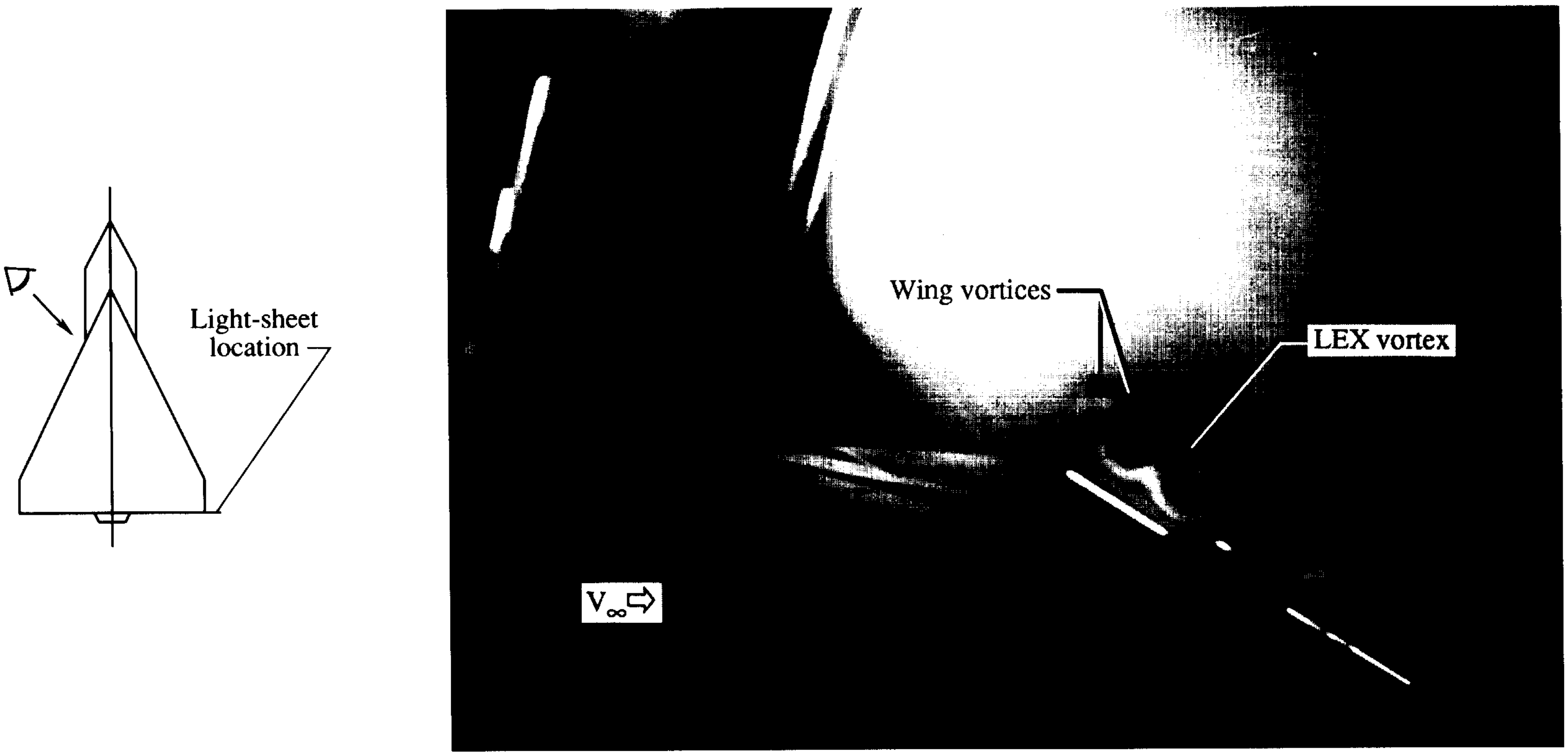

(c) $x/c = 1.00$.

Figure 112. Concluded.

ORIGINAL PAGE
BLACK AND WHITE PHOTOGRAPH

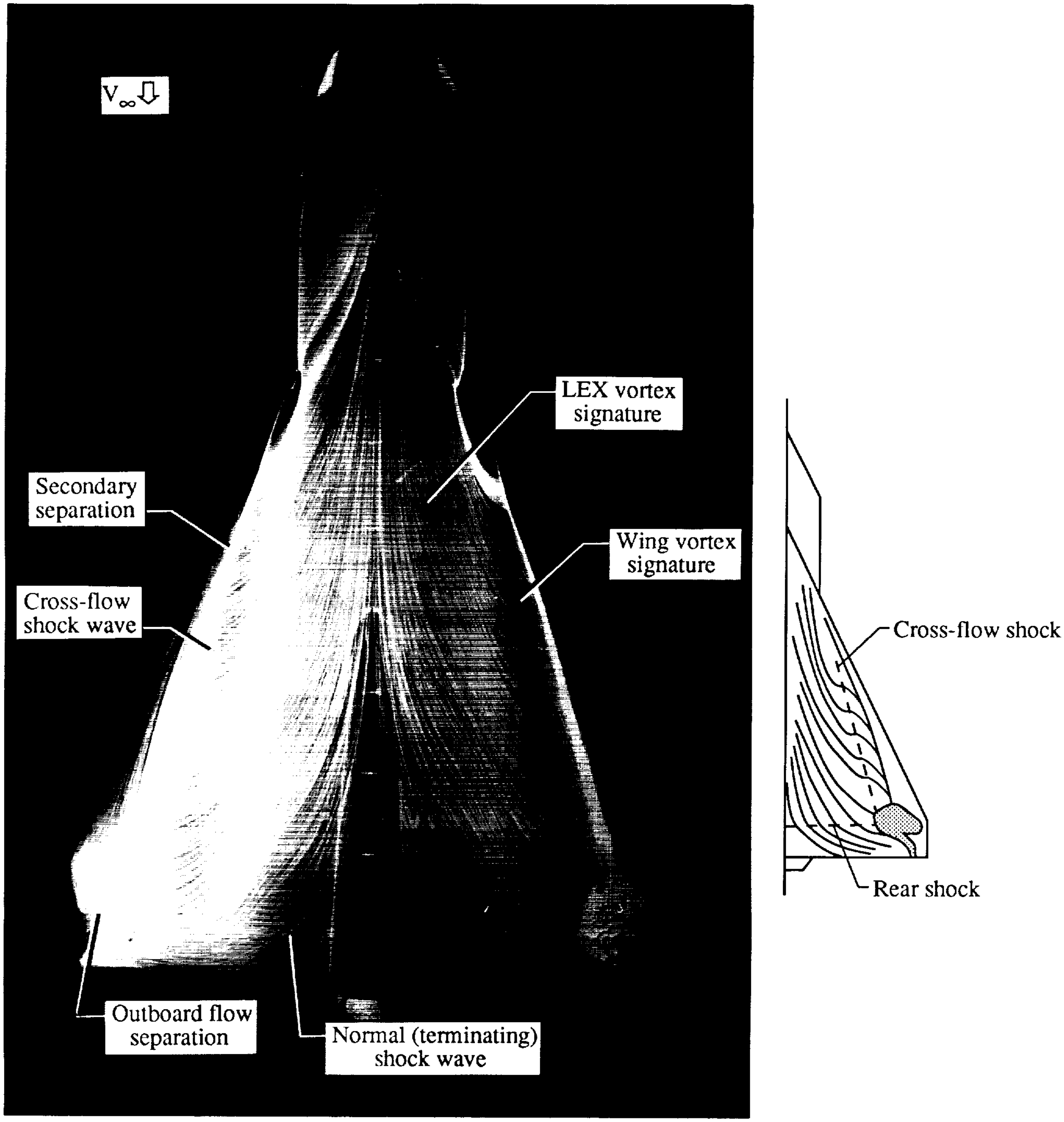

Figure 113. Wing upper surface oil flow pattern at $\alpha = 16^\circ$ and $M_\infty = 0.90$ with LEX on.

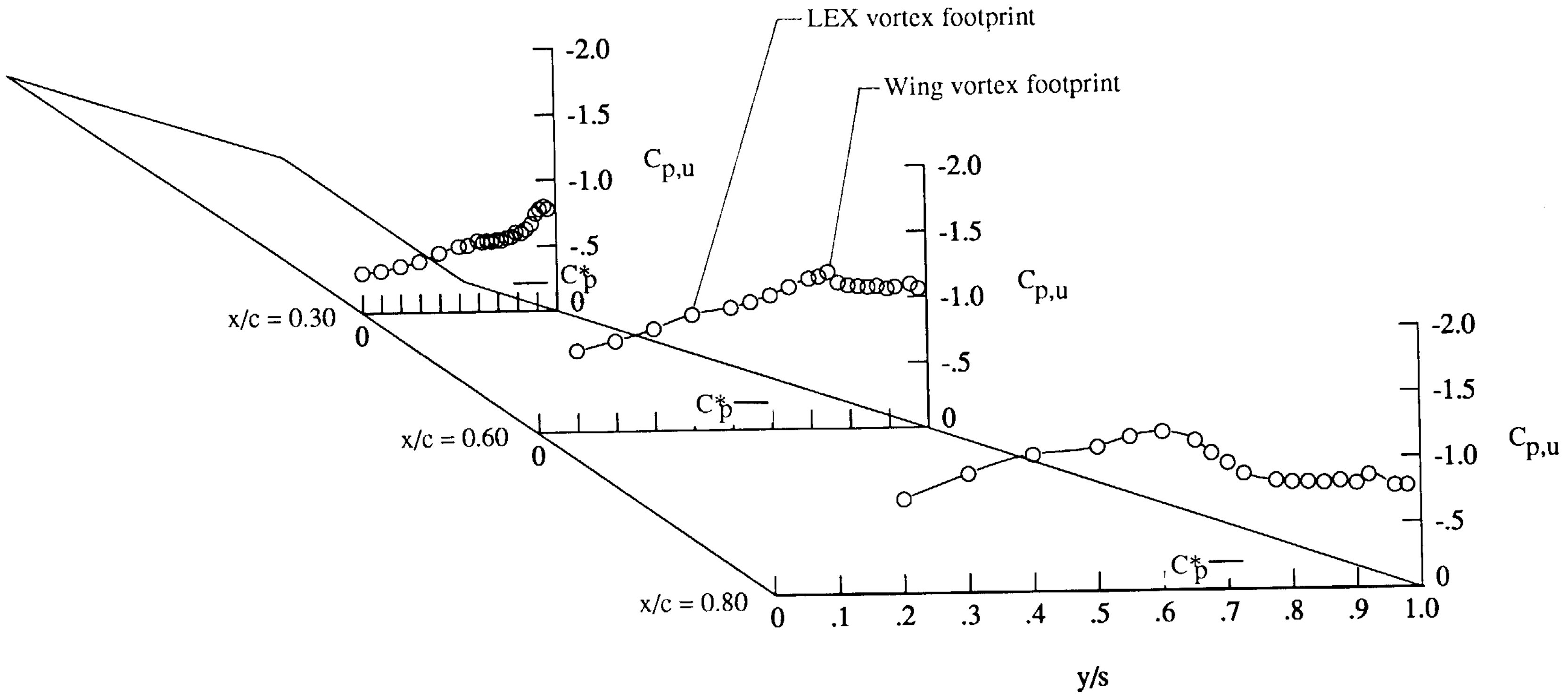

Figure 114. Wing upper surface static pressure distributions at $\alpha = 20°$ and $M_\infty = 0.90$ with LEX on.

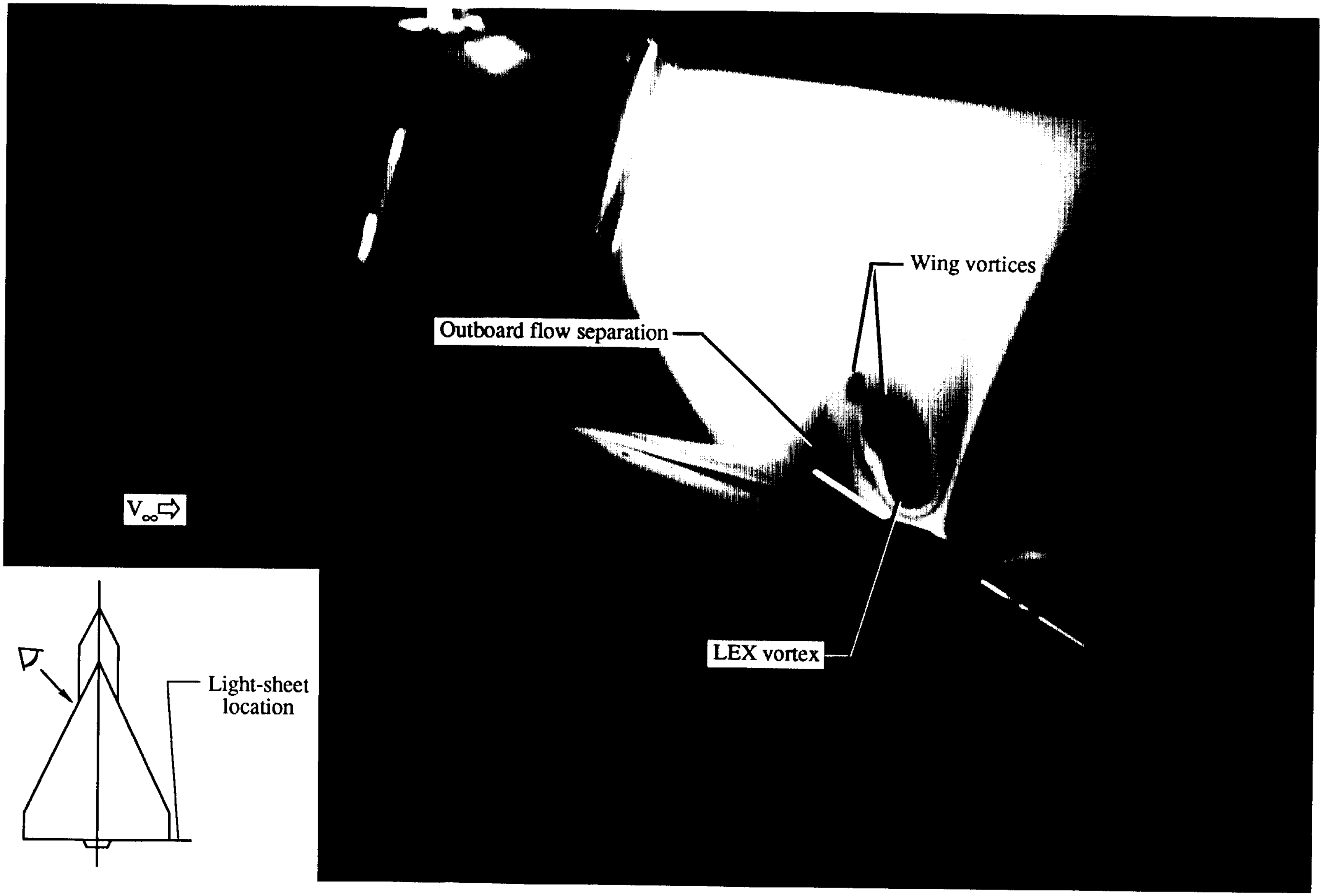

(a) $x/c = 1.00$.

Figure 115. Laser vapor screen flow visualizations at $\alpha = 20°$ and $M_\infty = 0.90$ with LEX on.

(b) $x/c = 1.10$.

Figure 115. Concluded.

ORIGINAL PAGE
BLACK AND WHITE PHOTOGRAPH

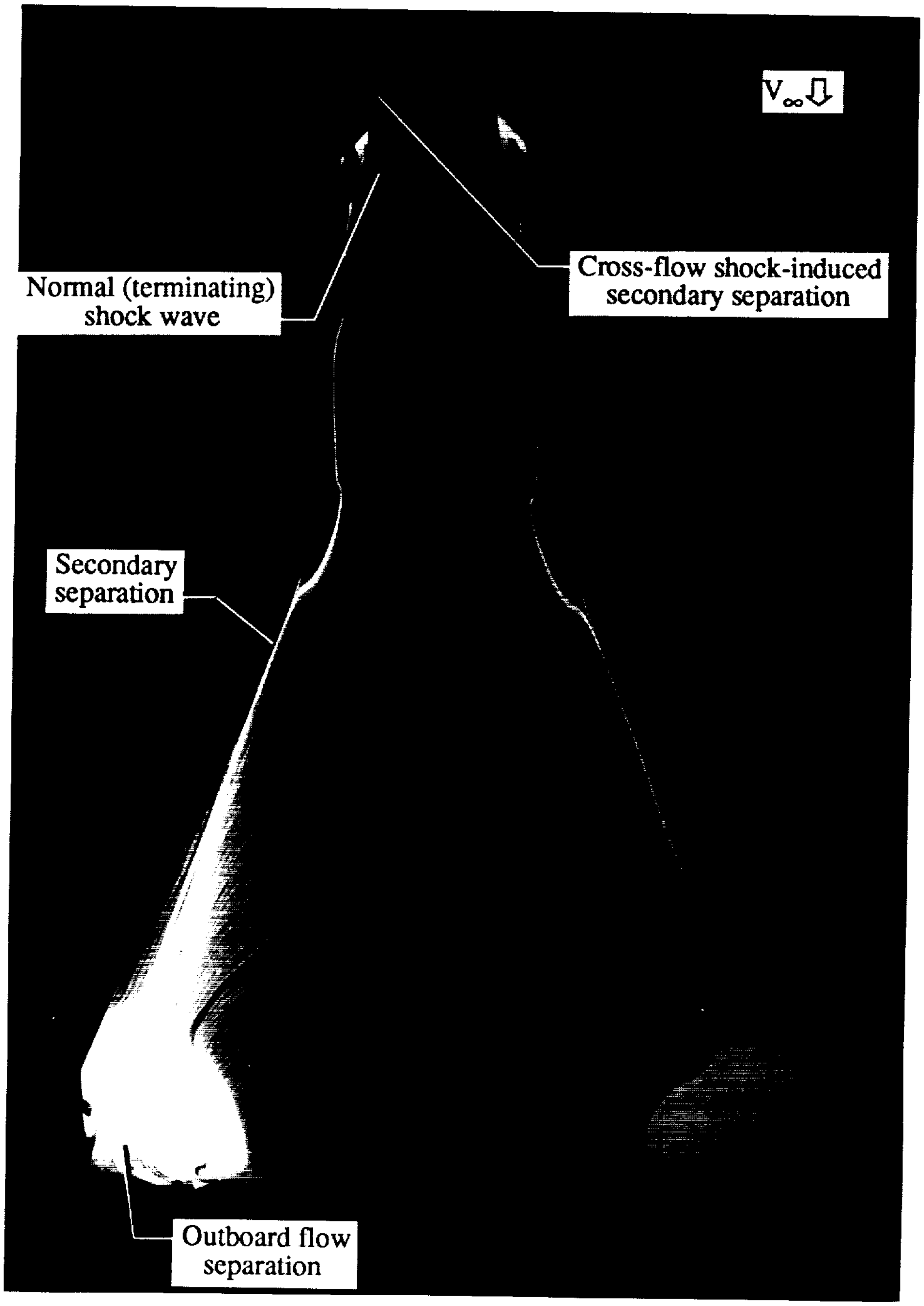

Figure 116. Wing upper surface oil flow pattern at $\alpha = 20°$ and $M_\infty = 0.90$ with LEX on.

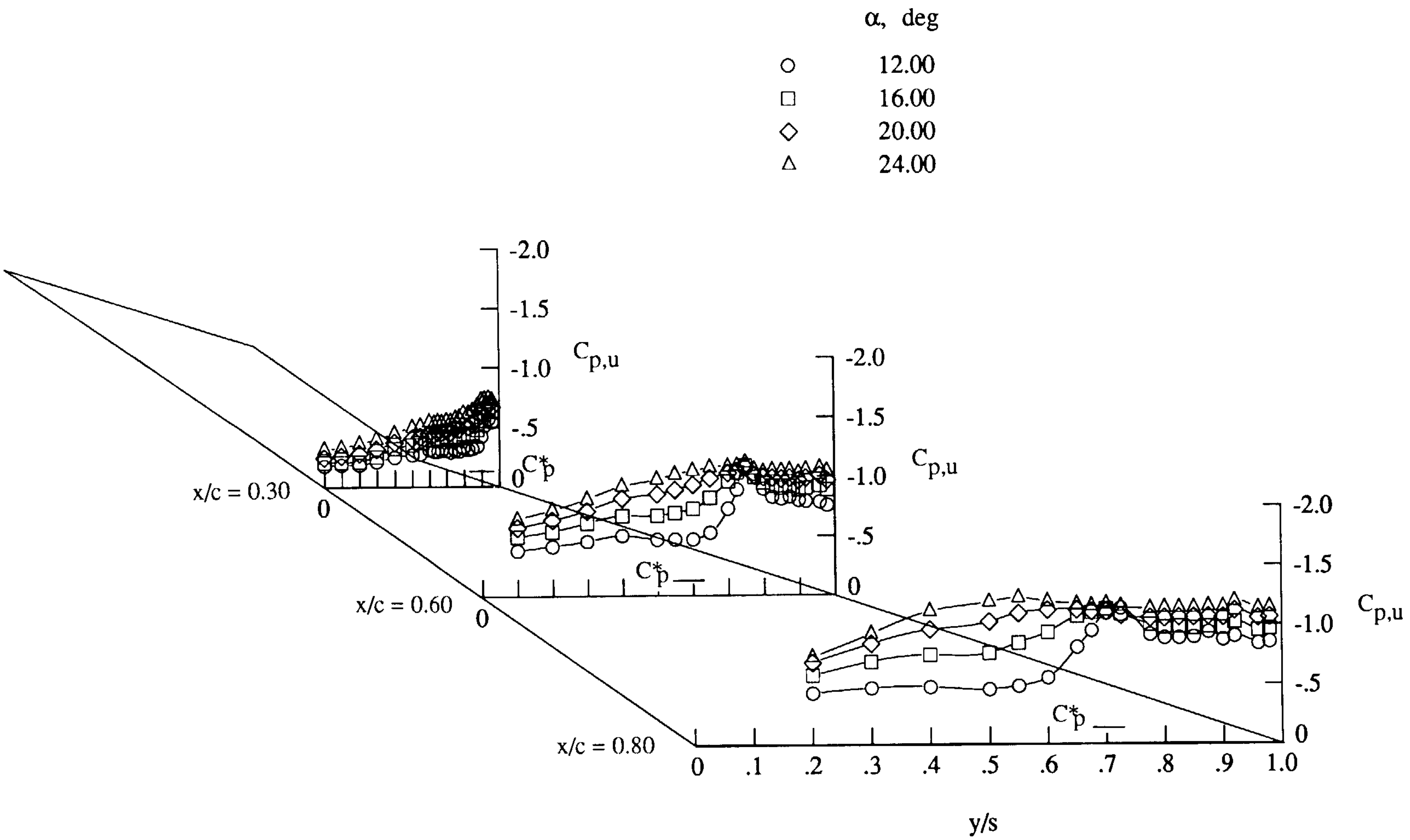

Figure 117. Wing upper surface static pressure distributions at $M_\infty = 0.95$ with LEX on.

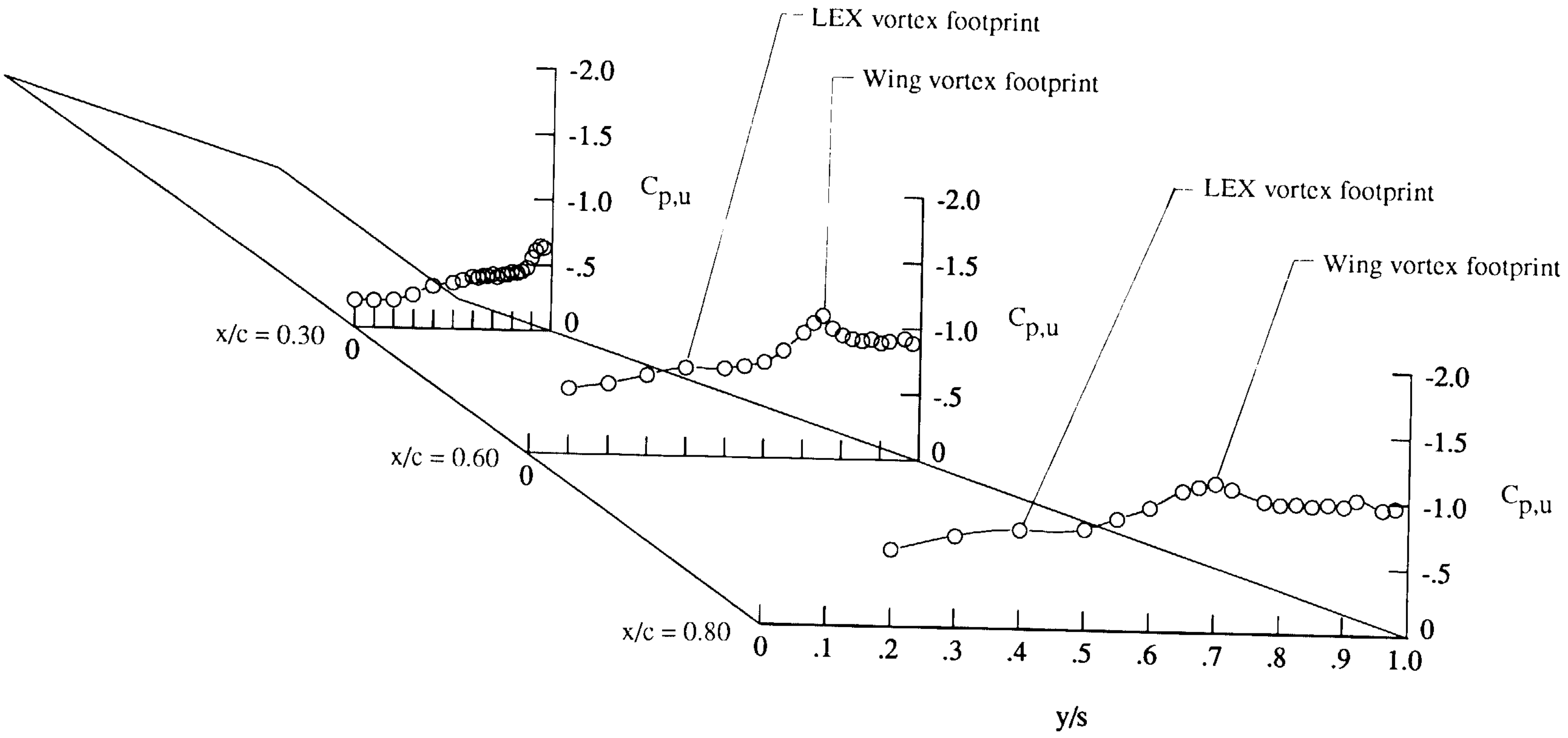

Figure 118. Wing upper surface static pressure distributions at $\alpha = 16°$ and $M_\infty = 0.95$ with LEX on.

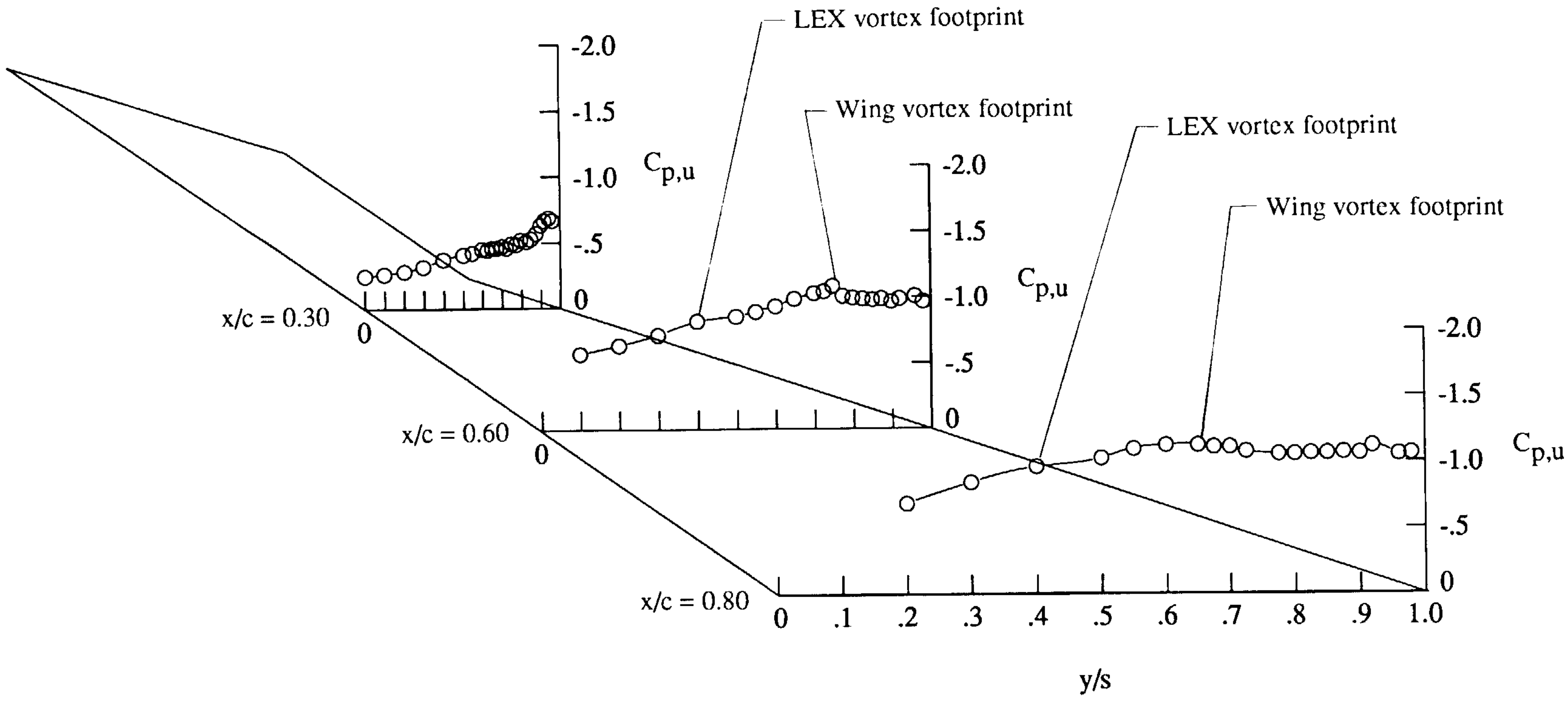

Figure 119. Wing upper surface static pressure distributions at $\alpha = 20°$ and $M_\infty = 0.95$ with LEX on.

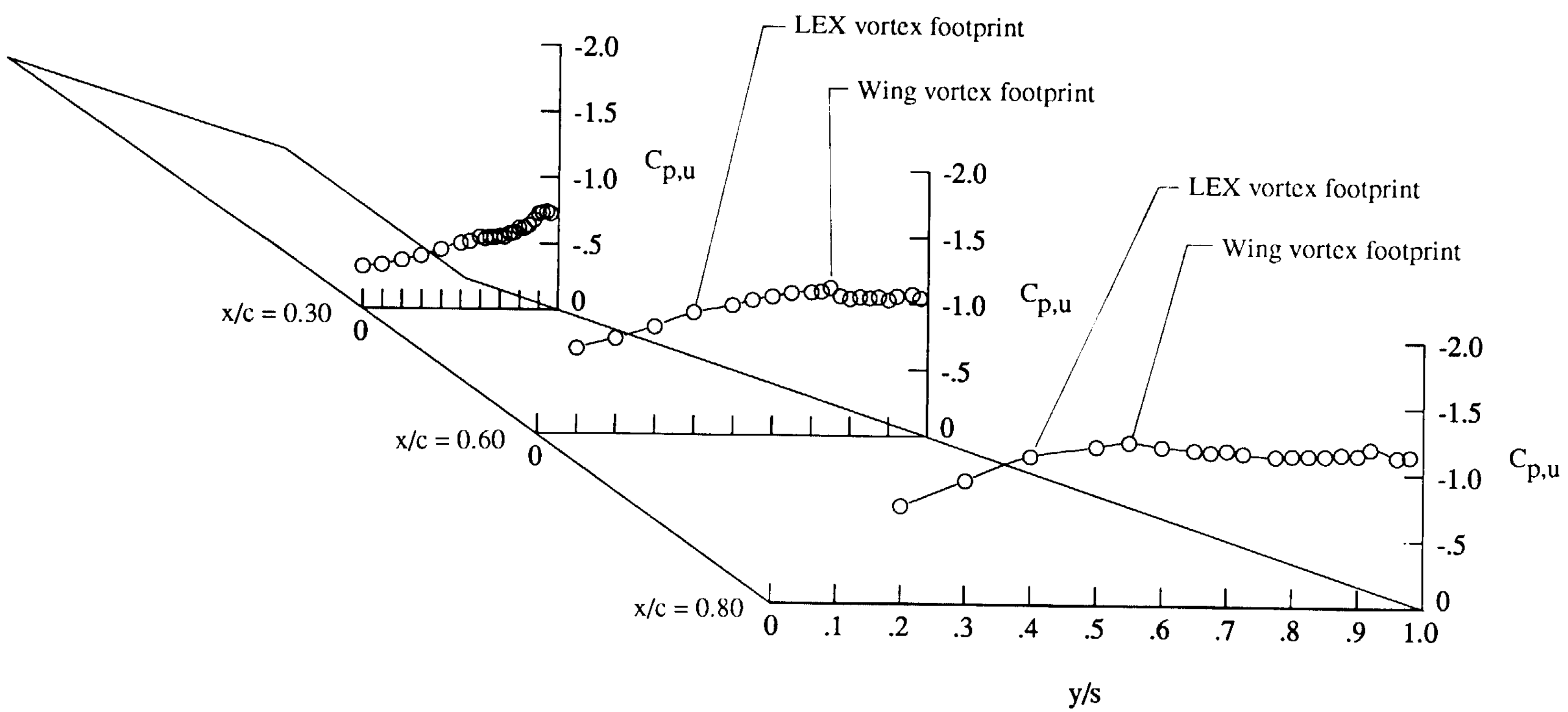

Figure 120. Wing upper surface static pressure distributions at $\alpha = 24°$ and $M_\infty = 0.95$ with LEX on.

ORIGINAL PAGE
BLACK AND WHITE PHOTOGRAPH

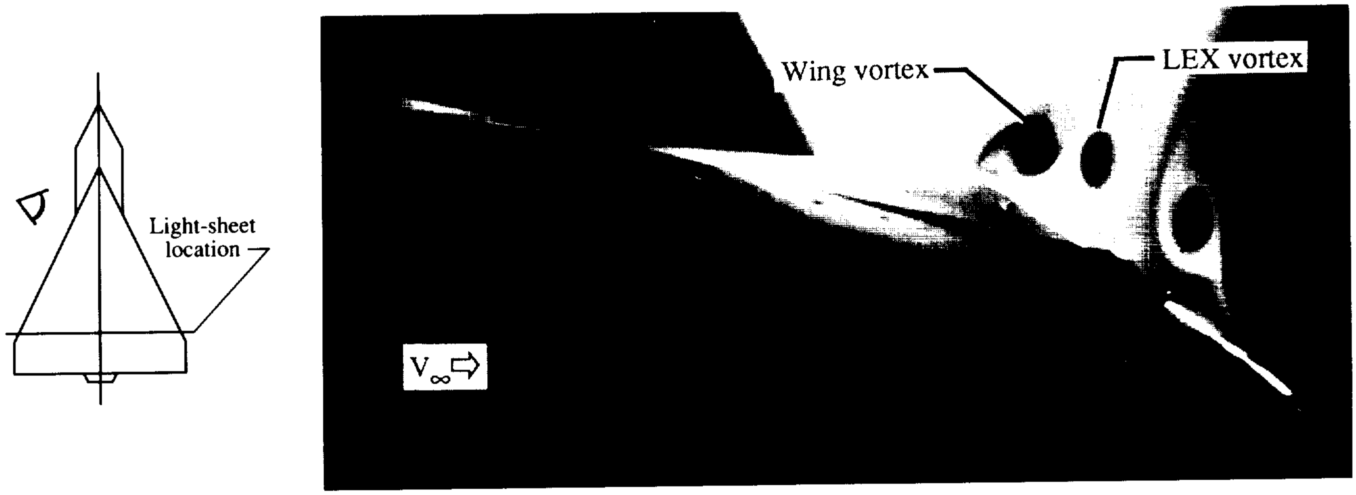

(a) $\alpha = 16°$.

(b) $\alpha = 20°$.

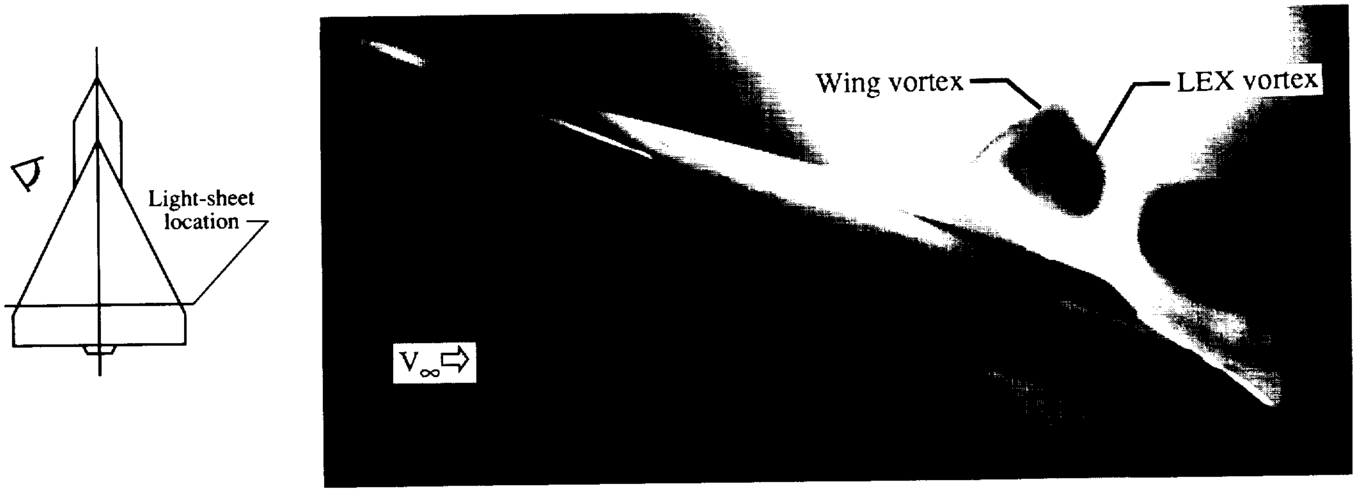

(c) $\alpha = 24°$.

Figure 121. Laser vapor screen flow visualizations at $x/c = 0.80$ and $M_\infty = 0.95$ with LEX on.

(a) $x/c = 0.80$.

Figure 122. Laser vapor screen flow visualizations at $\alpha = 20^\circ$ and $M_\infty = 0.95$ with LEX on.

(b) $x/c = 0.90$.

Figure 122. Continued.

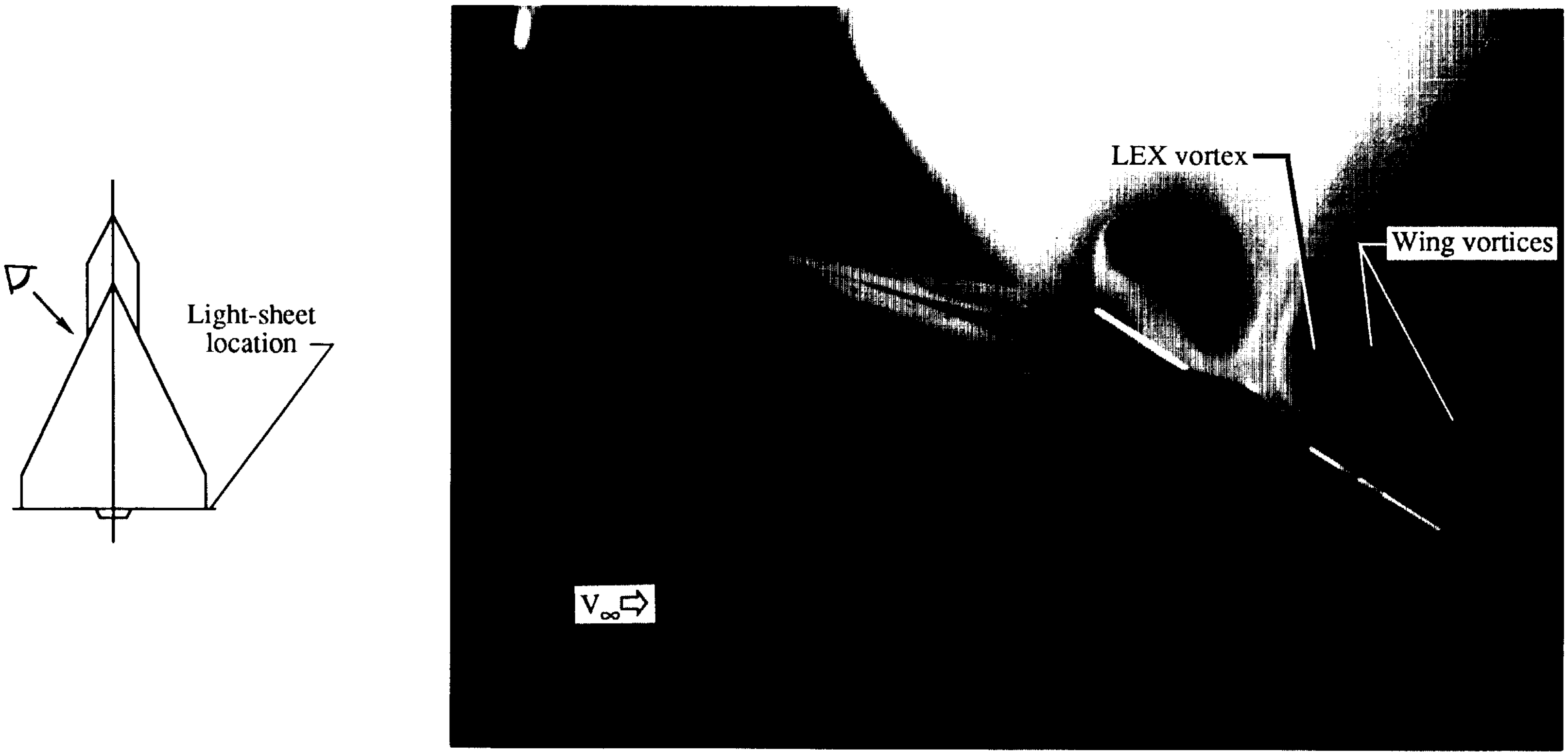

(c) $x/c = 1.00$.

Figure 122. Continued.

(d) $x/c = 1.10$.

Figure 122. Concluded.

ORIGINAL PAGE
BLACK AND WHITE PHOTOGRAPH

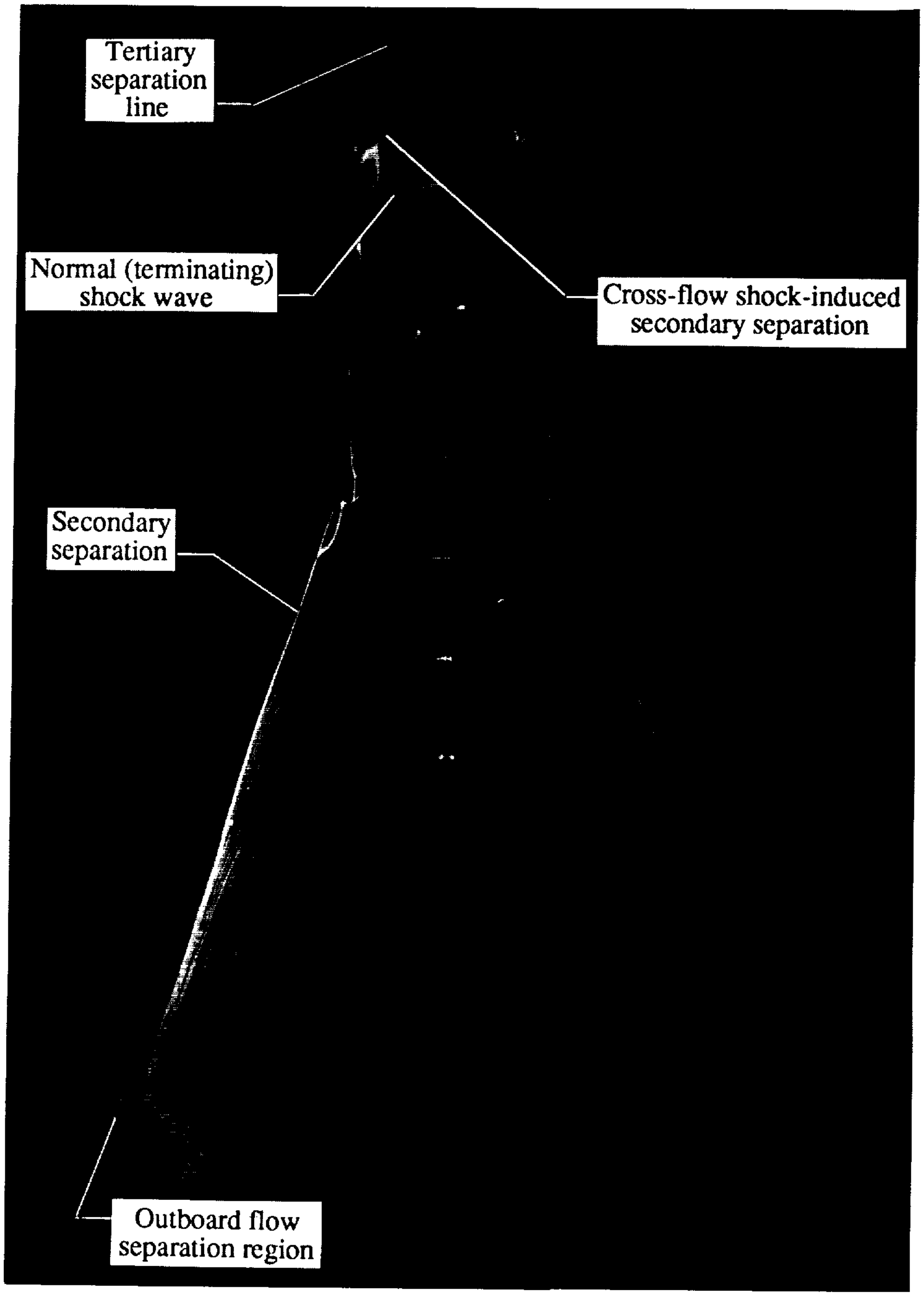

Figure 123. Wing upper surface oil flow pattern at $\alpha = 20°$ and $M_\infty = 0.95$ with LEX on.

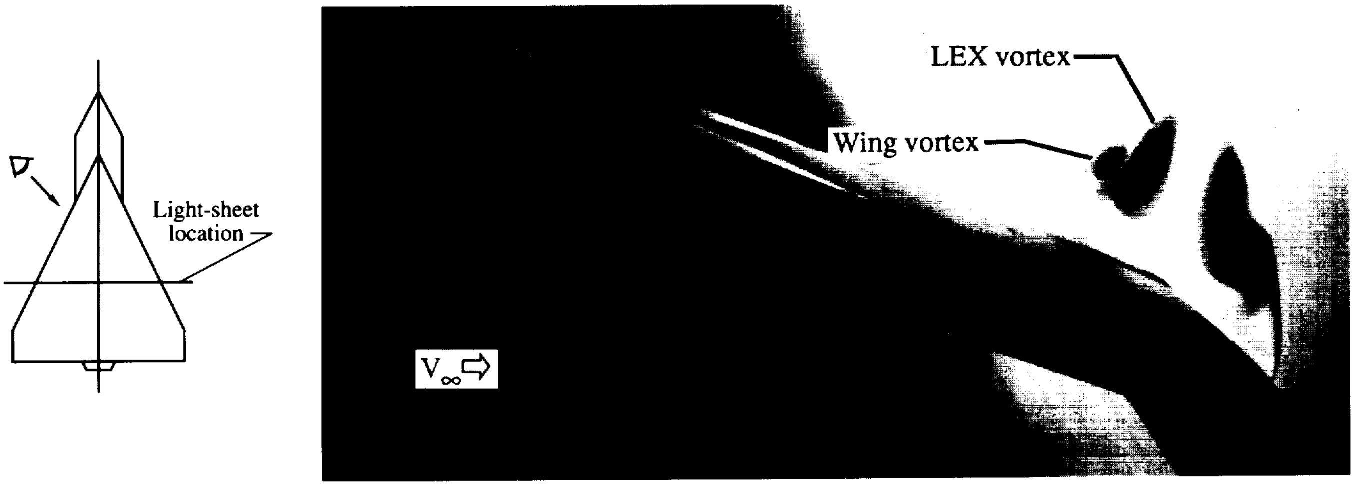

(a) $x/c = 0.60$.

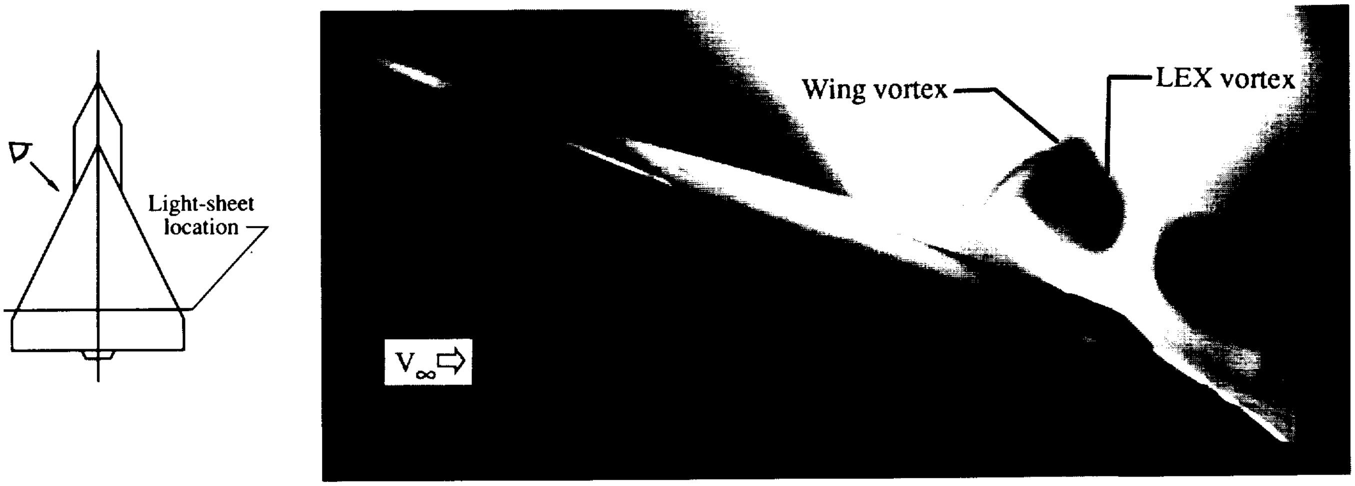

(b) $x/c = 0.80$.

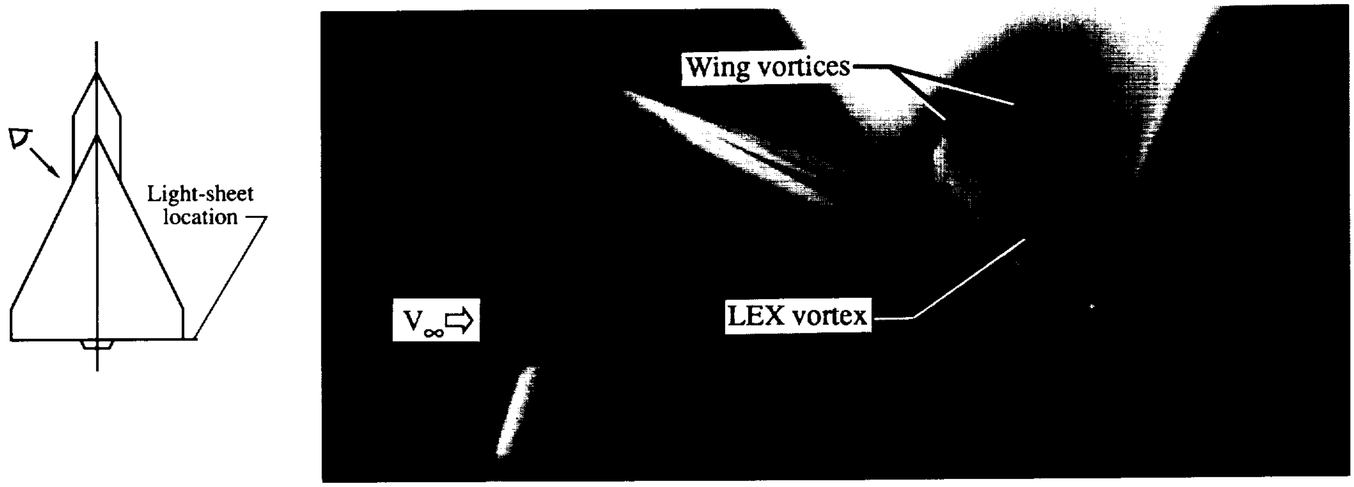

(c) $x/c = 1.00$.

Figure 124. Laser vapor screen flow visualizations at $\alpha = 24^\circ$ and $M_\infty = 0.95$ with LEX on.

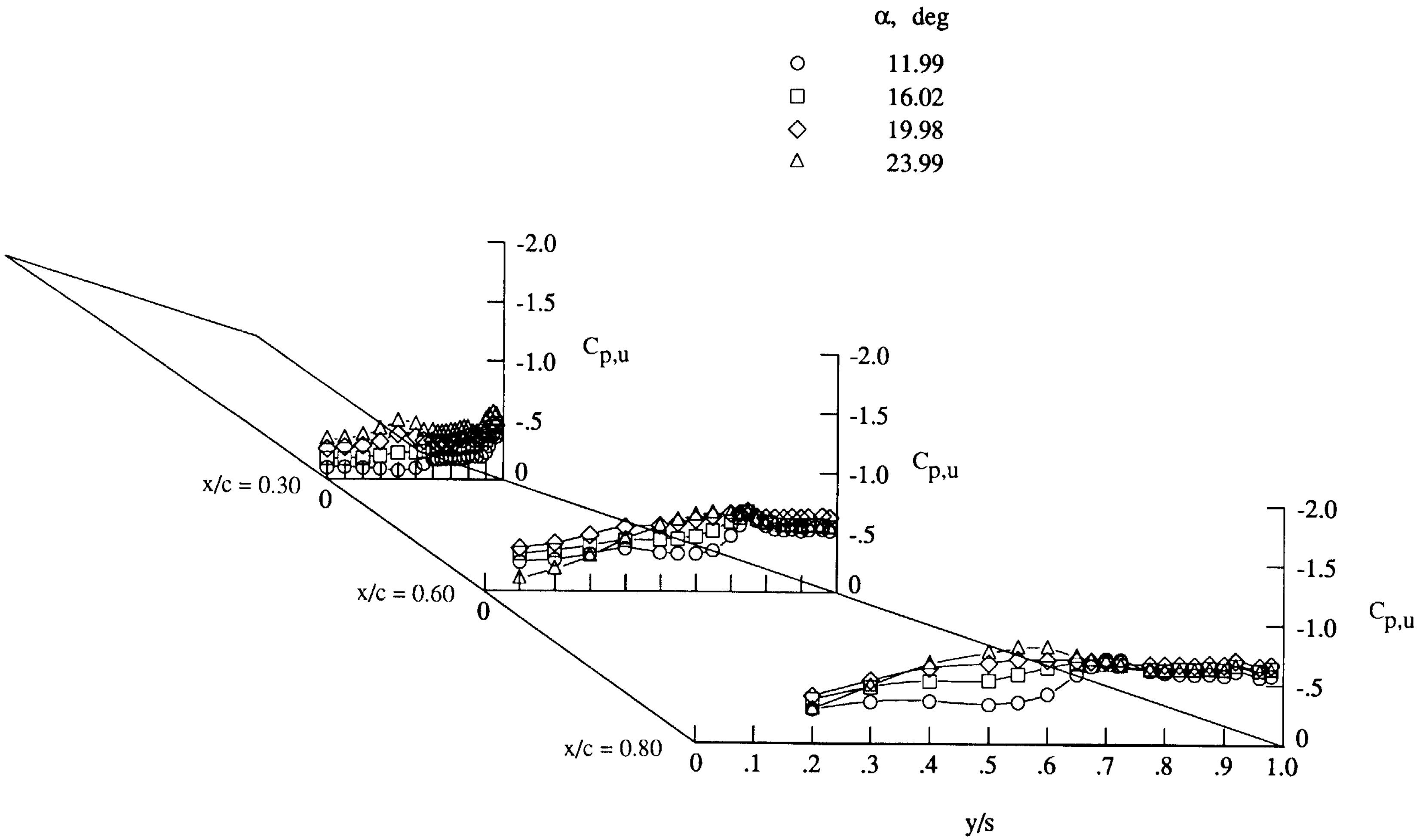

Figure 125. Wing upper surface static pressure distributions at $M_\infty = 1.20$ with LEX on.

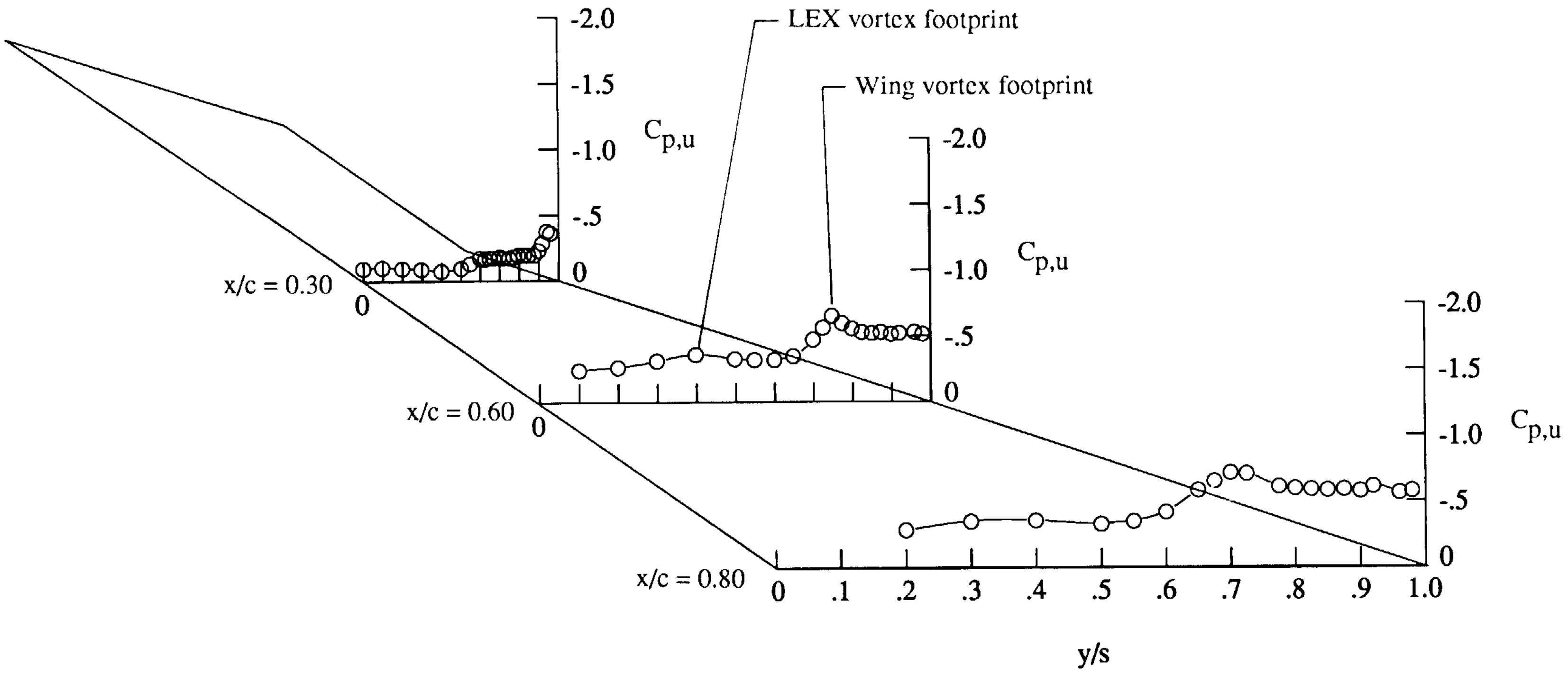

Figure 126. Wing upper surface static pressure distributions at $\alpha = 12°$ and $M_\infty = 1.20$ with LEX on.

ORIGINAL PAGE
BLACK AND WHITE PHOTOGRAPH

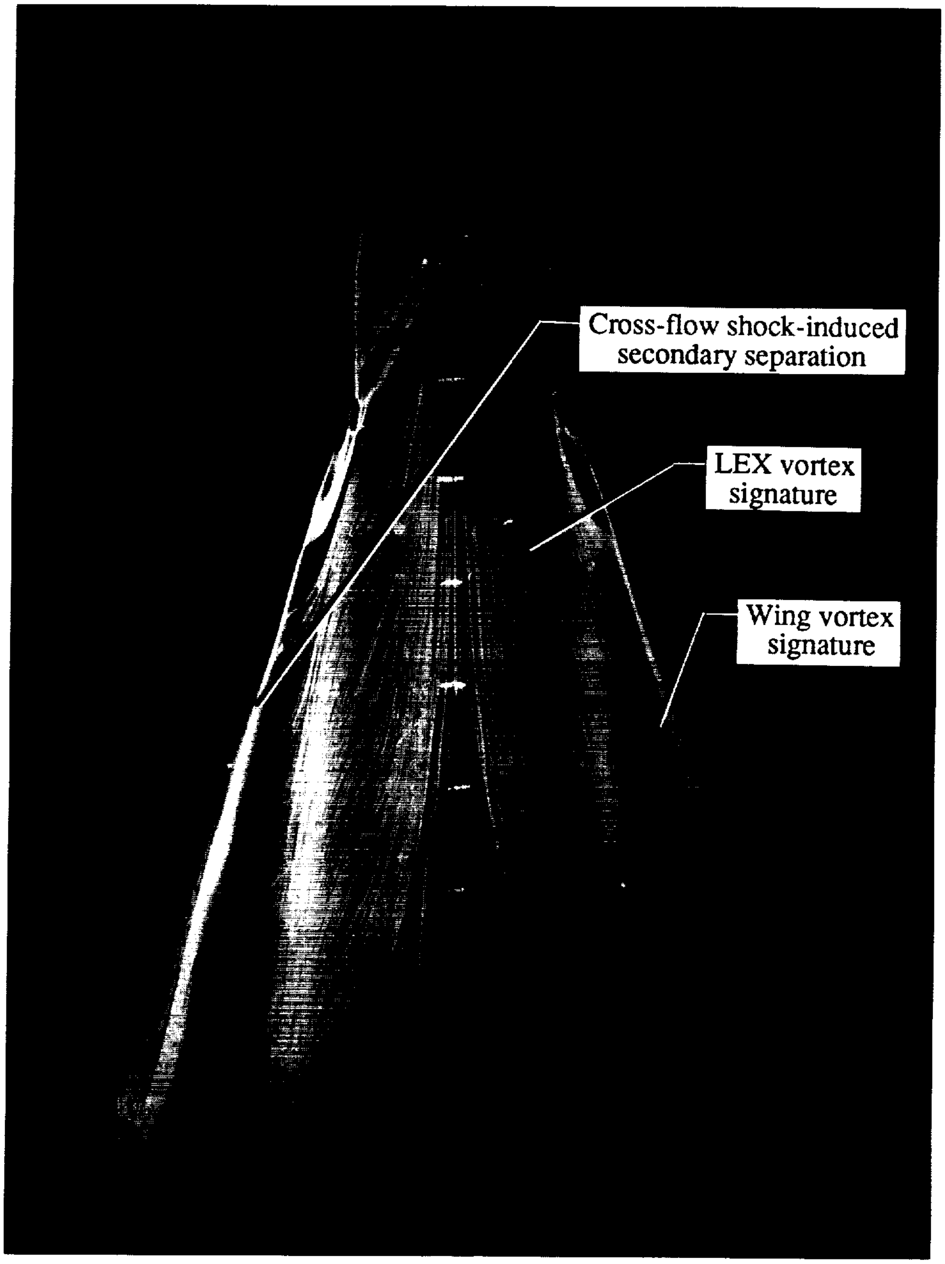

Figure 127. Wing upper surface oil flow pattern at $\alpha = 12°$ and $M_\infty = 1.20$ with LEX on.

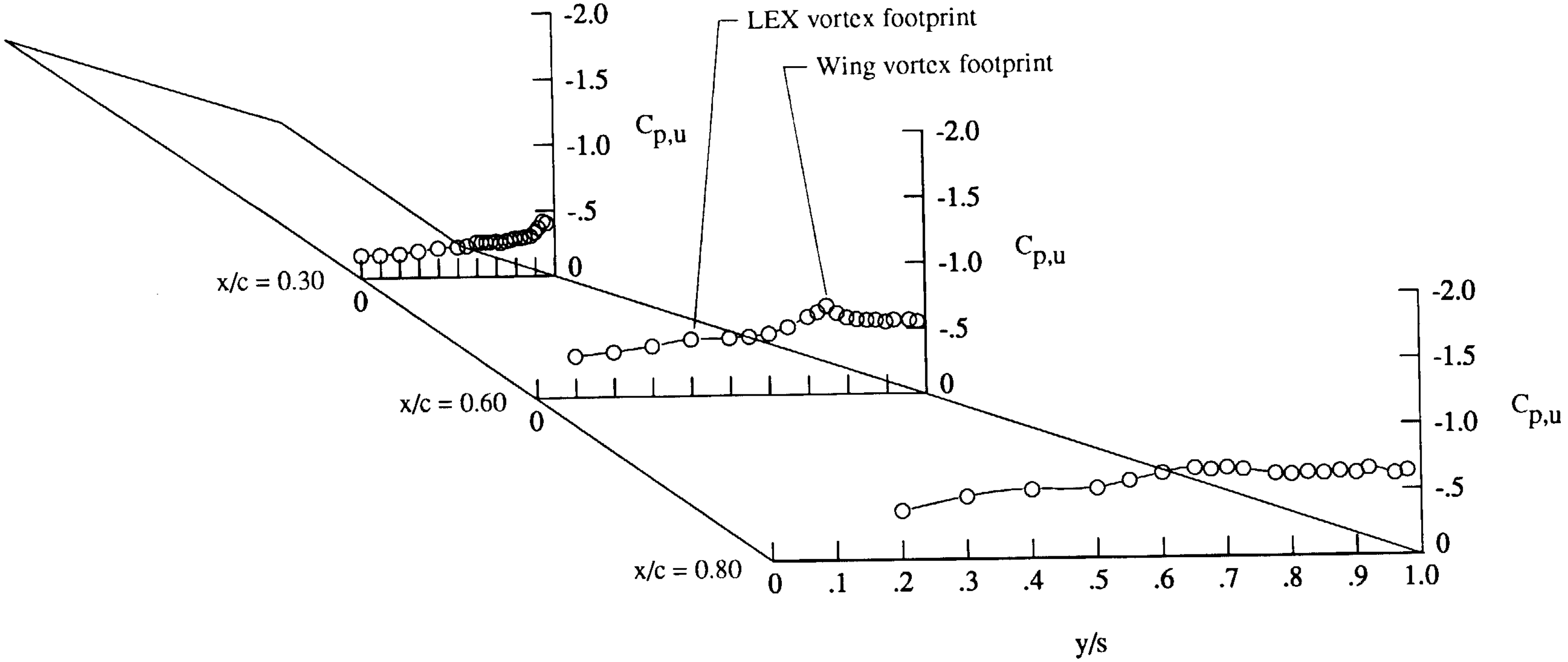

Figure 128. Wing upper surface static pressure distributions at $\alpha = 16°$ and $M_\infty = 1.20$ with LEX on.

ORIGINAL PAGE
BLACK AND WHITE PHOTOGRAPH

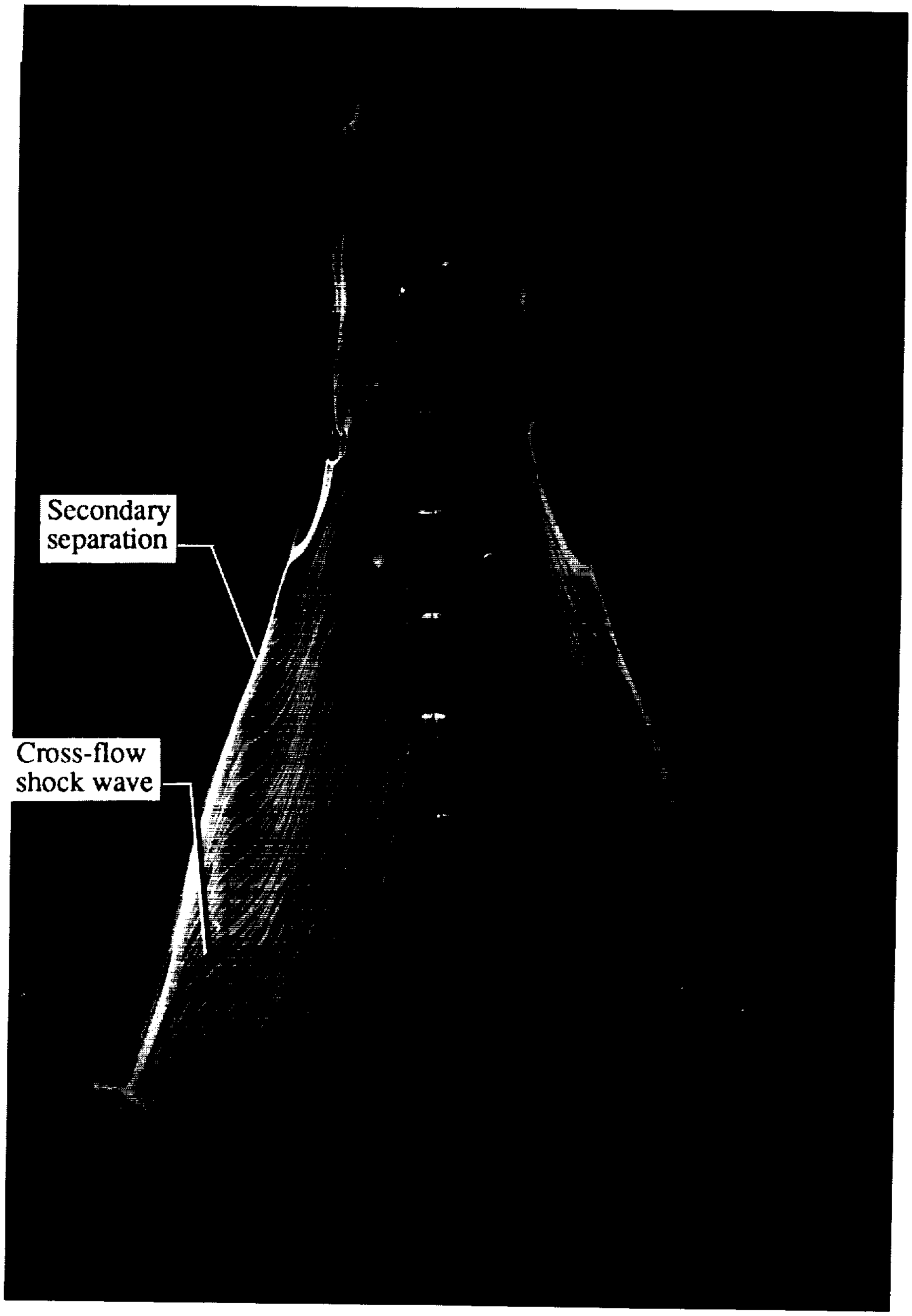

Figure 129. Wing upper surface oil flow pattern at $\alpha = 16°$ and $M_\infty = 1.20$ with LEX on.

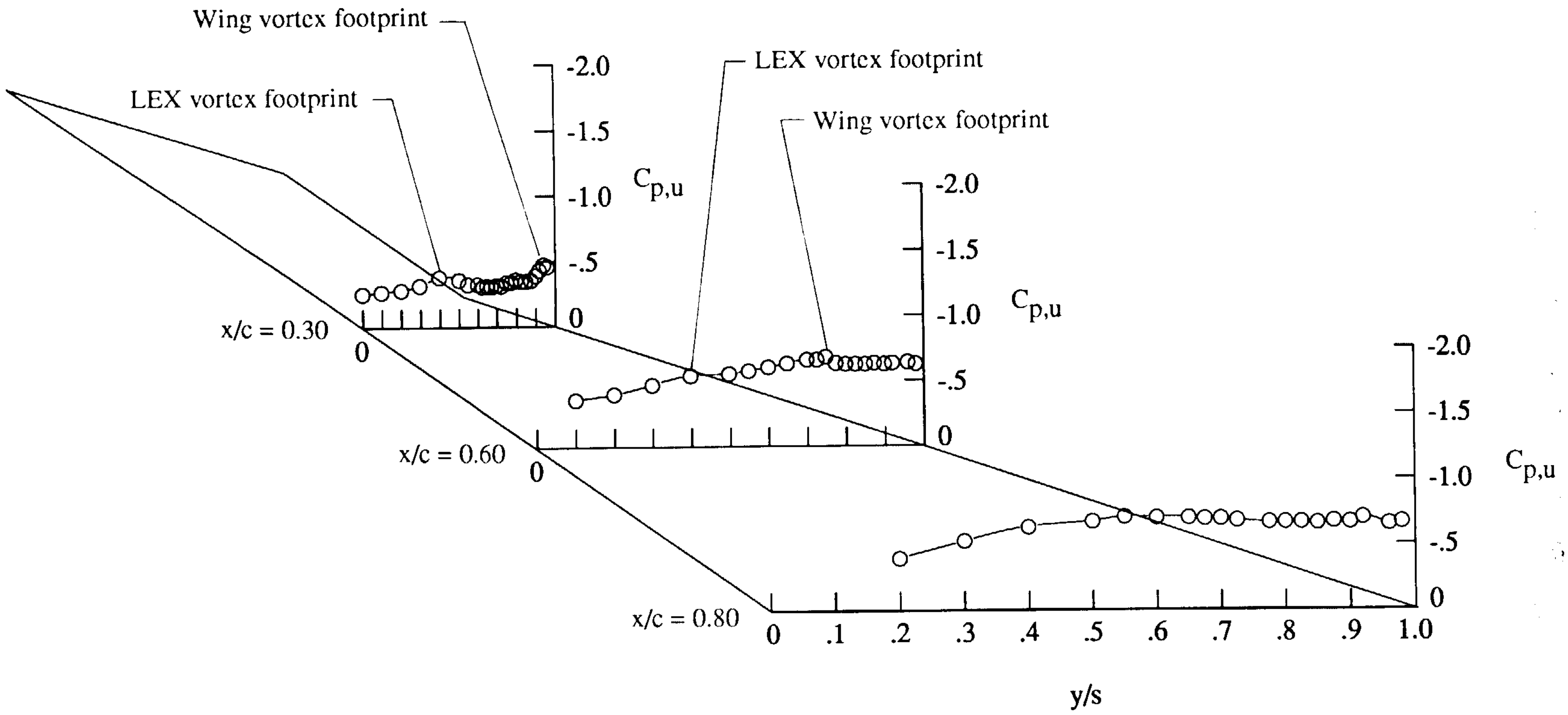

Figure 130. Wing upper surface static pressure distributions at $\alpha = 20°$ and $M_\infty = 1.20$ with LEX on.

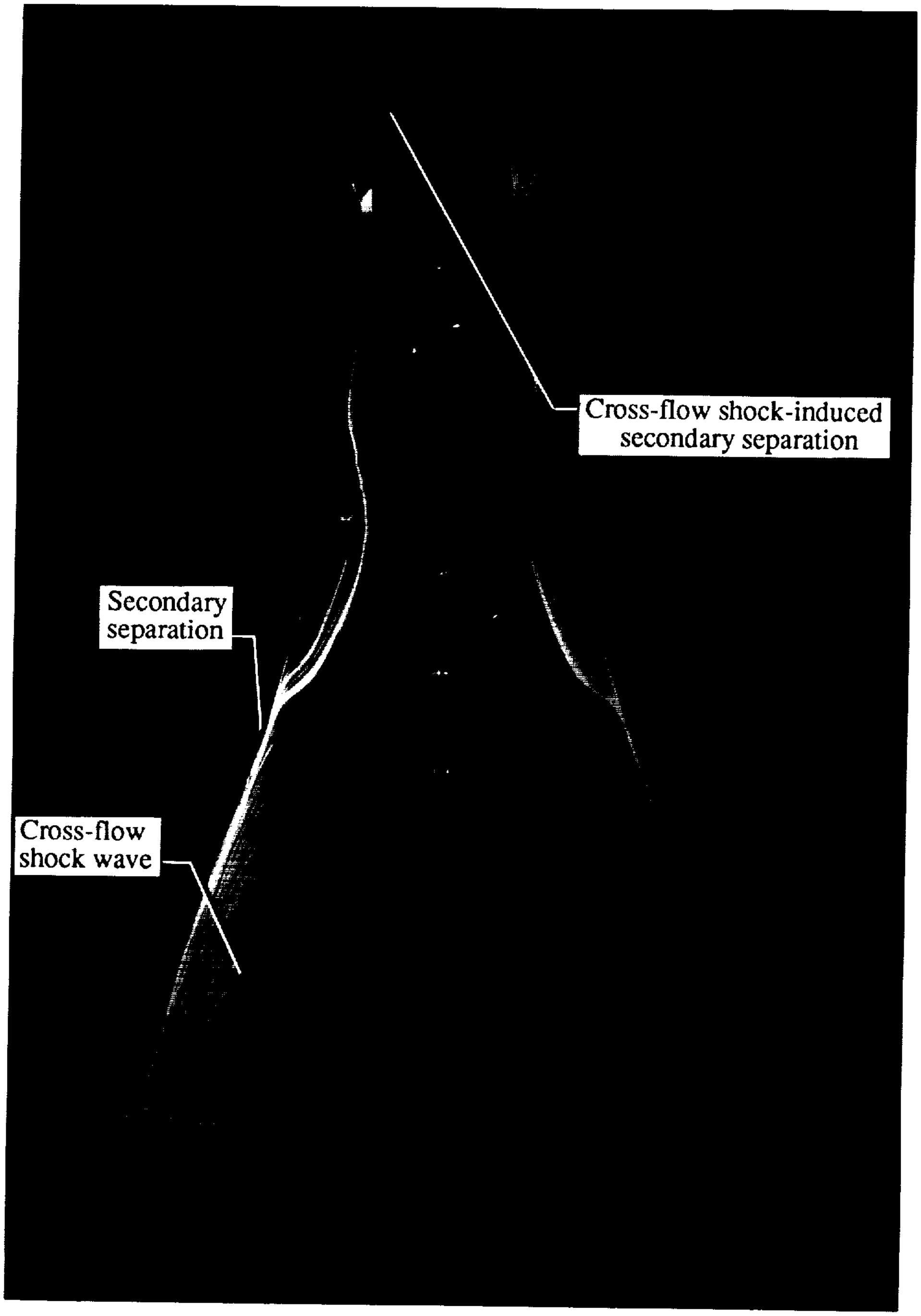

Figure 131. Wing upper surface oil flow pattern at $\alpha = 20^\circ$ and $M_\infty = 1.20$ with LEX on.

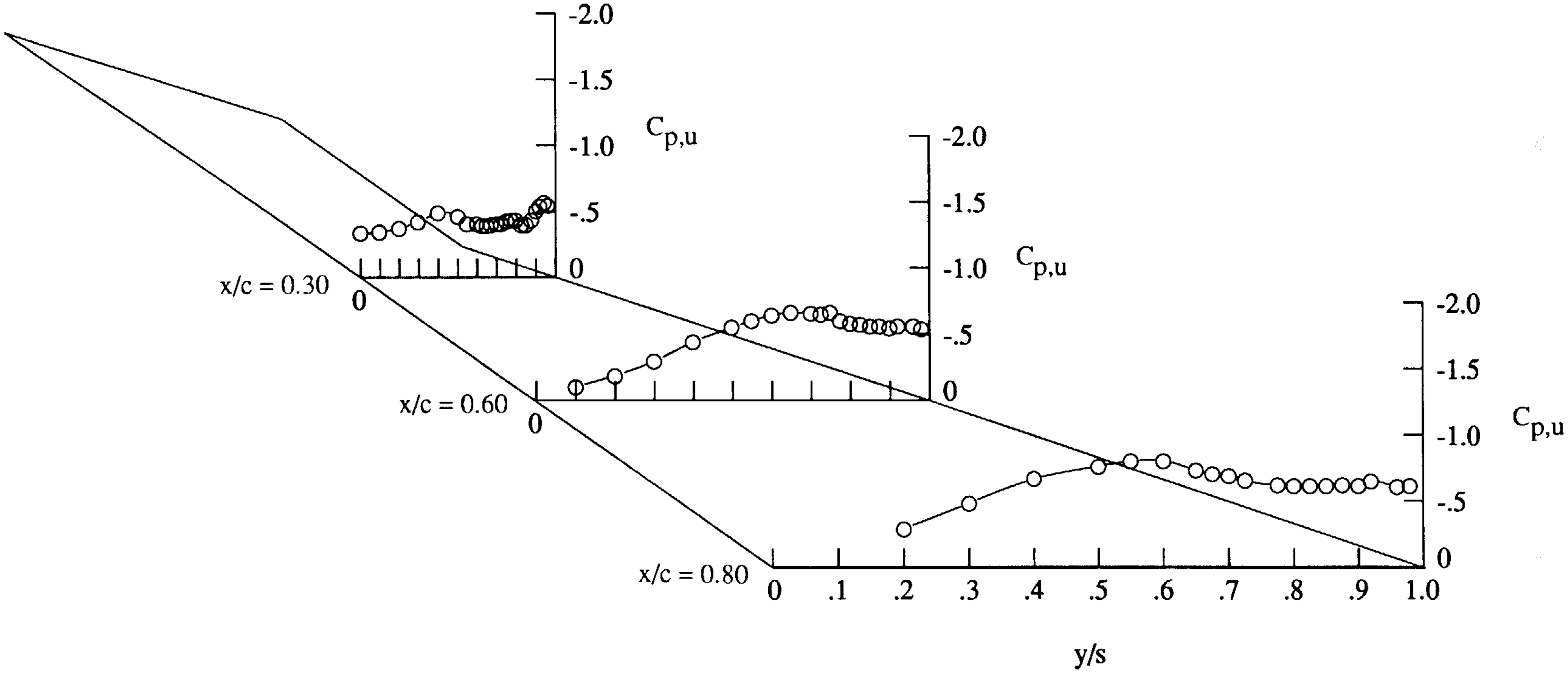

Figure 132. Wing upper surface static pressure distributions at $\alpha = 24°$ and $M_\infty = 1.20$ with LEX on.

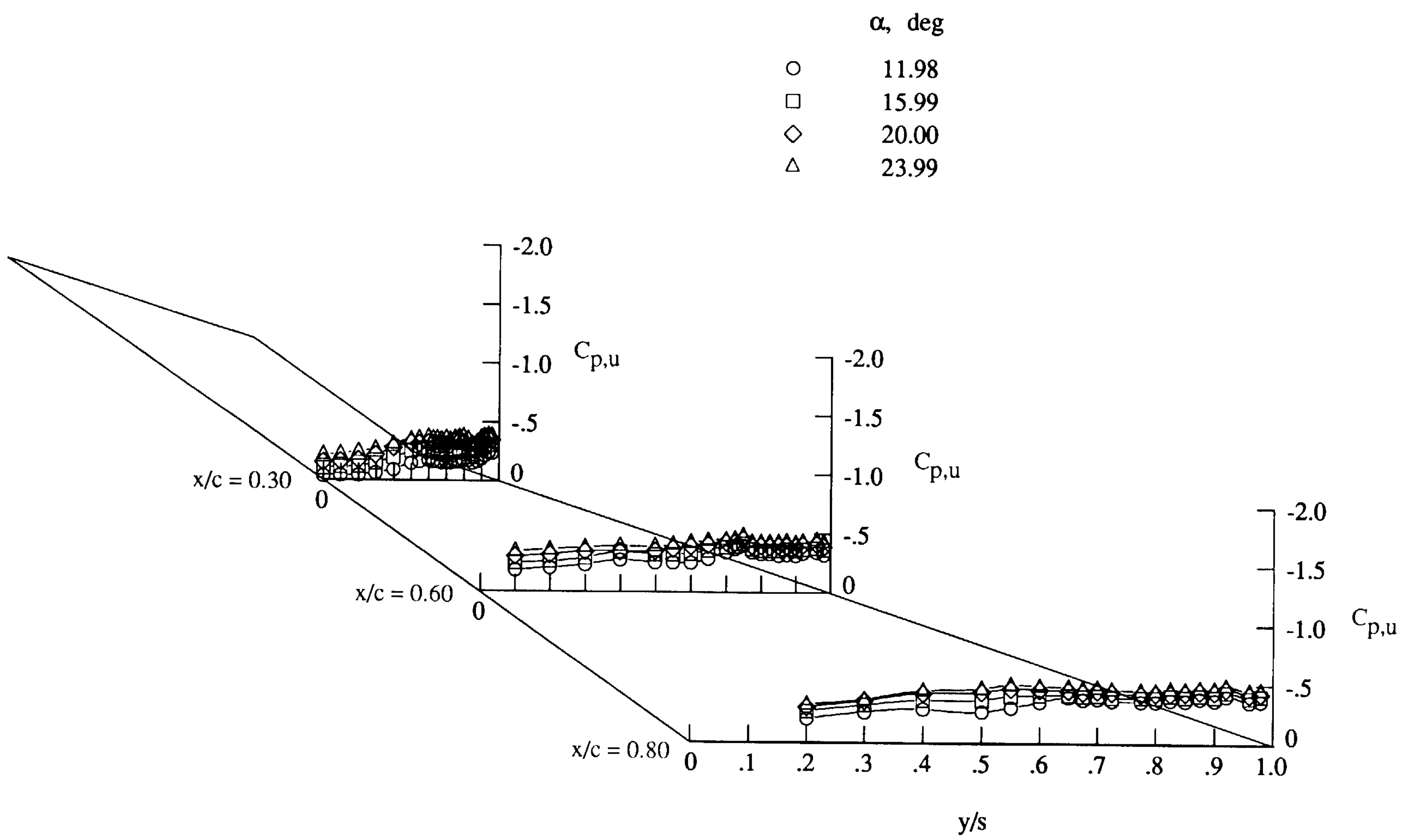

Figure 133. Wing upper surface static pressure distributions at $M_\infty = 1.60$ with LEX on.

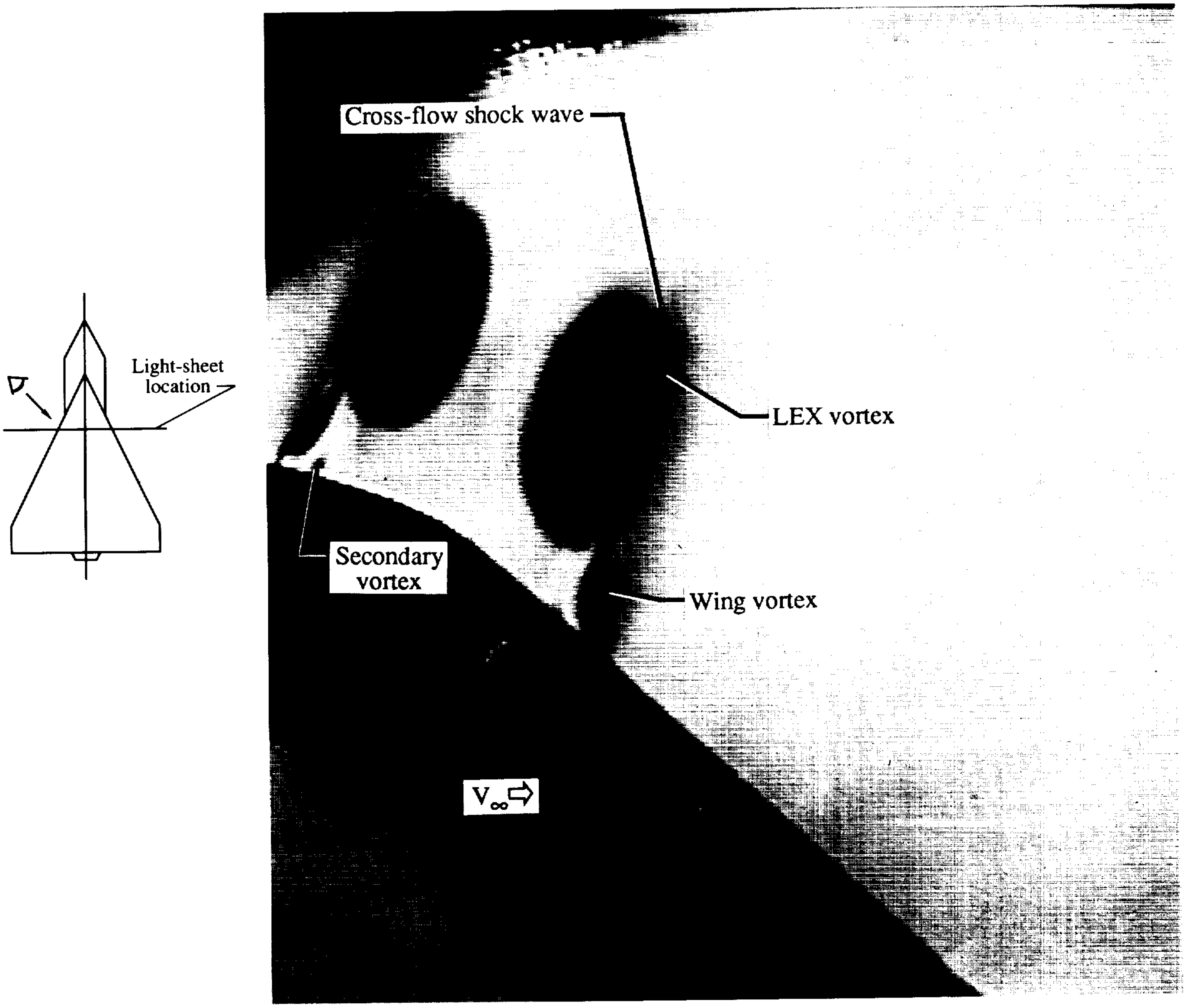

(a) $x/c = 0.30$.

Figure 134. Laser vapor screen flow visualizations at $\alpha = 24°$ and $M_\infty = 1.60$ with LEX on.

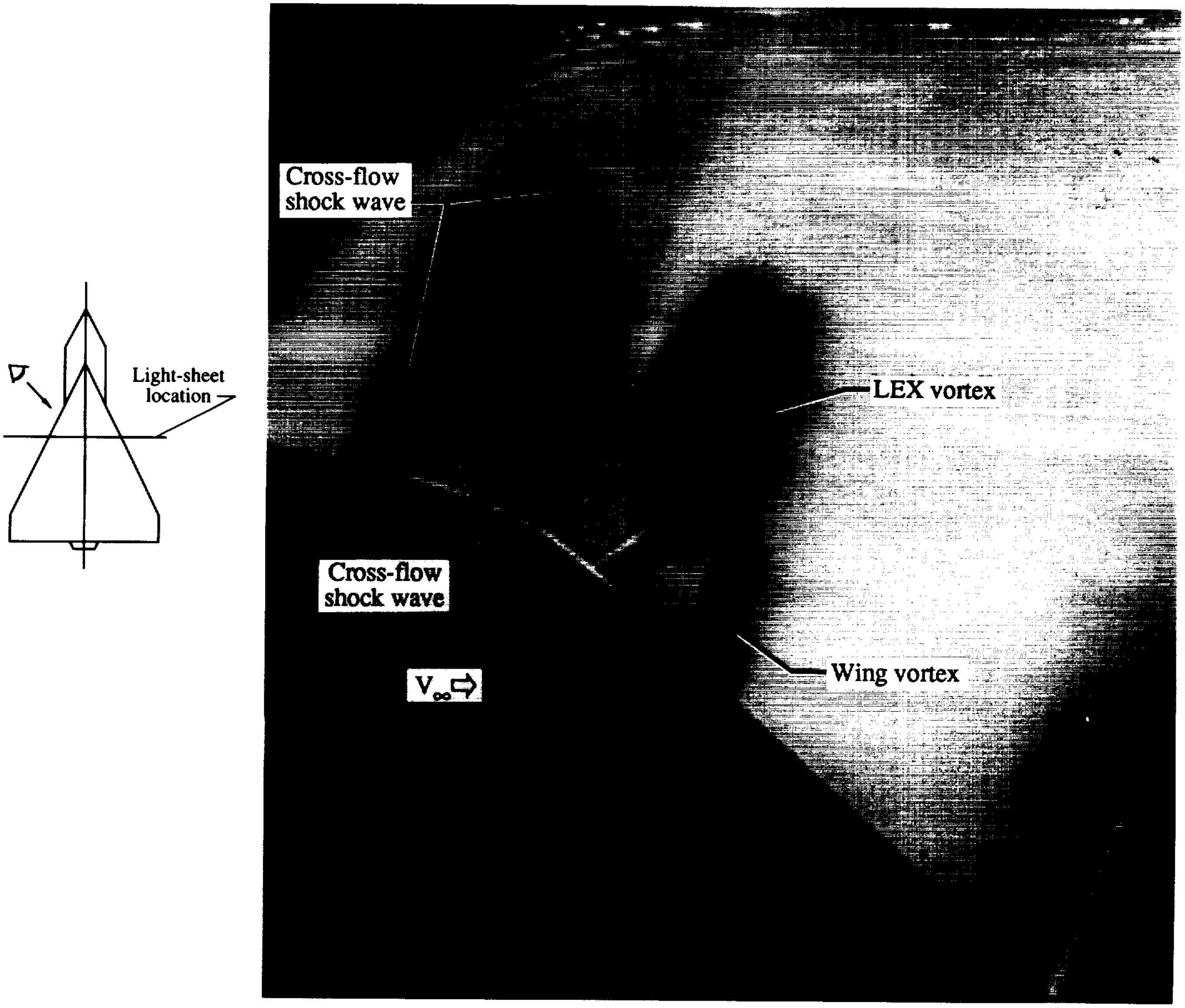

(b) $x/c = 0.40$.

Figure 134. Continued.

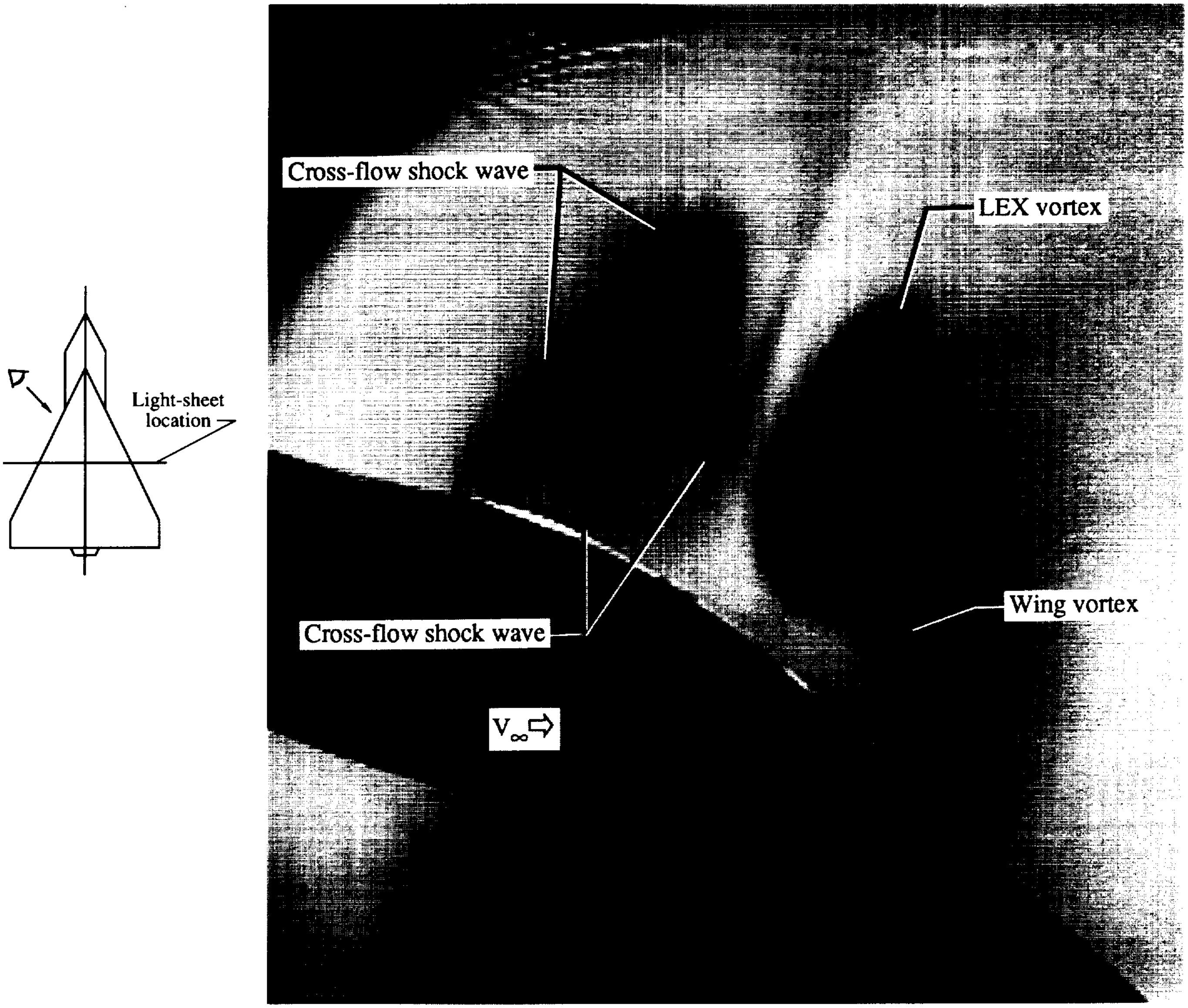

(c) $x/c = 0.50$.

Figure 134. Continued.

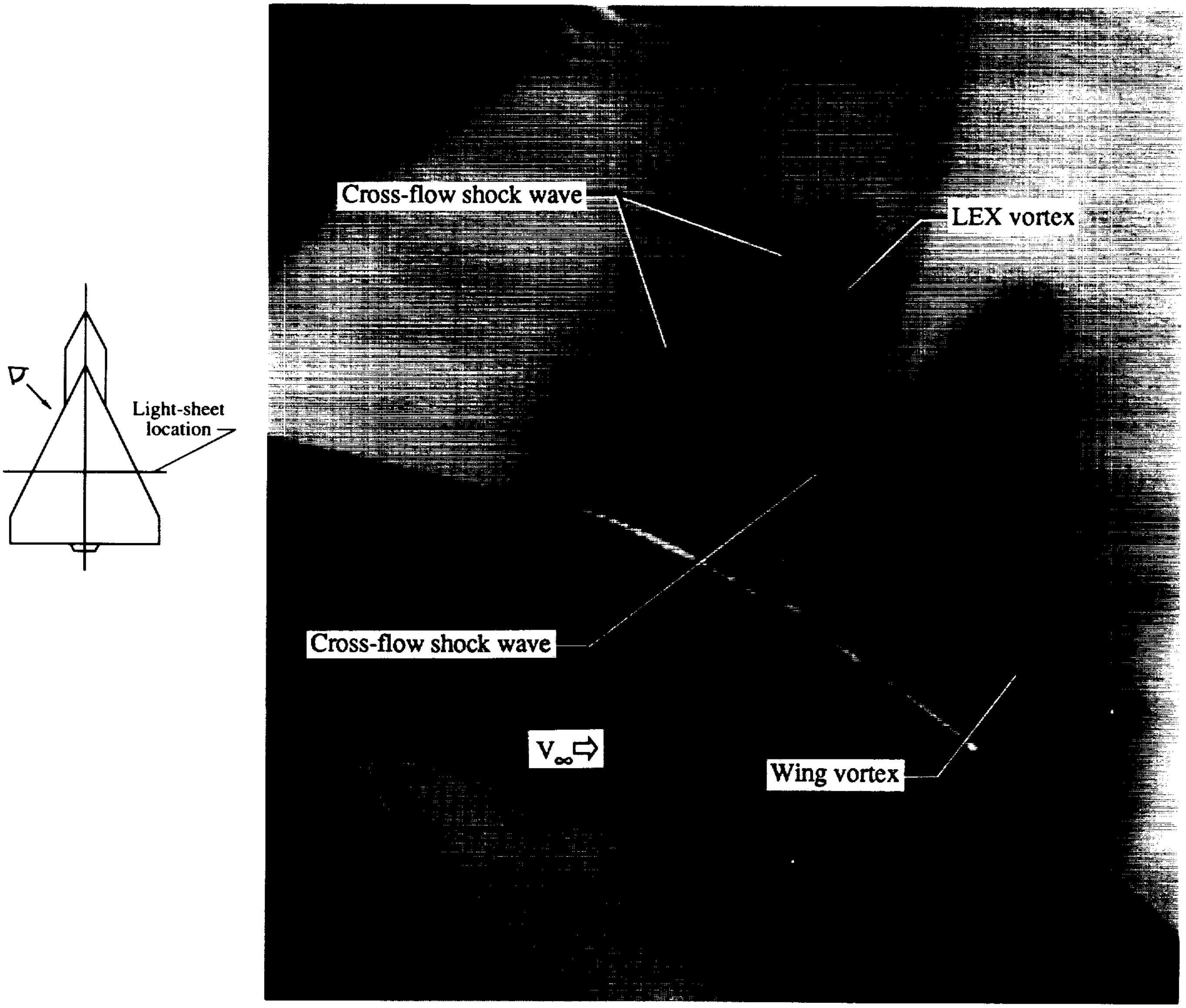

(d) $x/c = 0.55$.

Figure 134. Continued.

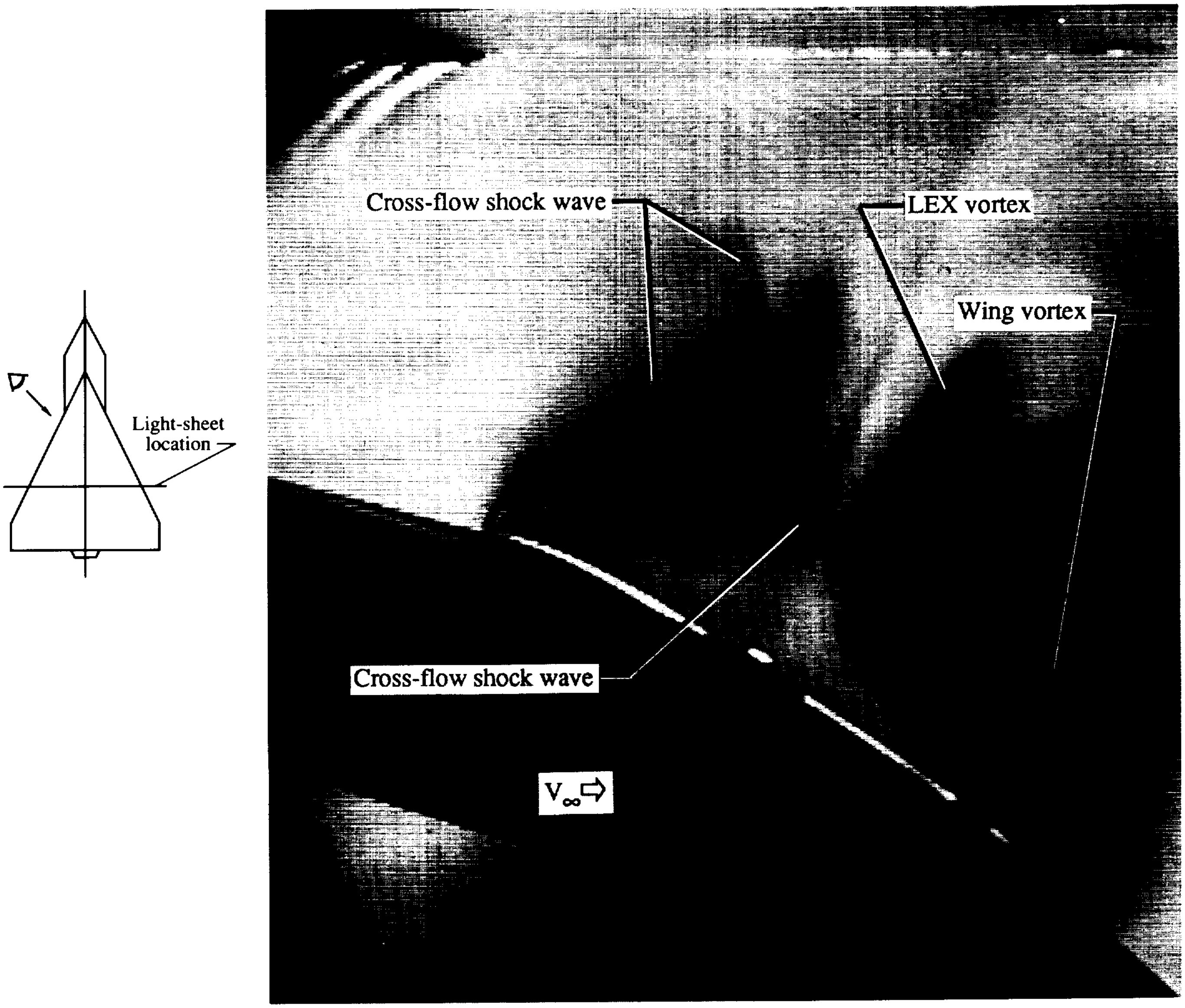

(e) $x/c = 0.60$.

Figure 134. Continued.

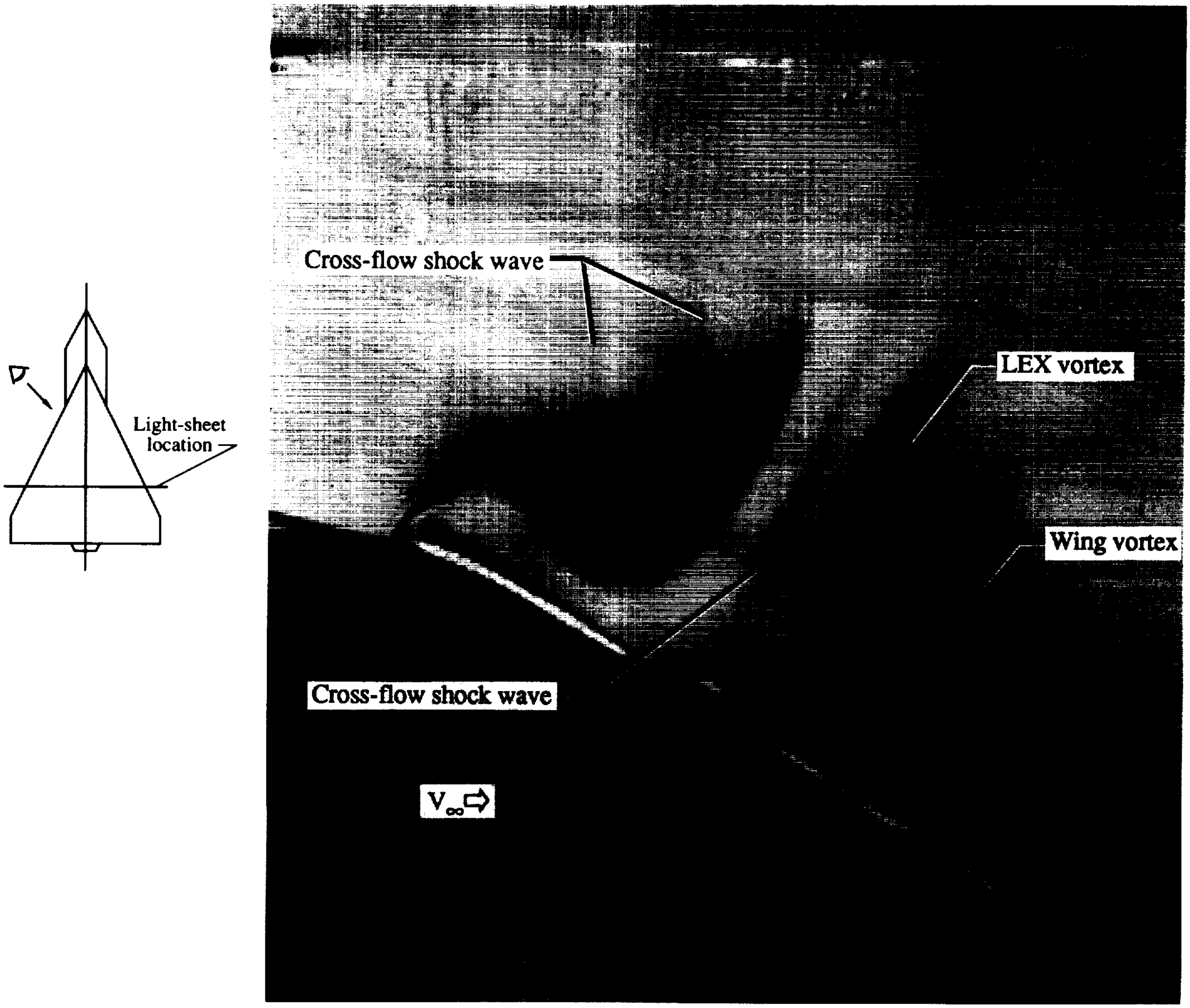

(f) $x/c = 0.65$.

Figure 134. Continued.

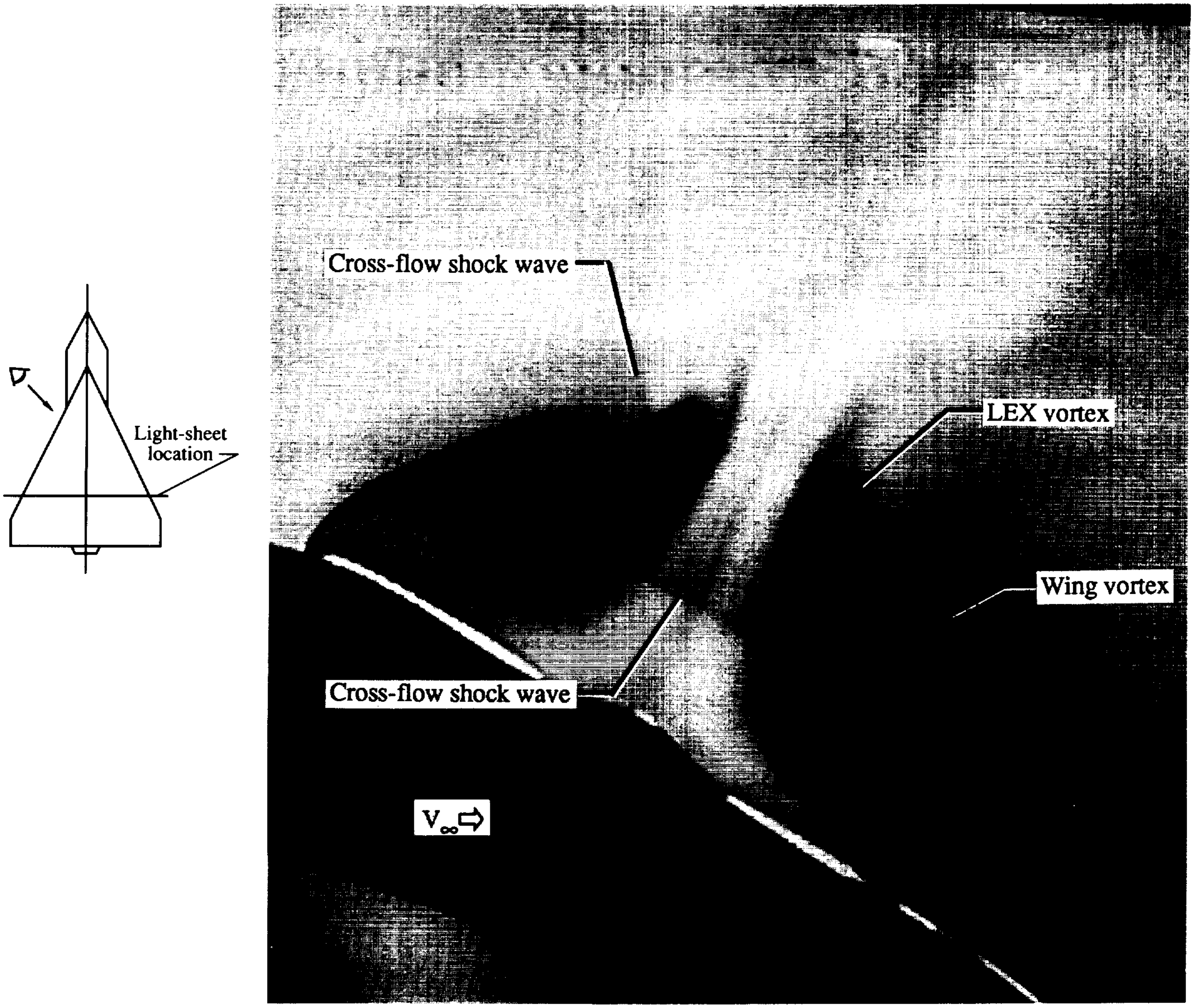

(g) $x/c = 0.70$.

Figure 134. Continued.

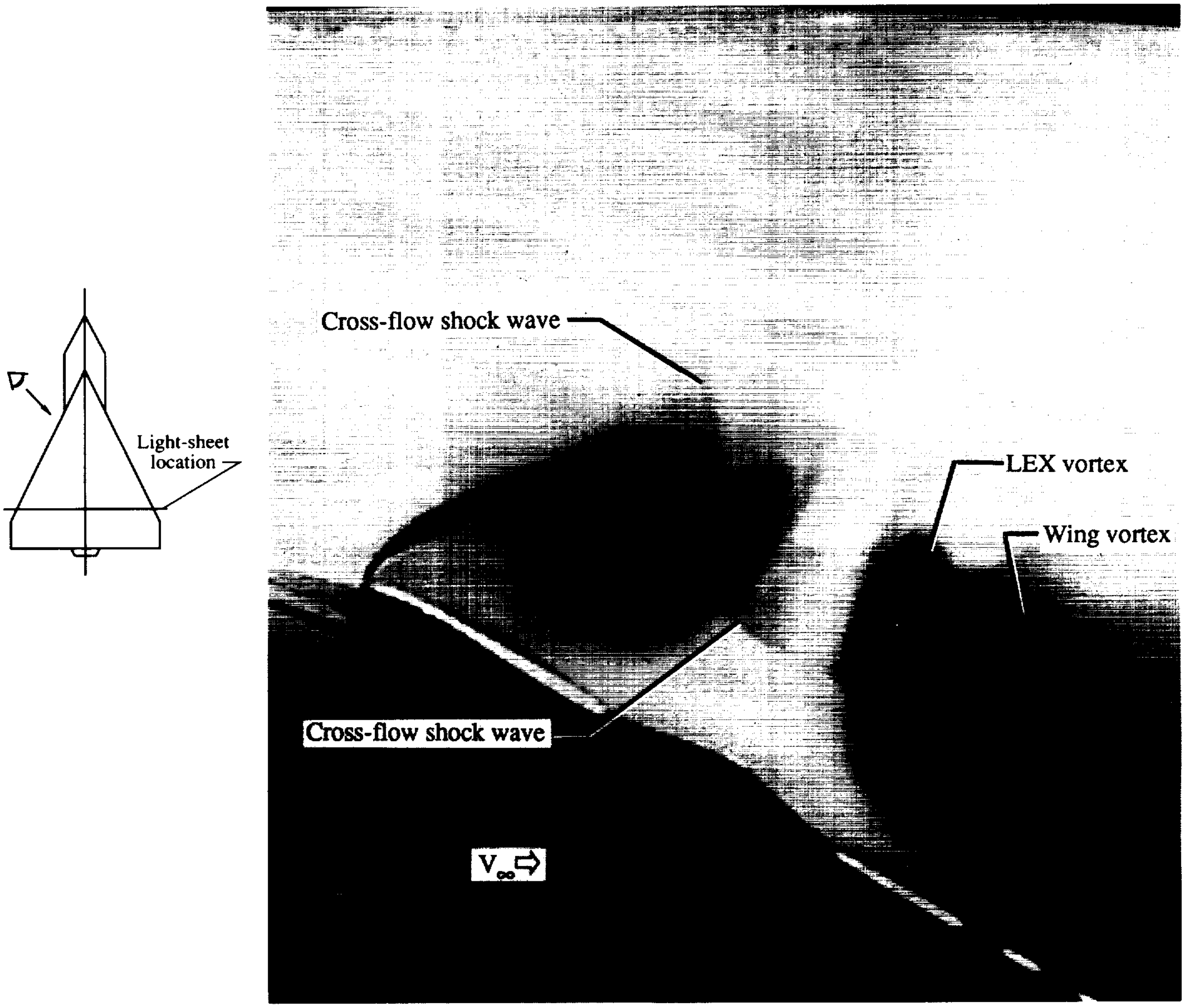

(h) $x/c = 0.80$.

Figure 134. Concluded.

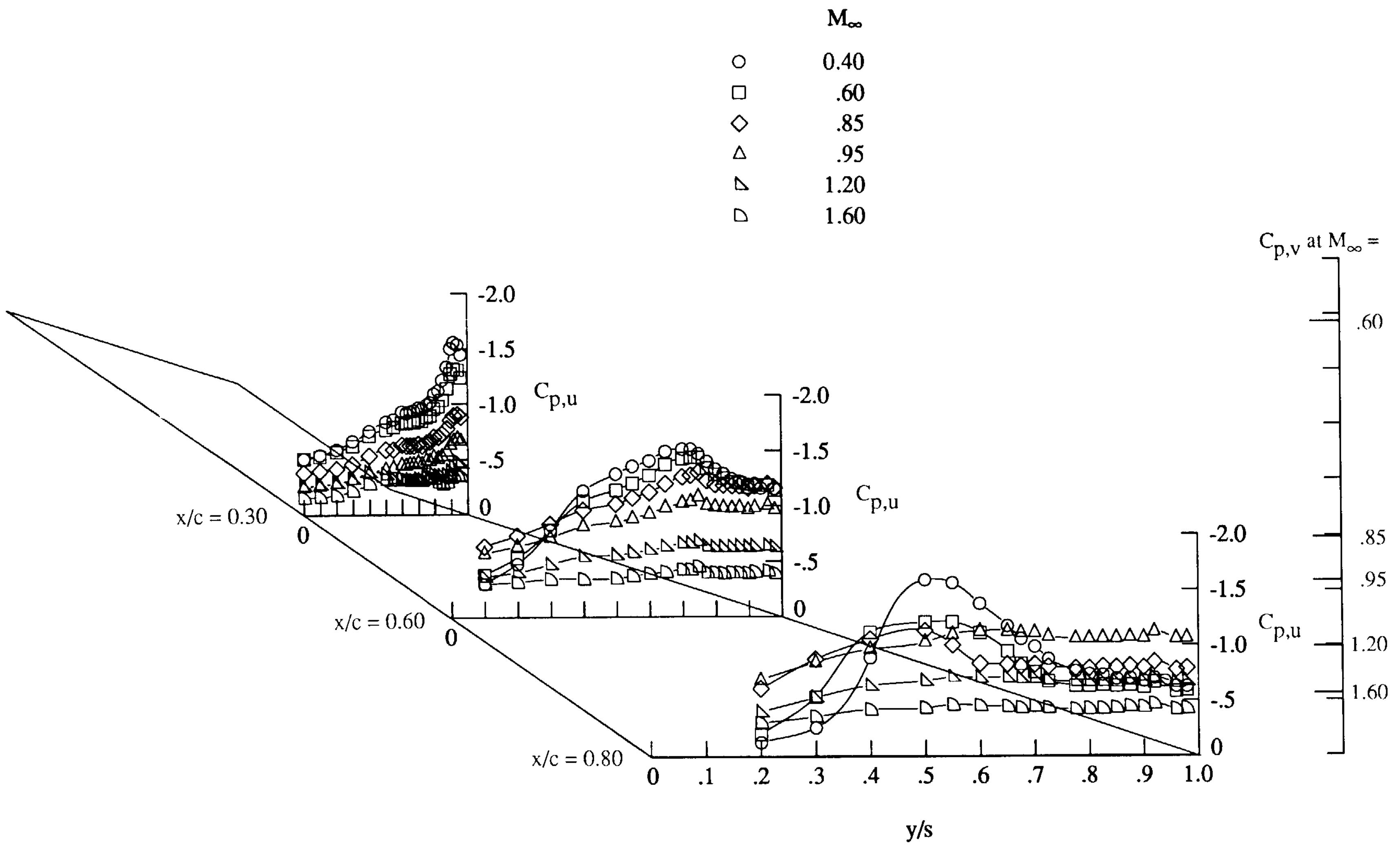

Figure 135. Effect of Mach number on wing upper surface static pressure distributions at $\alpha = 20°$ with LEX on.

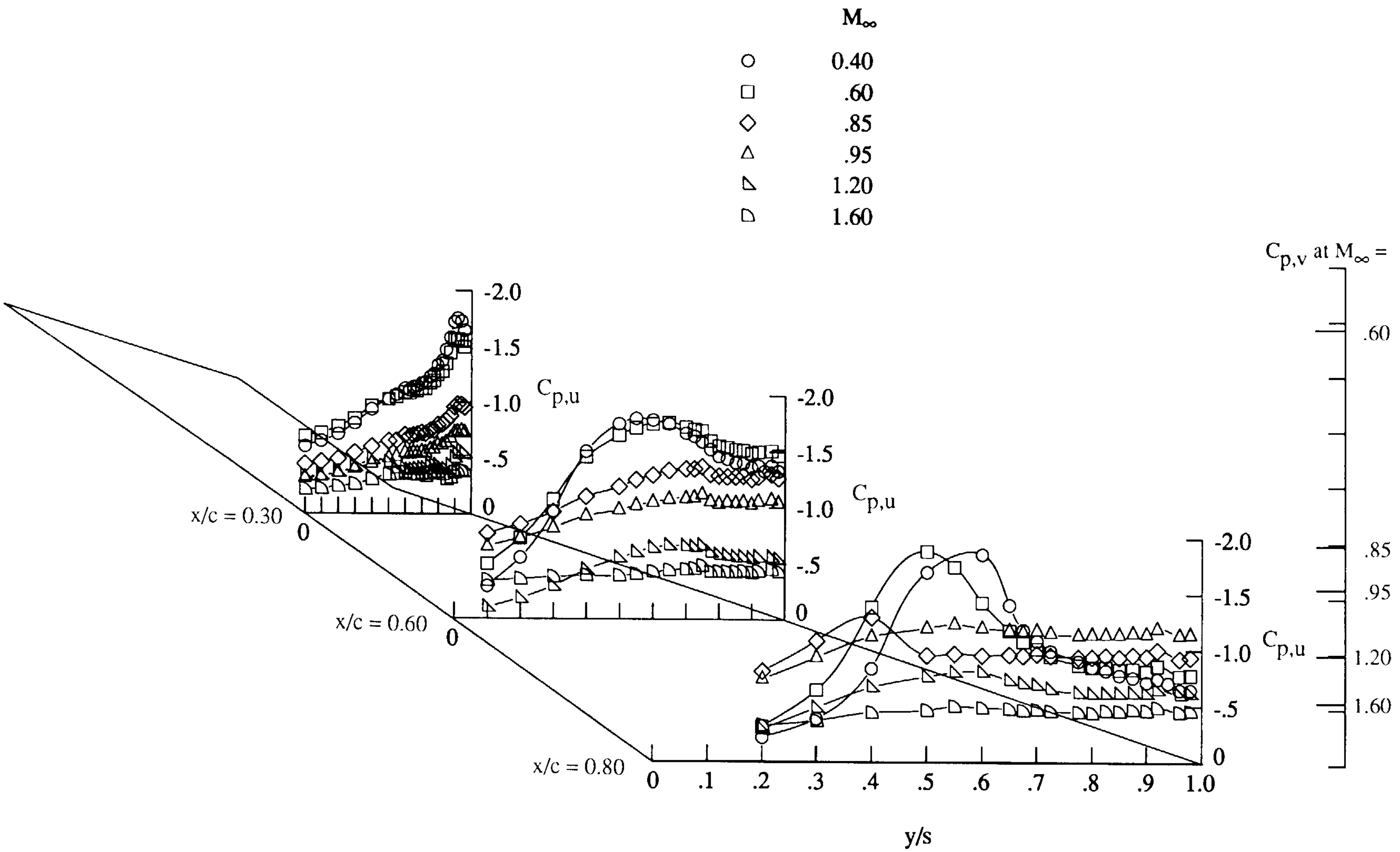

Figure 136. Effect of Mach number on wing upper surface static pressure distributions at $\alpha = 24°$ with LEX on.

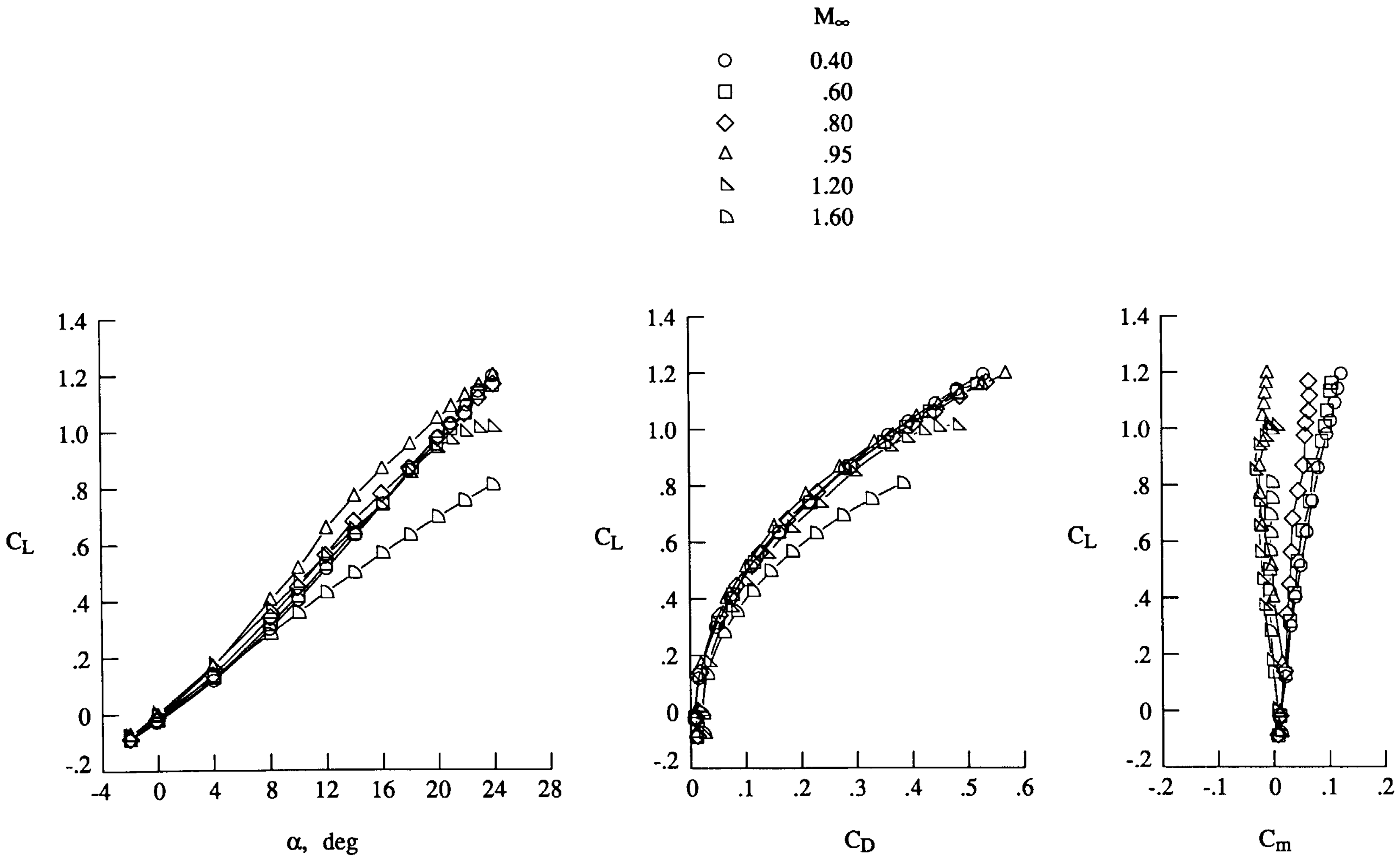

Figure 137. Effect of Mach number on lift, drag, and pitching-moment characteristics with LEX on.

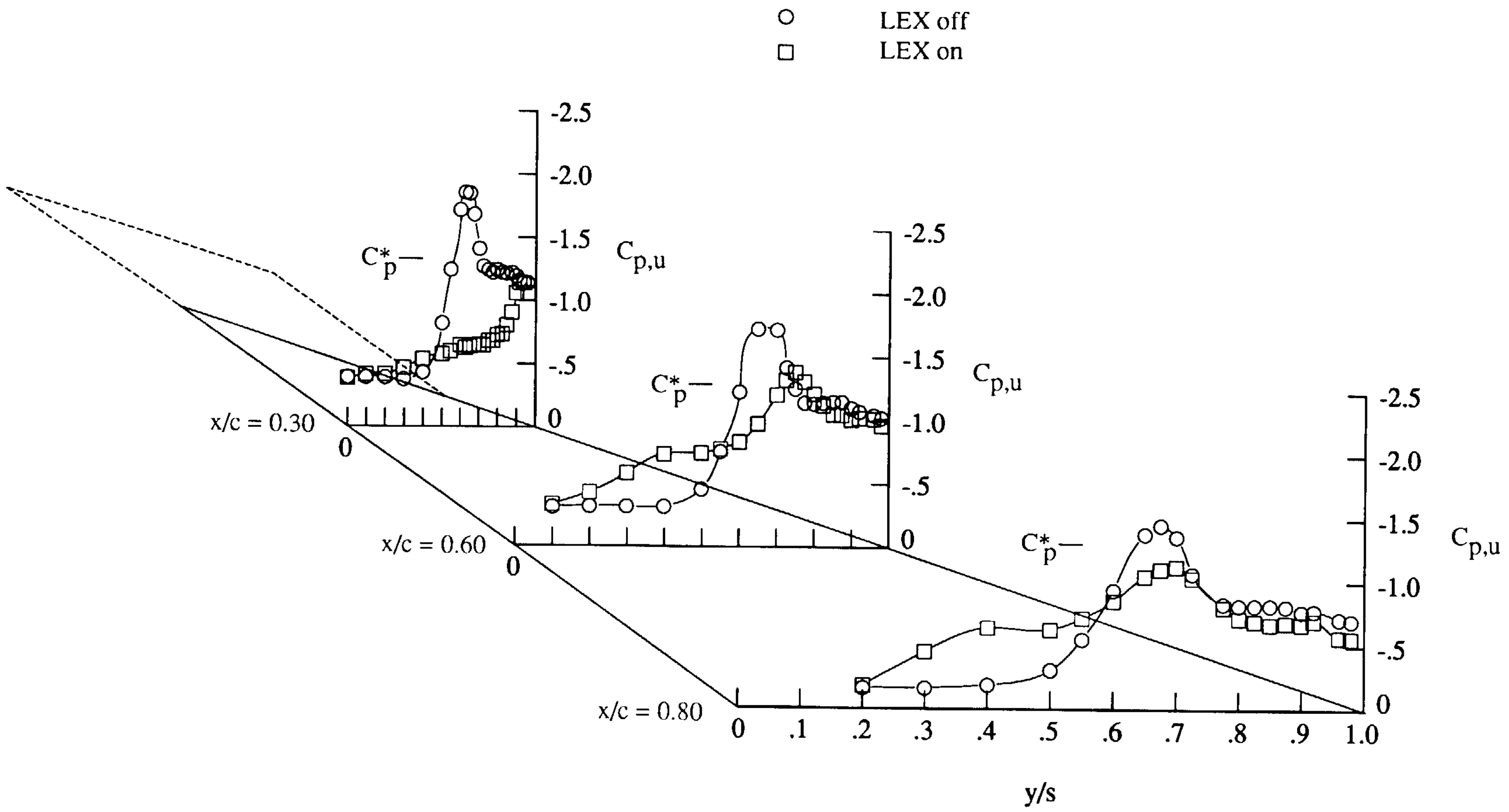

(a) $\alpha = 16°$.

Figure 138. Effect of LEX on wing upper surface static pressure distributions with $M_\infty = 0.60$.

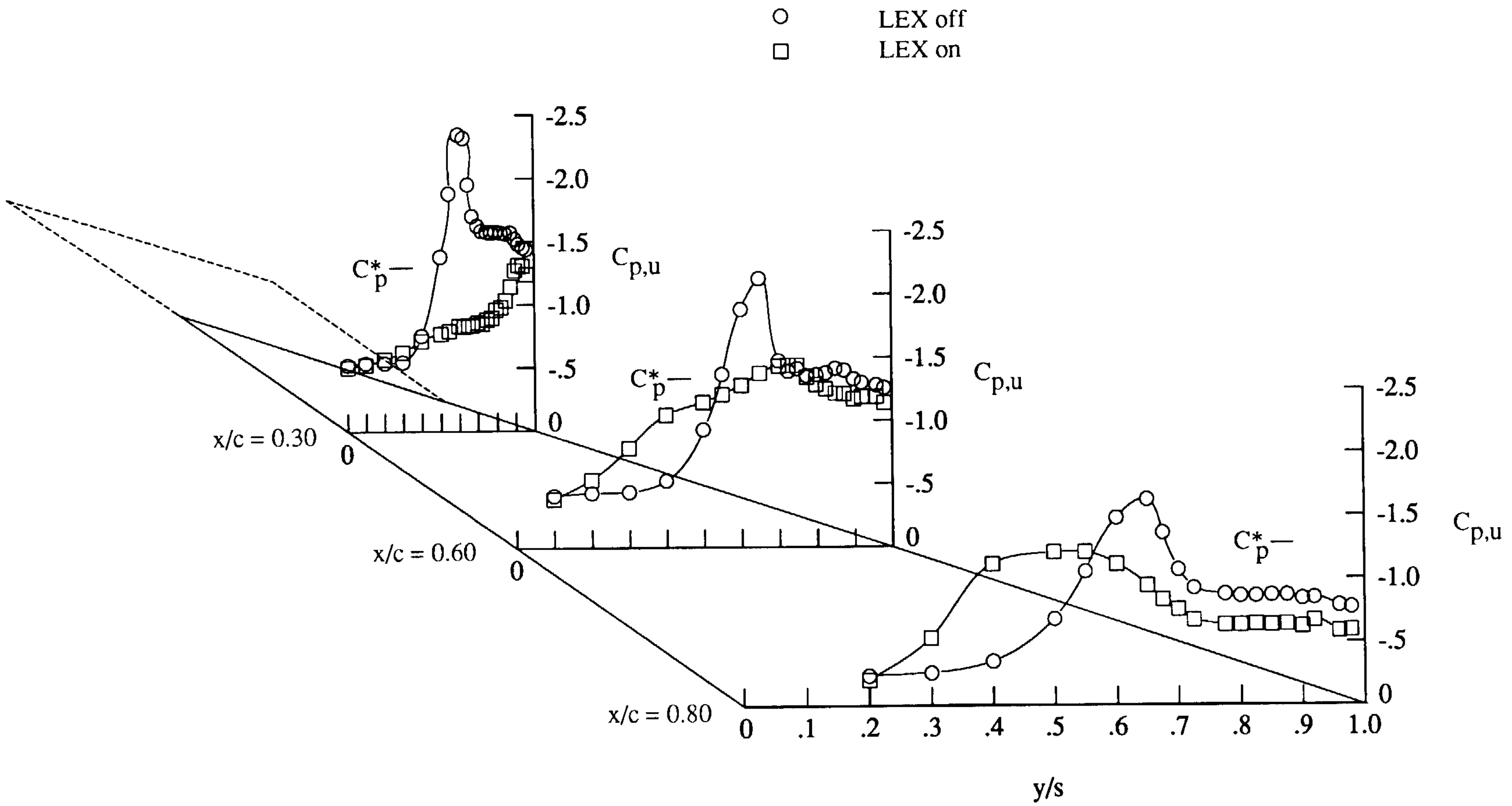

(b) $\alpha = 20°$.

Figure 138. Continued.

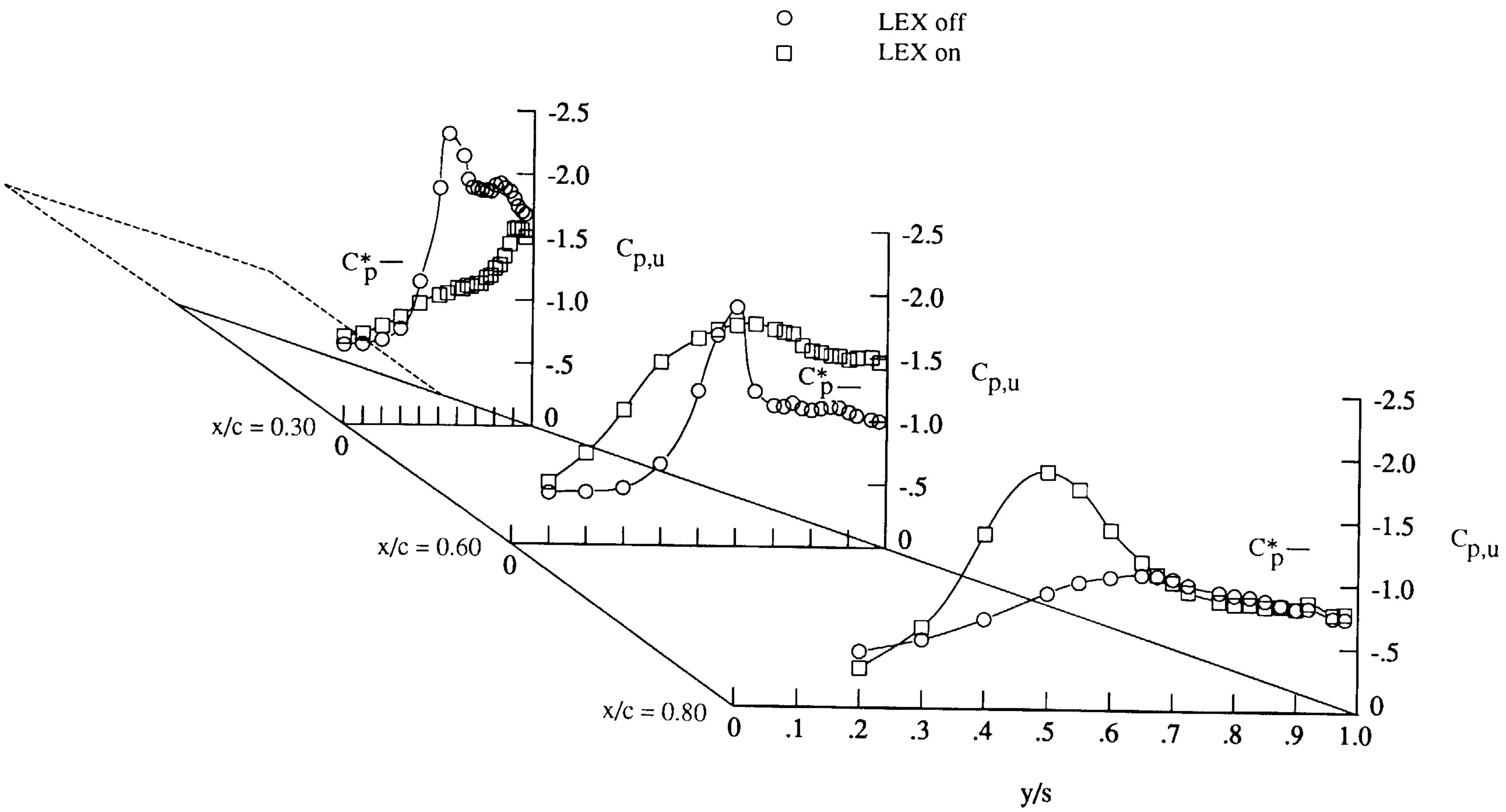

(c) $\alpha = 24°$.

Figure 138. Concluded.

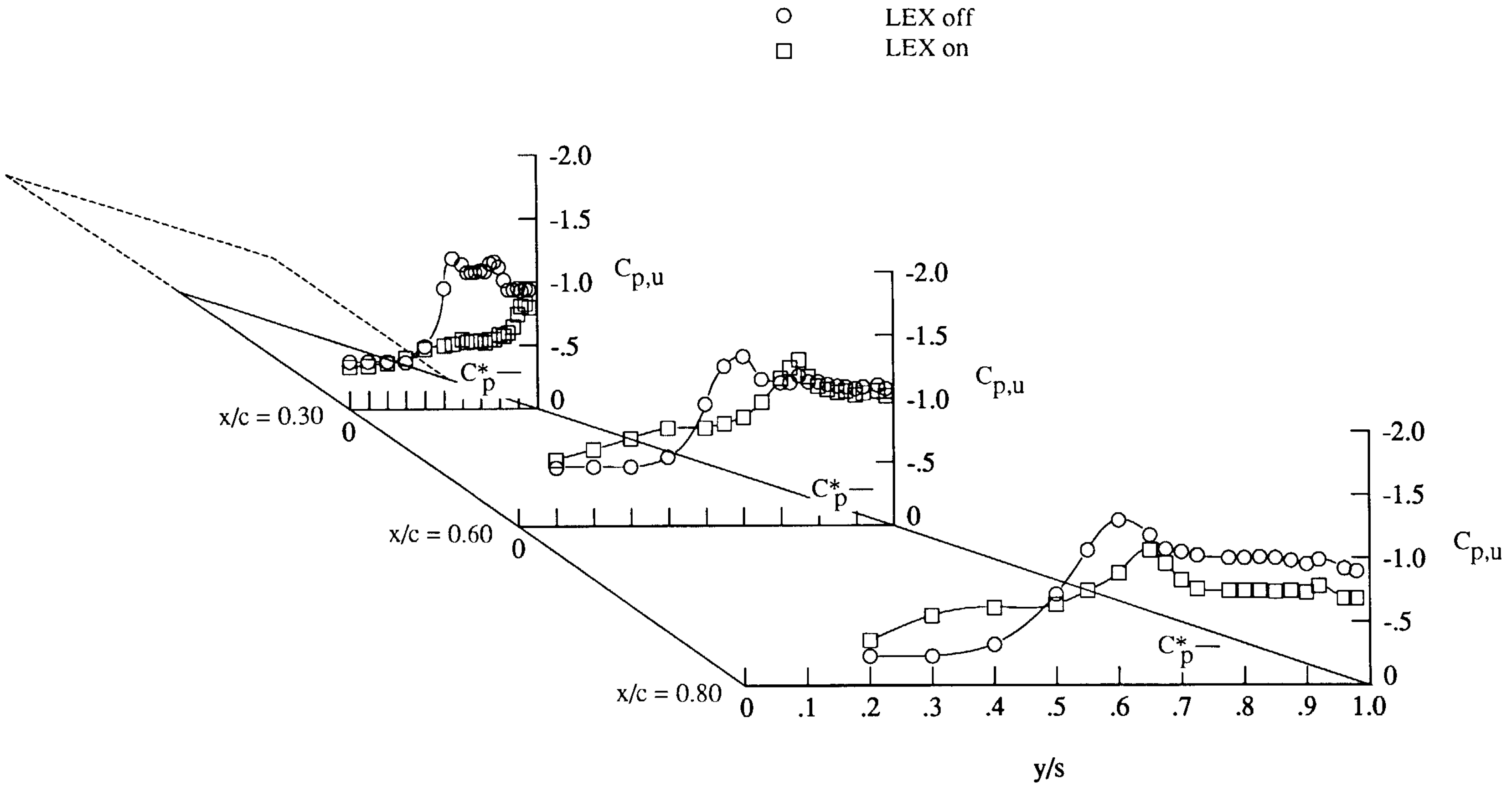

(a) $\alpha = 16°$.

Figure 139. Effect of LEX on wing upper surface static pressure distributions with $M_\infty = 0.85$.

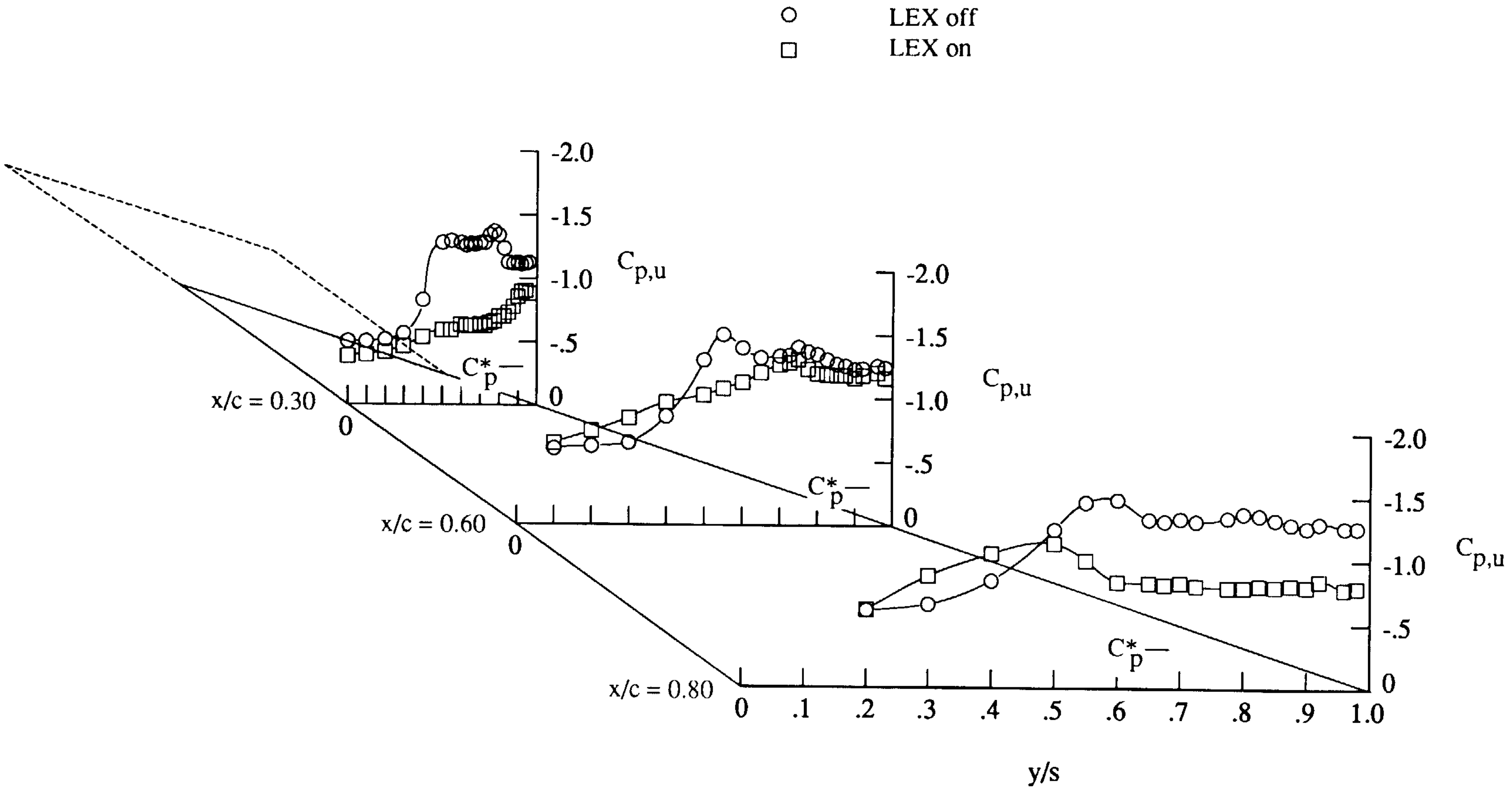

(b) $\alpha = 20°$.

Figure 139. Continued.

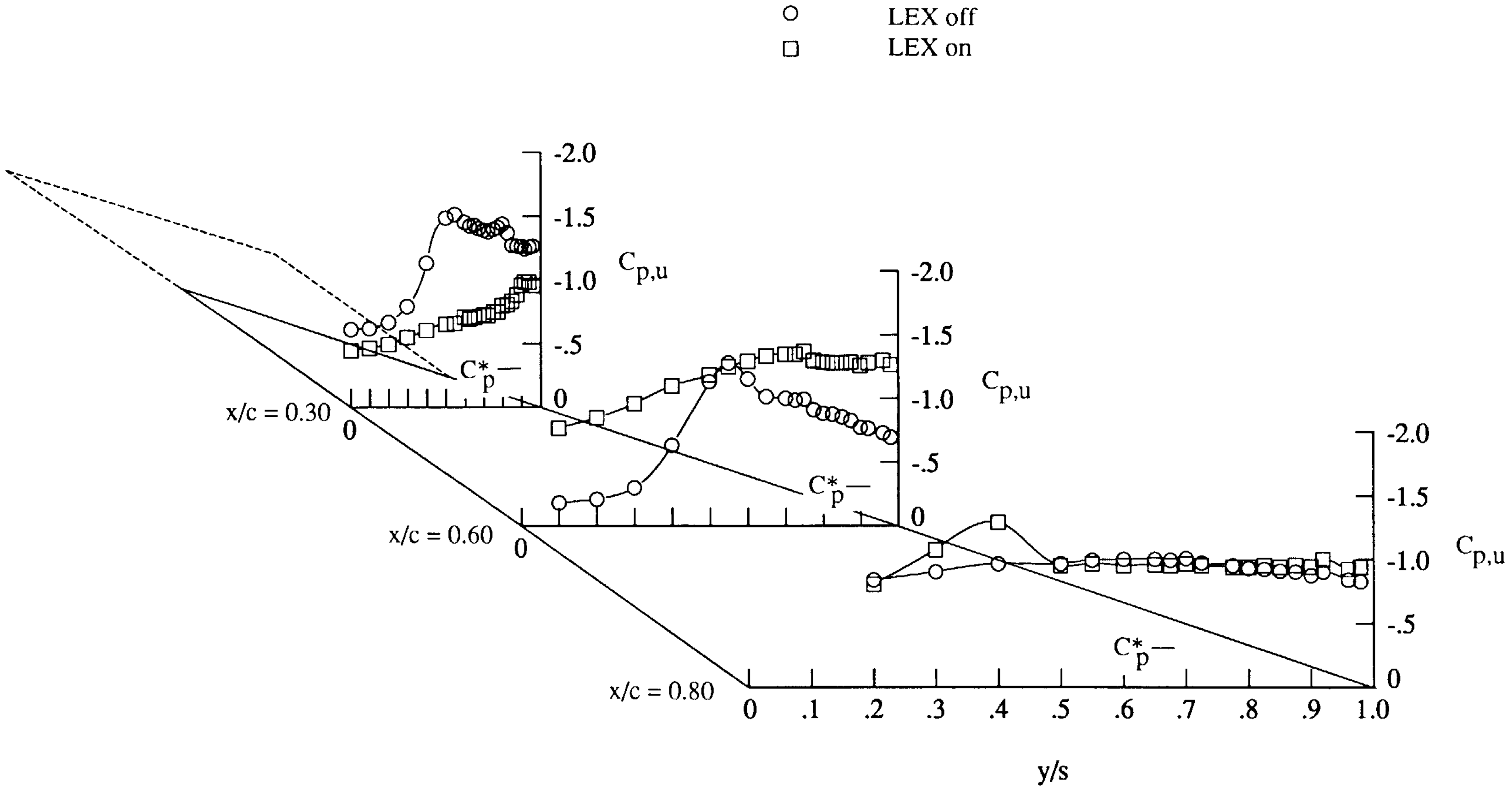

(c) $\alpha = 24°$.

Figure 139. Concluded.

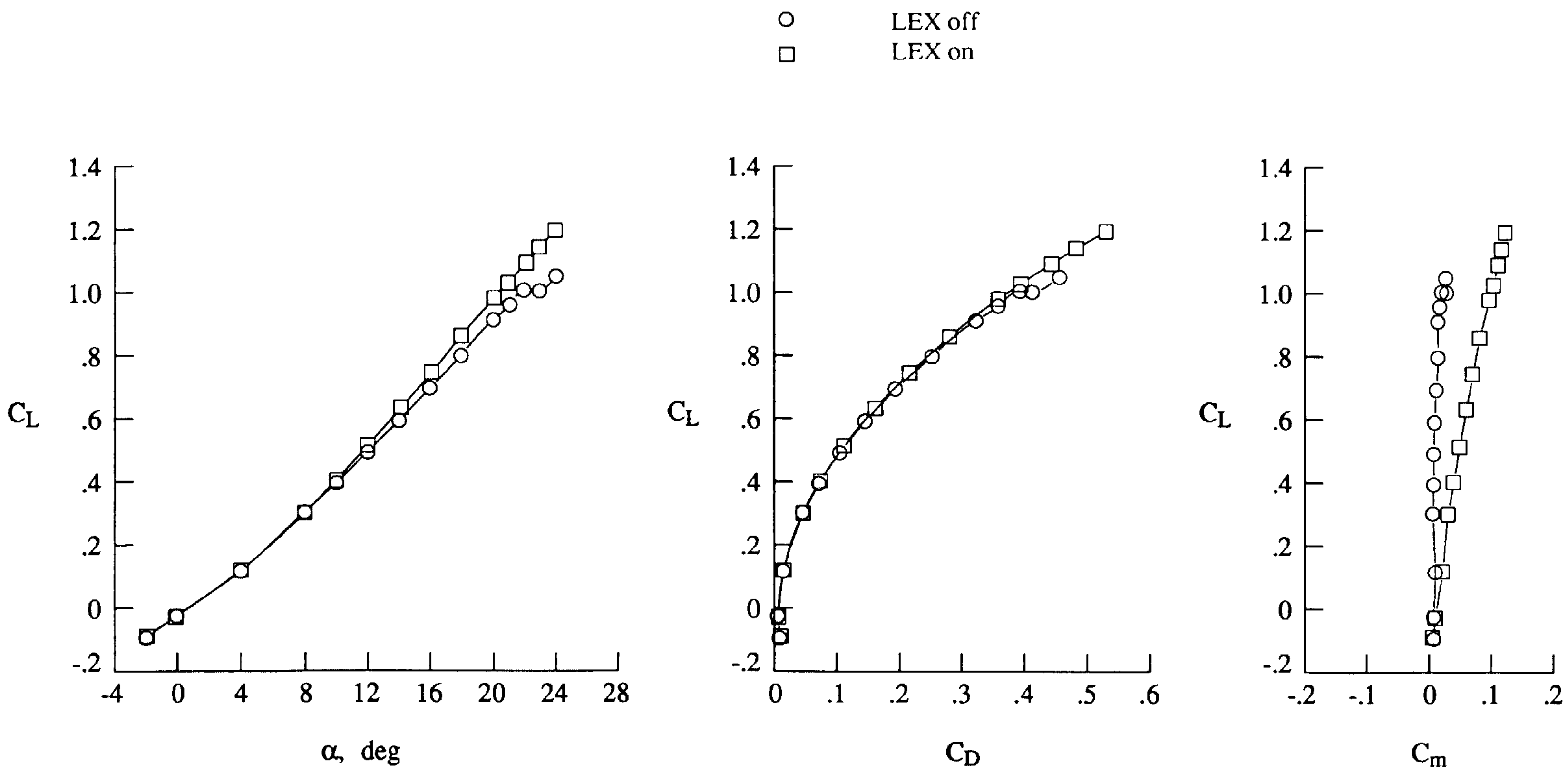

Figure 140. Effect of LEX on lift, drag, and pitching-moment characteristics with $M_\infty = 0.40$.

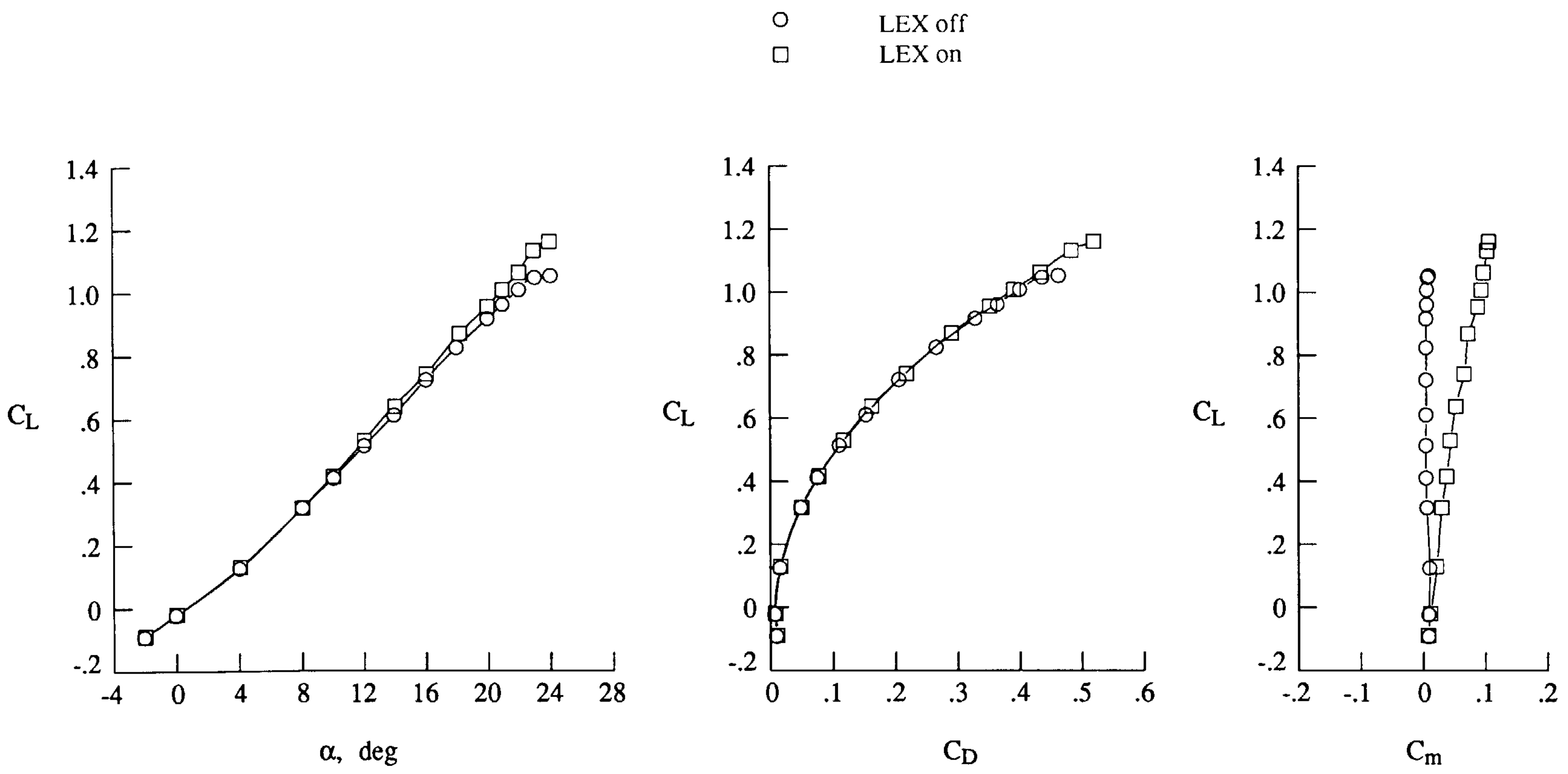

Figure 141. Effect of LEX on lift, drag, and pitching-moment characteristics with $M_\infty = 0.60$.

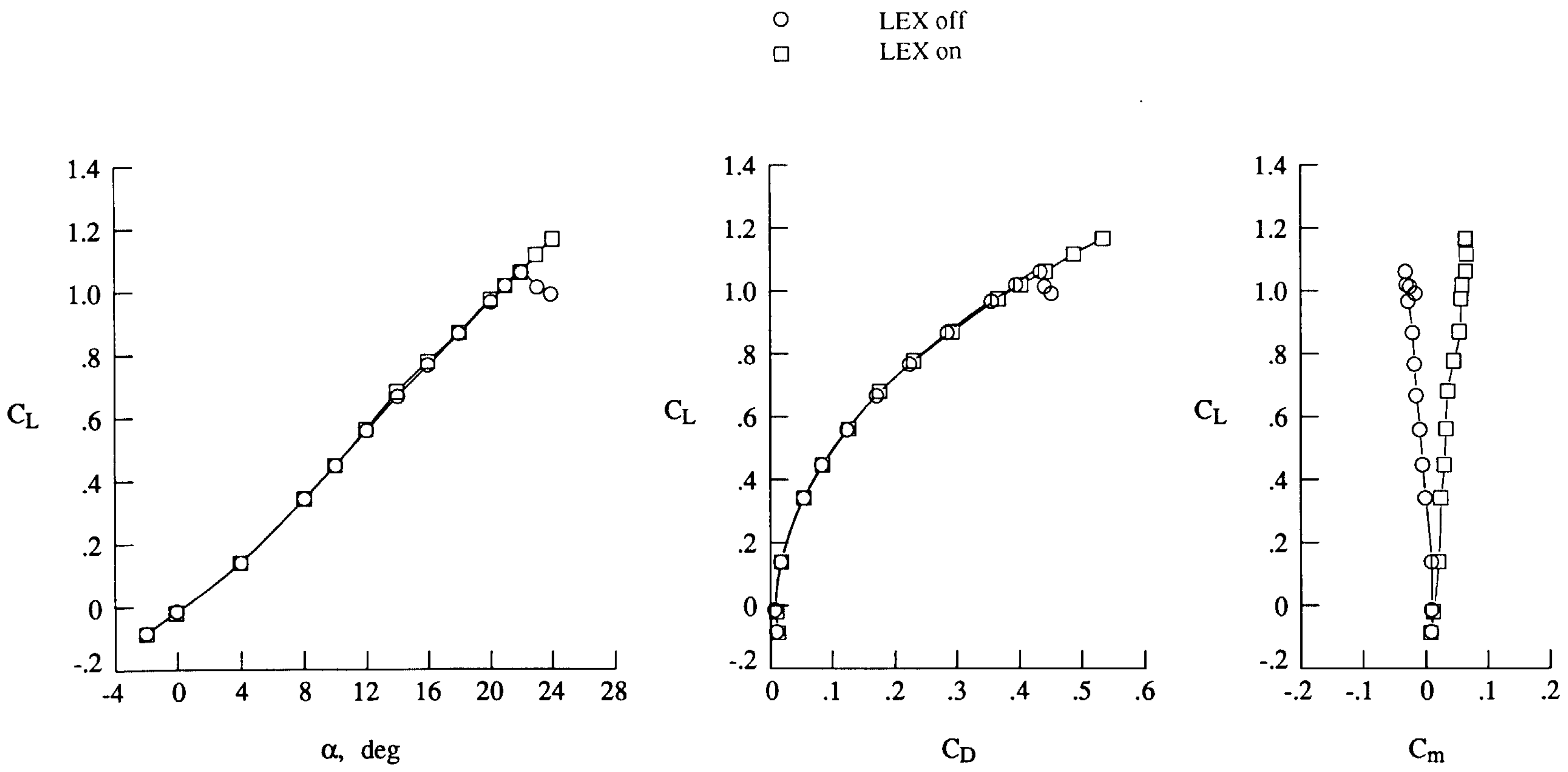

Figure 142. Effect of LEX on lift, drag, and pitching-moment characteristics with $M_\infty = 0.80$.

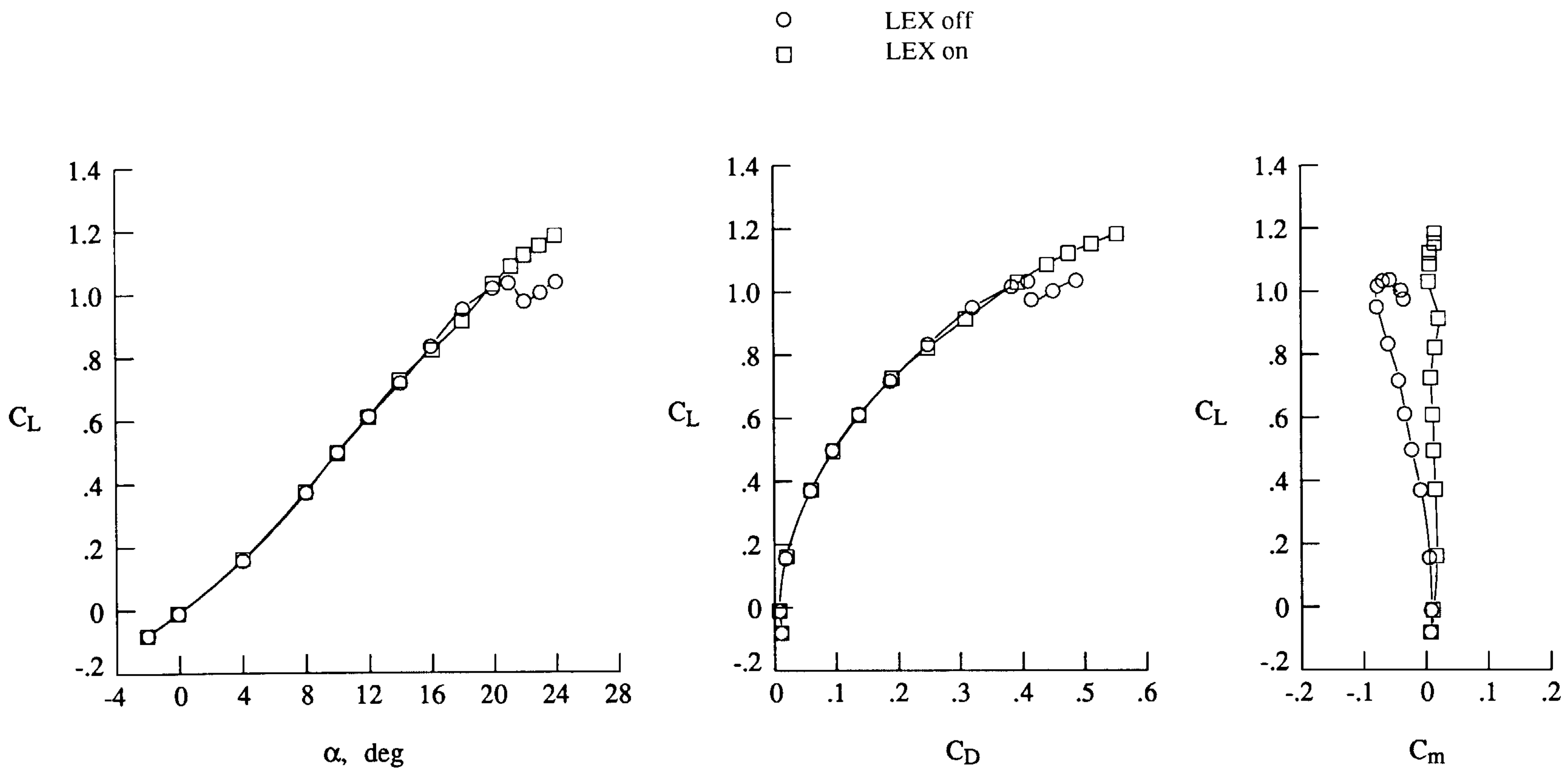

Figure 143. Effect of LEX on lift, drag, and pitching-moment characteristics with $M_\infty = 0.90$.

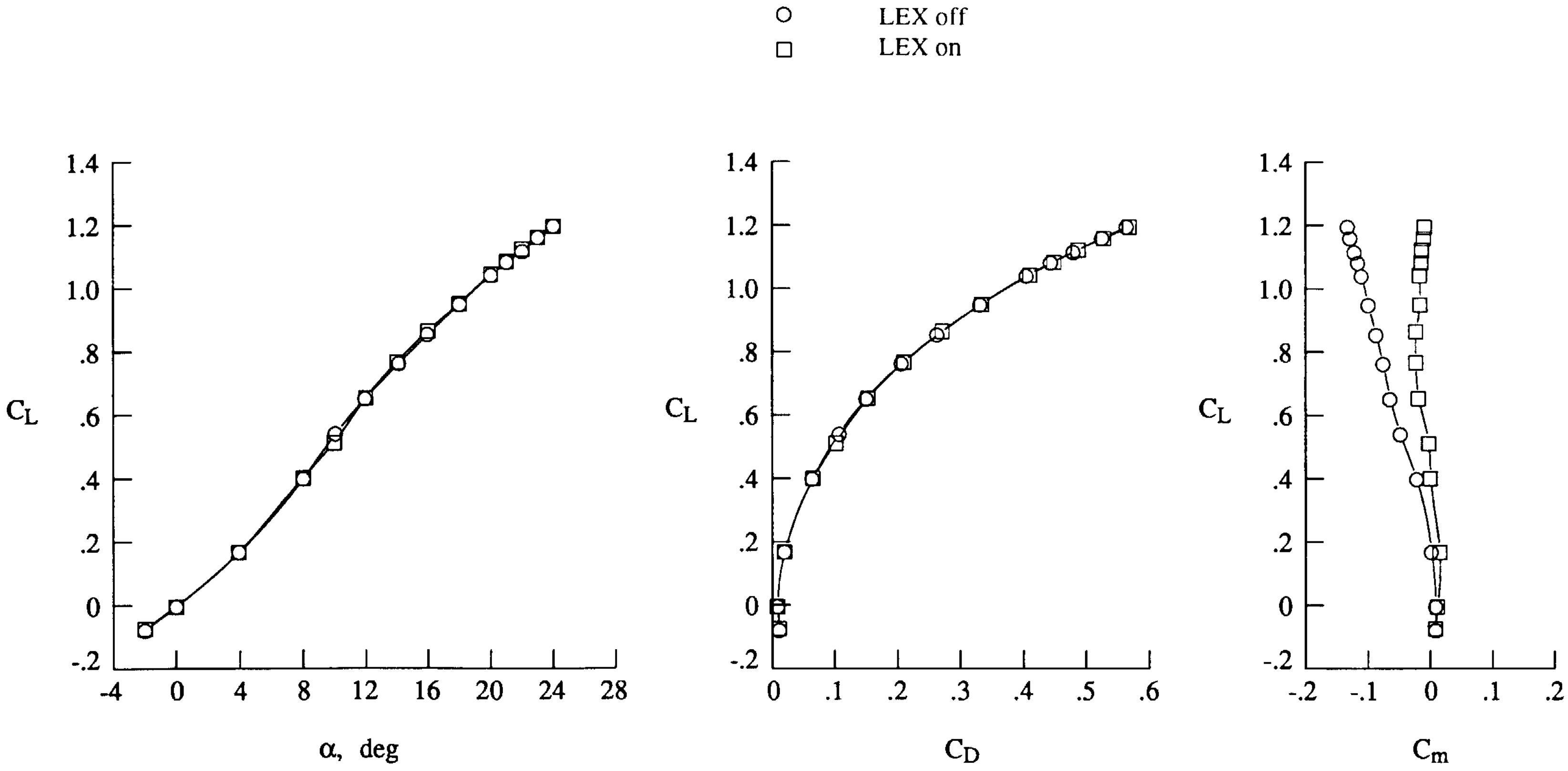

Figure 144. Effect of LEX on lift, drag, and pitching-moment characteristics with $M_\infty = 0.95$.

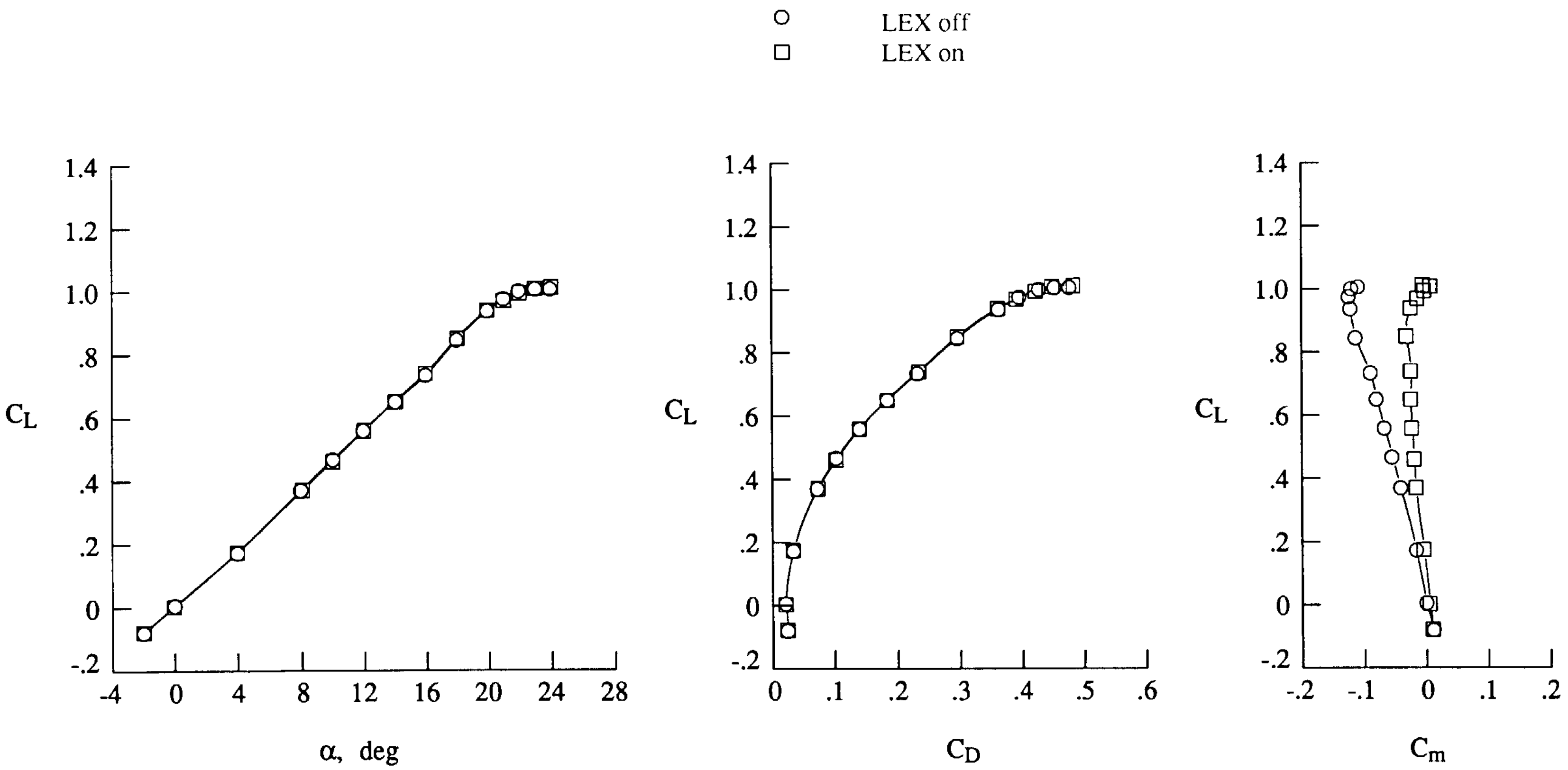

Figure 145. Effect of LEX on lift, drag, and pitching-moment characteristics with $M_\infty = 1.20$.

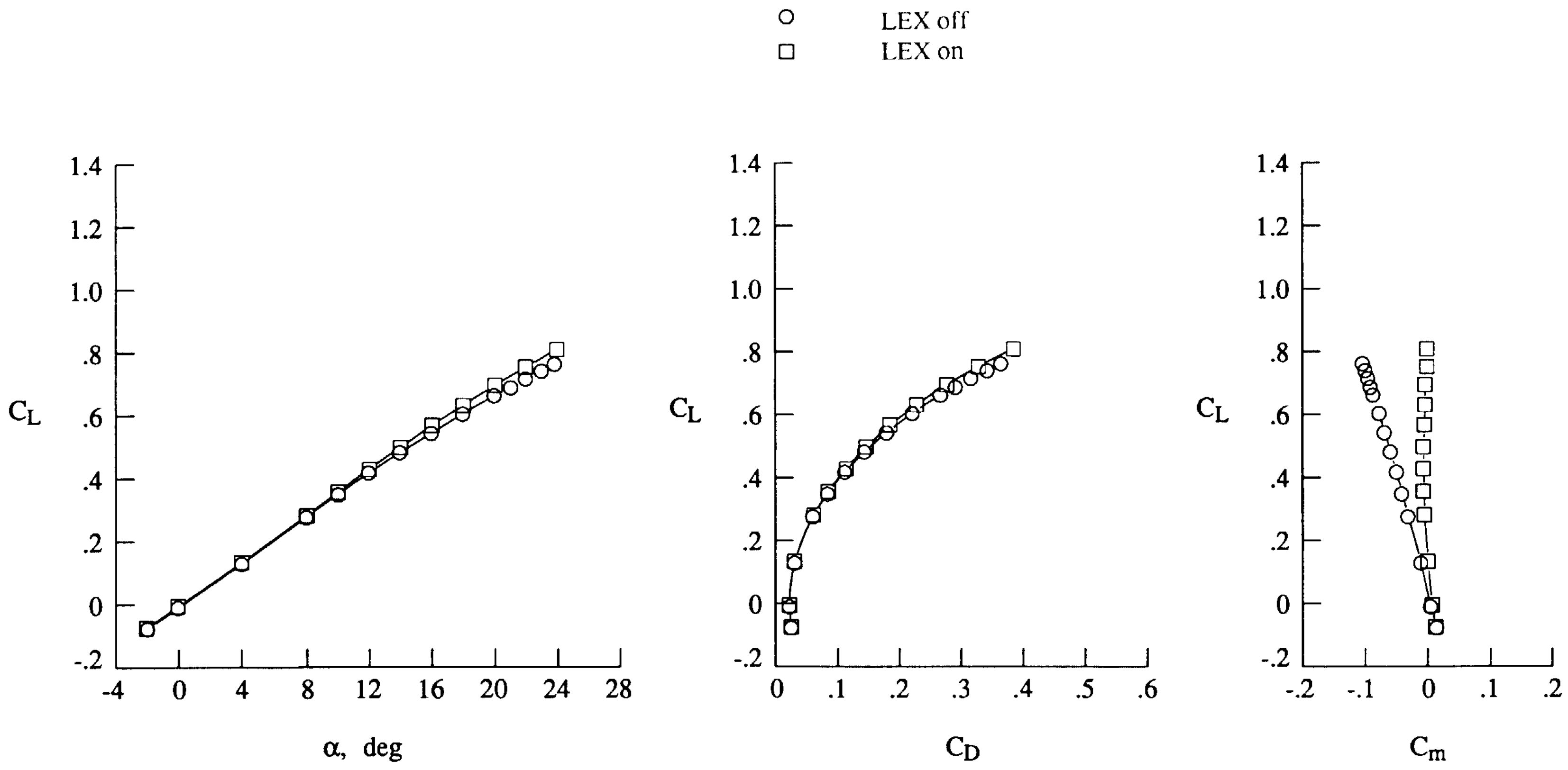

Figure 146. Effect of LEX on lift, drag, and pitching-moment characteristics with $M_\infty = 1.60$.

REPORT DOCUMENTATION PAGE	*Form Approved* *OMB No. 0704-0188*

1. AGENCY USE ONLY*(Leave blank)*	**2. REPORT DATE** November 1991	**3. REPORT TYPE AND DATES COVERED** Technical Paper

4. TITLE AND SUBTITLE Wind Tunnel Investigation of the Interaction and Breakdown Characteristics of Slender-Wing Vortices at Subsonic, Transonic, and Supersonic Speeds	**5. FUNDING NUMBERS** WU 505-68-71-03
6. AUTHOR(S) Gary E. Erickson	
7. PERFORMING ORGANIZATION NAME(S) AND ADDRESS(ES) NASA Langley Research Center Hampton, VA 23665-5225	**8. PERFORMING ORGANIZATION REPORT NUMBER** L-16803
9. SPONSORING/MONITORING AGENCY NAME(S) AND ADDRESS(ES) National Aeronautics and Space Administration Washington, DC 20546-0001	**10. SPONSORING/MONITORING AGENCY REPORT NUMBER** NASA TP-3114

11. SUPPLEMENTARY NOTES

12a. DISTRIBUTION/AVAILABILITY STATEMENT Unclassified–Unlimited Subject Category 02	**12b. DISTRIBUTION CODE**

13. ABSTRACT *(Maximum 200 words)*

The vortex-dominated aerodynamic characteristics of a generic model of a 65° cropped delta wing were studied in a wind tunnel at subsonic through supersonic speeds. The lee-side flow fields over the wing-alone configuration and the wing with a leading-edge extension (LEX) added were observed at free-stream Mach numbers from 0.40 to 1.60 using a laser vapor screen technique. These results were correlated with surface streamline patterns, upper surface static pressure distributions, and six-component forces and moments. The wing-alone model exhibited vortex breakdown and asymmetry of the breakdown location at subsonic and transonic speeds. An earlier onset of vortex breakdown over the wing occurred at transonic speeds because of the interaction of the leading-edge vortex with a normal shock wave. The development of a shock wave between the vortex and wing surface caused an early separation of the secondary boundary layer. With the LEX installed, wing vortex breakdown and vortex breakdown asymmetry did not occur up to the maximum angle of attack of 24° in the present test. The favorable interaction of the LEX vortex with the wing flow field reduced the effects of shock waves on the wing primary and secondary vortical flows. The direct interaction of the wing and LEX vortex cores diminished with increasing Mach number. The maximum attainable vortex-induced pressure signatures were constrained by the vacuum pressure limit at the transonic and supersonic speeds.

14. SUBJECT TERMS Vortex flows; Subsonic flow; Transonic flow; Supersonic flow; Leading-edge extension; Vortex interactions; Vortex breakdown; Flow visualization; Shock waves	**15. NUMBER OF PAGES** 223 **16. PRICE CODE** A10

17. SECURITY CLASSIFICATION OF REPORT Unclassified	**18. SECURITY CLASSIFICATION OF THIS PAGE** Unclassified	**19. SECURITY CLASSIFICATION OF ABSTRACT**	**20. LIMITATION OF ABSTRACT**

NSN 7540-01-280-5500

Standard Form 298(Rev. 2-89)
Prescribed by ANSI Std. Z39-18
298-102

NASA-Langley, 1991

National Aeronautics and
Space Administration
Code NTT

Washington, D.C.
20546-0001

National Aeronautics and
Space Administration

Washington, D.C.
20546

SPECIAL FOURTH CLASS MAIL
BOOK

L2 001 TP-3114 911120S090569A
NASA
CENTER FOR AEROSPACE INFORMATION
ACCESSIONING DEPT
P O BOX 8757 BWI ARPRT
BALTIMORE MD 21240